APPLIED COMPUTATIONAL ELECTROMAGNETICS SOCIETY JOURNAL

January 2020
Vol. 35 No. 1
ISSN 1054-4887

The ACES Journal is abstracted in INSPEC, in Engineering Index, DTIC, Science Citation Index Expanded, the Research Alert, and to Current Contents/Engineering, Computing & Technology.

The illustrations on the front cover have been obtained from the research groups at the Department of Electrical Engineering, The University of Mississippi.

THE APPLIED COMPUTATIONAL ELECTROMAGNETICS SOCIETY
http://aces-society.org

EDITORS-IN-CHIEF

Atef Elsherbeni
Colorado School of Mines, EE Dept.
Golden, CO 80401, USA

Sami Barmada
University of Pisa, ESE Dept.
56122 Pisa, Italy

ASSOCIATE EDITORS: REGULAR PAPERS

Mohammed Hadi
Kuwait University, EE Dept.
Safat, Kuwait

Alistair Duffy
De Montfort University
Leicester, UK

Wenxing Li
Harbin Engineering University
Harbin 150001, China

Maokun Li
Tsinghua University
Beijing 100084, China

Mauro Parise
University Campus Bio-Medico of Rome
00128 Rome, Italy

Yingsong Li
Harbin Engineering University
Harbin 150001, China

Riyadh Mansoor
Al-Muthanna University
Samawa, Al-Muthanna, Iraq

Antonio Musolino
University of Pisa
56126 Pisa, Italy

Abdul A. Arkadan
Colorado School of Mines, EE Dept.
Golden, CO 80401, USA

Salvatore Campione
Sandia National Laboratories
Albuquerque, NM 87185, USA

Wei-Chung Weng
National Chi Nan University, EE Dept.
Puli, Nantou 54561, Taiwan

Alessandro Formisano
Seconda Universita di Napoli
81031 CE, Italy

Piotr Gas
AGH University of Science and Technology
30-059 Krakow, Poland

Long Li
Xidian University
Shaanxa, 710071, China

Marco Arjona López
La Laguna Institute of Technology
Torreon, Coahuila 27266, Mexico

Paolo Mezzanotte
University of Perugia
I-06125 Perugia, Italy

Luca Di Rienzo
Politecnico di Milano
20133 Milano, Italy

Lei Zhao
Jiangsu Normal University
Jiangsu 221116, China

Sima Noghanian
University of North Dakota
Grand Forks, ND 58202, USA

Qiang Ren
Beihang University
Beijing 100191, China

Nunzia Fontana
University of Pisa
56122 Pisa, Italy

Atif Shamim
King Abdullah University of Science and Technology (KAUST)
Thuwal 23955, Saudi Arabia

Stefano Selleri
DINFO – University of Florence
50139 Florence, Italy

ASSOCIATE EDITORS: EXPRESS PAPERS

Lijun Jiang
University of Hong Kong, EEE Dept.
Hong, Kong

Shinichiro Ohnuki
Nihon University
Tokyo, Japan

Kubilay Sertel
The Ohio State University
Columbus, OH 43210, USA

Steve J. Weiss
US Army Research Laboratory
Adelphi Laboratory Center (RDRL-SER-M)
Adelphi, MD 20783, USA

Jiming Song
Iowa State University, ECE Dept.
Ames, IA 50011, USA

Amedeo Capozzoli
Univerita di Napoli Federico II, DIETI
I-80125 Napoli, Italy

Yu Mao Wu
Fudan University
Shanghai 200433, China

Maokun Li
Tsinghua University, EE Dept.
Beijing 100084, China

EDITORIAL ASSISTANTS

Matthew J. Inman
University of Mississippi, EE Dept.
University, MS 38677, USA

Madison Le
Colorado School of Mines, EE Dept.
Golden, CO 80401, USA

Shanell Lopez
Colorado School of Mines, EE Dept.
Golden, CO 80401, USA

Allison Tanner
Colorado School of Mines, EE Dept.
Golden, CO 80401, USA

EMERITUS EDITORS-IN-CHIEF

Duncan C. Baker
EE Dept. U. of Pretoria
0002 Pretoria, South Africa

Allen Glisson
University of Mississippi, EE Dept.
University, MS 38677, USA

Ahmed Kishk
Concordia University, ECS Dept.
Montreal, QC H3G 1M8, Canada

Robert M. Bevensee
Box 812
Alamo, CA 94507-0516, USA

Ozlem Kilic
Catholic University of America
Washington, DC 20064, USA

David E. Stein
USAF Scientific Advisory Board
Washington, DC 20330, USA

EMERITUS ASSOCIATE EDITORS

Yasushi Kanai
Niigata Inst. of Technology
Kashiwazaki, Japan

Alexander Yakovlev
University of Mississippi, EE Dept.
University, MS 38677, USA

Levent Gurel
Bilkent University
Ankara, Turkey

Mohamed Abouzahra
MIT Lincoln Laboratory
Lexington, MA, USA

Ozlem Kilic
Catholic University of America
Washington, DC 20064, USA

Erdem Topsakal
Mississippi State University, EE Dept.
Mississippi State, MS 39762, USA

Sami Barmada
University of Pisa, ESE Dept.
56122 Pisa, Italy

Fan Yang
Tsinghua University, EE Dept.
Beijing 100084, China

Rocco Rizzo
University of Pisa
56123 Pisa, Italy

William O'Keefe Coburn
US Army Research Laboratory
Adelphi, MD 20783, USA

EMERITUS EDITORIAL ASSISTANTS

Khaled ElMaghoub
Trimble Navigation/MIT
Boston, MA 02125, USA

Christina Bonnington
University of Mississippi, EE Dept.
University, MS 38677, USA

Kyle Patel
Colorado School of Mines, EE Dept.
Golden, CO 80401, USA

Anne Graham
University of Mississippi, EE Dept.
University, MS 38677, USA

Mohamed Al Sharkawy
Arab Academy for Science and Technology, ECE Dept.
Alexandria, Egypt

JANUARY 2020 REVIEWERS: REGULAR PAPERS

Sajjad Abazari Aghdam
Danial Abdorahimi
Erkan Afacan
Ghulam Ahmad
Iftikhar Ahmed
Rodolfo Araneo
Sami Barmada
Toni Björninen
Fangyuan Chen
Xunwang Dang
Sisir Das
Pasquale Dottorato
Alistair Duffy
Nunzia Fontana
Andrey Grigoriev
Yingsong Li
Yue Li
Raja Mchaalia
James McLean
Zohre Motevalli
Syeda Naqvi
Truong Khang Nguyen
Antonio Orlandi
John J. Pantoja
Camelia Petrescu
Lionel Pichon
Shi Pu
C.J. Reddy
Guo Shuai
Sellakkutti Suganthi
Steven Weiss
Xiaohua Yi

THE APPLIED COMPUTATIONAL ELECTROMAGNETICS SOCIETY JOURNAL

Vol. 35 No. 1 January 2020

TABLE OF CONTENTS – REGULAR PAPERS

A Portable Through-Wall Microwave Imaging System

Huseyin Aniktar

Sensor and Antenna Systems Group
Tubitak Bilgem, Gebze, Kocaeli P.O. 74, 41470, Turkey
huseyin.aniktar@tubitak.gov.tr

Abstract **─** A microwave imaging system requires the design and implementation of an imaging algorithm, a sufficiently sensitive/accurate vector network analyzer, and antennas. This work presents a simple imaging algorithm, design and implementation of a low-cost VNA and antennas that are able to operate at 4 - 6 GHz. The commercial VNAs are of general purpose and are too expensive for microwave imaging applications. The design trade-offs applied to VNA are presented and implemented circuits are demonstrated. Using the presented VNA, a hand-held imaging system is implemented that extracts scattering parameters to create the target image. S-parameters obtained from the pre-selected filters with the designed VNA are provided to demonstrate the quality of the design. Target images are created for a couple of commonly used walls to demonstrate the overall system performance.

Index Terms **─** Vector Network Analyzer, imaging and scattering, through-wall imaging.

I. INTRODUCTION

Microwave imaging systems have received more attention from researchers and engineers over the last decade. Especially, they have a frequent usage and importance in biomedical applications [1 - 4]. Typically, these systems collect the scattering parameters while the target object is illuminated with a microwave source. The scattering parameters are used to detect any disease signature and 2D/3D image creation. In the literature, different inversion algorithms are applied to the collected scattering data to create the target image [1 - 3, 7 - 9]. The hardware used to collect the scattering parameters must be able to differentiate the returning microwave energy when the target is available or not.

Another application area of the microwave imaging systems is in defense industry [5, 6]. Through-wall imaging utilizes the inverse-scattering techniques to create the image of the room. Nowadays, through-wall imaging technology is an important element of the counter-surveillance applications for most cities. The electromagnetic inverse-scattering approaches require the measurement capability of signal parameters like the magnitude and the phase. Most of the works presented in the literature use costly and heavy network analyzers to generate and receive microwave signals. In this work, a low-cost vector network analyzer (VNA) is designed and implemented for hand-held microwave imaging purpose. The implemented network analyzer is low cost, low power, light, and compact. The network analyzer has moderate performance according to its size, cost, and power consumption.

Microwave imaging has lots of application areas. Some of them are briefed as follows. A microwave imaging system with a portable and low-cost form might be a good option for these applications:

- Medical imaging for seeking diagnoses.
- Civil engineering purposes for examining deterioration and strength of structures.
- Security reasons for seeking bug, weapon and any other objects.

The paper is organized as follows: Part 1 is the introduction. Part 2 is the system description which explains the microwave imaging main ideas. Part 3 gives the VNA implementation steps and procedure. Part 4 gives the measurement results for both as a point of VNA and as a point of microwave imaging system. In Part 4 VNA performance is also compared to a COTS product to show the system performance level. The last part concludes the paper.

II. MICROWAVE IMAGING SYSTEM DESCRIPTION

The implemented microwave imaging system is presented in this section. The block diagram of the imaging system is given in Fig. 1. As shown in Fig. 1, the system consists of an antenna, RF/microwave circuit optimized for system specifications, digitizer, DSP (Digital Signal Processing) unit, and the main CPU (Central Processing Unit) to run the user imaging application. RF/Microwave circuit, digitizer, and DSP processing blocks constitute the main elements of a Vector Network Analyzer. The implementation detail of VNA is introduced in the next chapter.

The fundamental idea of microwave imaging systems is based on the measurement of reflected

Submitted On: September 27, 2018
Accepted On: January 2, 2020

electromagnetic energy from the target. The simplest scenario occurs when the target is placed in the same environment with the antenna without any obstacles between them. An amount of electromagnetic energy is absorbed by the target object and the rest is reflected back to the antenna.

The system will capture the returning energy to measure the inverse-scattering parameters in order to create the image. The system must be able to capture the differentiation at the inverse-scattering parameters when an object is placed in front of the antenna. When the antenna is placed over (X, Y) axes and electromagnetic energy flows through Z axis. Assume that the target object is placed at Z axis with a distance of 'z' from the antenna. g(z) is defined as scattering function for the points reflecting electromagnetic energy back to the antenna. The reflected electromagnetic field expression is written when we assume that the phase differentiation happens only at Z axis,

$$G(f) = \int_{-\infty}^{\infty} g(z) e^{-j2kz}\, dz\,, \tag{1}$$

where G(f) is the reflected electromagnetic field expression, and k is the wave number. In order to pass from frequency domain to space domain the expression given in (2) is used,

$$g(z) = \int_{-\infty}^{\infty} G(f) e^{-j2\pi f z}\, df\,. \tag{2}$$

It is easily seen that g(z) and G(f) constitute the Fourier Transformation pair. Therefore, the object image, g(z), is formed by applying Inverse Fourier Transformation to the reflected electromagnetic field expression of G(f) [8].

However, a target object is nearby to some other objects or in a different environment than the antenna in most of the applications in real world. In these cases, the clutter coming from unwanted objects or environment must be removed from the analysis as much as possible in order to obtain a meaningful image.

An example application is the through-wall imaging (TWI) [6 - 8]. In this kind of problems, the wall is between the target and antenna. The reflection from wall must be subtracted to measure the inverse scattering parameters reflected back from the target object. Therefore, the clutter reduction techniques must be applied to remove wall effect from the measurements [8].

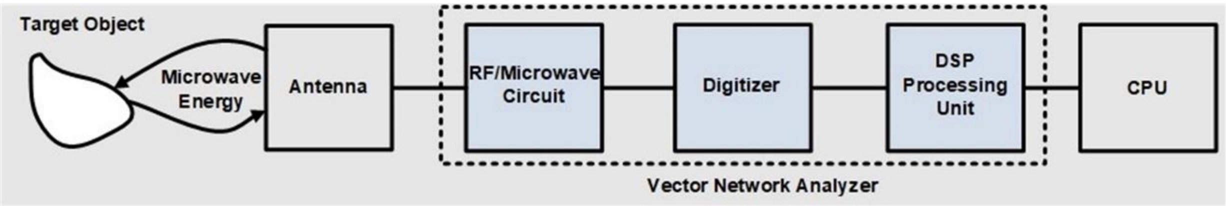

Fig. 1. The block diagram of implemented microwave imaging system.

III. VECTOR NETWORK ANALYZER IMPLEMENTATION

A network analyzer is a measurement equipment used to characterize a circuit (DUT- device under test) behavior. It draws out the transfer function of the DUT according to the known input signal and extracts the vector scattering parameters such as the complex reflection and the transmission coefficients.

Network analyzers might be considered in three categories. Scalar Network Analyzer (SNA) is a network analyzer that just characterizes the amplitude response of DUT. Vector Network Analyzer (VNA) characterizes both the amplitude and the phase response of DUT and extracts S-parameters. Vector Network Analyzers may be constructed incoherent or noncoherent fashion [12]. Recently, coherent VNA architectures are the most commonly used in measurement equipment since they provide larger measurement dynamic range, lower noise floor and ease of control. Coherent VNA's require tuned RF receiver/transmitter circuits and they require highly stable Phase Locked Loops to maintain the coherency. Noncoherent VNA designs are cheaper and simpler alternatives to expensive and complex coherent VNAs. Noncoherent VNAs consist of a kind of a Scalar Network Analyzer and some additional blocks to extract the vectorial information. Some examples for the noncoherent vector network analyzers are given in [10 - 13]. The third group is Large Signal Network Analyzers (LSNA) and they characterize the large signal behavior of DUT like linearity, harmonics, etc.

This work presents the implementation details of a coherent vector network analyzer to be used in a microwave imaging system. The description for the complete microwave imaging system is also provided.

A. Implementation details of VNA

The fundamental assessment of VNA lies on the sensitivity for the extraction of frequency response of a DUT. In order to achieve this, the system generates a signal at the target operating frequency and sends to DUT. Some of the electromagnetic energy is reflected back to the antenna and the system must be able to capture it. VNA has separate signal paths for the reference and the measurement channel. By utilizing the reference and the measurement channel signals, the phase and the magnitude responses of DUT are going to be calculated. This chapter presents the design of a miniature sized VNA and the design trade-offs.

VNA is commonly used as a laboratory measurement system. These systems are quite costly, heavy and it is almost impossible to utilize it in a portable system. There are different techniques to design low cost, miniature sized VNA in the literature. The operating frequency of VNA is one of the most important design parameters similar to other RF systems. As the operating frequency increases, the behavior of circuit/ system components changes and VNA performance starts to deviate from the design specifications. Therefore, at higher frequencies, the error of VNA starts to increase as well. For very high frequency applications, highly sensitive circuits and components must be used to bound the generated error. The most important design specification for VNA is the phase synchronization of a system at the operating frequency band. In order to satisfy this requirement, RF signal sources and the reference clock source for the digitizer must be common for the measurement and the reference channel. Another important design hint for the phase synchronized VNA design is the signal path equalization of the reference and measurement channel.

Each component in reference or measurement channel has its own phase and magnitude response. It is a good design practice to balance the circuit path for measurement and reference channel to reduce the mismatch between reference and measurement channels. The layout of the RF and the digitizer circuits is another important design concern since the path equalization is a critical requirement for the accuracy of phase and magnitude measurement. Wire lengths and properties are equalized for respective parts on the measurement and reference channels. It compensates the distortions generated by the circuit layout. The most challenging issue when to balance the reference and measurement channel is the input power levels that flow on each channel. The power level for the reference channel is a lot higher than the measurement channel. When the same circuit component is used on both channels, it puts a limit on the dynamic range of VNA. Still, it is impossible to get rid of all unbalances between the reference and measurement channel. The calibration procedure will be implemented to remove the residual errors on the measurements.

VNA is composed of four main blocks namely RF signal source, downconverter block, digitizer, and DSP block as shown in Figs. 2 and 3. Figure 2 shows S11 configuration of VNA, and Fig. 3 shows S21 configuration of VNA. Details of the DSP block are illustrated in Fig. 5. The first block is RF signal source and it generates the RF signal at a given frequency. RF signal is sent to target object by means of an antenna. Simultaneously, the generated RF signal is fed to the reference signal channel by utilizing a coupler. The critical design metric for the coupler is the RF isolation between the reference and the measurement channels. For the ideal VNA design, none of the reflected signals should be available on the reference channel and vice versa. On the other hand, in practical VNA systems, the reflected electromagnetic signal enters to the reference channel as well and it degrades the accuracy and the sensitivity of these systems. The reflected electromagnetic signal is fed to the measurement channel by use of a coupler. The sent and the received RF signals must be down converted to an IF frequency in order to get digitized.

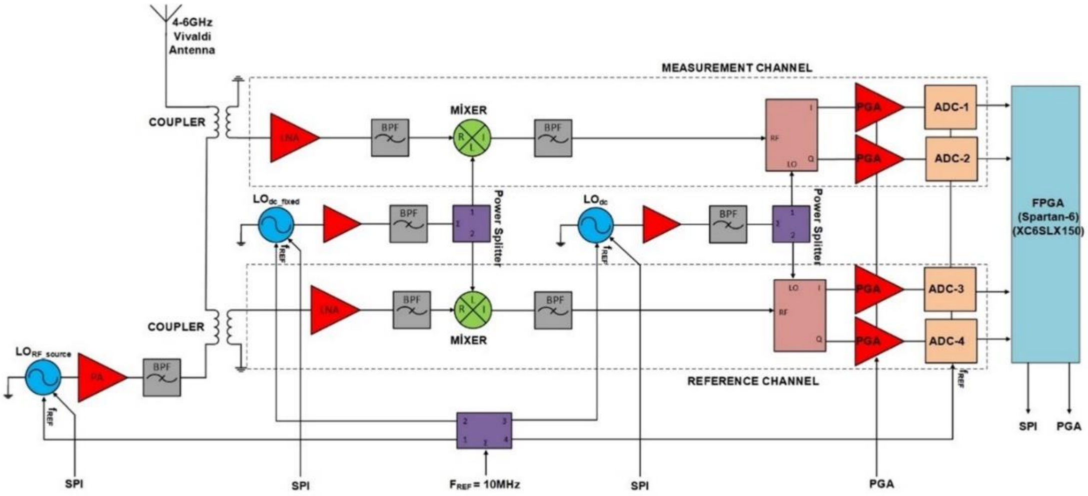

Fig. 2. Block diagram of implemented VNA as S11 configuration for imaging purpose.

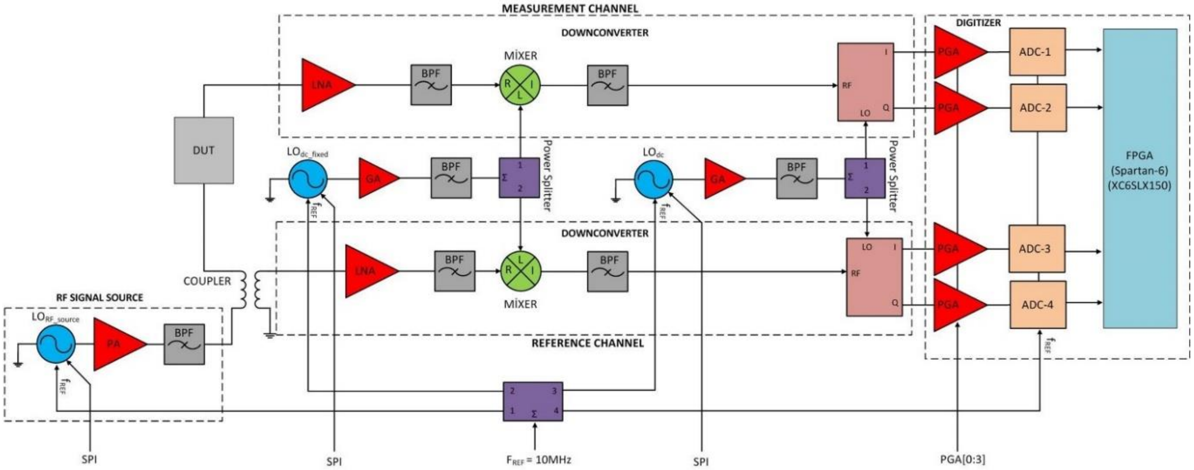

Fig. 3. Block diagram of implemented VNA as S21 configuration for component test.

The second part of the VNA system is the downconverter block. The RF signals on the measurement and reference channel must be down converted to an IF signal that can be properly digitized by an available ADC. In order to prevent any phase mismatch between the reference and magnitude channel, the same local oscillator (LO) outputs must be fed to the mixer stage with the symmetrically designed layout. Homodyne and heterodyne are two design options for the downconverter implementations. We designed two stages heterodyne downconverter scheme. It allows us to use an I/Q demodulator to generate quadrature signals as presented in Fig. 2. Heterodyne downconverter allows us to increase the operating bandwidth of the design. The photography of the implemented circuit blocks is given in Fig. 4. The coupler is used as COTS product from Lynx Components. It is a 10 dB coupler from 2 GHz to 8 GHz with around 40 dB isolation.

Fig. 4. Photography of the circuit blocks. (Downconverter, RF signal source, and FPGA block).

The digitizer is the third block of the VNA system, and its task is to convert the analog signals coming from I and Q paths on the reference and the measurement channel. Therefore, four ADC channels are required, and they must be simultaneously sampled channels. The digitizer is based on FPGA block and ADC unit. FPGA block is used as COTS product from Opal Kelly. This FPGA block is on our implemented four channel ADC mezzanine board. The most critical issue with this block is the successful implementation of phase synchronized design. The sampling clock for each ADC must be synchronous with each other. Otherwise, the measured phase and magnitudes include a large amount of error. In order to alleviate this design constraint, a quad 14-bit ADC chip with a single encode clock (Linear Technology LTC 2171) is utilized. The encode clock is fed to PLL block to generate the sampling clock and it is distributed to all ADC cores within the same IC. The digitized outputs are in serial LVDS (Low Voltage Differential Signaling) format and deserialization is implemented by the FPGA core. The serial LVDS output format is used to reduce the pin count needed to capture ADC data by FPGA core since there are 4 ADC cores in the system. The digitized data from four channels will be used to calculate the phase and the magnitude of each signal at the reference and measurement channels. It will be discussed in the digital signal processing part.

The last element of VNA is the Digital Signal Processing block. This block performs the data capture, and the arithmetic calculations implemented within FPGA fabric. The quad ADC outputs are converted to parallel data format by SerDes (Serializer/Deserializer) using the common frame and data bit clocks. This common clocking scheme ensures the phase coherency at the digitizer part. The applied arithmetic operations are given in Fig. 5. Phase Comparator operator shown in Fig. 5 is used to project all phase results to a defined range of [-π, π] as defined in (3):

$$\begin{matrix} \text{phase}=\text{phase}\ ,\pi>phase>-\pi \\ \text{phase}=\text{phase}-2\pi\ ,\text{phase}>\pi \\ \text{phase}=\text{phase}+2\pi\ ,\text{phase}<-\pi \end{matrix}. \tag{3}$$

The phase and magnitude calculations are averaged over 128 measurement samples to reduce erroneous measurements as shown in Fig. 5. The averaging method fails to provide the accurate results when the phase result approaches to limits namely {-π, π} since calculated phase values may cancel each other. In order to prevent this possibility, Phase Corrector operator is used. The operation of this block is defined in (4). Phase [0] is the first element of 128 measured phase results. In this way, the phase calculations at the limits are successfully implemented:

$$\begin{matrix} \text{phase}=-\text{abs}(\text{phase}) ,-170^{o}>phase[0]>-180^{o} \\ \text{phase}=\text{abs}(\text{phase}) ,180^{o}>phase[0]>170^{o} \end{matrix}, \tag{4}$$

Thru calibration is handled to extract the innate phase and magnitude calibration parameters to cancel the effect imposed from VNA hardware. The S parameters are obtained after canceling out the thru calibration parameters as shown in Fig. 5.

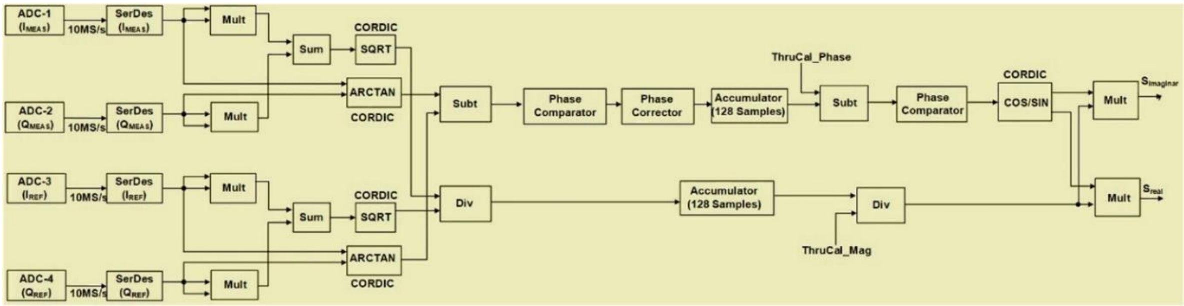

Fig. 5. Block diagram of DSP data path for S-parameter measurements.

Another important design metric of VNA is the sensitivity. The sensitivity of the system is determined by the noise figure, IF bandwidth and the sensitivity of the down converter and ADC bit width. The circuit sensitivity is calculated as follows:

$$\text{Sensitivity} = -174\text{dBm} + \text{NF} + \text{SNR} + 10\log(\text{BW}), \tag{5}$$

where SNR is the signal-to-noise ratio, and NF is the circuit noise figure in dB, BW is in Hz.

IF bandwidth is 100 kHz and operating frequency band is 4 - 6 GHz. The measured dissipated power is 19.424 W when the system is fully functional. The power dissipation map for each voltage source and circuit block is given in Table 1. The performance values handled on the VNA are listed in Table 2.

For SNR value of 10 dB, NF value of 14 dB and IF bandwidth of 100 kHz, the system sensitivity is estimated approximately as -100 dBm.

Table 1: Power map for each voltage source

Voltage Source (V)	RF Circuit (mA)	Digitizer & FPGA (mA)	10 MHz Clock (mA)	Total Power (W)
1.8	-	200	-	0.36
3.3	288	-	910	3.95
5	634	1728	-	11.81
12	275	-	-	3.3

Table 2: Implemented VNA specifications

Frequency (GHz)	IF BW (kHz)	Resolution (MHz)	NF (dB)	User Interface
4 - 6	100	1	14	USB

B. 4 - 6 GHz Vivaldi antenna

The Vivaldi antennas are traveling wave antennas having UWB (ultra-wideband) impedance matching and endfire radiation characteristics. The biggest advantage provided by the microstrip structure is its ability to be connected directly with the TR (Transmission-Receiver) modules placed behind it. The antenna needs no additional component for impedance matching with its integrated balun structure. This type of antenna is more suitable for imaging applications since its electrical characteristics [14, 15].

The antenna used for microwave imaging application is 4 - 6 GHz Vivaldi antenna. In the design and optimization of the antenna, numerical studies are carried on by using Computer Simulation Technologies Microwave Studio (CST MWS) which is mathematically based on Finite Integration Technique (FIT) [16]. It is very beneficial methodology to solve geometrically and structurally complex electromagnetic problems. In FIT, integral form of Maxwell's equations are discretely reformulated and then they become more suitable for computer calculations both in frequency and time domain analyses. The calculation domain is chosen in the beginning of the simulations and a proper meshing algorithm is applied on the geometry to split it several small grid cells. These cells should be dense enough to represent the curves and inclines very accurately. However, resource requirements are linearly increasing with the numbers of mesh nodes and problem size. A real-world electromagnetic problem usually includes more than one medium such as metallic surfaces and dielectric substrates. FIT allows to analyze a grid cell including two different materials which provides sparser mesh. Hence, electrically large structures can be simulated with minimum computational cost. User interface of CST MWS offers time and frequency domain solvers. The number of the simulation runs are proportional to the field monitors having discrete frequencies in frequency domain solver. In this study, time domain solver is used because it has ability to define and calculate a large number of filed monitors for the whole operating frequency band in one simulation run. FR-4 material is employed as substrate and its' specifications are used as in material library of CST MWS. The metallic parts of the antenna are assigned as perfect electric conductor (PEC). The antenna is meshed by using hexahedral mesh type resulting in approximately 5 million grid cells. Antenna port impedance is chosen as 50 Ω and it is excited by a Gaussian pulse which is default excitation waveform of CST MWS. The simulation is terminated when remaining energy in calculation domain reaches 40 dB less than of its' maximum value.

The photography and radiation pattern of the designed antenna is given in Figs. 6 and 7. Far-field gain of the antenna is measured as 5.8 dBi and 6 dBi at 4 GHz and 6 GHz respectively. S11 measurement results are -14.57 dB at 4 GHz and -18.75 dB at 6 GHz. The size of the antenna is 42 mm x 82 mm.

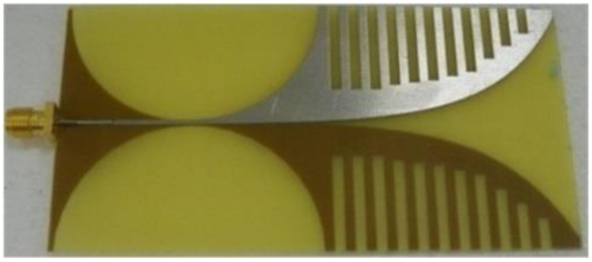

Fig. 6. 4 - 6 GHz Vivaldi antenna photography.

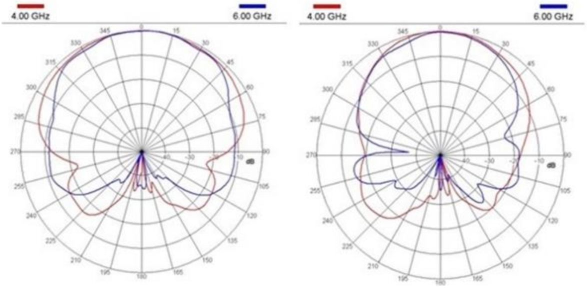

Fig. 7. Azimuth and elevation radiation patterns.

C. Calibration

One port calibration (Short, Open, Load) SOL method is applied to measure the errors and calibrate the VNA measurement system [10]. Scattering parameters are all about power; both reflected and the incident in a linear two-port system. It assumes that the system must be treated like a transmission line system. At first, the VNA system assumes that there is no measurement error and then short, open and load calibration kit measured respectively. The reference and the measurement channels are saved simultaneously. The phase coherencies of both channels are important for exact calibration. The magnitude and the phase errors between the reference and measurement channels are calculated. In the end, the correction factors are used to calculate the S parameters of DUT.

IV. MEASUREMENTS

In this section, S11-S21 magnitude and phase measurements with our low-cost miniature VNA and Agilent E8362C network analyzer are compared. The low-cost VNA is also used in the application of through-wall imaging system. Imaging system performance is also illustrated in this section.

A. S-parameter measurements

The low-cost miniature VNA performance is compared with Agilent E8362C VNA network analyzer as a reference. For comparison purpose, a bandpass filter is selected as a sample circuit namely Lorch 5000 (center frequency is 5 GHz and passband is 1.1 GHz, from Lorch Comp.). The filter response is measured with the Agilent VNA and the implemented low-cost VNA system. 2001 data points are collected between 4 - 6 GHz and the results are provided in Figs. 8 and 9. Magnitude and phase measurements of S11 and S21 with COTS and implemented VNA are reasonably close to each other.

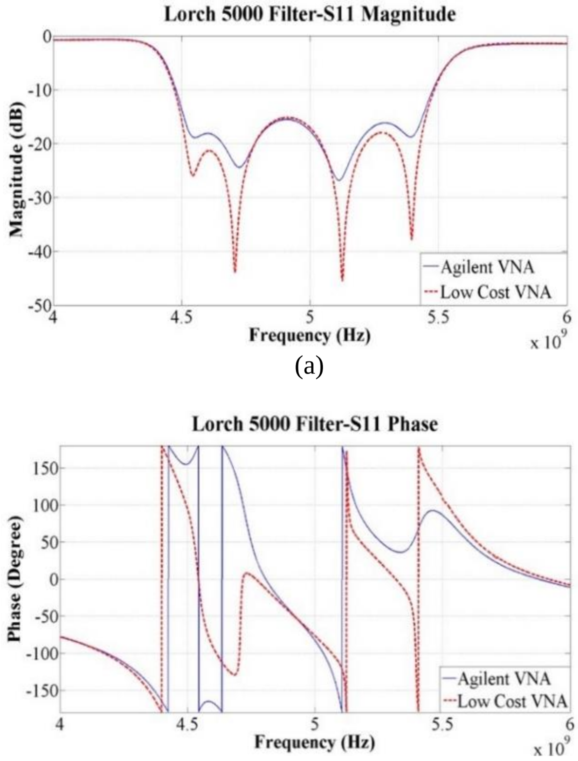

(a)

(b)

Fig. 8. Magnitude (a) and phase (b) measurements of S11 for Lorch 5000 filter.

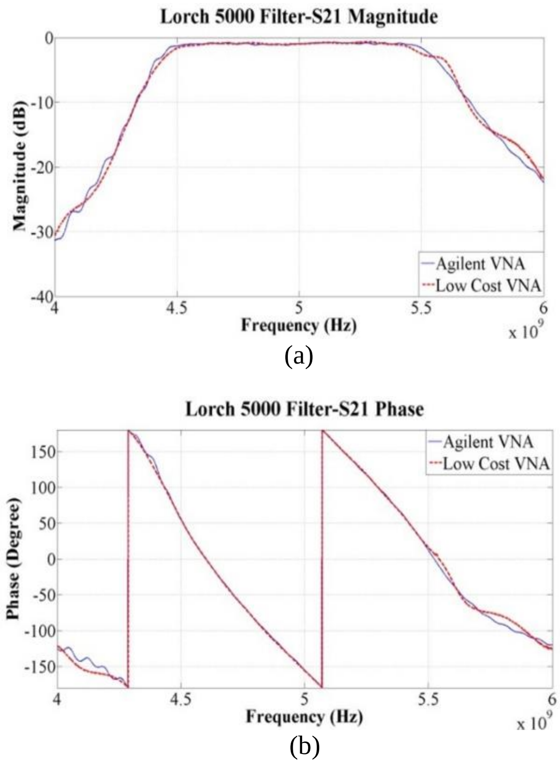

(a)

(b)

Fig. 9. Magnitude (a) and phase (b) measurement of S21 for Lorch 5000 filter.

B. Through-wall imaging measurements

Through-wall imaging (TWI) is targeting to illustrate the physical position and the orientation of objects behind the wall. As aforementioned, it is possible to create such an image by measuring dielectric properties of objects sitting another side of the wall. The differentiation of these properties makes it possible to create a snapshot of the target region. The system must be able to send high-frequency electromagnetic waves to the wall and measure the returning waves. The S-parameter measurement setup given in Fig. 1 used along with the DSP algorithm given in Fig. 5 is realized. The antenna is shown in Fig. 6 is used in the system.

In this work, S11 radar imaging method is implemented based on IFFT which is expressed in (1) and (2). Imaging antenna is moved on (X, Y) coordinates with 2 cm steps to cover 50 cm x 50 cm scanning region. The designed VNA scans from 4 GHz to 6 GHz with 1MHz steps and measures the S11-parameter at each (X, Y) point and this data converted to space domain by applying (2). This is basically a “Step Frequency Continuous Wave Radar” application. VNA system collects 2001 frequency data for each (X, Y) coordinate with 2 GHz bandwidth and 1 MHz step size. 4 - 6 GHz operating frequency selection is based on penetration depths on wall and resolution. When the frequency is lower, the penetration capability is better. On the other hand, when the frequency is higher, target resolution is better. There is a tradeoff. Bandwidth is also another important parameter for range resolution which is inversely proportional.

S11 measurements are taken at 625 points with 25 x 25 coordinate points. At each point reflected electromagnetic energy (G(f)) is measured on z-direction. For each (X, Y) coordinates, an image is composed based on reflected energy. Image resolution is improved by using bicubic interpolation.

The wall has a 5 cm thickness and 3 different objects are placed behind the wall. Measurement test setup and the prototype of the portable microwave imaging system are illustrated in Fig. 10. Red object is 4 x 50 x 4 cm^3 iron pipe, the yellow object is 4.5 x 4.5 cm^2 aluminum plate, and the gray object is 6 x 6 cm^2 printed circuit board. The covered region is 50 cm x 50 cm and the spacing resolution is 2 cm. 25 x 25 measurements are taken. S11 measurements are taken at 625 points.

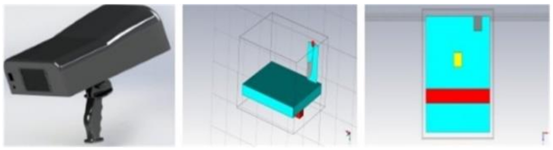

Fig. 10. Prototype of the imaging system and test setups illustrated in CST Microwave Studio.

The S parameter measurement results are fed to host PC with USB 2.0 connectivity to capture results and generate the image of the target region. In order to generate the image of the target region, the position information of the antenna is required and it is measured with a laser sensor that is connected to the sensor head. The measured S-parameters and calibration data are fed to the imaging algorithm based on IFFT [7]. The user must provide the frequency range and the frequency resolution information to FPGA and the final S-parameter results are fed back to the host user. The obtained S-parameter values are fed to final image creation algorithm. The outputs of IFFT are used to create the image of the target object using position information coming from laser sensors. Laser sensors are connected to the host PC with a RS232 interface.

In the development of the imaging algorithm, CST MWS is used to simulate the test environment. Time domain solver is also employed during these simulations and accuracy level is chosen as -40 dB with approximately 150 million meshes. The target objects and the test environment are modeled for the electromagnetic simulation to get accurate results to compare the actual result with the simulations. The S-parameters collected from the electromagnetic simulation is applied to image creation algorithm to create the images. In this way, the algorithm development becomes faster and easier. The image creation algorithm is optimized by using this method.

The image created from real data with portable microwave imaging system and the EM simulation data are illustrated in Figs. 11 and 12. The results are quite similar, and it shows that the model parameters for the environment and the target objects are properly set.

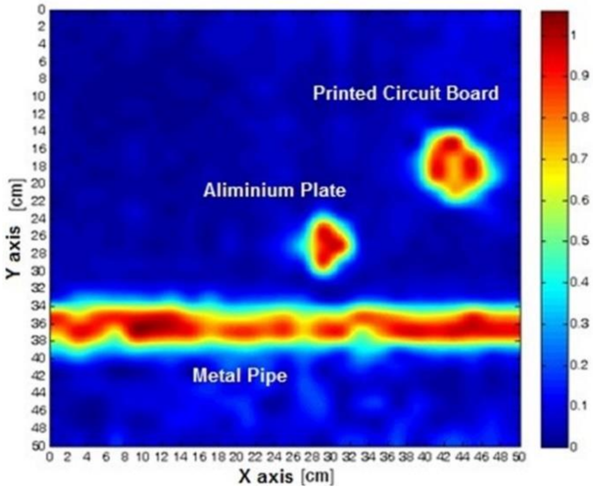

Fig. 11. Created image with portable imaging system.

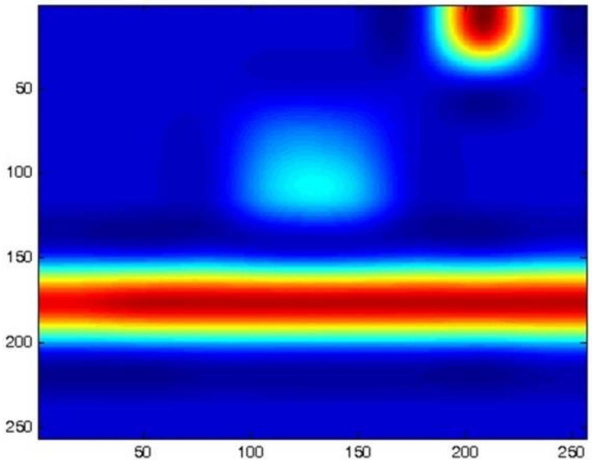

Fig. 12. Simulated image on CST MWS.

The same measurement setup is used to create the image of the object at different depth behind a wall made of different materials. In this way, it is possible to draw a relation between wall materials and wall thickness. The target object is a 5 cm x 5 cm metal plaque and the wood is the worst wall that can be imaged. In Table 3, through-wall imaging measurement results are given for different materials and depths. TWI radar has the capability to detect any objects through the wall based on dielectric contrast from the surrounding medium. The reflected signal depends on the size of the object and wavelength.

Table 3: Imaging performances for different walls

Smooth Plane Material	Target Object	Depth (cm)	Target Object Resolution
YTONG	Metal	10	5cm x 5cm
MARBLE	Metal	12	5cm x 5cm
WOOD	Metal	4	5cm x 5cm

V. CONCLUSION

In this work, a portable network analyzer, antenna and imaging algorithm design and implementations are presented. A low-cost portable VNA implementation is described step by step. Implemented network analyzer is capable to measure the S-parameters with a sufficient accuracy. The implemented microwave imaging system is capable of creating images of objects behind the wall with a simple IFFT imaging algorithm. Even high performances in harsh environments will be possible by employing more sophisticated algorithms.

Implemented portable VNA size is approximately 20cm x 30cm x 11cm, the weight is about 2kg, and the cost is less than 1500 dollars.

Portable imaging systems are good candidates for using on the investigation of infrastructure, wall and building strengths. It is also capable of using for medical imaging and electronic intelligence purpose.

ACKNOWLEDGMENT

The author is thankful to Serkan Kaya, Dursun Baran, Enes Karav, Eren Akkaya and Goksenin Bozdag for their contributions on this project.

REFERENCES

[1] B. Gorgi and B. Zakeri, “Time-reversal throughwall microwave imaging in rich scattering environment based on target initial reflection method,” *ACES Journal*, vol. 30, no. 6, pp. 626637, June 2015.

[2] T. Meyer, “Microwave imaging of high-contrast objects,” *Doctoral Dissertation*, Fakultat fur Elektrotechnik und Informationstechnik, Ottovon-Guericke Universitat Magdeburg, 1972.

[3] S. Y. Semenov, A. E. Bulyshev, A. Abubakar, V. G. Posukh, Y. E. Sizov, A. E. Souvorov, P. M. van den Berg, and T. C. Williams, “Microwave-tomographic imaging of the high dielectric-contrast objects using different image-reconstruction approaches,” *IEEE Trans. on Microwave Theory and Tech.*, vol. 53, no. 7, pp. 2284-2294, July 2005.

[4] Q. Fang, P. M. Meaney, and K. D. Paulsen, “Microwave image reconstruction of tissue property dispersion characteristics utilizing multiple-frequency information,” *IEEE Transactions on Microwave Theory and Techniques*, vol. 52, no. 8, pp. 1866-1875, Aug. 2004.

[5] I. Akduman, L. Crocco, and F. Soldovieri, “Experimental validation of a simple system

for through-the-wall inverse scattering," *IEEE Geoscience and Remote Sensing Letters*, vol. 8, no. 2, pp. 258 - 262, Mar. 2011.

[6] R. Solimene, F. Soldovieri, G. Prisco, and R. Pierri, "Three-dimensional through-wall imaging under ambiguous wall parameters," *IEEE Transactions on Geoscience and Remote Sensing*, vol. 47, no. 5, pp. 1310-1317, May 2009.

[7] S. Kaya and İ. Ölçer, "Duvar İçi Mikrodalga Görüntüleme algoritması: Microwave throughwall imaging algorithm," 19, *Sinyal İşleme ve Uygulamaları Kurultayı (SIU 2011)*, Kemer, Antalya, Apr. 2011.

[8] G. L. Charvat, "A low-power radar imaging system," *Doctoral Dissertation*, Michigan State University, East Lansing, MI, 2007.

[9] C. Gilmore, P. Mojabi, and J. LoVetri, "Comparison of an enhanced distorted born iterative method and the multiplicative regularized contrast source inversion method," *IEEE Transactions On Antennas and Propagation*, vol. 57, no. 8, pp. 2341-2351, Aug. 2009.

[10] K. Hoffmann and Z. Skvor, "A novel vector analyzer," *IEEE Transactions on Microwave Theory and Techniques*, vol. 46, no. 12, pp. 2520-2523, Dec. 1998.

[11] A. Fung, L. Samoska, G. Chattopadhyay, T. Gaier, P. Kangaslahti, D. Pukala, C. Oleson, A. Denning, and Y. Lau, "Two-port vector network analyzer measurements up to 508 GHz," *IEEE Transactions on Instrumentation and Measurement*, vol. 57, no. 6, pp. 1166 - 1170, June 2008.

[12] M. A. Abou-Khousa, M. A. Baumgarther, S. Kharkovsky, and R. Zoughi, "Novel and simple high frequency single-port vector network analyzer," *IEEE Transactions on Instrumentation and Measurement*, vol. 59, no. 3, pp. 534 - 542, Mar. 2010.

[13] C.-H. Tseng and T.-H. Chu, "An effective usage of vector network analyzer for microwave imaging," *IEEE Transactions on Microwave Theory and Techniques*, vol. 53, no. 9, pp. 2884 - 2891, Sept. 2005.

[14] R. Q. Lee and R. N. Simons, *Advances in Micro Strip and Printed Antennas*, John Wiley and Sons, USA, 1997.

[15] B. Türetken, U. Buluş, E. Başaran, E. Akkaya, K. Sürmeli, and H. Aniktar, *Microwave and Millimeter Wave Circuits and Systems: Emerging Design, Technologies and Applications*, John Wiley & Sons Publisher, Ch. 17, 2012.

[16] R. Marklein, *Review of Radioscience*, ISBN 9780471268666, Ch. 11, 2002.

Huseyin Aniktar Ph.D. was born in Istanbul, Turkey, in 1977. He received the B.Sc. degree in Electronics Engineering from the Istanbul Technical University, in 1998, and the M.Sc. degree in Electrical and Electronics Engineering from Middle East Technical University, Ankara, in 2001 and Ph.D. degree in electronics engineering from the Aalborg University, Denmark, in 2007. His main areas of research interest are RF and microwave circuits and systems.

A Simple Planar Antenna for Sub-6 GHz Applications in 5G Mobile Terminals

Zhirong An [1] and Mang He [2]

[1] School of Information and Electronics
Beijing Institute of Technology, Beijing, 100081, China
aiyindien@163.com

[2] School of Information and Electronics
Beijing Institute of Technology, Beijing, 100081, China
hemang@bit.edu.cn

Abstract **─** A simple planar antenna for sub-6 GHz applications in 5G mobile terminals is presented. The proposed antenna is composed of one multi-branch driven strip and three parasitic grounded strips, featuring simple design without using three-dimensional structure and lumped elements. The $|S_{11}| \leq$ -6dB impedance bandwidth of the antenna covers 700-960 MHz and 1600-5500 MHz bands with a compact size of 40×15×0.8 mm^3, which makes it fulfill the requirements of sub-6 GHz applications in the 5G terminals. The prototype of the antenna is fabricated, and the design is well validated by experimental results.

Index Terms **─** 5G terminals, multi-mode resonance, planar antenna, sub-6 GHz applications.

I. INTRODUCTION

With the rapid development of wireless communication technologies, 2G/3G/4G standard has been widely used. For current mobile terminal antennas, it is a basic requirement to cover 2G/3G/4G bands, including Long Term Evolution(LTE) 700/2300/2500 (698-787/2300-2400/2500-2690 MHz), UMTS (1920-2170 MHz), GSM 850/900 (824-894/880-960 MHz), DCS (1710-1880 MHz), and PCS (1850-1990 MHz) bands. However, to meet the recently proposed 5G NR standards, i.e., n77 (3300-4200 MHz), n78 (3300-3800 MHz), and n79 (4400-5000 MHz), such bandwidth is not enough. Therefore, it is highly desirable to design a 5G terminal antenna with wideband performance to fully cover all the 2G/3G/4G/5G bands.

Recently, several methods have been proposed to extend the bandwidth of mobile phone antennas, such as using matching networks with lumped elements [1, 2], frequency reconfigurable technique [3, 4], and multi-mode resonance technique [5, 6]. In [1], an octa-band WWAN/LTE monopole antenna with a lumped high-pass matching circuit was proposed. However, because the matching circuit is not ideal, the resistance of the matching circuit will introduce additional losses, at the same time, it also makes the working frequency band sensitive to the value of lumped elements. In [3], a reconfigurable antenna using a PIN diode for WWAN/ LTE application was also presented. PIN diode needs additional space for its DC control circuit and brings extra loss as well, which limits its practical usage. Compared with the above-mentioned two methods, multi-mode resonance technique is more convenient to fulfill the antenna optimization. In [5], a broadband antenna with multiple resonant modes was proposed for mobile handset applications, but a relatively large clearance area was needed in the design. In order to reduce the clearance area, limited designs folded the antenna into three-dimensional structures [7, 8]. Although doing so reduces the lateral size occupied by the antenna, it requires additional area in the vertical direction and at the same time it also increases the difficulty in manufacturing.

In this letter, a simple planar antenna design for sub-6 GHz applications in 5G mobile terminals is proposed. The presented antenna has a fully planar structure and no lumped elements are required, which makes it a simple structure and easy to be fabricated. Compared with other planar antenna designs, the antenna dimension provided in [5] and [6] is 68×15 mm^2 and 60×15 mm^2, respectively, while the antenna dimension provided in this paper is only 40×15 mm^2, which occupies at most 67% of the clearance areas in [5] and [6] but has a wider frequency band. The measured $|S_{11}| \leq$ -6dB bandwidth covers 700-960 and 1600-5500 MHz bands, in which all the LTE 700/2300/2500, UMTS, GSM 850/900, DCS, PCS, and n77, n78, n79 bands are included.

II. ANTENNA DESIGN

As shown in Fig. 1 (a), the antenna is printed on a 135×80×0.8 mm^3 FR4 substrate with ε_r=4.4 and tanδ=

Submitted On: July 4, 2019
Accepted On: December 28, 2019

0.02. The ground plane is a part of the bottom surface of the substrate with the size of 120×80 mm^2. The antenna is composed of one multi-branch driven strip and three parasitic grounded strips. The driven strip has three branches as shown in Fig. 1 (b), which is printed on the top surface of the substrate and is connected to a 50Ω coaxial line at the feeding point. The parasitic grounded strips consist of three parts: the L-shaped branch and the protrude stub are printed on the bottom surface of the substrate and are directly connected to the ground as shown in Fig. 1 (c); and the longer meandered branch shown in Fig. 1 (d) is etched on the top surface of the substrate and is connected to the ground through a via hole at the shorting point. By exhaustive parametric studies, the optimum dimensions of the antenna are listed in Table 1.

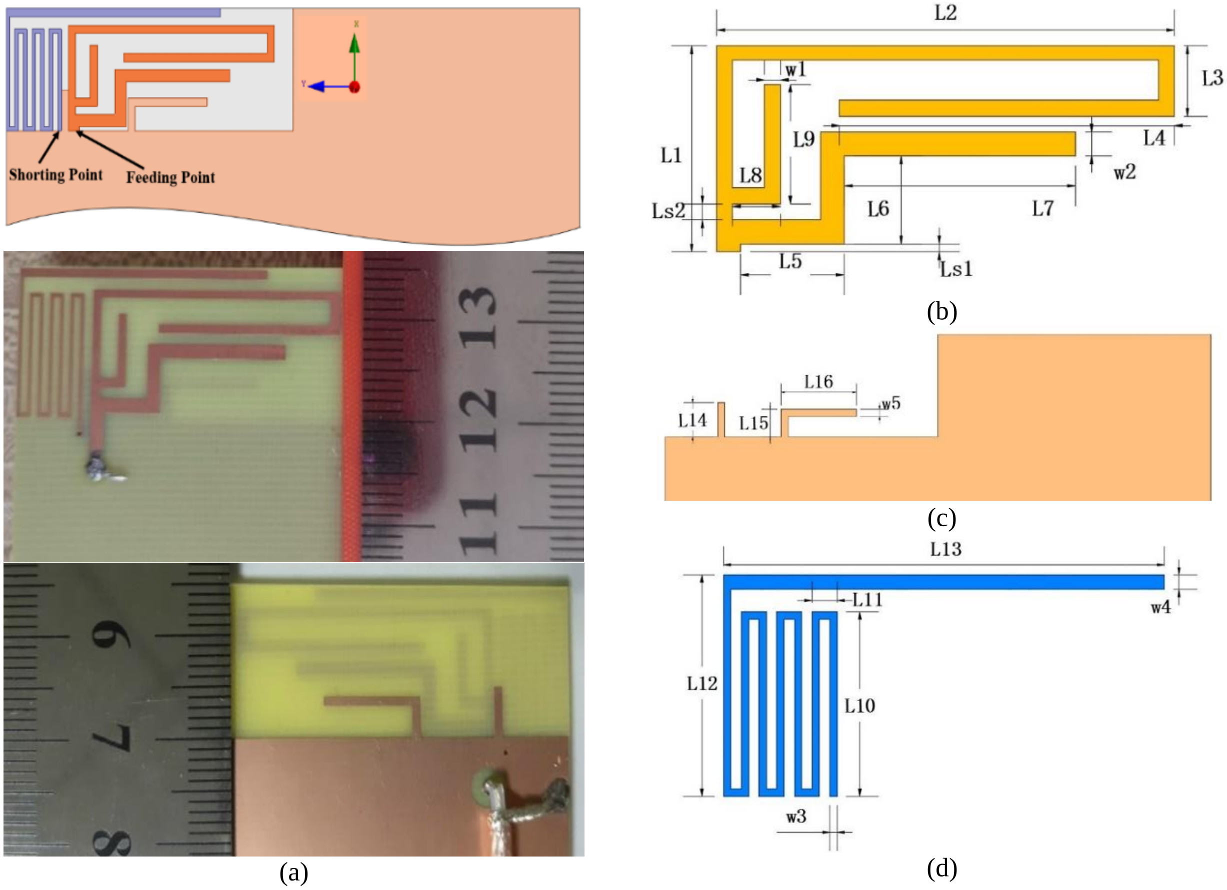

(a) (b) (c) (d)

Fig. 1. Geometry of the proposed antenna: (a) antenna configuration and the fabricated prototype, (b) the driven branch, (c) the L-shaped branch and protruded stub, and (d) the meandered branch.

Table 1: Optimum dimensions of the antenna (unit: mm)

Parameters	**L1**	**L2**	**L3**	**L4**	**L5**	**L6**
Values	12.9	28.7	4.4	21	6.5	5.5
Parameters	**L7**	**L8**	**L9**	**L10**	**L11**	**L12**
Values	14.5	3	7.5	12.5	1.7	15
Parameters	**L13**	**L14**	**L15**	**L16**	**w1**	**w2**
Values	29.9	5	4	11	1	1.5
Parameters	**w3**	**w4**	**w5**	**Ls1**	**Ls2**	
Values	0.5	1	1	0.5	1	

III. WORKING PRINCIPLE OF THE ANTENNA

The working principle of the proposed antenna can be explained through Fig. 2. The longer branch of Ref1, we call it branch1, operates like a monopole in the λ/4 mode and generates a resonance at 0.95 GHz, and the shorter one is called branch2 and has two resonances: at 2.1 GHz the branch operates in the λ/4 mode, while at 4.7 GHz it operates in the λ/2 mode. On this basis, in order to cover the n79 band up to 5.5 GHz, it is necessary to introduce a new resonance at higher frequency. At the same time, the introduction of the new resonance should not have too much influence on the existing resonances, especially on the resonance at 4.7 GHz, in order to avoid increasing the difficulty in tuning of the antenna's structure. Therefore, the insertion position of the new branch with respect to branch1 and branch2 should be close to the feeding point, while keeping an appropriate distance from branch2. To this end, a short branch called branch 3 is introduced between branch1 and branch2 as shown in Ref2. This new branch operates in its λ/4 mode and generates a new resonance at 5.3 GHz, and its effect is clearly seen in Fig. 2 (a) that the impedance bandwidth is much enhanced at high frequency end.

In addition, to include the LTE 700 and GSM 850 bands, it is necessary to generate a new resonance around 700 MHz. If a new branch is inserted into the structure of Ref2 as before, too many branches will crowd in small space, which will result in strong mutual coupling and each operating frequency of the antenna will become very difficult to control independently. Therefore, a parasitic meandered branch is introduced, which provides a λ/4 mode resonance at 0.75 GHz and at the same time two additional higher-order modes can also be generated at 2.2 GHz and 3.75 GHz, respectively.

Meanwhile, the $|S_{11}|$ versus frequency in Fig. 2 (b) indicates impedance mismatching of Ref3 from 2.7 to 3.5 GHz. To lower the reflection coefficients in this frequency range, a parasitic L-shaped branch, which is protruded from the ground on the bottom surface of the substrate and is without in touch with the driven strip, is introduced to form a new resonance around 3.35 GHz in between of 2.7 and 3.5 GHz. The parasitic branch works in the λ/2 mode at 3.35 GHz, and as shown in Fig. 2 (b) the new structure Ref4 improves reflection coefficients when compared with Ref3. However, due to the coupling between newly added L-shaped branch and branch2, impedance matching deteriorates around 4.5-5 GHz. To eliminate the mismatching, a grounded short stub is added between the meander strip and the driven branch, then the proposed antenna is formed. It can be seen from Fig. 2 that the grounded short stub improves the impedance matching of 4.5-5 GHz and the proposed antenna achieves the coverage of the required frequency band.

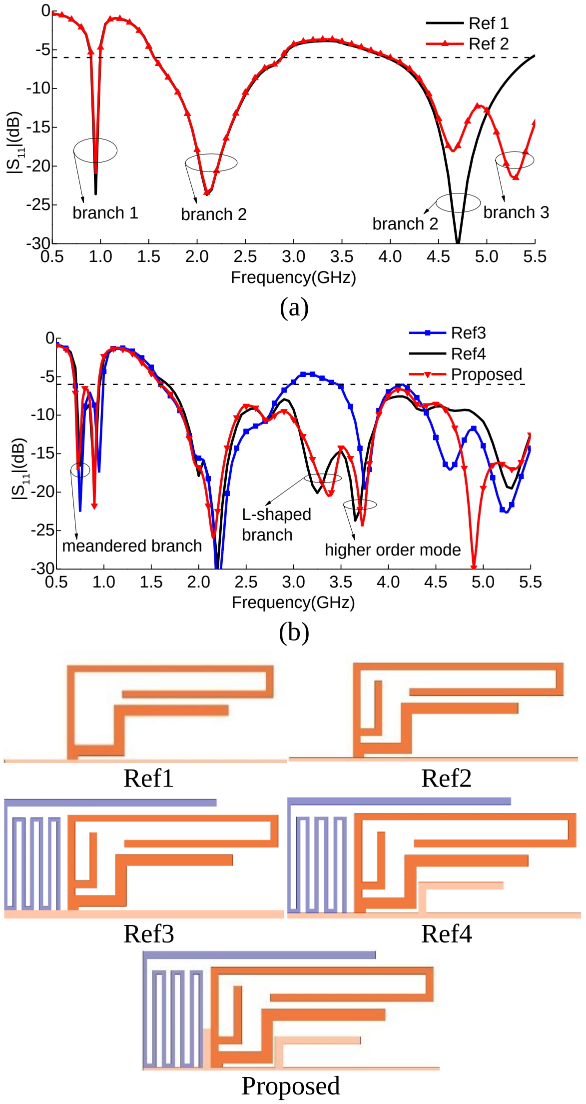

(a)

(b)

(c)

Fig. 2. Simulated $|S_{11}|$ of different antennas: (a) simulated result of Ref1 and Ref2, (b) simulated result of Ref3, Ref4 and proposed antenna, and (c) configuration of different antenna.

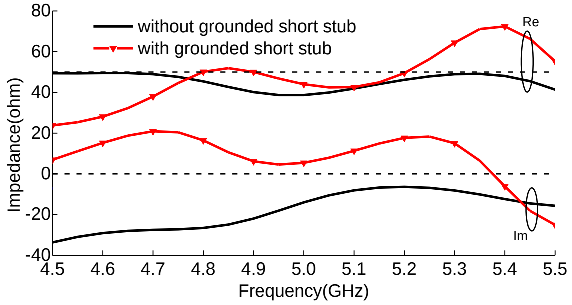

Fig. 3. Simulated impedance of different antennas.

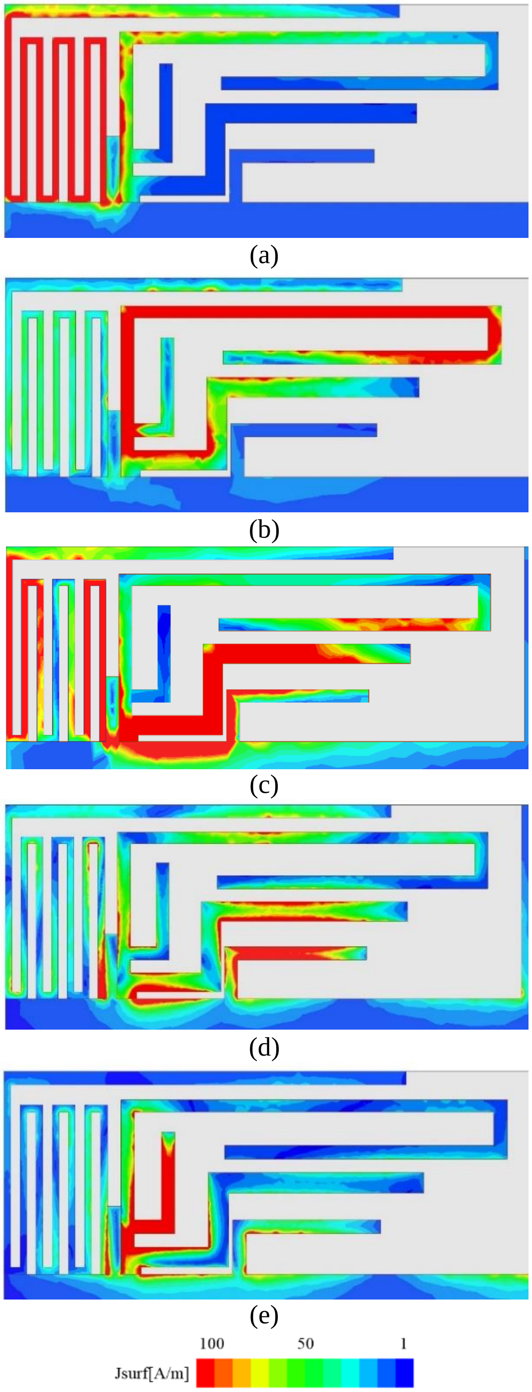
(a)

(b)

(c)

(d)

(e)

Fig. 4. Current distributions on the proposed antenna at different frequencies: (a) 0.75 GHz, (b) 0.95 GHz, (c) 2.1 GHz, (d) 3.35 GHz, and (e) 5.3 GHz.

To further understand the working principle of the grounded short stub, Fig. 3 gives the simulated impedance of Ref4 and proposed antenna. For an antenna, the definition of S_{11} is identical to the reflection coefficient,

$$S_{11} = \Gamma . \tag{1}$$

The voltage reflection coefficient Γ is the ratio between the reflected wave and the incidence wave. Γ is defined in (2):

$$\Gamma = \frac{Z_L - Z_0}{Z_L + Z_0} , \tag{2}$$

where Z_L is the antenna impedance and Z_0 is the characteristic impedance of the transmission line, which is normally 50Ω.

As can be seen from Fig. 3, the grounded short stub acts as a shunt inductor. It changes the imaginary part of the antenna impedance to approach zero, which improves the impedance matching at 4.9 GHz resonance.

The simulated current distributions on the proposed antenna at different frequencies are shown in Fig. 4, and it can be seen that the multiple branches of the antenna generate distinct resonant modes. Meanwhile, in various operating mode, the current mainly concentrates in the corresponding branch, and the coupling between the different branches is relatively small, which is beneficial to the design and optimization of the antenna.

In Fig. 5, the simulated $|S_{11}|$ with different values of Ls2 which is related to the position of branch 3 is presented. It can be seen that the position of branch3 significantly affects the match at 5.3 GHz, while other existing frequencies are almost unaffected.

IV. RESULTS AND DISCUSSION

A prototype of the antenna is fabricated, and the measured $|S_{11}|$ is given in Fig. 6, which agree well with the simulated results. The difference is mainly due to the uncertainty of the dielectric constant of the FR4 substrate. For current mobile antennas, most of them are on the basis of -6dB $|S_{11}|$, which is enough for practical application [1-8]. The measured impedance bandwidth with $|S_{11}| \leq$ -6dB is over 700-960 and 1600-5500 MHz, covering all the LTE 700/2300/2500, UMTS, GSM 850/900, DCS, PCS, and n77/78/79 bands.

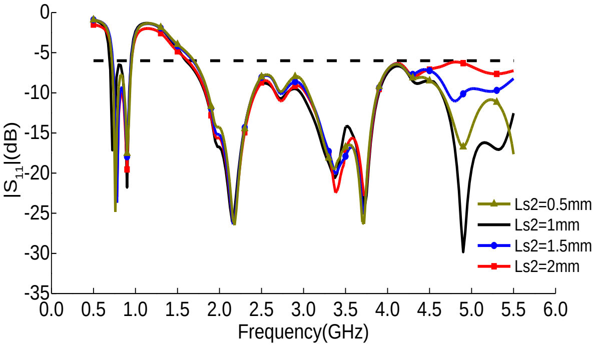

Fig. 5. Simulated $|S_{11}|$ with different values of Ls2.

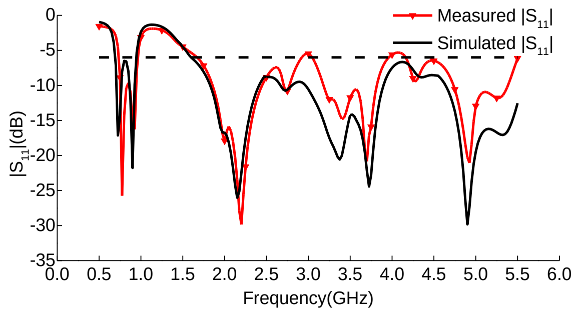

Fig. 6. Simulated and measured |S$_{11}$| of the proposed antenna.

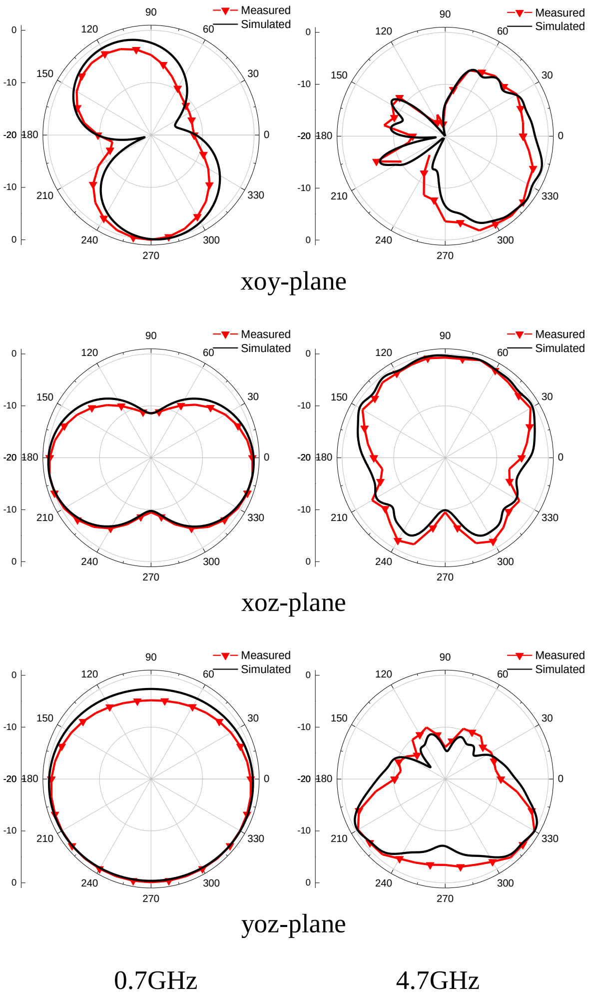

Fig. 7. Simulated and measured radiation patterns of the proposed antenna.

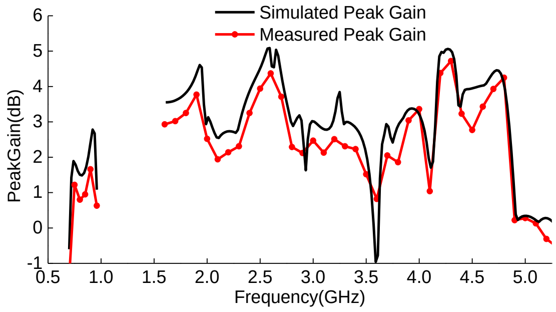

Fig. 8. Peak Gain of the proposed antenna.

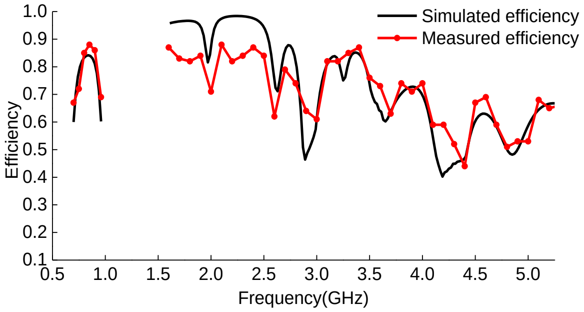

Fig. 9. Efficiency of the proposed antenna.

The simulated and measured radiation patterns at 0.7 GHz and 4.7 GHz is shown in Fig. 7. It can be observed that the antenna exhibits good monopole characteristics at 0.7 GHz, while at 4.7 GHz, since the branch2 is mainly parallel to the ground, the radiation is reflected by the ground and exhibits a unidirectional pattern. The measured and simulated peak gain are shown in Fig. 8. The measured gain ranges from -1.39 to 1.66 dBi at the low frequency band and from -1.09 to 4.72 at the high frequency band, respectively. For mobile antennas, the gain and the radiation pattern are not an important parameter, because it is mostly decided by the position in which an antenna is installed and the size of the grounding structure. The antenna element itself does not have much to do with deciding the gain and radiation patterns. In contrast, mobile antennas are more concerned with antenna efficiency. The measured efficiency is shown in Fig. 9 and agrees well with the numerical results. The efficiency is from 60% to 84% at the low frequency band and from 41% to 88% at the high frequency band, respectively. For this work, 1-1.6 GHz is not the desired operating frequency band, so the gain and efficiency of 1-1.6 GHz are not given in the figure.

Table 2: Comparison of the proposed antenna with previous works

	Operating Bands (MHz)	**Dimension (mm)**	**Gain (dBi)**	**Lumped Element Using**	**Efficiency (%)**
[1]	690-980, 1630-2740	80×8×5.8	0.3-5.6	Yes	50.2-94.5
[2]	690-1000, 1680-2950	56×5×0.8	1.3-5.2	Yes	54-83
[3]	808-965, 1696-3000	30×15×4	-2.2-3.1	Yes	28-71
[4]	698-960, 1710-2170, 2300-2690	60×10×0.8	0.5-1.45	Yes	40-84
[5]	698-1046, 1618-2703, 3018-4377, 4697-6000	68×15×0.8	0.4-5.6	No	50-87
[6]	660-1065, 1665-3000	60×15×0.8	0.5-3	No	42-88
[7]	690-970, 1680-2740	70×8×5.8	-0.06-4.02	No	51.4-86.9
[8]	670-1020, 1650-2920	80×6×5.8	1.43-4.48	No	63.2-97.2
Proposed	700-960, 1600-5500	40×15×0.8	-1.3-4.7	No	41-88

Table 2 shows performance comparison of the proposed antenna with previous works. Unlike the designs in [1-4], no lumped elements are required in the present design, which reduces the difficulty in antenna manufacturing. As well, it can be seen that the proposed antenna occupies at most 67% space to achieve comparable or even wider bandwidth as compared with the works presented in [5-6]. Actually, the fabrication of the antenna is even easier than those in [7] and [8], since the antenna is a fully planar structure and no vertical space is needed. Therefore, the proposed antenna has advantages of wide bandwidth, small size, and easy manufacturability, which makes it suitable for sub-6 GHz applications in 5G mobile terminals.

V. CONCLUSION

A simple wideband planar antenna for sub-6 GHz applications in 5G mobile terminals is presented. The antenna covers the desired frequency band by exciting multiple operating modes. The design process and working mechanism are described and analyzed in detail, and the measured results are in good agreement with the simulated ones. Low profile, wide bandwidth, and no need of lumped-element loadings makes this design has a good application value.

REFERENCES

[1] Y. Wang and Z. Du, “Wideband monopole antenna with less nonground portion for octa-band WWAN/ LTE mobile phones,” *IEEE Trans. Antennas Propag.*, vol. 64, no. 1, pp. 383-388, Jan. 2016.

[2] Y. Liu, Y. Luo, and S. Gong, “An antenna with a stair-like ground branch for octa-band narrow-frame mobile phone,” *IEEE Antennas Wireless Propag. Lett.*, vol. 17, no. 8, pp. 1542-1546, Aug. 2018.

[3] Y. Xu, Y. Liang, and H. Zhou, “Small-size reconfigurable antenna for WWAN/LTE/GNSS smartphone applications,” *IET Microw., Antennas Propag.*, vol. 11, no. 6, pp. 923-928, 2017.

[4] Y. Liu, P. Liu, Z. Meng, L. Wang, and Y. Li, “A planar printed nona-band loop-monopole reconfigurable antenna for mobile handsets,” *IEEE Antennas Wireless Propag. Lett.*, vol. 17, no. 8, pp. 1575-1579, Aug. 2018.

[5] X. Wang, Y. Wu, W. Wang, and A. A. Kishk, “A simple multi-broadband planar antenna for LTE/GSM/UMTS and WLAN/WiMAX mobile handset applications,” *IEEE Access*, vol. 6, pp. 74453-74461, 2018.

[6] C. Deng, Y. Li, Z. Zhang, and Z. Feng, “Planar printed multi-resonant antenna for octa-band WWAN/LTE mobile handset,” *IEEE Antennas Wireless Propag. Lett.*, vol. 14, pp. 1734-1737, 2015.

[7] R. Tang and Z. Du, “Wideband monopole without lumped elements for octa-band narrow-frame LTE smartphone,” *IEEE Antennas Wireless Propag. Lett.*, vol. 16, pp. 720-723, 2017.

[8] D. Huang, Z. Du, and Y. Wang, “An octa-band monopole antenna with a small nonground portion height for LTE/WLAN mobile phones,” *IEEE Trans. Antennas Propag.*, vol. 65, no. 2, pp. 878-882, Feb. 2017.

Cross Dipole Antenna for 4G and Sub-6 GHz 5G Base Station Applications

Geetharamani Gopal [1] and Aathmanesan Thangakalai [2*]

[1] Department of Mathematics
UCE- BIT Campus, Anna University, Tiruchirappalli, Tamilnadu, 620024, India
geetharamani@aubit.edu.in

[2*] Department of Information and Communication Engineering
UCE- BIT Campus, Anna University, Tiruchirappalli, Tamilnadu, 620024, India
cegnesan@gmail.com

Abstract **─** Cross dipole antenna for base station applications is presented in this paper. The proposed antenna consists of simple dipole elements and modified balun structure for the improved performance. The proposed design is simple and suitable for 4G and sub-6 GHz 5G base station applications. The antenna is fabricated using low-cost FR4 epoxy substrate with a dielectric permittivity of 4.4. The height of the substrate is 1.6 mm and loss tangent is 0.02. In order to confirm the proposed design, the antenna is measured and compared with the simulation results. The proposed antenna is achieved 13.8 dBi of realized peak gain in the 1.341 to 3.834 GHz frequency range along the bandwidth of 2.492 GHz with VSWR < 1.5. The proposed antenna obtains stable radiation patterns and stable gain over the frequency range. The cross dipole antenna structure with the proper radiation performance makes the proposed antenna suitable for base station applications.

Index Terms **─** Antennas, base station antenna, cross dipole antenna.

I. INTRODUCTION

Base station antenna is the most important factor in the network coverage of wireless mobile services. There is a demand for base station antenna with a wide frequency band, stable pattern, and high cross polarization ratio. Therefore, in this paper cross dipole antenna for covering 4G and Sub-6 GHz 5G frequency bands is presented. The proposed antenna will offer wideband impedance along with stable gains over the frequency and high polarization ratio. The categories of base station antennae and the design principles are discussed in [1,2]. The basic principles such as wideband impedance, stable patterns in the wide frequency band, high cross polarization ratio in wide-angle range for base station antenna are discussed in [3]. Simulation is playing an increasingly important role in making sure that designs meet specification [4]. Therefore, the proposed antenna is designed using Finite Integration Technique based tool, which uses the FDTD method for solving Maxwell's equations in grid forms in [5]. The simulation tool, which is selected for this research, is the CST microwave studio. Since features such as antenna matching and integration of circuit elements, multiple antenna systems and phased arrays, installed performance and co-site interference [6] are useful in designing base station antennae. In [7] a wideband differentially fed dual-polarized stacked patch antenna with tuned slots discussed for 1.66 -2.75 GHz having 8.7 dBi gain. In [8] a broadband ±45° dual-polarized antenna with y-shaped feeding lines, which operates in 1.7-2.7 GHz frequency with the 8 dBi gain. In [9] a compact broadband dual-polarized antenna array is given for 1.427-2.9 GHz frequency with a gain of 8 dBi. In [10] a wideband omnidirectional antenna array is presented with a low gain variation of 7±1.5 dBi in 1.54-2.75 GHz frequency range. In [11] a low-profile dual-polarized high isolation MIMO antenna arrays for wideband base station applications are discussed for 2.4-3 GHz frequency with 10.2 dBi gain. Broadband stacked f-probe patch antenna and its array for base station are discussed in [12] for 1.7-2.69 GHz frequency having a varying gain of 7.9-8.9 dB. In [13] a low-profile wideband circularly polarized crossed-dipole antenna with wide axial-ratio and gain beam width given for 1-1.68 GHz frequency operation with 5 dBi gain. In [14] surface wave enhanced broadband planar antenna for wireless applications is presented for 3.4-5.5 GHz frequency range with 4.6 dBi gain. In [15] gain enhancement of bow-tie antenna using fractal wideband artificial magnetic conductor ground is discussed for 1.64 – 1.94 GHz frequency range with 6.5 dBi gain. The recent works related to this research is identified in [17-21]. From the literature review, a demand for a single base station antenna to cover a wide frequency range is identified. Therefore, in this paper cross dipole antenna is presented to make stable radiation pattern over the entire frequency range which covers

Submitted On: August 21, 2019
Accepted On: December 15, 2019

different wireless mobile communication standards such as 2G, 3G, 4G and the sub-6 GHz 5G applications. The development of the antenna consists of three stages, and initially a single dipole element [16] is designed and its balun structure is modified for the wideband operation next, the two element antenna is developed. Finally, the cross dipole antenna was obtained by the joining of two pairs of dipole structures at the center. At each stage the input matches and radiation parameters are analyzed for the effective progress of the proposed structure. To finish the development process parameters such as input match, radiation patterns, gain, and efficiency are compared for validating the fabricated and simulated antenna structure. The comparison of performance of the proposed antenna with the reference works is also given in the results and discussion part to prove the proposed antenna can serve for base station applications. There are four sections in this paper. An introduction with the literature review in Section 1 and its evolution of design along with the design methodology of the proposed antenna in Section 2. Section 3 consists of a cross dipole antenna and its results. Section 4 concludes the paper.

II. ANTENNA DESIGN

In this section, the design methodology followed in this antenna design is presented. The proposed antenna shown is in Fig. 1. The overall dimension of the single antenna element is 76*42 mm^2. The antenna consists of a simple dipole structure at the top side of the substrate at Fig. 1 (a) and a microstrip balun structure at the bottom side of the rectangular FR4 substrate at Fig. 1 (b). The dimensions for the front view of the antenna consists of, a=42 mm, b=76 mm, c=37.50 mm, d=23 mm, e=27 mm, f=15 mm, g=1 mm, h= 12.50 mm, i= 11.50 mm, j= 4.50 mm. The FR4 substrate is covered with the double-sided copper cladding with an electrical conductivity of 5.8e+007 with a thickness of t= 0.035 mm. The evolution of the proposed design is depicted in Fig. 2 and Fig. 3.

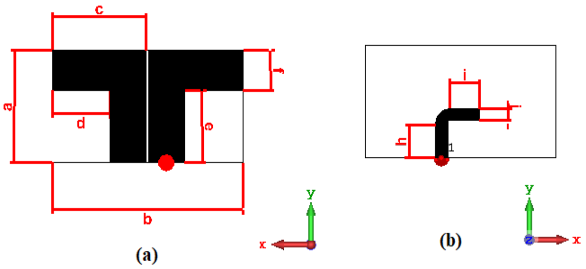

Fig. 1. Geometry of the proposed antenna: (a) top layer and (b) bottom layer.

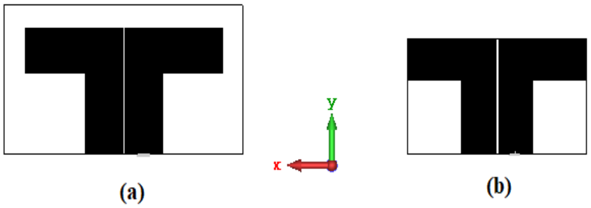

Fig. 2. Evolution of the dipole.

In step 1 a simple dipole of 50*100 mm^2 dimension is designed with the straight balun shown in Fig. 2 (a) which has dual resonant frequencies 1.4 GHz and 2.6 GHz then overall dimension reduced by removal of extra space around the radiating patch following step 2 for size reduction, which is depicted in Fig. 2 (b). It has resulted in the widening of bandwidth from 1.4 GHz to 3.1 GHz. The advantage of using balun is that it acts as an unbalanced to balanced transformer from the feed line to the two printed dipole strips. An integrated balun between the microstrip line and the CPS line to match the input impedance of the antenna to the 50-ohm feed line, and the end of the microstrip line is shorted using a shorting pin at the feeding point is shown in Fig. 2 (a). Step 3 microstrip balun is modified into a curved structure to improve the impedance matching process is shown in Fig. 3 (b).

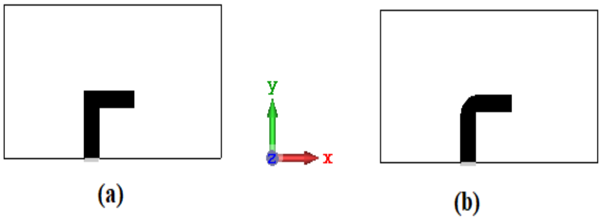

Fig. 3. Evolution of modified balun.

The capacitive gap between the dipole elements is chosen as 1 mm for better isolation between the dipole elements. When the proposed antenna is compared with the traditional dipole antenna with straight balun having narrow bandwidth and the proposed dipole antenna which provides wider bandwidth of 2.64 GHz from 1.30 to 3.94 GHz. Finally, the proposed antenna is obtained with a reduced dimension of 42*76 mm^2. Input match which is obtained during the evolution of design is shown in Fig. 4. The CST software discrete port is used for excitation purposes with the input impedance of 50 ohms.

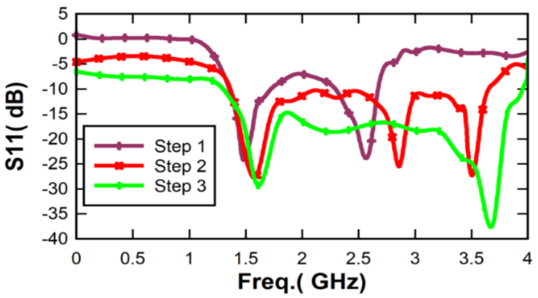

Fig. 4. Input match response to the evolution of design.

III. RESULTS AND DISCUSSION

A. Analysis of single dipole element

The proposed antenna was successfully simulated. Then it is fabricated in 1.6 mm thickness FR4 epoxy substrate with loss tangent tan δ=0.02 and dual layer copper with a thickness of 0.035 mm by using a chemical etching method. A photograph of the fabricated prototype antenna is shown in Fig. 5 (a), front view Fig. 5 (b). Back view of the sub-miniature-A (SMA) connector connected to the bottom side for excitation of the antenna. Figure 5 (c) clearly shows the feeding point soldered properly to prevent the outer connector from affecting the balun structure. Hence, it prevents the energy radiated in an expected way. The comparison of simulated and measured S11 values is given in Fig. 6. The return loss (|S11| dB) of the fabricated prototype is measured using the vector network analyzer (Fieldfox RF Analyzer N9912A by Agilent Technologies). It has a bandwidth of 2.64 GHz and VSWR of <1.5 in the same frequency range.

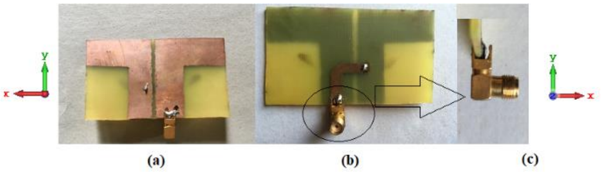

Fig. 5. Prototype of the proposed single element dipole antenna: (a) front view, (b) back view, and (c) feeding point.

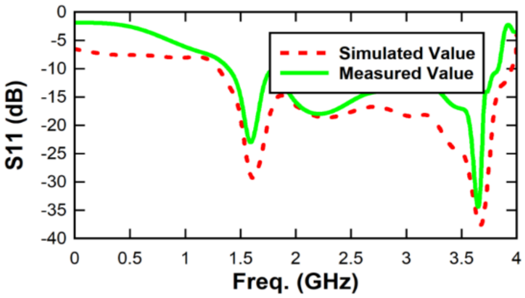

Bn

Fig. 6. Comparison of simulated and measured S11.

The values of simulated and measured S11 were close to each other, and the deviations were also observed due to the fabrication process. The surface current is an important variable because it controls the major properties of an antenna such as input impedance, radiation pattern, resonant frequency and bandwidth the simulated surface current distribution is shown in Fig. 7. At Fig. 7 (a) the current flow from the balun to the ends of the dipole resonates with the antenna at the lower bands of frequency. On the other hand, the current distribution is at Fig. 7 (b) is highly dense around the central region of the antenna while a small density among the dipole elements is responsible for the mid-band region. At Fig. 7 (c) the current density is equally spread among the entire resonating elements responsible for the higher bands of frequency. The realized gain vs frequency for single element antenna is given in Fig. 15. Furthermore, the proposed single element antenna finally achieved the realized peak gain of 3 dBi over the frequency band. It is also close to a simulated peak gain of 3.19 dBi.

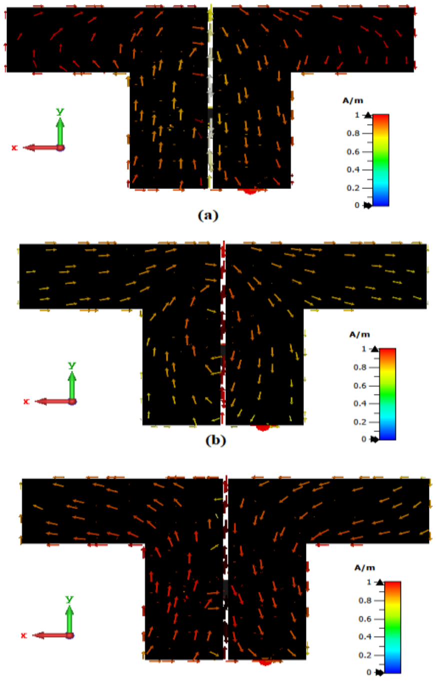

Fig. 7. Surface current distribution: (a) at 1.6 GHz, (b) 2.5 GHz, and (c) 3.8 GHz.

B. Analysis of two element dipole antenna

In order to improve the gain of single element dipole antenna, the two element dipole antenna is developed, and its results are investigated in this section. The proposed two element dipole antenna is shown in Fig. 8. The overall dimension of the proposed two element antenna is 190*42 mm^2. The two dipole antennas are joined together where the distance between the two dipoles is 38 mm which is chosen as it is half the width of a single dipole antenna. These two dipole antenna elements are fabricated and measured, and their results are discussed. The fabricated prototype of the two element dipole antenna is shown in Fig. 9. The realized gain vs frequency of the two element antenna is shown in Fig. 15. The proposed two element dipole antenna is achieved the stable realized peak gain of 5.8 dBi over the frequency band, it is also like the simulated peak gain of 6.1 dBi. The analysis of the E plane, H plane, Co and Cross polarization of the radiation pattern is important because it gives the overall information on how the antenna radiates in the space.

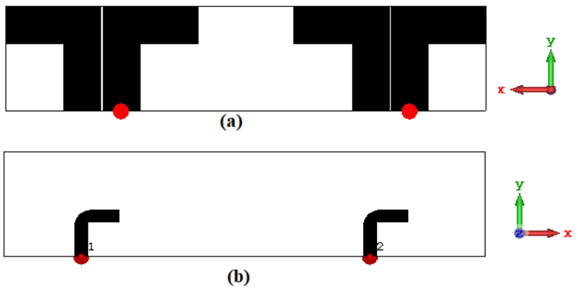

Fig. 8. Two element dipole antenna.

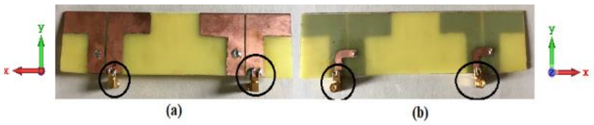

Fig. 9. Fabricated prototype of two element dipole antenna.

Therefore, the radiation pattern is shown in Fig. 10, Fig. 11 for the single and two element antennas at the center frequency of 2.5 GHz. The measured co polarization is 0.153 dBi for single element antenna and for two element antenna it is 3.09 dBi. The cross polarization is -8.35 dBi for single element antenna and for two element antenna it is -12 dBi. The measured radiation efficiency of the single element antenna is found as 82.56% and for the two-element antenna, it is 83.65%.

C. Analysis of cross dipole antenna

The simulated cross dipole antenna is shown in Fig. 12 (a). The balun structure used is shown in Fig. 12 (b). The two element dipole antenna is made a cross by joining at the center of the two elements. The fabricated prototype of the proposed antenna is shown in Fig. 13. The far field radiation patterns such as radiation pattern, gain, and radiation efficiency measurements of the proposed antenna in anechoic chamber. The radiation parameters measured at the center frequency 2.5 GHz are shown in Fig. 14. The realized peak gain increases to 14.9 dBi during the simulation process and the measured gain is 13.8 dBi. The measured radiation efficiency of the proposed cross dipole antenna is found as 93.25%. The realized gain values for the single, two elements and cross dipole antenna are given in Fig. 15. The stable gain is observed in the frequency range of 1.341-3.834 GHz. The simulated and measured efficiency vs frequency plot is shown in Fig. 16. The stable efficiency is also observed in the frequency range of 1.341-3.834 GHz. In order to know the advantage of the proposed cross dipole antenna, we compare the proposed antennas and the previously reported antennas.

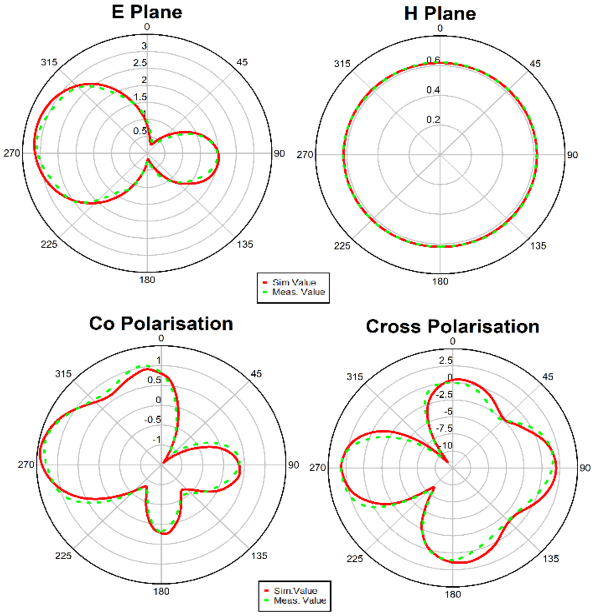

Fig. 10. Radiation patterns of a single element antenna.

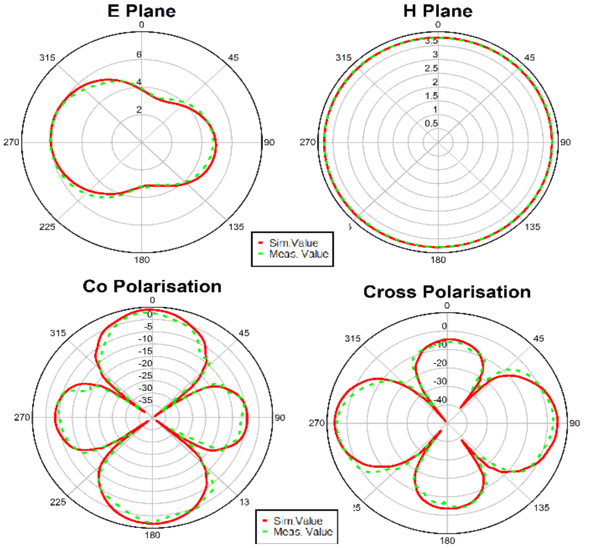

Fig. 11. Radiation patterns of two element antenna.

The comparison for the resonance frequencies, size, substrate material and gains of these antennas is presented in Table 1. From the above discussions, we can see that the proposed antenna is achieved improved bandwidth and gain to cover 4G and sub-6 GHz 5G base station applications.

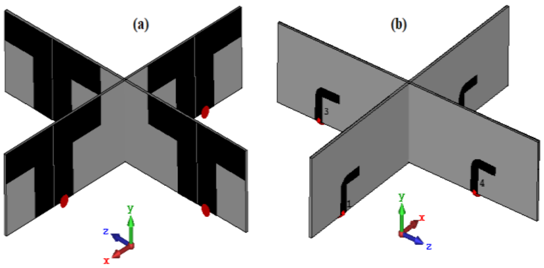

Fig. 12. Simulated cross dipole antenna: (a) dipole elements, and (b) balun structure.

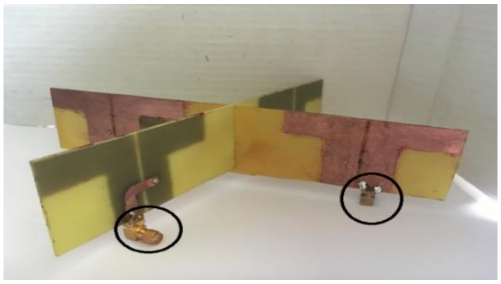

Fig. 13. Fabricated cross dipole antenna.

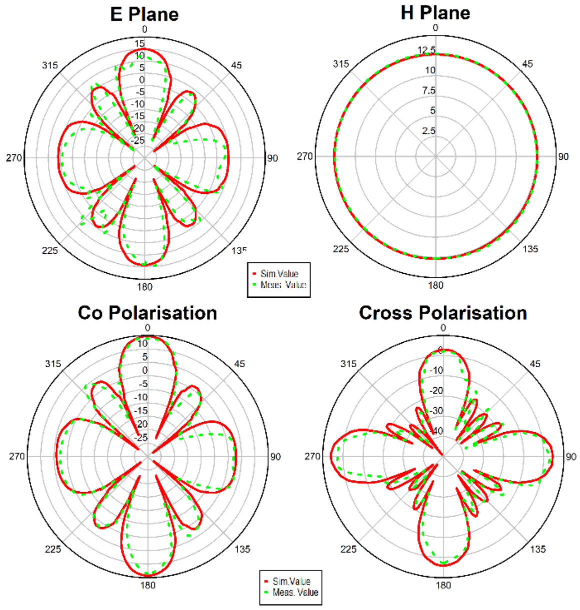

Fig. 14. Radiation patterns of cross element.

Table 1: Comparison between the proposed antenna performance and other reported antennas

Ref.	Frequency (GHz)	Size (mm)	Substrate Material	Gain (dBi)
7	1.66-2.75	140*140	FR4, ε_r=4.4, t=0.8 mm, loss tangent =0.02	8.7
8	1.7-2.7	140*55*34	FR4, ε_r=4.4, t=0.8 mm, loss tangent =0.02	8
9	1.427-2.9	990*134.11*33.83	Arlon AD300, ε_r=3, t=0.762 mm, loss tangent =0.03	8
10	1.54-2.75	63.6*190	FR4, ε_r=2.55, t=1 mm, loss tangent =0.02	7±1.5
11	2.4-3.00	1112*364*12	FR4, ε_r=4.4, t=3 mm, loss tangent =0.01	10.2
12	1.7-2.69	460*180*30	FR4, ε_r=4.4, t=1.6 mm, loss tangent =0.02	7.9-8.9
13	1-1.68	97*81*20.4	FR4, ε_r=3.38, t=0.8 mm, loss tangent =0.01	5
14	3.4-5.5	60*120	RT Duroid, ε_r=10.2, t=1.27 mm, loss tangent =0.01	4.6
15	1.64-1.94	70*50*22	FR4, ε_r=4.4, t= 3 mm, loss tangent =0.01	6.5
23	1.64-3.00	100*70*45	FR4, ε_r=4.4, t= 0.8 mm, loss tangent =0.02	6-8
This work	1.341-3.834	190*76*42	FR4, ε_r=4.4, t=1.6 mm, loss tangent =0.02	13.8

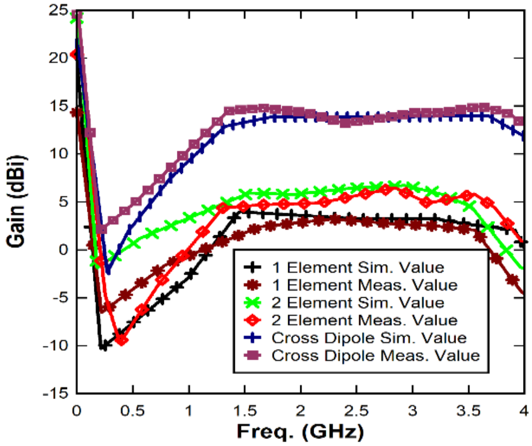

Fig. 15. Realized gain vs Frequency.

The measured co polarization is 6.02 dBi for single element antenna. The cross polarization is -2.98 dBi for the proposed cross dipole antenna. The cross polarization values obtained from the measurement are quite high due to the fabrication tolerance.

The amount of isolation achieved by the proposed antenna is calculated using the parameter Envelope Correlation Coefficient (ECC) which is calculated by using S-parameter coefficients. It is calculated using the equations provided in [22]. The simulated and measured values of ECC for the cross dipole antenna in Fig. 17. which shows that the ECC values lies below 0.3 makes the proposed antenna is suitable for base station applications.

Simulated 3D Farfield Pattern at 2.5 GHz is shown in Fig. 18 which displays the realized gain pattern at E plane which achieved 14.9 dBi of simulated realized gain.

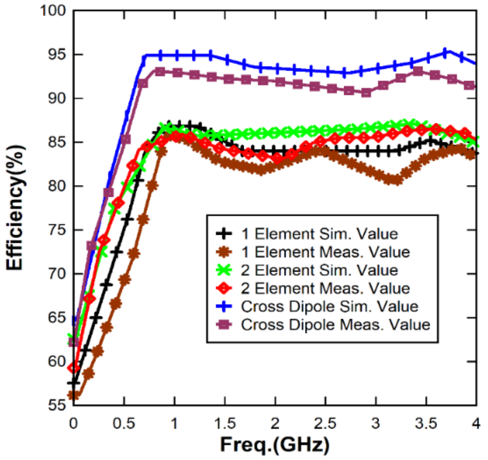

Fig. 16. Efficiency vs. Frequency.

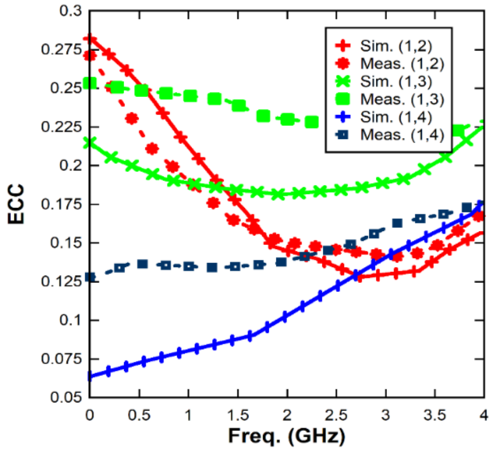

Fig. 17. Simulated and Measured ECC Vs Frequency.

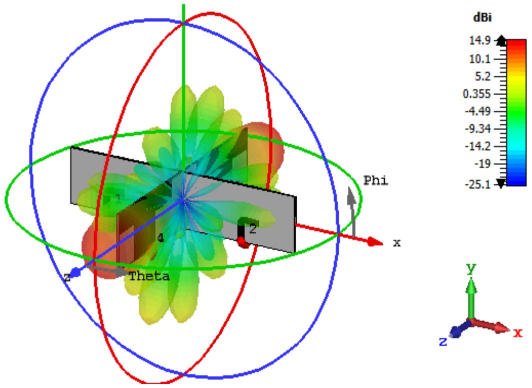

Fig. 18. Simulated 3D Farfield Pattern.

VI. CONCLUSION

In this paper, cross dipole antenna is proposed, and its performance parameters are analyzed and discussed in detail. The antenna operates at 1.341 to 3.834 GHz frequencies with a bandwidth of 2.492 GHz. The proposed antenna is simulated, optimized, fabricated, and measured for the validation of design. The proposed antenna obtains stable radiation patterns and stable gain and also acceptable ECC over the frequency range therefore it is suitable for 4G and sub-6 GHz 5G base station applications.

REFERENCES

[1] C. A. Balanis, *Antenna Theory: Analysis and Design*, John Wiley & Sons, Singapore, 2005.

[2] Z. N. Chen and K.-M. Luk, *Antennas for Base Stations in Wireless Communications*, McGraw-Hill Professional, USA, 2009.

[3] Q. X. Chu, Y. Luo, and D. L. Wen, “Three principles of designing base-station antennas,” *International Symposium on Antennas and Propagation (ISAP)*, Hobart, TAS, pp. 1-3, 2015.

[4] F. Hirtenfelder and J. Mollet, “Phased array simulations using finite integration technique,” *JINA Conference*, USA, pp. 1-6, 2004.

[5] T. Weiland, “RF & microwave simulators - from component to system design,” *33rd European Microwave Conference Proceedings (IEEE Cat. No.03EX723C)*, vol. 2, pp. 591-596, 2003.

[6] M. Rütschlin and T. Wittig, “State of the art antenna simulation with CST studio suite,” *9th European Conference on Antennas and Propagation (EuCAP)*, Lisbon, pp. 1-5, 2015.

[7] Z. Tang, J. Liu, Y. M. Cai, J. Wang, and Y. Yin, “A wideband differentially fed dual-polarized stacked patch antenna with tuned slot excitations,” *IEEE Transactions on Antennas and Propagation*, vol. 66, no. 4, pp. 2055-2060, Apr. 2018.

[8] Q. X. Chu, D. L. Wen, and Y. Luo, “A broadband 45 degree dual-polarized antenna with Y-shaped feeding lines,” *IEEE Transactions on Antennas and Propagation*, vol. 63, no. 2, pp. 483-490, Feb. 2015.

[9] Q. Zhang and Y. Gao, “A compact broadband dual-polarized antenna array for base stations,” *IEEE Antennas and Wireless Propagation Letters*, vol. 17, no. 6, pp. 1073-1076, June 2018.

[10] Y. Yu, J. Xiong, and R. Wang, “A wideband omnidirectional antenna array with low gain variation,” *IEEE Antennas and Wireless Propagation Letters*, vol. 15, pp. 386-389, Dec. 2016.

[11] H. Zhai, L. Xi, Y. Zang, and L. Li, “A low-profile dual-polarized high-isolation MIMO antenna arrays for wideband base-station applications,” *IEEE Transactions on Antennas and Propagation*,

vol. 66, no. 1, pp. 191-202, Jan. 2018.

[12] Y. Jin and Z. Du, "Broadband stacked f-probe patch antenna and its array for base station," *IEEE International Wireless Symposium*, Shenzhen, pp. 1-4, 2015.

[13] W. J. Yang, Y. M. Pan, and S. Y. Zheng, "A low-profile wideband circularly polarized crossed-dipole antenna with wide axial-ratio and gain beamwidths," *IEEE Transactions on Antennas and Propagation*, vol. 66, no. 7, pp. 3346-3353, July 2018.

[14] K. M. K. H. Leong, Y. Qian, and T. Itoh, "Surface wave enhanced broadband planar antenna for wireless applications," *IEEE Microwave and Wireless Components Letters*, vol. 11, no. 2, pp. 62-64, Feb. 2001.

[15] Y. W. Zhong, G. M. Yang, and L. R. Zhong, "Gain enhancement of bow-tie antenna using fractal wideband artificial magnetic conductor ground," *Electronics Letters*, vol. 51, no. 4, pp. 315-317, 2015.

[16] A. Kashkool, S. Yahya, H. Al-Rizzo, A. Al-Wahhamy, and A. A. Issac, "On the design and simulation of antennas on ultra-thin flexible substrates," *ACES Journal*, vol. 33, no. 7, pp. 798-801, July 2018.

[17] L.-Y. Chen, J.-S. Hong, and M. Amin, "A compact CPW-fed MIMO antenna with band-notched characteristic for UWB system," *ACES Journal*, vol. 33, no. 7, pp. 818-821, July 2018.

[18] Z. Liu, Y. Li, J. Liu, Y. Zhang, X. Wu, and Y. Zhou, "A broadband dual-polarized antenna for TD-SCDMA system," *ACES Journal*, vol. 32, no. 12, pp. 1121-1124, Dec. 2017.

[19] V. Rafiei, H. Saygın, and S. Karamzadeh, "Circularly polarized aperture-coupled microstrip-line fed array antenna for WiMAX/C bands applications," *ACES Journal*, vol. 32, no. 12, pp. 1117-1120, Dec. 2017.

[20] M. Sierra-Castañer, "Review of recent advances and future challenges in antenna measurement," *ACES Journal*, vol. 33, no. 1, pp. 99-102, Jan. 2018.

[21] R. L. Li, B. Pan, T. Wu, K. Lim, J. Laskar, and M. M. Tentzeris, "A broadband printed dipole and a printed array for base station applications," 2008 *IEEE Antennas and Propagation Society International Symposium*, San Diego, CA, pp. 1-4, 2008.

[22] S. Chouhan, D. K. Panda, M. Gupta, and S. Singhal, "Multiport MIMO antennas with mutual coupling reduction techniques for modern wireless transreceive operations: A review," *Int. J. RF Microw. Comp. Aided Engg*., 2017.

[23] S. X. Ta, C. D. Bui, and T. K. Nguyen, "Wideband quasi-yagi antenna with broad-beam dual-polarized radiation for indoor access points," *ACES Journal*, vol. 34, no. 5, pp. 654-660, May 2019.

Geetharamani. G is working as an Associate Professor in Department of Mathematics, UCE BIT Campus, Anna University, Trichy. She received her Ph.D in Gandhigram Rural University. She received M.E. (CSE) in Anna University, Chennai. She received M.Phil in National College, Trichy, She received M.Sc. in Bharathidasan University. She received PGDCA in Alagappa University.

Aathmanesan. T pursuing Ph.D. in Anna University, He received his M.Tech. degree in College of Engineering Guindy, Anna University Chennai. He completed his B.E. ECE in Anna University Chennai. His area of research are microwave and THz antennas.

Input Resistance Changes and Related Performances of a Normal-Mode Helical Antenna in a Human Body Application

N. Q. Dinh [1], D. T. Dung [2], Y. Yamada [3], and N. Michishita [4]

[1] Faculty of Radio-Electronics Engineering
Le Quy Don Technical University, Hanoi, Vietnam
dinhnq@mta.edu.vn

[2] Telecommunication University, Khanhhoa, Vietnam
dangtiendung@tcu.edu.vn

[3] Malaysia-Japan International Institute of Technology
Universiti Teknologi Malaysia, Kuala Lumpur, Malaysia
yoshihide@utm.my

[4] Department of Electrical and Electronic Engineering
National Defense Academy, Yokosuka, Japan
naobumi@nda.ac.jp

Abstract ─ Recently, ingestible capsule endoscopy has been developed to ease the dosimetry process in the stomach and tract. In this application, a helical antenna is used because its shape is suitable for a capsule. The electric performance of a coil antenna can be analyzed by the normal-mode helical antenna (NMHA) concept. Previously, the design equations for NMHA have already been developed in free space application. Application of NMHA in the human body is innovative. Antenna design equations and electrical performance should be clarified. Presently, only self-resonant structure equations are clarified.

In this paper, fundamental electric performances such as the input resistance, bandwidth and radiation characteristics are clarified through electromagnetic simulations and experiments. As for a human body tissue, the muscle is selected and a muscle phantom is used for measurements. It is made clear, that the input resistance and the bandwidth are increased by the increase of the human body conductivity, while the antenna gains are decreased.

Index Terms ─ Human body, NMHA, phantom, RF.

I. INTRODUCTION

Recently, radio frequency (RF) sensors inside human bodies have been developed for healthcare applications [1-2]. In implantable RF sensors, small antennas, such as a planar inverted F-antenna and microstrip antenna, were studied [3-4]. In addition, a helical antenna had been used as a very small implantable antenna for a capsule endoscopy system [5-6]. The helical antenna is promising because of its suitable structure for a capsule. However, antenna design method and performances were not made clear. The fundamental design is a self-resonant condition that creates input impedance to pure resistance and achieves higher antenna efficiency. Previously, a structural deterministic equation for a self-resonant condition was developed for ease in practical applications [7]. Researches of NMHA in a human body condition are very limited. Recently, a self-resonant equation in a human body condition was developed [8]. Some studies for input resistance changes and related performance changes were reported [9].

In this paper, fundamental electric performances such as the input resistance, bandwidth and radiation characteristics are clarified through electromagnetic simulations and experiments. In electromagnetic simulations, a commercial simulator FEKO is employed. In calculation, because antenna size is very small such as one tenth of a wavelength and input resistance is less than 0.1 Ω, antenna segment size is optimized to be 1/100 wavelength. The accuracy of simulation results are taken care. As for measurement, a human body phantom is fabricated. The dielectric constants $\varepsilon_r = 52.7$, $\sigma = 0.15$ and $\varepsilon_r = 53.3$, $\sigma = 0.89$ are achieved. Calculated and measured results of the input impedance, bandwidth and radiation characteristics are compared and good agreements are ensured.

Submitted On: July 17, 2019
Accepted On: December 15, 2019

II. DESIGN EQUATIONS OF NMHA

NMHA have been a well-known antenna. All of its important design equations are nearly clarified in a free space application. However, for use in a human body, equations are still under development. To understand NMHA, present situations are summarized in this chapter. A fundamental performance can be recognized by the equivalent current model shown in Fig. 1 [7].

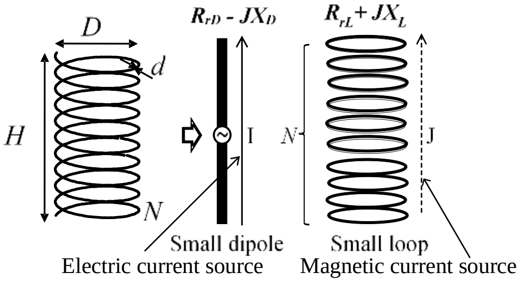

Fig. 1. Equivalent current model of the NMHA.

The coil current is modeled by a straight current and several loop currents. The straight current corresponds to a small dipole with a radiation resistance (R_{rD}) and capacitive reactance (X_D). The loop currents correspond to a small loop with a radiation resistance (R_{rL}) and inductive reactance (X_L). The input impedance is expressed by equation (1):

$$Z_{in} = R_{rD} + R_{rL} + R_l + J(X_L - X_D). \quad (1)$$

Here, R_l expresses the ohmic resistance of the antenna wire. Furthermore, the input resistance (R_{in}) and radiation resistance (R_{rad}) are given as follows:

$$R_{in} = R_{rD} + R_{rL} + R_l, \quad (2)$$

$$R_{rad} = R_{rD} + R_{rL}. \quad (3)$$

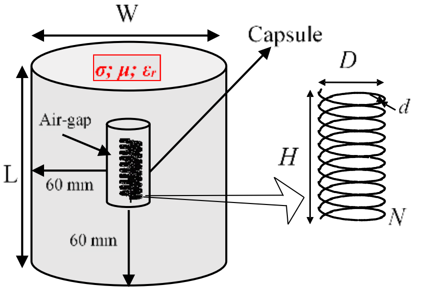

Fig. 2. Simulation model.

The situation of NMHA inside a human body is shown in Fig. 2. NMHA is placed in a capsule and is surrounded by a dielectric material with permittivity and conductivity of ε_r and σ, respectively. The present situations of important equation developments are summarized in Table 1. In a free space condition, all fundamental design equations are clarified. Other electric characteristics relating to impedance matching, stored electromagnetic power, and bandwidth are summarized in paper [10]. In a human body condition, the resistance, reactance, and self-resonant structure are affected by ε_r and σ of the surrounding material. The most important equation for self-resonant structure has already been developed [8], whereas those for resistances are still under development. The equations related to Table 1 are shown in the following.

Table 1: Overview of important design equations

Item		In Free Space	In a Human Body
Resistances	Radiation (R_{rD}; R_{rL}) Ohmic (R_l)	Equations relating to antenna parameters are derived [10]	Equation are under developing
Reactances	Capacitive (X_D) Inductive (X_L)	Equations relating to antenna parameters are derived [7]	Deterministic equation is developed [8]
Self-resonant structure	$X_D = X_L$	Deterministic equation is developed [7]	Deterministic equation is developed [8]

A. In free space

Design equations for R_{rD}, R_{rL} and R_l are expressed as follows:

$$R_{rD} = 20\pi^2 \left(\frac{H}{\lambda}\right)^2, \quad (4)$$

$$R_{rL} = 320\pi^6 \left(\frac{D}{2\lambda}\right)^4 N^2, \quad (5)$$

here, λ is the wavelength in free space,

$$R_l = 0.6 \frac{L_t}{d} \sqrt{\frac{120}{\sigma\lambda}}, \quad (6)$$

here, L_t, d and σ are the total length, diameter, and conductivity of antenna wire, respectively.

The capacitive and inductive reactances are expressed as follows [7]:

$$X_D = \frac{279\lambda H_A}{N\pi(0.92H + D)^2}, \quad (7)$$

$$X_L = \frac{600\pi \times 19.7ND^2}{\lambda(9D + 20H)}. \quad (8)$$

The self-resonance is given by $X_D = X_L$ and expressed as follows:

$$\frac{279\frac{H}{\lambda}}{N\pi\left(0.92\frac{H}{\lambda} + \frac{D}{\lambda}\right)^2} = \frac{600\pi \times 19.7N\left(\frac{D}{\lambda}\right)^2}{9\frac{D}{\lambda} + 20\frac{H}{\lambda}}. \quad (9)$$

B. In human body

The inductive (X_L) and capacitive (X_D) reactances are expressed as follows [9]:

$$X_L = \omega L_W = \sqrt{\frac{1}{\varepsilon_r}}\frac{600\pi \times 19.7 ND^2}{\lambda_g(9D+20H)}, \tag{10}$$

$$X_D = \frac{1}{\omega C} = \sqrt{\varepsilon_r}\frac{125H\lambda_g}{\pi N(1.1H+D)^2}. \tag{11}$$

Here, λ_g is the wavelength in the material and is expressed as follows:

$$\lambda_g = \frac{\lambda_0}{\sqrt{\varepsilon_r \mu_r}}. \tag{12}$$

The self-resonant equation of NMHA is expressed by the equation (13):

$$\sqrt{\frac{1}{\varepsilon_r}}\frac{600\pi \times 19.7 N\left(\frac{D}{\lambda_g}\right)^2}{9\frac{D}{\lambda_g}+20\frac{H}{\lambda_g}} = \sqrt{\varepsilon_r}\frac{125\frac{H}{\lambda_g}}{\pi N(1.1\frac{H}{\lambda_g}+\frac{D}{\lambda_g})^2}. \tag{13}$$

III. ELECTROMAGNETIC SIMULATION

A. Simulation model

The simulation model is shown in Fig. 2. NMHA is placed at the center of a dielectric cylinder with radius of 30 mm and height of 60 mm. A very small air gap of 1.0 mm is placed between the antenna and the dielectric material.

B. Simulation parameters

The simulation parameters are summarized in Table 2. The effects of ε_r and σ on the antenna resistances are the main focus. As for a human tissue, a muscle is selected with $\varepsilon_r = 53$, and $\sigma = 0.89$ (S/m) given. To clarify the effect of σ, different values with $\sigma = 0.15$ (S/m) is considered.

Table 2: Simulation parameters

Parameters	Values
Method	FEKO 7.0 (MoM)
Frequency	402 MHz
Wavelength (λ_g)	102.5 (mm)
Dielectric Constant (Muscle)	$\varepsilon_r = 53$, $\mu_r = 1$; $\sigma = 0.15, 0.89$ (S/m); $\rho = 1040$ (kg/m^3)
Segment size of material	$\lambda_g/40$
Number of turns (N)	5; 7; 9
Metallic wire	Copper ($\sigma = 58 * 10^6$ [1/Ωm])
Diameter of Antenna wire (d)	0.5 mm
Segment size of antenna wire	$\lambda_g/100$

For the calculation of the antenna wire and dielectric material, the method of moment (MoM) scheme is used. In order to calculate very small size antenna (between 0.05 λ_g to 0.2 λ_g) and very small input resistances (around 0.1 Ω or less) accurately, segment size of the antenna wire are carefully determined. At the segment size of $\lambda_g/100$, calculated results converged. For a dielectric material, the segment size of $\lambda_g/40$ is selected.

C. Antenna structure

Based on the self-resonant equation of equation (13), the antenna structures are determined. A comparison of the structure obtained from equation (13) and that of simulation results are shown in Fig. 3, where both values conform to each other. The antenna structures are only dependent with ε_r and not with σ. At a given N value, the antenna diameter (D) change is minimal for length (L) changes. This change is similar to that of the compression of a wire spring in which an increase of N, decreases the D. The point A indicate the study antenna structure of $D = 8$ mm, $H = 20$ mm, $N = 9$.

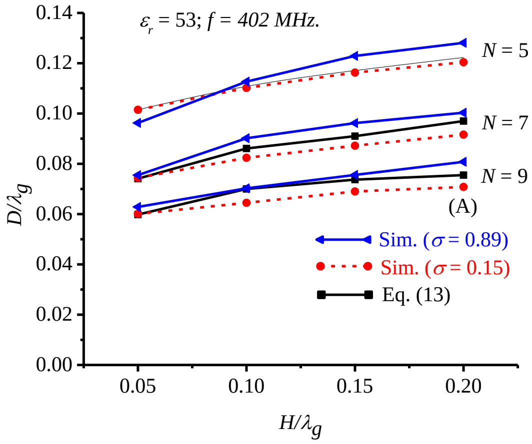

Fig. 3. Comparison of self-resonant structures.

D. Input impedance

The Smith chart display of the input impedance is shown in Fig. 4 and the resistance values are shown in Table 3.

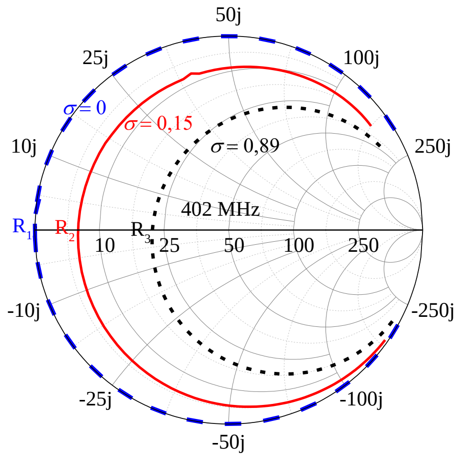

Fig. 4. Antenna input impedance.

Table 3: Antenna resistance value

σ (S/m)	R_{rD}+R_{rL} (Ω)	R_l (Ω)	R_{in} (Ω)
0.00	0.078	0.0357	0.44
0.15	0.078	0.0357	8.58
0.89	0.078	0.0357	22.80

With the increase of σ value, the input resistance is increased. When a low-resistance antenna is placed near a wave absorber, the resistance increases, because the increase of σ corresponds to an increase of wave absorbing ability; there by, a very small resistance at σ = 0 (S/m) is dramatically increased by the increase of σ.

E. Antenna gain

The effects of σ in the radiation characteristics are investigated. The antenna efficiency (η) and antenna gain (G) are shown in Table 4. Here, η is calculated by equation:

$$\eta = \frac{R_{rad}}{R_{in}}, \tag{14}$$

where η is significantly decreased by an-increase in R_{in}, in the case of existence of σ value.

Table 4: Antenna resistance value

σ (S/m)	R_{rad} (Ω)	R_{in} (Ω)	η (%)	η (dB)	G (dBi)
0.00	0.078	0.44	17.93	-7.4	-17.5
0.15	0.078	8.58	0.91	-20.4	-18.7
0.89	0.078	22.80	0.34	-24.7	-24.5

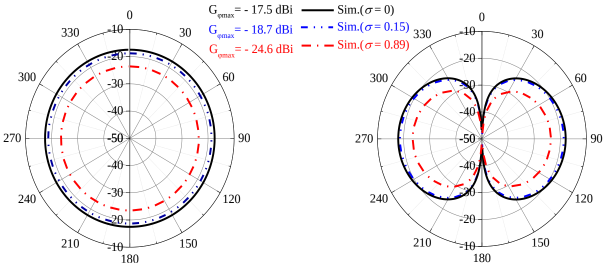

(a) Horizontal plane (b) Vertical plane

Fig. 5. Radiation patterns.

The radiation patterns of the electric field are shown in Fig. 5. In the vertical plane, the radiation pattern forms ***8*** shape. The antenna gain (***G***) is expressed as follows:

$$G = \eta + G_{pat} - L_a \text{(dBi)}, \tag{15}$$

here, G_{pat} indicates the character ***8*** shape radiation pattern as shown in Fig. 5 (b), G_{pat} becomes 2 dBi. L_a indicates the attenuation of the electromagnetic power through the absorbing material. At σ = 0.15 and σ = 0.89, L_a becomes 1 dB and 3 dB, respectively. So, Antenna gains of 18.7 dBi and 24.5 dBi are considered adequate. In the case of σ = 0, antenna gain is reduced from the η value. In order to investigate this reason, electric field distributions of σ = 0 and σ = 0.15 are obtained as shown in Fig. 6. In the case of σ = 0 shown in Fig. 6 (a), electric field spreads widely out of the antenna. However, the case of σ = 0.15, electric field degradates rapidly out of the antenna. So, reflections caused by the surface impedance mismatch become larger in the case of σ = 0 case. These reflections may become main reason of 10 dB degradation.

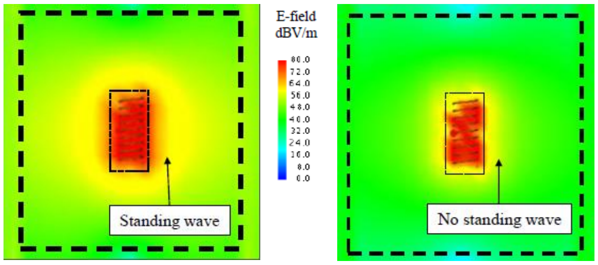

(a) σ = 0 (b) σ = 0.15

Fig. 6. Near field.

IV. EXPERIMENTAL RESULTS

A. Phantom

To measure the antenna electrical characteristics inside a human body, human body phantoms are fabricated, which are composed of chemical powders, such as Agar, Polyethylene, Sodium chloride, Sodium dehydroacetate, monohydrate and Xanthan gum [11-12]. These chemical powders are mixed with distilled water and then heated. To complete a phantom, the heated material is placed in a case. The fabricated phantoms are shown in Fig. 7.

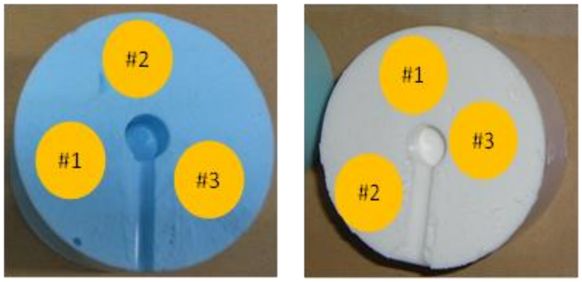

(a) Phan tom 1 (σ = 0.15) (b) Phan tom 2 (σ = 0.89)

Fig. 7. Experiment of phantom.

A round hole and a guide groove are provided for installation of the antenna and feed cable, respectively. Positions #1, #2, and #3 indicate the locations used for the measurement of the dielectric constants, using a dielectric probe kit of Keysight N150/A. With this module, the measured dielectric constant (ε_m) is expressed as a complex value as follows:

$$\varepsilon_m = \varepsilon_r - j\varepsilon_i = \varepsilon_r - j\frac{\sigma}{\omega\varepsilon_0}, \tag{16}$$

here, ε_0 is the permittivity of a vacuum.

Then, σ is obtained by the next expression:

$$\sigma = 2\pi f \varepsilon_i \varepsilon_0. \tag{17}$$

The measured results of ε_r, ε_i, and σ at #1, #2, and #3 locations are summarized in Table 5. In the process of putting the melted phantom in the container, the phantom densitie become different by the cooling speed differences of the phantom parts. To achieve the same value as a muscle (ε_r = 58.8 and σ = 0.84) is rather difficcult. So, the value ε_r = 53.3 and σ = 0.89 is used as a representative of a muscle. For phantom 1, the average values of ε_r and σ are 52.7 and 0.15, respectively. For the phantom 2, the average values of ε_r and σ are 53.3 and 0.89, respectively.

Table 5: Measurement results of phantom

Parameters	**Phantom 1**			**Phantom 2**		
	ε_r	ε_i	σ	ε_r	ε_i	σ
#1	54.5	6.8	0.1511	53.0	41.0	0.9111
#2	55.4	7.0	0.1555	52.7	40.8	0.9066
#3	49.0	5.8	0.1288	54.3	39.0	0.8666
Averages	52.7	6.5	0.1450	53.3	40.3	0.8940

B. Input impedance

The measurement set up is shown in Fig. 8. The antenna with a feed cable is set at the center hole and the guide groove as shown in Fig. 8 (a). The antenna size is D = 8 mm, H = 20 mm, N = 9. A plastic insulator is placed between the phantom and antenna with a cable to avoid antenna contact with the phantom.

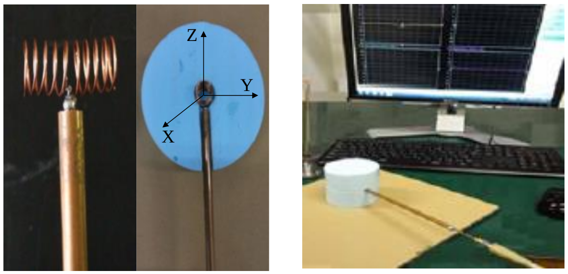

(a) NMHA in phantom (b) Input impedance measurement by VNA

Fig. 8. Experimental of input impedance setup.

For the input impedance measurement shown in Fig. 8 (b), the antenna portion is covered by an upper phantom. The measured input impedances are shown in Fig. 9.

The measured results of σ = 0.15 and σ = 0.89 phantoms conform well to the calculated results. Therefore, the increase of the input resistance using the σ value is ensured in the experiment.

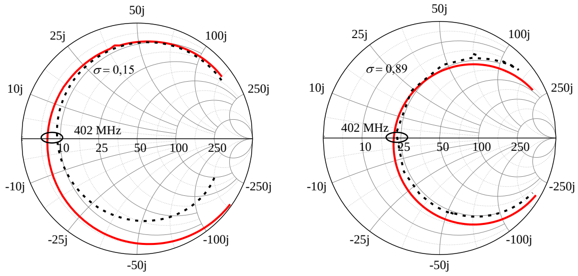

(a) Phantom 1 (σ = 0.15) (b) Phantom 2 (σ = 0.89)

Fig. 9. Input imperdance of NMHA in phantom.

C. Bandwidth

The bandwidth can be expressed by R_{in} as follows. The R_{in} and antenna Q factor are related by equation (18):

$$Q = \frac{X_L}{R_{in}}, \tag{18}$$

here, X_L is the input inductance shown in equation (10) and equation (11).

Then, the bandwidth (BW) at the specified VSWR is expressed by the equation (19):

$$\mathrm{BW} = \frac{VSWR - 1}{Q\sqrt{VSWR}}. \tag{19}$$

As a result, BW becomes proportional to R_{in}.

The measured and simulation results of the antenna VSWR characteristics are shown in Fig. 10.

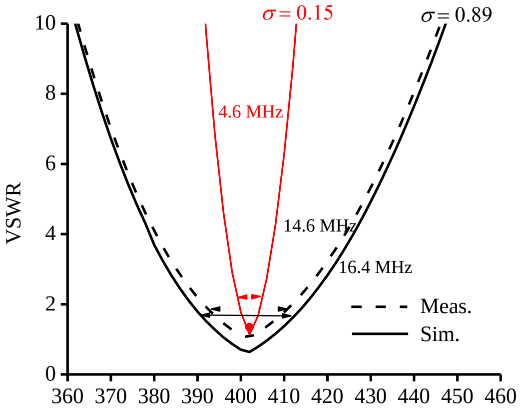

Fig. 10. Comparisons of antenna bandwidth in phantom.

The calculated and measured results at σ = 0.15 and σ = 0.89 conform well to each other. At VSWR = 2, the bandwidth of NMHA in phantom 1 and phantom 2 are 4.6 MHz and 16.4 MHz and correspond to a fractional bandwidth of approximately 1.2% and 4.1%. The bandwidth extensions correspond to the increases of R_{in} in Table 4.

D. Radiation patterns

The set-up of the radiation pattern measurement is shown in Fig. 11. The structure of Fig. 8 (b) that NMHA is covered by a phantom is set on a turntable. The measured antenna is seen in front and the transmission dipole antenna is seen in the opposite side. To measure very small signal level around -20 dBi, the leakage current and reflected wave from the surroundings are carefully reduced. To suppress leakage current on the feeding cable, the cable is covered by a radio wave absorber sheet.

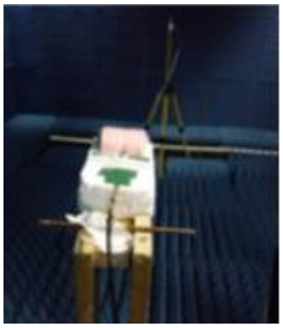

Fig. 11. Experimental of radiation setup.

1). Radiation pattern with phantom 1 (σ = 0.15)

The measured and calculated radiation patterns in the horizontal and vertical planes are shown in Fig. 12 and Fig. 13, respectively. The measured antenna gain is obtained by comparing received levels with the reference half wavelength dipole antenna. Both results agree well at the main polarization and cross polarization.

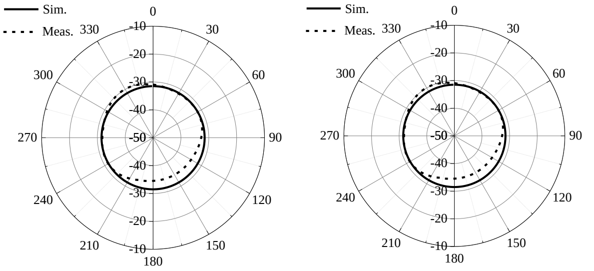

(a) Xross pol. (b) Co-pol.

Fig. 12. Horizontal plane.

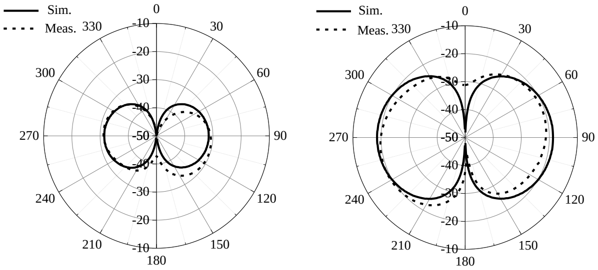

(a) Xross pol. (b) Main pol.

Fig. 13. Vertical plane.

2). Radiation pattern with phantom 2 (σ = 0.89)

The measured and calculated radiation patterns in the horizontal and vertical planes are shown in Fig. 14 and Fig. 15, respectively. Both results agree well at the main polarization and cross polarization.

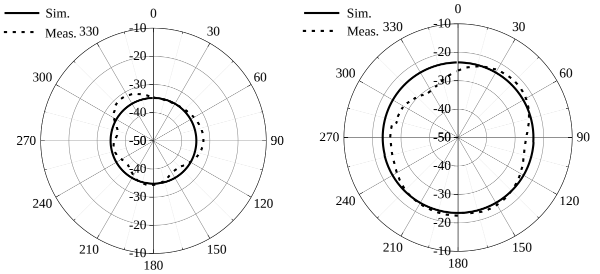

(a) Xross pol. (b) Co-pol.

Fig. 14. Horizontal plane.

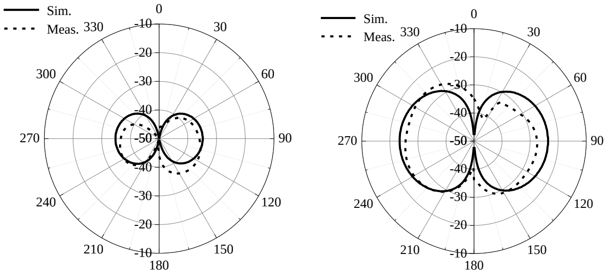

(a) Xross pol. (b) Main pol.

Fig. 15. Vertical plane.

V. CONCLUSIONS

To clarify the electrical characteristics of a normal-mode helical antenna (NMHA) placed in a human body, the change in the input resistance and antenna gain at different conductivity are obtained by simulations and measurements. When the conductivity (σ) is changed: at 0, 0.15, and 0.89 (S/m), the input resistance (R_{in}) become: 0.44, 8.58, and 22.8 (Ω), respectively. With an increase in R_{in}, the antenna efficiency (η) is also changed: -7.4, -20.4, and -24.7 (dBi) for σ = 0, 0.15, and 0.89 (S/m), respectively. The accuracy of the simulated results confirmed through measurement using a human body phantom, and the two results agree well. Thus, a new finding that the input resistance increases as conductivity increases is established.

REFERENCES

[1] ACA, "Planning for medical implant communications systems (MICS) & related devices," Australian Communications Authority, Sydney, NSW, Australia, 2003.

[2] ASGE, "Wireless capsule endoscopy," American Society Gastrointestinal Endoscopy, Downers Grove, IL, USA, 2013.

[3] T. Karacolak, A. Z. Hood, and E. Topsakal,

"Design of a dual-band implantable antenna and development of skin mimicking gels for continuous glucose monitoring," *IEEE Trans. Microw. Theory Techn*., vol. 56, no. 4, pp. 1001-1008, Apr. 2008.

[4] K. Jaehoon and Y. Rahmat-Samii, "Implanted antennas inside a human body: Simulations, designs, and characterizations," *IEEE Trans. Microw. Theory Techn*., vol. 52, no. 8, pp. 1934-943, Aug. 2004.

[5] J. Faerber, et al., "In vivo characterization of a wireless telemetry module for a capsule endoscopy system utilizing a conformal antenna," *IEEE Trans. Biomed. Circuits Syst.*, vol. 12, no. 1, pp. 95-105, Feb. 2018.

[6] C. Liu, Y. X. Guo, and S. Xiao, "Circularly polarized helical antenna for ISM-band ingestible capsule endoscope systems," *IEEE Trans. Antennas Propag*., vol. 62, no. 12, pp. 6027-6039, Dec. 2014.

[7] N. Q. Dinh, N. Michishita, Y. Yamada, and K. Nakatani, "Deterministic equation for self-resonant structures of very small normal-mode helical antennas," *IEICE Trans. Commun*., vol. E94-B, no. 5, pp. 1276-1279, May 2011. Online ISSN: 1745-1345, Print ISSN: 0916-8516.

[8] N. T. Tuan, Y. Yamada, N. Q. Dinh, R. H. M. Baharin, K. B. Kamardin, D. T. Dung, and N. Michishita, "Deterministic equation of self resonant structures for normal-mode helical antennas implanted in a human body," *IEEE Antennas and Wireless Propagation Letters*, vol. 17, no. 8, pp. 1377-1381, Aug. 2018. Print ISSN: 1536-1225, Online ISSN: 1548-5757, DOI: 10.1109/LAWP.2018.2846600.

[9] N. T. Tuan, M. B. R. Hanan, Y. Yamada, D. T. Dung, N. Q. Dinh, and N. Michishita, "Radiation characteristics of small nomal-mode helical antenna for internal human body sensing," *IIEEJ-International Workshop on Image Electronics and Visual Computing*, General session 5A-3, Danang, Vietnam, Mar. 2017.

[10] D. T. Dung, N. Q. Dinh, D. Q. Trinh, and Y. Yamada, "Investigating equations used to design very small normal-mode helical antenna in free space," *International Journal of Antennas and Propagation*, vol. 2018, Article ID 7967468, 7 pages, DOI: 10.1155/2018/7967468.

[11] C. Gabriel, "Compilation of the dielectric properties of body tissues at RF and microwave frequencies," Technical Report AL/OE-TR-1996-0037, Brooks Air Force.

[12] T. Takimoto and T. Onishi, "Characteristics of biological tissues equivalent phantoms applied to UWB communications," *IEICE Trans*., pp. 1674-1681, 2005.

N. Q. Dinh is currently an Associate Professor at Faculty of Radio-Electronics Engineering, Le Quy Don Technical University Vietnam. He received the B.E, M.E. and D.E. degrees in Department of Electrical & Electronic Engineering, National Defense Academy, Yokosuka, Japan, in 2006, 2008, and 2011, respectively. Since 2011, he has been a Research Associate at the Faculty of Radio-Electronics Engineering, Le Quy Don Technical University, Hanoi, Vietnam. His research interests include very small antennas, array antennas, UWB antennas, and MIMO antennas, BTS antennas. He is a member of the Institute of Electronics, Information and Communication Engineers (IEICE), Japan. He was the recipient of the Young Scientist Award of the IEICE Antennas and Propagation Society Japan Chapter, Japan (2011).

D. T. Dung received the B.E degree in Electronic Engineering from Le Quy Don Technical University, Hanoi, Viet Nam in 2006, and M.E in Telecommunications Engineering from Posts and Telecommunications Institute of Technology, Hochiminh, Viet Nam in 2011. He is currently working for Telecommunication University, Khanhhoa, Vietnam. His research interest include antenna for medical application, very small antennas.

Y. Yamada received the B.E. and M.E. degrees on Electronics from Nagoya Institute of Technology, Nagoya, Japan in 1971 and 1973, respectively. And he received the D.E. degree on Electrical Engineering from Tokyo Institute of Technology, Tokyo, Japan in 1989. In 1973, he joined the Electrical Communication Laboratories of Nippon Telegraph and Telephone Corporation (NTT). Till 1984, he was engaged in research and development of reflector antennas for terrestrial and satellite communications. From 1985, he engaged in R&D of base station antennas for mobile radio systems. In 1993, he moved to NTT Mobile Communications Network Inc. (NTT DoCoMo). In 1995, he was temporarily transferred to YRP Mobile Telecommunications Key Technology Research Laboratories Co., Ltd. At the same time, he was a Guest Professor of the cooperative research center of Niigata University, and a Lecturer of Science University of Tokyo, both from 1996 to 1997. In 1998, he changed his occupation to a Professor of National Defense Academy, Kanagawa, Japan. In 2014, he had started working as a Professor at Malaysia-Japan International Institute of Technology, Universiti Teknologi Malaysia, Kuala Lumpur, Malaysia. Now, he is interested in very small antennas, array antennas, aperture antennas and electromagnetic simulation of radar cross section. He received the best paper award and the best tutorial paper award from IEICE in 2013 and 2014, respectively. He is a Fellow member of the IEICE and a member of JSST of Japan. He is also a senior member of IEEE AP society and a member of the ACES.

N. Michishita received the B.E., M.E., and D.E. in Electrical and Computer Engineering from Yokohama National University in 1999, 2001, and 2004, respectively. He joined the Department of Electrical and Electronic Engineering, National Defense Academy, as a Research Associate in 2004, and currently holds the title of Associate Professor. He was a Visiting Scholar at the University of California, Los Angeles, from 2006 to 2007. He received the Young Engineer Award from the IEEE AP-S Japan Chapter and IEICE in 2004 and 2005, respectively. His current research interests include metamaterial antennas and electromagnetic analysis. He is a member of the IEEE.

A Low Profile Miniaturization Low Frequency Wideband Antenna Using Passive Lumped Elements Loading

Yinfeng Xia [1], Yingsong Li [1, 2*], and Wei Xue [1]

[1] College of Information and Communication Engineering
Harbin Engineering University, Harbin150001, China
*liyingsong@ieee.org

[2] Key Laboratory of Microwave Remote Sensing
National Space Science Center
Chinese Academy of Sciences, Beijing 100190, China

Abstract **─** In this paper, a low profile miniaturization low frequency sleeve monopole antenna loaded with passive lumped (PL) elements is proposed, which can be utilized for HF, VHF, UHF, and P band applications. The proposed antenna is fed by coplanar waveguide (CPW) and composed of feeding line, modified T-shaped radiation patch, sleeve structure and loaded passive lumped elements. An original monopole antenna is operating at 231 MHz with a small fractional bandwidth of 31.8%. By modifying the T-shaped radiation patch and adding the sleeve structure, the fractional bandwidth can be improved by 11%. To further enhance its performance, several passive lumped elements are integrated with the antenna. The design procedure is presented and analyzed in detail. The simulated results demonstrate that a fractional bandwidth of 192.2% from 10-500 MHz can be achieved for the proposed antenna system, which is also in agreement with the measured result.

Index Terms **─** Low profile, miniaturization, passive loading, ultra-wideband.

I. INTRODUCTION

High data transmission, miniaturization, multifunction wireless communication system has become a hot topic in the modern wireless communication system development. To meet the demands, antenna, as an intrinsic and essential component of wireless communication system, is also developing toward the same tendency. Multiband antennas can support many sub-systems and then realize multifunction [1-3]. However, more communication frequency bands are required with the increasing of functions of devices, which will make the antenna design more difficult. MIMO antenna array may also be a good choice to improve data transmission. Yet, strong coupling will be inevitable between the MIMO antenna array elements and extra decoupling work is needed to reduce the mutual interferences [4-5]. To solve these problems and meet the wireless communication system developing tendency, miniaturization wideband antenna may be one of the best options.

Nonetheless, the miniaturization of antenna is contradictory with the bandwidth especially at low frequency [6-7]. As is known to us, low frequency antennas usually exist with the form of large size, which is related to its wavelength. Decreasing the size of low frequency antennas will degrade its performance. To trade-off the contradiction, many methods have been proposed [8-13]. So far, the most popular method is to utilize the non-foster circuit (NFC) to match an electrically small antenna (ESA) [13]. In [14-19], NFC matched ESAs have been reported. However, in most of the reported literatures, the bandwidth has been improved, which just compared with the bandwidth of antenna itself resonance. Thus, the achieved bandwidth of these antennas is not enough to cover wide low frequency band, such as for HF, VHF, UHF applications together. In [19], a fractional of 169% from 18 MHz to 218 MHz has been obtained, which is also using the NFC matching method. Yet, the proposed antenna has a height of 30 cm and a ground plane of 20×16 cm^2, which will occupy large volume for the wireless communication system. Therefore, designing a low profile, miniaturization, wideband antenna for low frequency wireless communication is urgent and indispensable.

In this paper, a miniaturization low profile planar sleeve monopole antenna is proposed, which is realized with passive lumped element loading. The proposed antenna is fed by CPW and composed of modified T-shaped radiation patch, feeding line, ground plane and loaded with passive lumped elements. The original model of the proposed antenna operates at 231 MHz with a small fractional bandwidth of 31.8%. To improve its bandwidth, the T-shaped radiation patch is modified, and

Submitted On: August 24, 2019
Accepted On: December 15, 2019

sleeve structure is introduced into the antenna structure to improve its performance a little. To further enhance its bandwidth, lumped elements are integrated to the antenna structure. By properly optimizing the structure and adjusting the values of these lumped elements, a -10 dB fractional bandwidth of 192.2% from 10-500 MHz can be obtained. Moreover, the measured result is in agreement with the simulated one.

II. DESIGN OF THE PROPOSED ANTENNA

In this section, the design procedure of the proposed antenna is presented, which can be developed by three steps. Each step is corresponded with an antenna model. By analyzing the antenna models, the design principle can be well understood.

A. Design of the antenna 1

The structure of the antenna 1 is depicted in Fig. 1, where the top view and side view are given, respectively. The designed antenna 1 is fed by coplanar waveguide composed (CPW) and composed of feeding line, T-shaped radiation patch, part ground plane, which is printed on a FR4 substrate with a relative permittivity of 4.4, a loss tangent of 0.02 and a thickness of h=1.6 mm. The antenna 1, as the original antenna, is a monopole-like antenna. The entire size of the antenna is W1×L1=330×320 mm^2. The width S of the feeding line and the gap g between the feeding line and the part ground plane are calculated and obtained from CPW structure theory [20], which are set 3 mm and 0.5 mm, respectively. To enhance the -10 dB bandwidth of the antenna 1, it is optimized in the HFSS. The optimized dimensions are: W2=100 mm, W3=120 mm, L2=300 mm, and L3=50 mm.

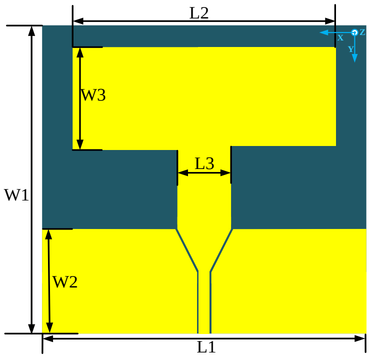

(a) Top view

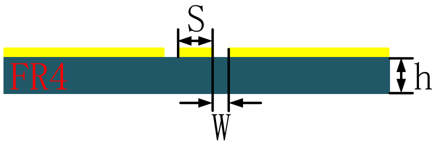

(b) Side view

Fig. 1. The geometry of the designed antenna 1.

The performance of the designed antenna 1 is given in Figs. 2 and 3, where the simulated reflection coefficient (S11) and the simulated radiation patterns are presented, respectively. From Fig. 2, it can be concluded that the designed antenna 1 operates at 231 MHz with a -10 dB fractional bandwidth of 31.8%. Moreover, the antenna 1 has an omnidirectional radiation pattern, which is depicted in Fig. 3.

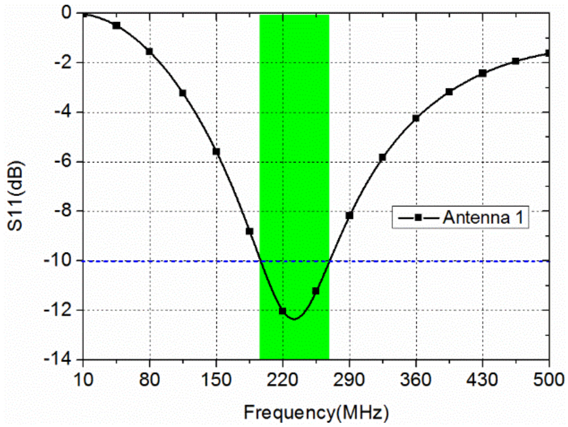

Fig. 2. The simulated S11 of the designed antenna 1.

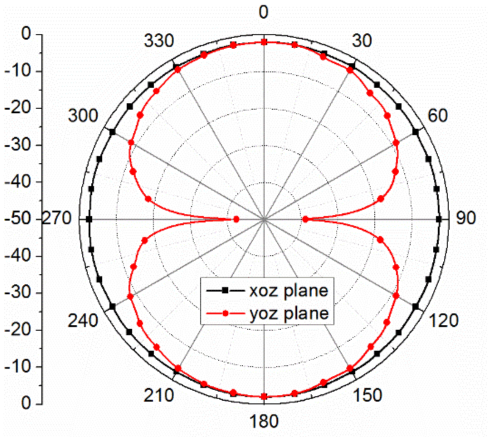

Fig. 3. The radiation patterns of designed antenna 1.

To understand the principle of the antenna 1, the current distribution is shown in Fig. 4. From Fig. 4, it can be observed that the current is mainly distributed on the feeding line, the ground plane, the T-shaped radiation patch. Based on the simulated current distribution, the size of the T-shaped radiation patch can be optimized to enhance its performance. To analyze the effects on the resonance of the antenna, key parameters of the patch are selected to analyze and investigate the effects on the performance of the designed antenna 1. The simulated results are given in Figs. 5 and 6.

The width L2 and the length W3 of the T-shaped radiation patch are selected to analyze its effects on the performance of the designed antenna 1. The T-shaped radiation patch is composed of a rectangle patch marked by L2, W3 and a line marked by L3. In fact, increasing the values of W3 or L2 can improve the bandwidth of the antenna 1 which is given in Figs. 5 and 6. From Fig. 5, it can be observed that the center resonance frequency shifts toward to lower frequency and the -10 dB bandwidth can also be improved a little with the increasing of L2. Also, the same conclusion can be draw from the Fig. 6, which is that the center resonance frequency shifts toward to higher frequency band and the -10 dB bandwidth can also be improved a little with the increasing of W3. Thus, properly optimizing both parameters can control the center resonance frequency and bandwidth of the designed antenna 1.

Based on the analysis for the designed antenna 1, it can be concluded that the bandwidth of the antenna 1 can be improved by optimizing the dimensions of the designed antenna 1. To make the structure more compact, the width L2 is set by 300 mm, and the length W3 is optimized to improve the performance of the antenna 1. To enhance the bandwidth of the antenna 1, the antenna 2 is developed, which is based on the configuration of antenna 1 and integrates the sleeve theory.

B. Design of the antenna 2

The configuration of the developed antenna 2 is presented in Fig. 7, which has the same basic structure with the designed antenna 1. In addition, the T-shaped radiation patch is modified by adding two pairs of parasitic branches. Two sleeve structures are also connected to the ground plane, which is beneficial to improve the impedance matching for the designed antenna 1.

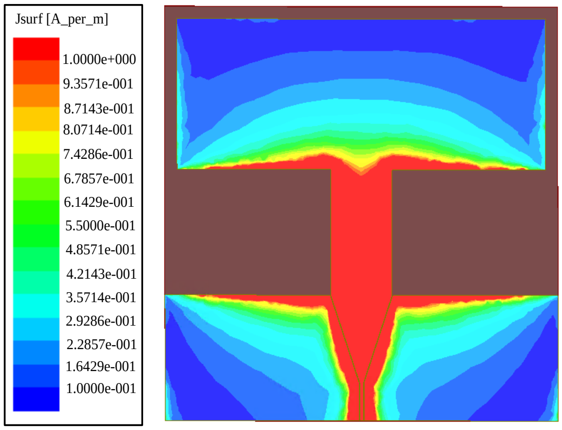

Fig. 4. The current distribution of designed antenna 1.

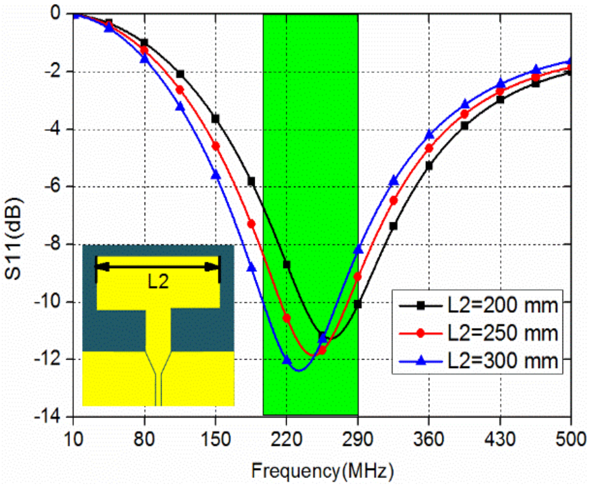

Fig. 5. The effect of L2 on the performance of the designed antenna 1.

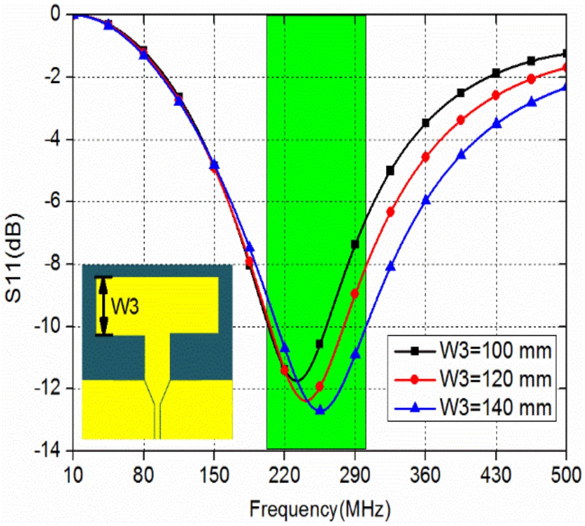

Fig. 6. The effect of W3 on the performance of the designed antenna 1.

The simulated reflection coefficient (S11) is depicted in Fig. 8, which indicates that the antenna 2 has a -10 dB fractional bandwidth of 42.8% covering from 180 MHz to 278 MHz. By comparing with the result of the designed antenna 1, it can be concluded that the fractional bandwidth has been improved by 11%. Moreover, the developed antenna 2 has also an omnidirectional radiation patterns presented in Fig. 9. However, the peak gain has been decreased by 0.39 dBi for the developed antenna 2.

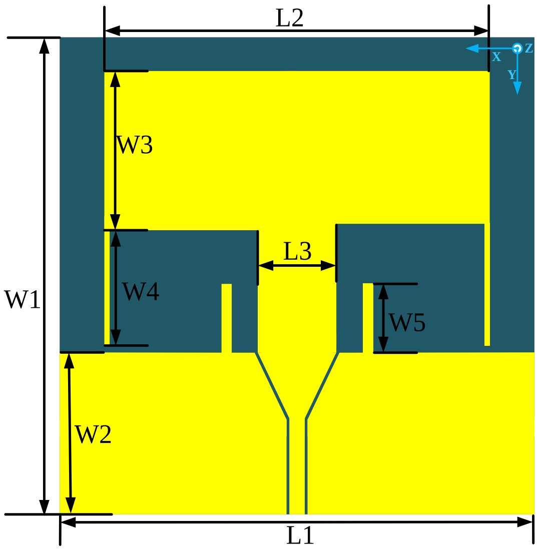

Fig. 7. The configuration of the designed antenna 2.

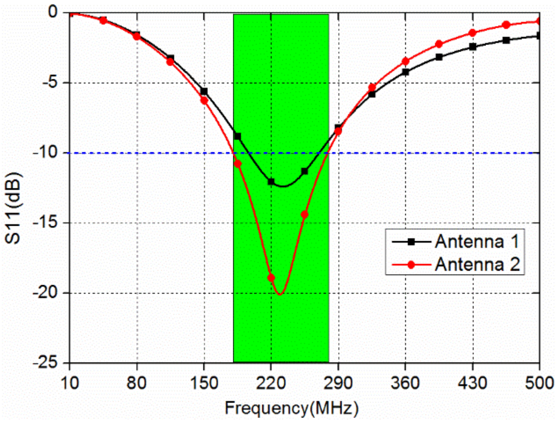

Fig. 8. S11 comparison of antenna 1 and antenna 2.

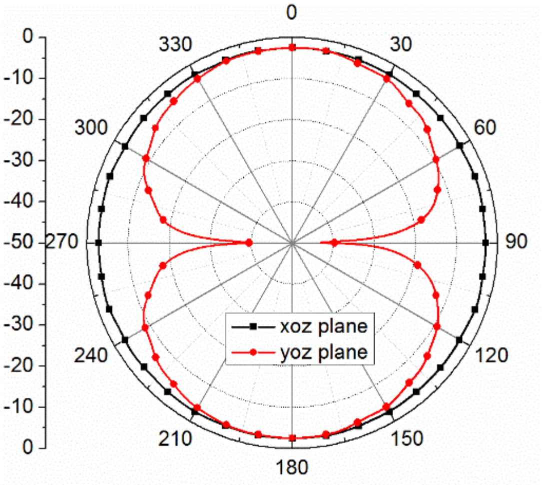

Fig. 9. The radiation patterns of devised antenna 2.

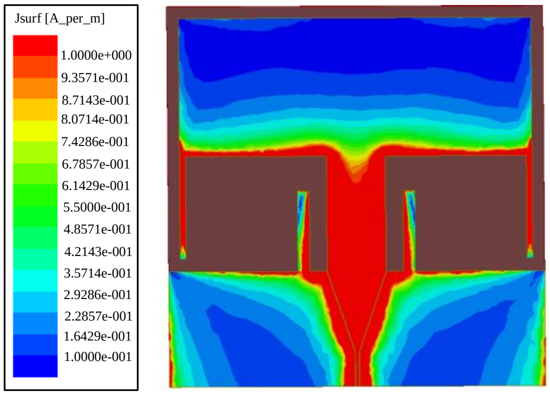

Fig. 10. The current distribution of the devised antenna 2.

The current distribution of the devised antenna 2 is given in Fig. 10, which can give an understanding for the antenna 2 design. From the current distribution, it can be seen that the current distribution concentrates on the feeding line, the ground plane, the T-shaped radiation patch, the parasitic branches and the sleeve structure. The parasitic branches and sleeve structure integrated into the designed antenna 1 can prolong the current path, which can be equivalent to the inductor loading to cancel the resistance of designed antenna 1. Thereby, the bandwidth of antenna 1 can be enhanced.

Although the bandwidth of the developed antenna 2 has achieved a -10 dB fractional bandwidth of 42.8%, it still cannot meet the demand of modern broadband wireless communication for wide range of detection at low frequency. To solve the problems and further enhance the bandwidth of the antenna 2, the antenna 3 is proposed as the final design of the low frequency wide band antenna.

C. Design of the antenna 3

The geometry of the antenna 3 is shown in Fig. 11, where passive lumped elements are integrated into the antenna structure that is based on the configuration of the designed antenna 2. These passive lumped elements include an inductor, a capacitance, and five resistances. The parasitic branches are connected to the ground by both resistance R4 and R5. The sleeve structures are attached with the T-shaped patch by both resistance R2 and R3. The resistance R1 and the inductor L1 are incorporated into the feeding line. While the capacitance C1 is set at the bottom of the substrate, which will make the soldering more convenient. The inductor L1 and the capacitance C1 are selected to make the proposed 3 resonate at high frequency band. And, five resistances R1, R2, R3, R4, and R5 are chosen to make the proposed antenna match to 50Ω. Thus, the bandwidth of the original antenna can be greatly enhanced by properly adjusting these elements in the HFSS.

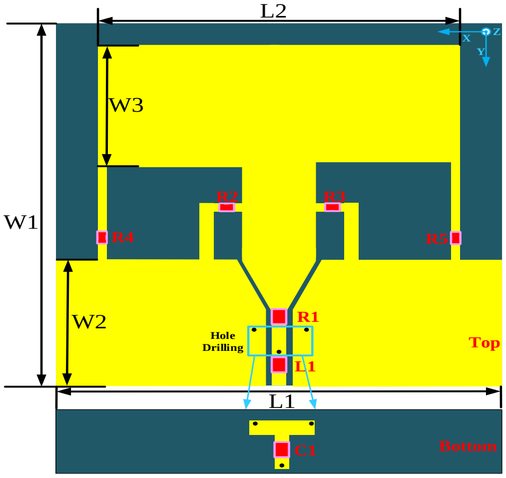

Fig. 11. The geometry of devised antenna 3.

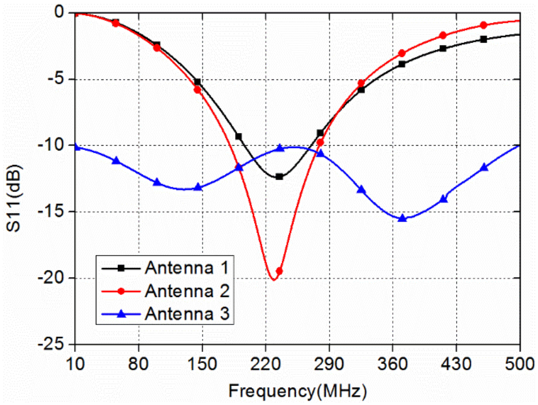

Fig. 12. Comparison of S11 for the designed three antennas.

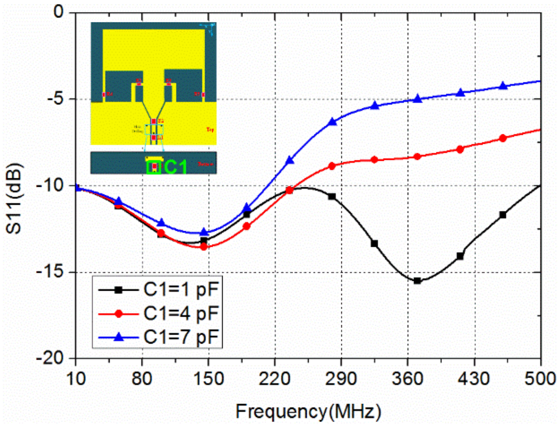

Fig. 13. The effect of C1 on the performance of the devised antenna 3.

The devised antenna 3 is modeled and optimized by the HFSS. By properly adjusting these values of the lumped elements, an ultra-wideband wideband can be obtained and named as antenna 3. And, the simulated reflection coefficients (S11s) is presented in Fig. 12, where the devised antenna 3 can achieve a -10 dB fractional bandwidth of 192.2% ranging from 10 MHz to 500 MHz that has been enhanced greatly in comparison with the simulated S11 of antenna 1 and antenna 2.

III. ANALYSIS AND MEASUREMENT

The final designed antenna 3 and its performance are depicted herein. To analyze the design principle, two parameters (the capacitance C1 and the resistance R1) are selected to investigate the effects for the finalized antenna 3. The results are show in Figs. 13 and 14. From Fig. 13, it can be observed that the bandwidth of the designed antenna has been deceased with the increasing of C1, especially, which means that C1 has great effect on the higher frequency band. Similarly, the inductor L1 has the same effect on the antenna 3. From Fig. 14, it can be concluded that the R1 has great effect for the antenna 3 in the entire frequency band. The three elements, namely C1, L1, and R1, are the most sensitive components. Thus, properly optimizing the three key elements and then adjusting the other four resistances can obtain a good performance for the antenna 3.

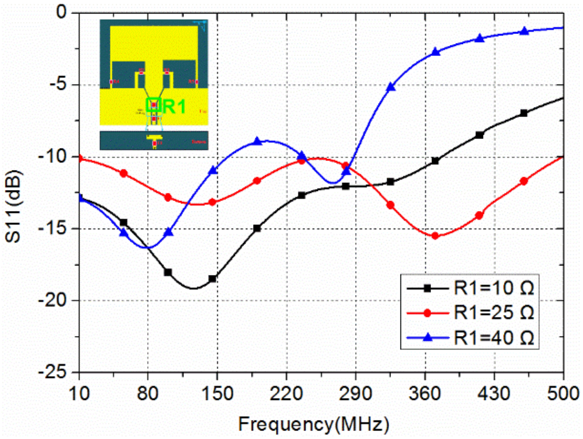

Fig. 14. The effect of R1 on the performance of the devised antenna 3.

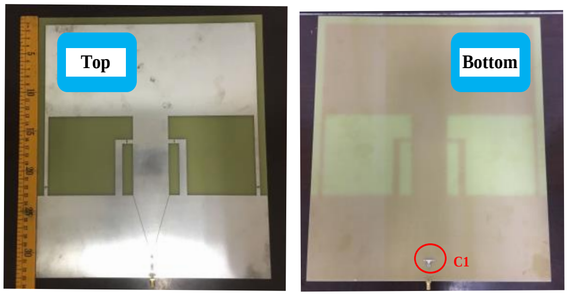

Fig. 15. The photograph of the fabricated antenna.

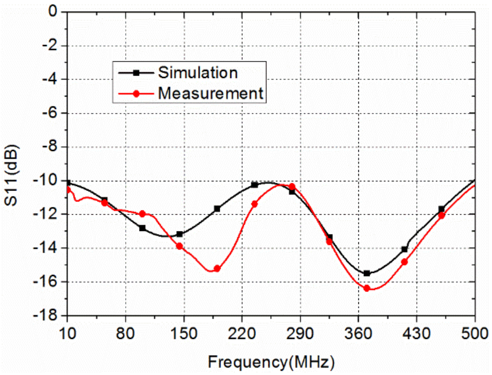

Fig. 16. Comparison of S11 of the simulation and measurement.

At last, to validate the simulated results, the antenna 3 is fabricated and these passive lumped elements are soldered into the fabricated antenna, which is shown in Fig. 15. To improve the accuracy of the experiment, these passive elements are used with the high accuracy of 1%. The reflection coefficient (S11) of the fabricated antenna is measured by employing the Keysight ENA Series Network Analyzer E5061B. The comparison of the simulated and measured results is depicted in Fig. 16.

From the Fig. 16, it can be concluded that the fabricated antenna has also a -10 dB fractional bandwidth of 192.2% ranging from 10 MHz to 500 MHz, which is in agreement with the simulated result. However, there is some difference between the simulation and measurement, which may be caused by the fabrication error, the parasitic effects of the electronic components, the soldering and stability of the substrate. To better evaluate the performance of the proposed antenna, the measured total efficiency and radiation patterns may be needed. However, the operating frequency band at low frequency is difficult to measure in practical, which means that an extremely large anechoic chamber is required for the measurement. In fact, it is difficult to measure the radiation patterns at very low frequency.

IV. CONCLUSION

In this paper, a low profile miniaturization sleeve monopole antenna loaded with passive lumped elements is proposed, which can be utilized for HF, VHF, UHF, and P band applications. The proposed antenna is divided into three antenna models to discuss the design procedure. The performance of each antenna model is analyzed in detail. The bandwidth of the proposed antenna has been improved step by step. At last, the final designed antenna loaded with lumped elements achieves a -10 dB fractional bandwidth of 192.2% ranging from 10 MHz to 500 MHz, which is greatly enhanced comparing with the results of the former two designed antennas. Moreover, the measured result is in agreement with the simulated one. In the future, the metasurface and filtering methods [21-23] can be well investigated on such antenna development, and the wide bandwidth beamforming based on adaptive techniques [24-28] is still an amazing topic.

ACKNOWLEDGMENTS

This paper is supported by the National Key Research and Development Program of China (2016YFE0111100), Key Research and Development Program of Heilongjiang (GX17A016), the Science and Technology innovative Talents Foundation of Harbin (2016RAXXJ044), the Natural Science Foundation of Beijing (4182077), China Postdoctoral Science Foundation (2017M620918, 2019T120134), the Fundamental Research Funds for the Central Universities (HEUCFG201829, 2072019CFG0801), and Opening Fund of Acoustics Science and Technology Laboratory (SSKF2016001).

REFERENCES

[1] D. G. Lopez, M. Ignatenko, and D. S. Filipovic, “Low-profile tri-band inverted-F antenna for vehicular applications in HF and VHF bands,” *IEEE Trans. Antennas Propag.*, vol. 63, no. 11, pp. 4632-4639, Nov. 2015.

[2] Y. Xia, W. Xue, Y. Li, and L. Zhao, “A dual-band WLAN antenna with reactive loading,” *Applied Computational Electromagnetics Society Journal*, vol. 34, no. 7, pp. 1026-1031, July 2019.

[3] W. An, X. Wang, H. Fu, J. Ma, X. Huang, and B. Feng, “Low-profile wideband slot-loaded patch antenna with multiresonant modes,” *IEEE Antennas Wireless Propag Lett.*, vol. 17, no. 7, pp. 1309-1313, Jul. 2018.

[4] J. Jiang, Y. Xia, and Y. Li, “High isolated X-band MIMO array using novel wheel-like metamaterial decoupling structure,” *Applied Computational Electromagnetics Society Journal*, accepted 2020.

[5] S. Luo, Y. Li, Y. Xia, and L. Zhang, “A low mutual coupling antenna array with gain enhancement using metamaterial loading and neutralization line structure,” *Applied Computational Electromagnetics Society Journal*, vol. 34, no. 3, pp. 411-418, Mar. 2019.

[6] L. J. Chu, “Physical limitations of omni-directional antennas,” *J. Appl. Phys.*, vol. 19, no. 12, pp. 1163-1175, May 1948.

[7] A. D. Yaghjian and S. R. Best, “Impedance, bandwidth, and Q of antennas,” *IEEE Trans. Antennas Propag.*, vol. 53, no. 4, pp. 1298-1324, Aug. 2005.

[8] R. W. Ziolkowski, “An efficient, electrically small antenna designed for VHF and UHF applications,” *IEEE Antennas Wireless Propag Lett.*, vol. 7, pp. 217-220, Apr. 2008.

[9] L. Mattioni and G. Marrocco, “Design of a

broadband HF antenna for multimode naval communications-part II: extension to VHF/UHF ranges," *IEEE Antennas Wireless Propag Lett.*, vol. 6, pp. 83-85, Mar. 2007.

[10] K. Ghaemi and N. Behdad, "A low-profile, vertically polarized ultrawideband antenna with monopole-like radiation characteristics," *IEEE Trans. Antennas Propag.*, vol. 63, no. 8, pp. 3699-3705, Aug. 2015.

[11] A. Loutridis, "Study of UHF and VHF compact antenans," *Ph.D. Thesis*, Dublin Institute of Technology, Ireland, 2015.

[12] K. Ghaemi, R. Ma, and N. Behdad, "A small-aperture, ultrawideband HF/VHF direction-finding system for unmanned aerial vehicles," *IEEE Trans. Antennas Propag.*, vol. 66, no. 10, pp. 5109-5120, Oct. 2018.

[13] J. T. Aberle, "Two-port representation of an antenna with application to non-foster matching networks," *IEEE Trans. Antennas Propag.*, vol. 56, no. 5, pp. 1218-1222, May 2008.

[14] J. Church, J. C. S. Chieh, L. Xu, J. D. Rockway, and D. Arceo, "UHF electrically small box cage loop antenna with an embedded non-Foster load," *IEEE Antennas Wireless Propag. Lett.*, vol. 13, pp. 1329-1332, Jul. 2014.

[15] Y. Xia, Y. Li, and S. Zhang, "A non-foster matching circuit for an ultra-wideband electrically small antenna," *13th European Conference on Antennas and Propagation*, Krakow, Poland, 2019.

[16] T. Shi, M. Tang, Z, Wu, H. Xu, and R. W. Ziolkowski, "Improved signal-to-noise ratio, bandwidth-enhanced electrically small antenna augmented with internal non-Foster elements," *IEEE Trans. Antennas Propag.*, vol. 67, no. 4, pp. 2763-2768, Jan. 2019.

[17] C. R. White, J. S. Colburn, and R. G. Nagele, "A non-foster VHF monopole antenna," *IEEE Antennas Wireless Propag Lett.*, vol. 11, pp. 584-587, Jun. 2012.

[18] M. M. Jacob and D. F. Sievenpiper, "Non-foster matched antennas for high-power applications," *IEEE Trans. Antennas Propag.*, vol. 65, no. 9, pp. 4461-4469, Sept. 2017.

[19] Y. Xia, W. Xue, Y. Li, W. Shi, and B. Li "A low frequency ultra-wideband electrically small monopole antenna for HF/VHF application," *Applied Computational Electromagnetics Society Journal*, vol. 34, no. 7, pp. 1050-1057, Jul. 2019.

[20] R. N. Simons, *Coplanar Waveguide Circuits, Components and Systems*, New York: John Wiley & Sons, 2004.

[21] K. Yu, Y. Li, and X. Liu, "Mutual coupling reduction of a MIMO antenna array using 3-D novel meta-material structures," *Applied Computational Electromagnetics Society Journal*, vol. 33, no. 7, pp. 758-763, Jul. 2018.

[22] F. Liu, J. Guo, L. Zhao, et al., "Dual-band meta-surface-based decoupling method for two closely packed dual-band antennas," *IEEE Transactions on Antennas and Propagation*, 10.1109/TAP.2019. 2940316, 2019.

[23] W. Wang, J. Ran, N. Hu, W. Xie, Y. Wu, and A. Kishk, "A novel differential filtering patch antenna with high selectivity," *International Journal of RF and Microwave Computer-Aided Engineering*, vol. 29, no. 10, e21880, Oct. 2019.

[24] X. Zhang, T. Jiang, Y. Li, et al., "A novel block sparse reconstruction method for DOA estimation with unknown mutual coupling," *IEEE Communications Letters*, vol. 23, no. 10, pp. 1845-1848, 2019.

[25] Y. Li, Z. Jiang, O. M. O. Osman, et al., "Mixed norm constrained sparse APA algorithm for satellite and network echo channel estimation," *IEEE Access*, vol. 6, pp. 65901-65908, 2018.

[26] Y. Li, Z. Jiang, W. Shi, et al., "Blocked maximum correntropy criterion algorithm for cluster-sparse system identifications," *IEEE Transactions on Circuits and Systems II: Express Briefs*, vol. 66, no. 11, pp. 1915-1919, 2019.

[27] W. Shi, Y. Li, and L. Zhao, "Controllable sparse antenna array for adaptive beamforming," *IEEE Access*, vol. 7, pp. 6412-6423, 2019.

[28] W. Shi, Y. Li, and Y. Wang, "Noise-free maximum correntropy criterion algorithm in non-gaussian environment," *IEEE Transactions on Circuits and Systems II: Express Briefs*, 10.1109/ TCSII. 2019. 2914511, 2019.

Mutual Coupling Reduction of Dual Polarized Low Profile MIMO Antenna Using Decoupling Resonators

Faizan Faraz [1], **Xiaoming Chen** [1], **Qinlong Li** [1], **Jiazhi Tang** [1], **Jianxing Li** [1],
Tayyab. A. Khan [2], **and Xiaotong Zhang** [3]

[1] Faculty of Electronic and Information Engineering
Xi'an Jiaotong University, Xi'an 710049, China
farazfaizan@stu.xjtu.edu.cn, xiaoming.chen@mail.xjtu.edu.cn, liql519@mail.xjtu.edu.cn

[2] Department of Electrical Engineering
City University of Hong Kong, Hong Kong 850761, China

[3] College of Biomedical Engineering & Instrument Science
Zhejiang University, Hangzhou 310029, China

Abstract **─** This paper presents a resonator based decoupling structure for 2×2 dual polarized array antenna. The designed structure consists of two decoupling resonators placed between the antenna elements. The proposed decoupling structure can effectively enhance the isolation and has negligible impact on the radiation patterns.

Index Terms **─** Decoupling, dual-polarized array, resonator.

I. INTRODUCTION

Dual polarized and compact array antennas are highly desirable in multiple-input multiple-output (MIMO) systems. However, mutual coupling becomes inevitable in compact MIIMO antennas [1]. A series of mutual coupling reduction techniques have been proposed in the literature. For example, the mutual coupling can be reduced using the defected ground structure (DGS) [2], electromagnetic band gap (EBG) [3], neutralization line [4], parasitic element [5], metamaterial [6]-[8], shorting vias [9], interference cancellation chip [10], hybrid topology optimization [11], decoupling surface [12], decoupling ground [13], dual polarized slot antenna [14]-[17], split ring resonator (SRR) [18], etc. However, the DGS tends to increase the backward radiation; the neutralization line and shorting via methods are mainly suitable for two-element MIMO antenna and are difficult to be extended to MIMO antennas with more than two elements; and most of these techniques works only for single polarized antennas and may distort the radiation pattern, except for [12] and [13], which however inevitably incase the profile of the array.

In this work, we focus on the SRR based decoupling technique for low profile arrays. The SRR decoupling structures have been studied in [18]-[21]. The SRR unit has been used as metasurface element for decoupling [6]. The SRRs presented in [6],[18],[19] are only valid for single-polarized two-port array. The authors in [20] presented a SRR-based superstrate, which works for linear arrays with more than two ports. However, the SRR structure increases the profile. SRR walls were used to decouple a 2×2 array with circular polarization [21]. Moreover, the three-dimensional (3D) SRR structure in [21] dictates a relatively high profile and manufacturing cost.

In this paper, we propose a decoupling resonator (DR) structure to reduce the mutual coupling of a 2×2 dual polarized low profile microstrip array antenna at 3.5 GHz. Two cells of DRs are placed between antennas with an edge-to-edge spacing of $0.14\lambda_0$ (center-to-center spacing of $0.39\lambda_0$). The proposed DR structure can effectively suppress the surface wave in the H-plane, while a small E-plane coupling is achieved by array design itself. Thus, unlike the previous SRR works with single linear polarization, effective mutual coupling is achieved for a dual polarized array. The proposed DR structure effectively reduces the H-plane coupling below -20 dB without degrading either the isolation in the E-plane or the isolation between orthogonal polarizations. Moreover, it is shown that the proposed DR structure does not distort the radiation patterns of the array, which is a highly desirable feature for array decoupling.

II. ANTENNA STRUCTURE AND RESULTS

A dual polarized 2×2 microstrip array antenna with eight SRR decoupling structures is shown in Fig. 1 (a) and Fig. 1 (b) shows the DR unit. A square patch with a

Submitted On: September 19, 2019
Accepted On: November 11, 2019

dimension of 21.8 mm is used as the array element. The edge-to-edge spacing between the adjacent elements is 12 mm (0.14λ_0, where λ_0 denotes the wavelength in free space). The microstrip element is fed by two coaxial ports in the horizontal and vertical directions at a distance of 3.4 mm from the center. The two positions was found to give good impedance matching. The antenna ports are marked as numbers 1-8 in Fig. 1 (a). The substrate is Rogers 4350B with a dielectric constant of 3.48 and a thickness of h = 1.524 mm. The ground has a size of 120 mm × 120 mm. The array has a resonating frequency at 3.5 GHz. The dimensions of proposed DR unit are summarized in Table 1.

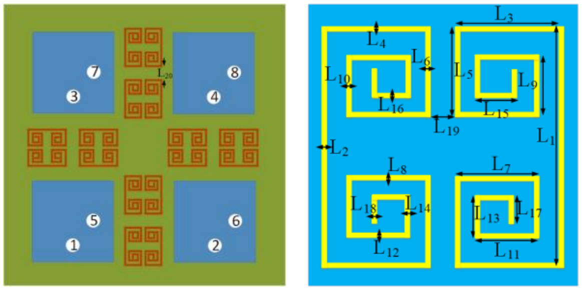

(a) (b)

Fig. 1. (a) Dual polarized MIMO antenna with DR decoupling structures; (b) proposed DR unit.

Table 1: Parameters of proposed antenna

Parameters	Values (mm)	Parameters	Values (mm)
L_1	7.90	L_{11}	1.30
L_2	0.25	L_{12}	0.20
L_3	2.40	L_{13}	1.60
L_4	0.25	L_{14}	0.20
L_5	3.00	L_{15}	0.75
L_6	0.20	L_{16}	0.20
L_7	2.00	L_{17}	1.00
L_8	0.30	L_{18}	0.20
L_9	2.60	L_{19}	0.90
L_{10}	0.25	L_{20}	9.00

All simulations are carried out in CST microwave studio in this work. Figure 2 shows the S-parameters of the 2×2 array without DR. As can be seen, given the array design (i.e., element separation, patch size, dielectric, etc.), the H-plane coupling dominates, i.e., the worst mutual coupling of -12 dB occurs in the H-plane (between ports 1 and 2), the mutual coupling in the E-plane (between ports 1 and 3) is below -20 dB, and the mutual coupling between the two polarization in the same patch (between ports 1 and 5) is negligible. Therefore, the effort for mutual coupling reduction is exerted in designing the DR to bring down the H-plane coupling, without degrading either the E-plane coupling or the polarization isolation.

To explain the decoupling mechanism, we analyze the resonator by increasing its number of turns in five steps, see steps a-e in Fig. 3 (a). The corresponding H-plane coupling (S_{21}) is shown in Fig. 3 (b). As can be seen, the initial design (step a) has a resonance at 3.8 GHz. The resonance shifts towards lower frequency as the number of turns increases. The final design (step e) has a resonance at the required frequency of 3.5 GHz.

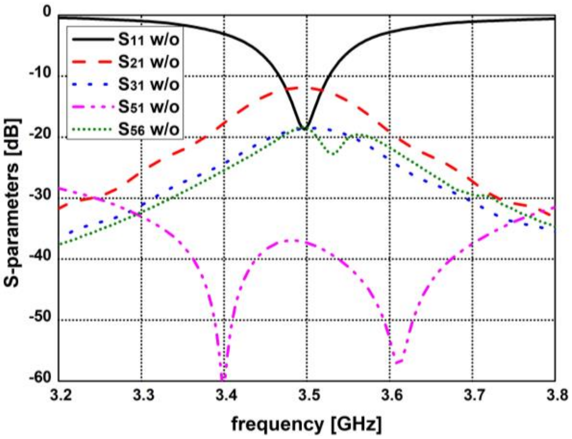

Fig. 2. S-parameters without (w/o) decoupling structure.

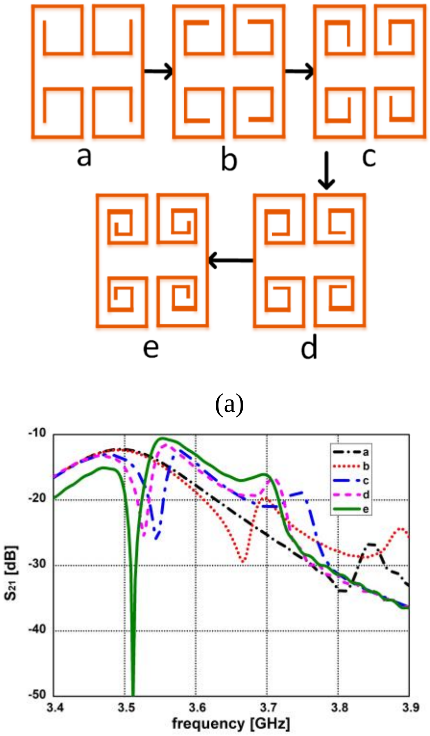

(a)

(b)

Fig. 3. (a) Design process of the proposed DR and (b) the corresponding S_{21}.

Figure 4 shows that the mutual impedance of two antennas with and without the DR structure. As can be seen, the DR structure reduces the mutual impedance between antenna ports 1 and 2 to about zero at 3.5 GHz. The surface wave is trapped by the DR units, resulting in low mutual coupling.

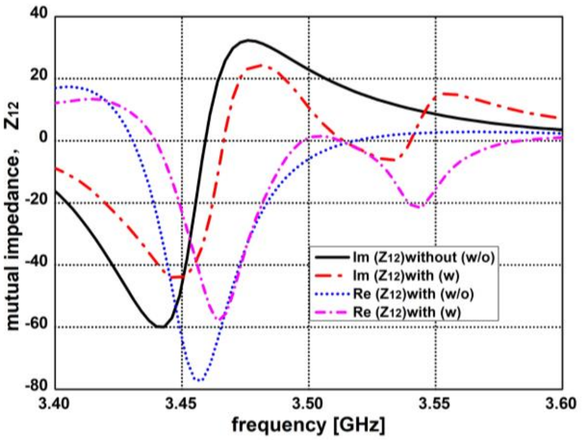

Fig. 4. Mutual impedance Z12 with and without DR structure.

It is found that optimal H-plane decoupling is achieved by inserting two DR units between the adjacent array elements (cf. Fig. 1 (a)). Figure 5 compares the S-parameters of the array antenna with and without the DR based decoupling structure. As can be seen, the DR can greatly reduce the H-plane mutual coupling (S_{21}) by more than 20 dB at the resonating frequency.

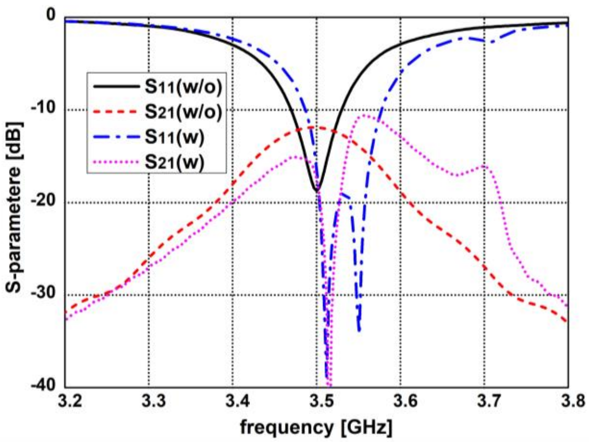

Fig. 5. Comparisons of S-parameters with (w) and without (w/o) DR structure.

Figure 6 shows a photo of the fabricated prototype of the dual polarized 2×2 array with DR based decoupling structure. Figure 7 shows the comparisons of the simulated and measured S-parameters with (w) the DR based decoupling structure. There are in general good agreements between the simulated and measured S-parameters. The small discrepancies are mainly attributed to imperfect soldering and manufacturing tolerance.

Fig. 6. Fabricated prototype of dual polarized antenna with DR structure.

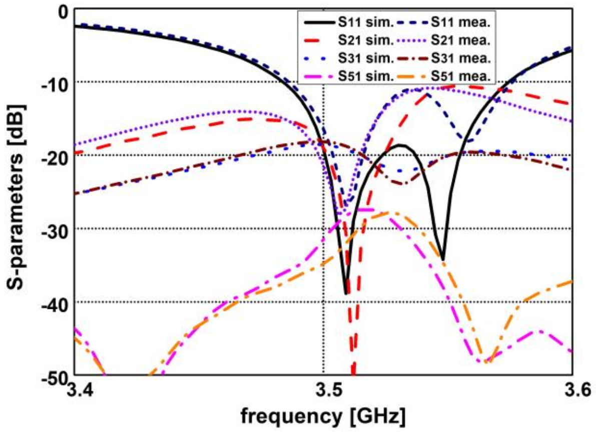

Fig. 7. Comparison of simulated and measured S-parameters with DR structure.

To further illustrate the decoupling property of the DR structure, the absolute surface currents with and without the DR decoupling structure are plotted in Fig. 8. Specifically, Fig. 8 (a) shows the surface current distribution of the 2×2 array without the DR decoupling structure; Fig. 8 (b) shows the surface current distribution of the 2×2 array with a single DR unit between the adjacent array elements; Fig. 8 (c) shows the surface current distribution of the 2×2 array with the proposed decoupling structure (i.e., two DR units between adjacent array elements). As can be seen, the with one DR unit between the adjacent array elements, the coupling is reduced. Yet there is still noticeable amount of coupling left. By inserting two DR units between adjacent array elements, the coupling is reduced significantly.

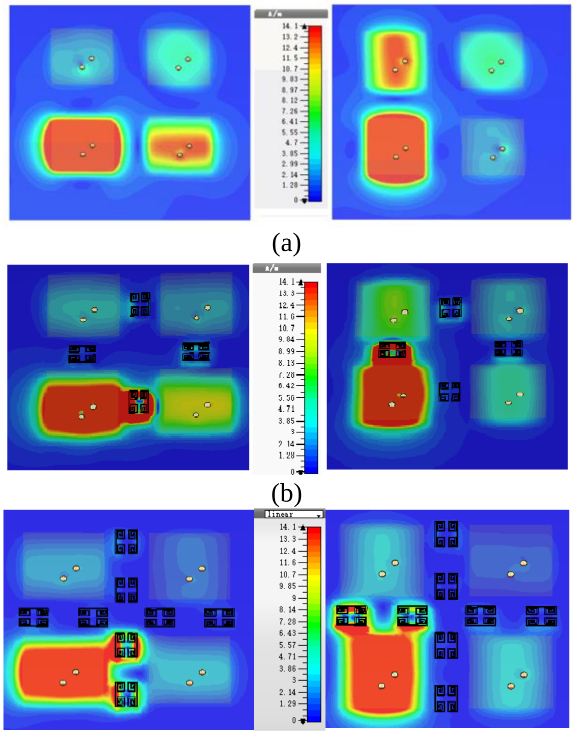
(a)

(b)

(c)

Fig. 8. Surface current distribution at 3.5 GHz: (a) without DR, (b) with a single DR between adjacent array elements, and (c) with two DRs between adjacent array elements.

Figure 9 shows the comparisons of simulated radiation patterns with and without decoupling structure. In addition, the measured radiation pattern of the prototype (with decoupling structure) is plotted in the same figure. As can be seen, due to antenna misalignment, imperfect soldering, and manufacturing tolerance, small discrepancy exists between the simulated and measured radiation patterns. Nevertheless, there is still reasonable agreement between them. The slight tilt in the radiation pattern is probably due to the asymmetrical location of the antenna in the finite ground plane. More importantly, the good agreement between the simulated radiation patterns with and without the decoupling structure indicate that the DR has little effect on the radiation pattern. Note that the total radiation efficiency of the proposed antenna with the DR structure is about 66%, where the total radiation efficiency of the antenna without the DR structure is about 73%. So the DR structure introduced some losses. But the losses are not significant.

III. CONCLUSION

In this paper, a DR structure for dual polarized 2×2 array antenna was proposed. By designing the array antenna itself, small E-plane coupling was achieved, while the severe H-plane coupling could be reduced by more than 20 dB at the resonating frequency using the proposed DR decoupling structure. In this way, DR based mutual coupling reduction was achieved for dual polarized low profile array. Moreover, the DR decoupling structure does not distort the radiation pattern of the array, which is a highly desirable feature of the decoupling technique.

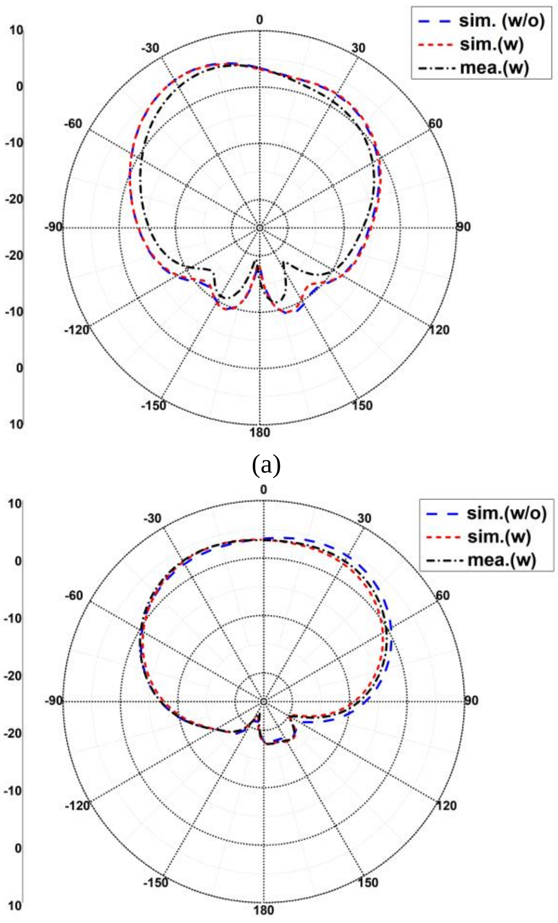

(a)

(b)

Fig. 9. Radiation patterns of simulated (sim.) without (w/o), simulated (sim.) and measured (mea.) with (w) DR decoupling structure: (a) vertical polarization; (b) horizontal polarization.

ACKNOWLEDGMENT

This work is supported in part by the National Natural Science Foundation of China under Grants 61801366, 61901354, and by the State Key Laboratory of Millimeter Waves under Grant K201933.

REFERENCES

[1] X. Chen, S. Zhang, and Q. Li, “A review of mutual coupling in MIMO systems,” *IEEE Access*, vol. 6, pp. 24706-24719, 2018.

[2] M. S. Sharawi, A. B. Numan, M. U. Khan, and D. N. Aloi, “A dual-element dual-band MIMO antenna system with enhanced isolation for mobile terminals,” *IEEE Antennas Wireless Propag. Lett.*, vol. 11, pp. 1006-1009, 2012.

[3] H. Yi and S. Qu, “A novel dual-band circularly polarized antenna based on electromagnetic band-gap structure,” *IEEE Antennas Wireless Propag. Lett.*, vol. 12, pp. 1149-1152, Sep. 2013.

[4] S. Wang and Z. Du, “Decoupled dual-antenna system using crossed neutralization lines for LTE/ WLAN smartphone applications,” *IEEE Antennas Wireless Propag. Lett.*, vol. 14, pp. 523-526, 2014.

[5] B. K. Lau and J. B. Andersen, “Simple and efficient decoupling of compact arrays with parasitic scatterers,” *IEEE Transactions on Antennas and Propagation*, vol. 60, no. 2, pp. 464-472, Feb. 2012.

[6] Z. Wang, L. Zhao, Y. Cai, S. Zheng, and Y. Yin, “A meta-surface antenna array decoupling (MAAD) method for mutual coupling reduction in a MIMO antenna system,” *Scientific Reports*, vol. 8, no. 1, 2018.

[7] K. Yu, Y. Li, and X. Liu, “Mutual coupling reduction of a MIMO antenna array using 3-D novel meta-material structures,” *ACES Journal*, vol. 33, no. 7, July 2018.

[8] S. Luo, Y. Li, Y. Xia, and L. Zhang, “A low mutual coupling antenna array with gain enhancement using metamaterial loading and neutralization line structure,” *ACES Journal*, vol. 34, no. 3, Mar. 2019.

[9] M. Abdullah, X. Chen, Q. Li, and A. A Kishk, “Mutual coupling and correlation of closely spaced patch antennas,” *Electron. Lett.*, vol. 55, no. 13, pp. 724-726, 2019.

[10] L. Zhao, F. Liu, X. Shen, G. Jing, Y.-M. Cai, and Y. S. Li, “A high-pass antenna interference cancellation chip for mutual coupling reduction of antennas in contiguous frequency bands,” *IEEE Access*, vol. 6, pp. 38097-38105, July 2018.

[11] S. Zhu, X. Yang, J. Wang, and B. Wang, “Design of MIMO antenna isolation structure based on a hybrid topology optimization method,” *IEEE Trans. Antennas Propag.*, in press.

[12] K.-L. Wu, C. Wei, X. Mei, and Z. Zhang, “Array-antenna decoupling surface,” *IEEE Trans. Antennas Propag.*, vol. 65, no. 12, pp. 6728-6738, Dec. 2017.

[13] S. Zhang, X. Chen, and G. F. Pedersen, “Mutual coupling suppression with decoupling ground for massive MIMO antenna arrays,” *IEEE Trans. Veh. Technol.*, vol. 68, no. 8, pp. 7273-7282, 2019.

[14] Y. Li, Z. Zhang, J. Zheng, and Z. Feng, “Compact azimuthal omnidirectional dual-polarized antenna using highly isolated colocated slots,” *IEEE Transactions on Antennas and Propagation*, vol. 60, no. 9, Sep. 2012.

[15] Y. Li, Z. Zhang, J. Zheng, and Z. Feng, “Design of dual-polarized monopole-slot antenna with small volume and high isolation,” *IEEE Transactions on Antennas and Propagation*, vol. 60, no. 5, May 2012.

[16] Y. Li, Z. Zhang, Z. Feng, and M. F. Iskander, “Design of omnidirectional dual-polarized antenna in slender and low-profile column,” *IEEE Transactions on Antennas and Propagation*, vol. 62, no. 4, Apr. 2014.

[17] Y. Li, Z. Zhang, J. Zheng, and Z. Feng, “Dual-polarised monopole-slot co-located MIMO antenna for small-volume terminals,” *Electron. Lett.*, vol. 47, no. 23, Nov. 2011.

[18] A. Habashi, J. Nourinia, and C. Ghobadi, “Mutual coupling reduction between very closely spaced patch antennas using low-profile folded split-ring resonators (FSRRs),” *IEEE Antennas Wireless Propag. Lett.*, vol. 10, pp. 862-865, 2011.

[19] O. F. Siddiqui and O. M. Ramahi, “Mutual coupling reduction between microstrip patch antennas using slotted-complementary split-ring resonators,” *IEEE Antennas Wireless Propag. Lett.*, vol. 55, pp. 876-878, 2010.

[20] M. Li, B. G. Zhong, and S. W. Cheung, “Isolation enhancement for MIMO patch antennas using near-field resonators as coupling-mode transducers,” *IEEE Trans. Antennas Propag.*, vol. 67, no. 2, pp. 755-763, 2019.

[21] A. A. Gheethan, P. A. Herzig, and G. Mumcu, “Compact 2×2 coupled double loop GPS antenna array loaded with broadside coupled split ring resonators,” *IEEE Antennas Wireless Propag. Lett.*, vol. 61, no. 6, pp. 3000-3008, 2013.

Faizan Faraz is currently working towards his master degree in the school of Electrical and Information Engineering from Xi’an Jiaotong University, Xi’an, China.

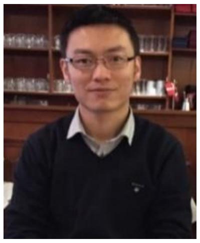

Xiaoming Chen is currently a Professor at Xi’an Jiaotong University, Xi’an, China. His research areas include 5G multi-antenna techniques, and over-the-air (OTA) testing. He serves as an Associate Editor (AE) for the journal of IEEE Antennas and Wireless Propagation Letters and received the outstanding AE awards in 2018 and 2019. He received the URSI (International Union of Radio Science) Young Scientist Awards in 2017 and 2018.

Qinlong Li is a Lecturer in Xi’an Jiaotong University. His current research interests include millimeter-wave antennas, base station antennas.

Jiazhi Tang is currently pursuing the Ph.D. degree in Xi’an Jiaotong University. His research interest is metasurface.

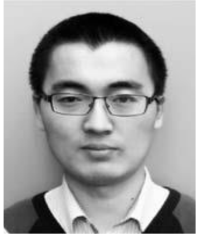

Jianxing Li (S'15–M'18) is currently an Associate Professor in Xi'an Jiaotong University, Xi'an, China. His current research interests include antennas, microwave and mmW circuits, and metamaterials.

Tayyab. A. Khan is pursuing his Ph.D. degree in City University of Hong Kong. His current research interests include antenna designing, metasurfaces, and metamaterials.

Xiaotong Zhang is an Associate Professor Zhejiang University. His current research interests include state-of-the-art RF coil design at ultra-high fields, numerical electro-magnetic modeling and computation, and functional biomedical imaging for both human and non-human primate.

Design Strategy for Compact Bandpass Filters Using Meander Line Resonators

Abdul Sami [1], MuhibUr Rahman [2*], Hamza Ahmad [3], and Shahid Bashir [4]

[1] National University of Sciences & Technology (NUST)
Islamabad, Pakistan

[2*] Department of Electrical Engineering
Polytechnique Montreal, Montreal, QC H3T 1J4, Canada

[3] Gandhara Institute of Science and Technology
Peshawar, Pakistan

[4] University of Engineering and Technology
Peshawar, Pakistan

Abstract **─** The purpose of this manuscript is to present a compact design strategy for bandpass filters using Meander Line Resonators (MLR) in combination with Stub Loaded Resonators (SLR). The proposed resonator has been designed and analyzed using even-odd mode analysis. Open-ended stubs are loaded at an appropriate position in the dual-mode resonator to achieve tri, quad, and quintuple passbands. To reduce the circuit size and create transmission zeros at our desired frequencies, a symmetrical meandered shape resonator is loaded with open-ended identical stubs which are bent towards each other. A design strategy is presented step by step and the approach is validated using simulation and experiments.

Index Terms **─** Band-pass filters (BPFs), dual BPF, even and odd mode analysis, stub loaded resonators (SLR), triple BPF, quad BPF.

I. INTRODUCTION

Multiband filters are considered as one of the essential parts of multi-band transceivers. Planar filters are having a vital part in the RF front end to obtain the preferred and high-quality signals. In order to provide smooth communication by a multiband transceiver, it is necessary to have BPFs which have small circuit size and high selectivity to avoid any interference with nearby frequency bands. Multiband BPF's have many direct and indirect advantages and can be used in different applications for various purposes. Different multiband BPF's are developed in this regard having different functionalities and different characteristics [1-8].

Various dual bandpass filters are designed using DGS, SIRs, and SLR [6-17]. Recently, a tri-band response is achieved by means of a combination of SLR termed as SLDMRs [9]. Two SLDMRs combined with intra-resonator coupling between inner and outer rings are utilized to obtain a triple passband response. However, the size of the filter is large, and five transmission zeros are achieved. The same technique has been adopted in [12] to achieve tri-band performance with good selectivity by analyzing the loaded and unloaded quality factor. Six transmission zeros are achieved instead of five transmission zeros. The use of SIR in multiband BPFs is also exploited and several geometries are developed in [10, 11]. They utilized higher-order modes to create additional passbands. Also, such an approach generates an additional loss and greatly increases the overall size of the circuit.

Also, in [11] they presented a very compact wideband bandpass filter using a quasi-elliptic resonator in combination with DGS. The presented filter is advantageous in terms of insertion loss, 3-dB fractional bandwidth, and with two transmission zeros. The proposed filter was implemented in frequency scanning beam array antenna to increase its bandwidth. Also, in [16-18], they designed and developed a stop band filters based on slot resonators and then integrated within the antenna to achieve the corresponding notched band performance. Similarly, in [19, 20] they designed a band stop filters and then integrated within the antenna. However, this time they made the achieved stop bands tunable by utilizing active components within the filter.

Furthermore, in [21] they presented and claimed a very compact quintuple band bandpass filter utilizing multimode stub loaded resonator. A single symmetric resonator is loaded with a short-ended stub in the middle along with four pairs of open-ended stubs. The proposed bandpass filter operates at GSM-900, LTE2300, WiMAX

Submitted On: July 9, 2019
Accepted On: December 28, 2019

(3.5 GHz), WLAN (5.4 GHz), and RFID (6.8 GHz). Likewise, in [22] quad BPF is accomplished using the technique of splitting a single wideband into multiple passbands.

This technique is complex and independent tuning of each passband is challenging. In this manuscript, we present a compact design strategy for bandpass filters using Meander Line Resonators (MLR) in combination with Stub Loaded Resonators (SLR). The presented resonator is designed and analyzed using even-odd mode analysis due to its symmetrical geometry. Open-ended stubs are loaded at an appropriate position in the dual-mode resonator to achieve tri and quad passbands. To reduce the circuit size and create transmission zeros at our desired frequencies, a symmetrical meandered shape resonator is loaded with open-ended identical stubs which are bent towards each other. A design strategy is presented step by step and the approach is validated using simulation and experiments.

This manuscript is arranged in the following manner: Section II deals with the recommended resonator analysis and to show the derivation of its corresponding even and odd mode frequencies. Section III provides the corresponding geometry of the designed filters based on the analysis in Section II along with the simulated and measured results, which is followed by the conclusion in Section IV.

II. RESONATOR ANALYSIS

A basic SLR comprising of one shorted stub and eight open stubs are provided in Fig. 1. It is further decomposed into even and odd mode circuits as shown in Figs. 1 (b) and (c), respectively. This even and odd mode can further be decomposed into five resonant circuits as shown in Fig. 1 (d) to Fig. 1 (m), respectively. Now, the resonant odd and even mode frequencies are calculated as in Table 1.

Table 1: Corresponding even and odd mode resonances

Even Mode Frequencies	**Odd Mode Frequencies**
$f_{even1} = \frac{(2n-1)c}{4(L_1+L_2+L_3+L_4+L_5+L_s)\sqrt{\varepsilon_{eff}}}$	$f_{odd1} = \frac{(2n-1)c}{4(L_1+L_2+L_3+L_4+L_5)\sqrt{\varepsilon_{eff}}}$
$f_{even2} = \frac{(2n-1)c}{4(L_2+L_3+L_4+L_5+L_s+L_6)\sqrt{\varepsilon_{eff}}}$	$f_{odd2} = \frac{(2n-1)c}{4(L_2+L_3+L_4+L_5+L_6)\sqrt{\varepsilon_{eff}}}$
$f_{even3} = \frac{(2n-1)c}{4(L_3+L_4+L_5+L_7+L_s)\sqrt{\varepsilon_{eff}}}$	$f_{odd3} = \frac{(2n-1)c}{4(L_3+L_4+L_5+L_7)\sqrt{\varepsilon_{eff}}}$
$f_{even4} = \frac{(2n-1)c}{4(L_4+L_5+L_8+L_s)\sqrt{\varepsilon_{eff}}}$	$f_{odd4} = \frac{(2n-1)c}{4(L_4+L_5+L_8)\sqrt{\varepsilon_{eff}}}$
$f_{even5} = \frac{(2n-1)c}{4(L_5+L_9+L_s)\sqrt{\varepsilon_{eff}}}$	$f_{odd5} = \frac{(2n-1)c}{4(L_5+L_9)\sqrt{\varepsilon_{eff}}}$

Table 2: Geometrical dimensions for single/dual/tri-BPF's (all values are in mm)

Parameter	**Value**	**Parameter**	**Value**	**Parameter**	**Value**
L_m	5	L_s	2.25	W_r	2
L_f	3.25	W_s	1	W_1	0.5
W_6	1	W_7	4	L_1	14.1
L_4	4	L_5	7.02	L_6	7.07
G_1, G_2, G_3	0.5	Via	0.5	W_4	0.5
L_3	4.6	L_8	4	W_2	1.75
W3	2.17	L_2	4	L_7	5.85

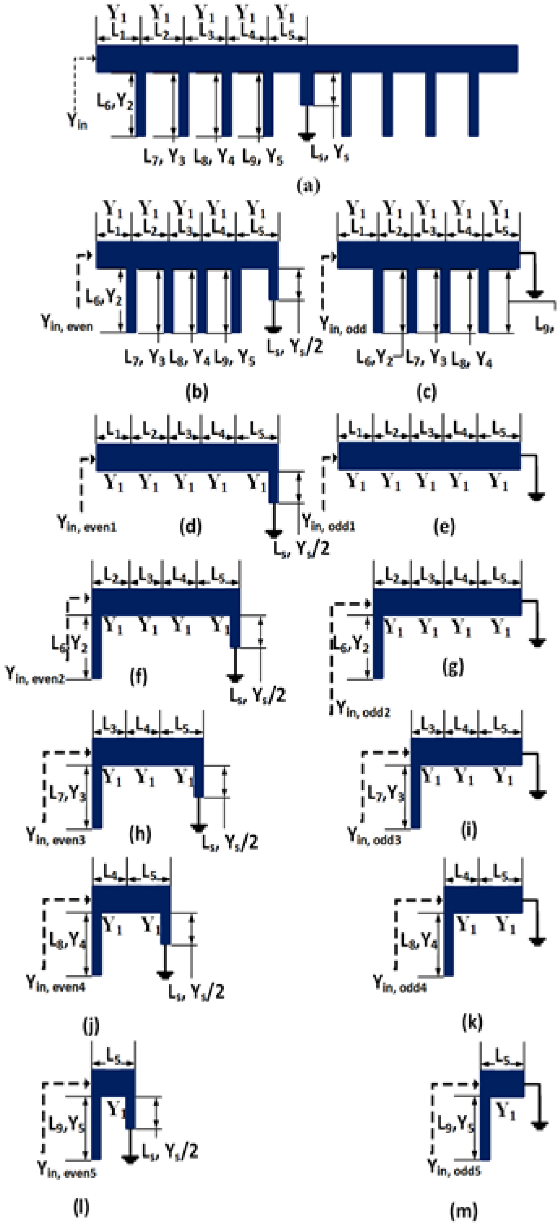

Fig. 1. Decomposition of the proposed SLR: (a) Basic SLR, (b) even mode circuit, (c) odd mode circuit (d, f, h, j, l) even mode equivalent circuits, and (e, g, i, k, m) odd mode equivalent circuits.

III. RESULTS AND DISCUSSION

Designed single, dual, triple, quad, and quintuple band bandpass filters are simulated using commercially available software ANSOFT HFSS and fabricated as well. The filters are also measured, and its frequency response is provided in each case. First, the optimization of different parameters is performed, and the final optimized parameters of the filters are provided in Table 2.

Figure 2 shows the corresponding single BPF with a simulated frequency response in Fig. 3. The proposed single BPF is designed for 1 GHz center frequency. Similarly, Fig. 4 shows the corresponding dual BPF with simulated frequency response in Fig. 5. Now the dual BPF is designed for 1 GHz and 2.5 GHz and it can be well seen from Fig. 5. Three transmission zeros are observed in this case.

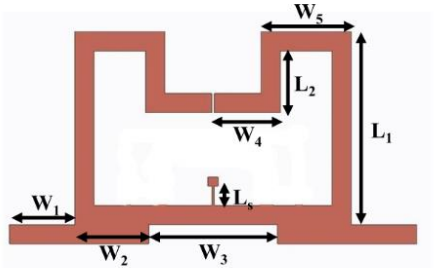

Fig. 2. Developed single BPF.

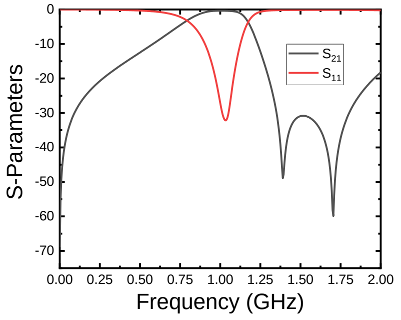

Fig. 3. Single BPF response.

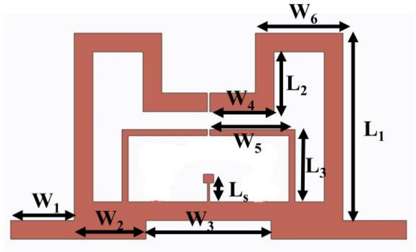

Fig. 4. Developed dual BPF.

Figure 6 shows the corresponding tri BPF aimed to operate at GSM-900, LTE-2300, and WiMAX (3.5 GHz). The measured and simulated frequency response including S_{11} and S_{21} of the developed tri-band BPF is also shown in Fig. 7. The developed tri-band BPF is aimed for useful wireless applications such as GSM-900, LTE-2300, and WiMAX (3.5 GHz). The middle frequencies of the developed tri-band BPF are 0.9550 GHz, 2.2948 GHz, and 3.5246 GHz. The corresponding 3-dB fractional bandwidth of the corresponding center frequencies is 45.25%, 20.32% and 6.09% for the 1st, 2nd, and 3rd passbands, respectively. The measured insertion loss in the three passbands is 0.32, 0.63 and 1.38 including losses from the SMA connectors. Six transmission zeros are created in the simulated frequency response at frequencies 1.43 GHz, 1.68 GHz, 3.008 GHz, 3.33 GHz, 4.0 GHz, and 5.33 GHz with more than 28 dB attenuations in order to get sharp skirt selectivity for the passbands. The geometrical dimensions of the tri-BPF are mentioned in Table 2.

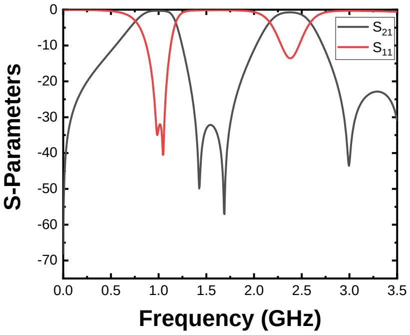

Fig. 5. Dual BPF response.

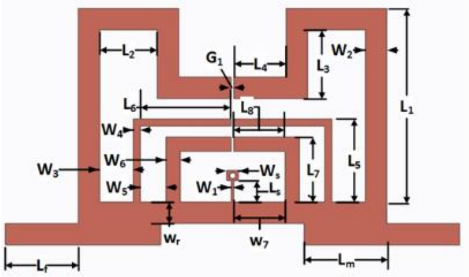

Fig. 6. Developed tri BPF.

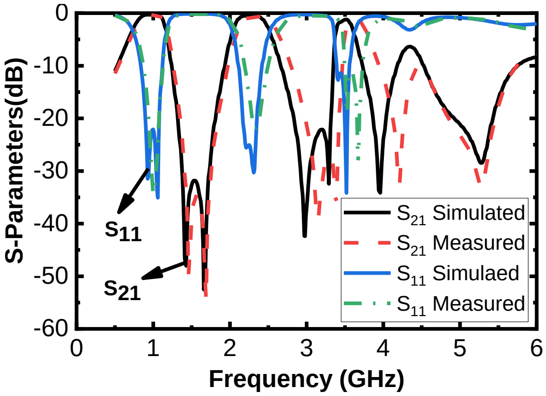

Fig. 7. Tri BPF response.

Figure 8 shows the corresponding quad BPF aimed to operate at GSM-900, LTE-2300, WiMAX (3.50 GHz) and WLAN (5.40 GHz). The frequency response of the measured and simulated results of quad-band BPF is given in Fig. 9. It is obvious that the measured and simulated frequency response agrees very well. The developed quad-band BPF is tuned for useful wireless applications which are GSM-900, LTE-2300, WiMAX (3.50 GHz) and WLAN (5.40 GHz). The operating frequencies of the quad-band BPF are 0.946 GHz, 2.2079 GHz, 3.59 GHz, and 5.4663 GHz. The percentage 3-dB fractional bandwidth all passbands are 42.64%, 21.31%, 7.074%, and 7.414%, respectively. The measured insertion loss of all the four passbands at their center frequencies including SMA connectors are 0.31 dB, 0.56 dB, 1.59 dB, and 1.63 dB respectively. Seven transmission zeros are generated with more than 28 dB attenuation at 1.39 GHz, 1.60 GHz, 2.98 GHz, 3.36 GHz, 4.11 GHz, 5.05 GHz, and 5.88 GHz in order to get high selectivity pass-band filter response. The corresponding dimensions of the quad BPF are tabulated in Table 3.

Table 3: Geometrical dimensions for quad BPF's (all values are in mm)

Parameter	**Value**	**Parameter**	**Value**	**Parameter**	**Value**
L_m	7	L_s	2	W_r	2
L_f	3.25	W_s	1	W_1	0.5
W_6	0.8	W_7	0.95	L_1	15.1
L_2=L_4	4	L_5	7.5	L_6	6.575
W_8	0.5	W_9	1	W_{10}	2.75
G_1, G_2, G_3, G_4	0.5	Via	0.5	W_4	1
W_2	1.75	W_3	2.17	L_7	5.85
L_3	4.6	L_8	4.2	L_{10}	2.75

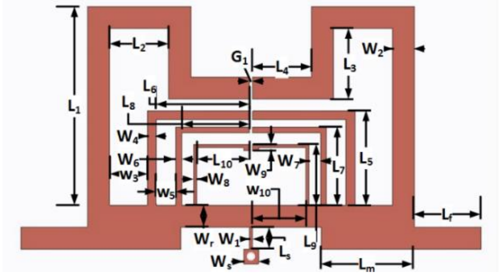

Fig. 8. Developed quad BPF.

Figure 10 shows the corresponding quintuple BPF aimed to operate at GSM-900, LTE2300, WiMAX (3.5 GHz), WLAN (5.4 GHz) and RFID (6.8 GHz). The resonance frequencies of the designed filter are calculated by using the equations mentioned in Table 1. It is seen that there is a slight difference between calculated and aimed frequencies. However, it is optimized using parametric analysis to obtain the exact resonance frequencies as desired. The designed quintuple BPF is also measured and its frequency response is provided. The simulated vs. measured S21 response are shown in Figs. 7 and 8, respectively. Good matching can be seen between the simulated and measured response of the proposed filter. Figure 11 shows that the proposed quintuple band bandpass filter is tuned to frequency bands, GSM-900, LTE2300, WiMAX (3.5 GHz), WLAN (5.4 GHz) and RFID (6.8 GHz). The operating mid frequencies of quintuple band bandpass filter are 0.96 GHz, 2.22 GHz, 3.58 GHz, 5.41 GHz, and 6.64 GHz with corresponding 3dB FBW of 36.03%, 20.95%, 7.27%, 8.57%, and 3.37%. The measured insertion loss is 0.38dB, 0.59dB, 1.47dB, 1.53dB and 2.4dB at GSM-900, LTE2300, WiMAX, WLAN and RFID frequency bands, respectively. The geometrical dimensions of the quintuple-BPF are mentioned in Table 4. The step by step fabricated prototypes of all filters are shown in Figs. 12 (a-c).

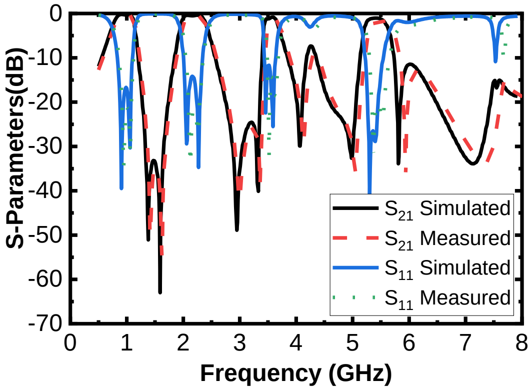

Fig. 9. Quad BPF response.

Table 4: Geometrical dimensions for quintuple BPF's (all values are in mm)

Parameter	Value	Parameter	Value	Parameter	Value
L_1	32.25	L_2	2.75	L_3	0.85
L_4	3.5	L_5	2.875	L_6	13.975
L_7	10.2	L_8	7.75	L_9	5.75
W_1	1.75	W_2	1	L_f	3.25
W_3	0.5	L_s	1.25	G_1-G_5	0.5
W_s	1	W_4	0.5	W_5	0.75
W_f	1.7	L_m	3		

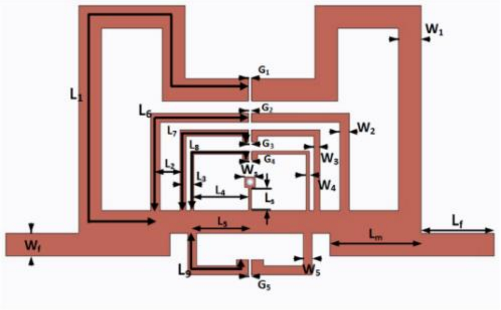

Fig. 10. Developed quintuple BPF.

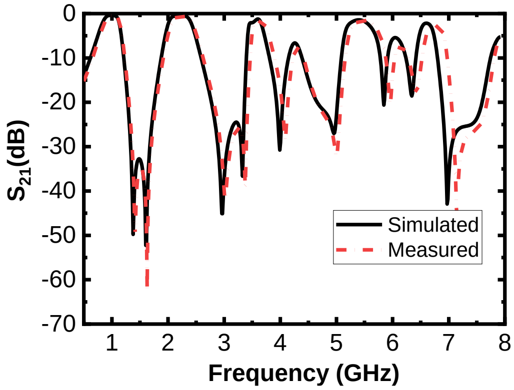

Fig. 11. Quintuple BPF response.

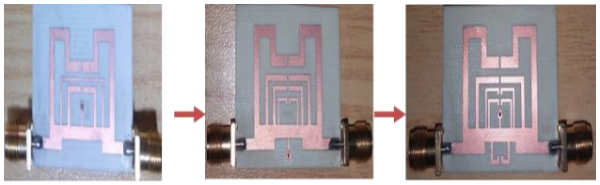

(a) (b) (c)

Fig. 12. Fabricated filters: (a) Tri BPF, (b) quad BPF, and (c) quintuple BPF.

IV. CONCLUSION

Design strategy for compact bandpass filters using Meander Line Resonators (MLR) in combination with Stub Loaded Resonators (SLR) is presented. The proposed resonator is analyzed using the even-odd mode analysis. Open-ended stubs are loaded at an appropriate position in the dual-mode resonator to achieve tri, quad, and quintuple passbands. To reduce the circuit size and create transmission zeros at our desired frequencies, a symmetrical meandered shape resonator is loaded with open-ended identical stubs which are bent towards each other. A design strategy is presented step by step and the approach is validated using simulations and experiments.

REFERENCES

[1] X. Y. Zhang, J. X. Chen, Q. Xue, and S. M. Li, "Dual-band bandpass filters using stub-loaded

resonators," *IEEE Microwave and Wireless Components Letters*, vol. 17, pp. 583-585, 2007.

[2] L. C. Liang, H. Di, and B. Wu, "Design of tri-band filter based on stub loaded resonator and DGS resonator," *IEEE Microwave and Wireless Components Letters*, vol. 20, pp. 265-267, 2010.

[3] S. W. Lan, M. H. Weng, S. J. Chang, C. Y. Hung, and S. K. Liu, "A tri-band bandpass filter with wide stopband using asymmetric stub loaded resonators," *IEEE Microwave and Wireless Components Letters*, vol. 25, no. 1, pp. 19-21, Jan. 2015.

[4] M. Rahman, W. T. Khan, and M. Imran, "Penta-notched UWB antenna with sharp frequency edge selectivity using combination of SRR, CSRR, and DGS," *Int. J. Electron. Commun.* (*AEÜ*), vol. 93, pp. 116-122, 2018.

[5] M. Rahman, D. S. Ko, J. D. Park, "A Compact Multiple Notched Ultra-Wide Band Antenna with an Analysis of the CSRR-TO-CSRR Coupling for Portable UWB Applications," *Sensors*, 17, 2174, 2017.

[6] M. Rahman and J. D. Park, "The smallest form factor UWB antenna with quintuple rejection bands for IoT applications utilizing RSRR and RCSRR," *Sensors*, 18, 911, 2018.

[7] N. Kumar and Y. Singh, "Compact tri-band bandpass filter using three stub-loaded open loop resonators with wide stopband and improved bandwidth response," *Electronics Letters*, vol. 50, no. 25, pp. 1950-1952, Dec. 2014.

[8] Y. H. Cho and S. W. Yun, "A tri-band bandpass filter using stub loaded SIRS with controllable bandwidths," *Microwave and optical technology letters*, vol. 56, no. 12, pp. 2907-2910, Apr. 2014.

[9] M. Rahman and J.-D. Park, "A compact tri-band bandpass filter using two stub-loaded dual mode resonators," *Progress in Electromagnetic Research M*, vol. 64, pp. 201-209, 2018.

[10] X. J. W. Wu and C. Miao, "Compact microstrip dual-/tri-/quad-band bandpass filter using open stubs loaded shorted stepped-impedance resonator," *IEEE Transactions on Microwave Theory and Techniques*, vol. 61, no. 9, pp. 3187-3199, Sept. 2013.

[11] M. Rahman, M. NaghshvarianJahromi, S. S. Mirjavadi, and A. Hamouda, "Bandwidth enhancement and frequency scanning array antenna using novel UWB filter integration technique for OFDM UWB radar applications in wireless vital signs monitoring," *Sensors*, vol. 18, no. (9), p. 3155, 2018.

[12] M. Rahman, D. S. Ko, and J. D. Park, "A compact tri- band bandpass filter utilizing double mode resonator with 6 transmission zeros," *Microwave and Optical Technology Letters*, vol. 60, no. 7, 1767-1771, 2018.

[13] Z. M. Hejazi, "A fast design approach of compact microstrip multiband bandpass filters," *Microwave and Optical Technology Letters*, vol. 54, no. 4, pp. 1075-1079, 2012.

[14] A. Sami, M. Rahman, and S. Bashir, "Design of compact tri and quad band band-pass filters using stub loaded resonators for wireless applications," *SN Applied Sciences*, vol. 1, no. 9, p. 1019, 2019.

[15] W. W. H. and Y. R. Yuan, "A new quadband bandpass filter using asymmetric stepped impedance resonator," *Microwave and Wireless Components Letters*, vol. 21, no. 4, pp. 203-205, Apr. 2011.

[16] M. Nejatijahromi, M. Rahman, and M. Naghshvarianjahromi, "Continuously tunable WiMAX band-notched UWB antenna with fixed WLAN notched band," *Progress In Electromagnetics Research Letters*, vol. 75, 97-103, 2018.

[17] M. NejatiJahromi, M. NagshvarianJahromi, and M. Rahman, "A new compact planar antenna for switching between UWB, narrow band and UWB with tunable-notch behaviors for UWB and WLAN applications," *Applied Computational Electromagnetics Society Journal*, vol. 33, no. 4, Apr. 2018.

[18] M. NejatiJahromi, M. NagshvarianJahromi, and M. Rahman, "Compact CPW fed switchable UWB antenna as an antenna filter at narrow-frequency bands," *Progress In Electromagnetics Research C*, 81, 199-209, Jan. 2018.

[19] M. Rahman, M. NaghshvarianJahromi, S. S. Mirjavadi, and A. Hamouda, "Compact UWB band-notched antenna with integrated Bluetooth for personal wireless communication and UWB applications," *Electronics*, 8, 158, 2019.

[20] M. Rahman, M. NaghshvarianJahromi, S. S. Mirjavadi, and A. Hamouda, "Resonator based switching technique between ultra wide band (UWB) and single/dual continuously tunable-notch behaviors in UWB radar for wireless vital signs monitoring," *Sensors 2018*, 18, 3330, 2018.

[21] A. Sami and M. Rahman, "A very compact quintuple band bandpass filter using multimode stub loaded resonator," *Progress In Electromagnetics Research*, vol. 93, pp. 211-222, 2019.

[22] W. F. Q. Huang and X. -W. Shi, "A compact quadband bandpass filter using novel stub loaded SIR structure," *Microwave and Optical Technology Letters*, vol. 56, no. 3, pp. 538-542, Mar. 2014.

Abdul Sami pursued his Bachelor´s degree in Electrical Engineering in 2013 from University of Engineering and Technology (UET) Peshawar. In 2015, he obtained his Master's degree in Electrical Engineering from National University of Sciences and Technology (NUST), Islamabad. From October 2016, he worked in "Center for Intelligent Systems and Network Research (CISNR)" at UET Peshawar as a Research Assistant. He has journal publications in the area of microwave filters for wireless applications. His current research interests include design of passive components for space applications in the frequency spectrum of microwave and millimeter-wave.

MuhibUr Rahman pursued his Bachelor's degree in Electrical Engineering in 2014 from University of Engineering and Technology, Peshawar, Pakistan, and M.S. degree in Electrical Engineering from National University of Sciences and Technology (NUST), Islamabad, Pakistan in March 2016. He worked as a Research Assistant at Dongguk University, Seoul, South Korea. Currently, he is working toward his Ph.D. degree in Polytechnique Montreal, Canada. He published number of index journals and taken various patents. He is an active reviewer of various well-reputed antenna and microwave journals. His current research interests include microwave electronics, linear and nonlinear transmission lines, material characterization, and algebraic topology, deep-learning, and mm-wave antennas.

Hamza Ahmad received a Bachelor's degree in Electrical (Communication) Engineering from the University of Engineering and Technology, Peshawar, Pakistan, in September 2014, an M.S. degree in Electrical Engineering from NUST Islamabad, Pakistan in 2017. He was also a Research Fellow at RIMMS NUST, Islamabad, Pakistan from September 2016 to August 2017. Currently he is a Lecturer at Gandhara Institute of Science and Technology Peshawar, Pakistan.

Shahid Bashir received the B.Sc. degree in Electrical Engineering from the University of Engineering and Technology Peshawar (UET Peshawar), Peshawar, Pakistan, and the Ph.D. degree in Mobile Communications from Loughborough University, Loughborough, U.K., in 2009. He is currently an Assistant Professor with the Electrical Engineering Department, UET Peshawar. He has published in various reputed journals and conferences.

EMC Coupling Between Two Composite Right/Left-Handed (CRLH) Transmission Lines on PCBs

Irfanullah, Shahid Khattak, and Imdad Khan

Department of Electrical and Computer Engineering
COMSATS University Islamabad, Abbottabad Campus, Pakistan
eengr@cuiatd.edu.pk

Abstract **─** Unintentional electromagnetic coupling (crosstalk) between PCB lands is an important aspect of the design of an electromagnetically compatible product. In this paper, analytical model to predict crosstalk between two composite right/left-handed (CRLH) transmission lines in close proximity on PCBs is developed, and validated with full-wave simulation and measurement results. A cascaded seven unit cells CRLH transmission line (TL) acting as source of the electromagnetic emission was placed in close proximity to another seven unit cells CRLH transmission line acting as receptor of the emission on PCBs. Then the near- and far-end crosstalk voltages induced from the generator CRLH-TL to receptor TL for various separations between them were analyzed. It is shown that the crosstalk voltages computed with developed analytical model agrees well with full-wave simulation and measured results. Furthermore, it is shown that the left-handed capacitance and inductance design parameters of CRLH-TL can be used to reduce the crosstalk voltages induced on the receptor circuit leading to a cost-effective solution for shielding of near-by CRLH-TL receptor circuits printed on PCBs for various engineering applications.

Index Terms **─** CRLH, crosstalk, coupler, EMC.

I. INTRODUCTION

An important aspect of the design of an electromagnetically compatible product is crosstalk. This essentially refers to the unintended electromagnetic coupling between wires and PCB lands that are in close proximity. The crosstalk analysis (i.e., to determine the near-end and far-end voltages) between conventional coupled cables and coupled PCB lands has been widely studied in the literature, see for example [1-3, 16-18]. Recently, characteristics of the composite right/left-handed (CRLH) metamaterial transmission lines (MTM-TLs) from intentional/tight coupling point of view (for example directional couplers) has been investigated [4-6]. While a lot of attention has been paid to the intentional coupling between CRLH-TLs, not much work (except in [7]) has been done on these couplers from an unwanted electromagnetic compatibility (EMC) coupling perspective. In the research community there is a growing interest to use CRLH-TLs in the design of feed network for antenna arrays [8-10], particularly by placing multiple RH/CRLH-TLs in the feed network to obtain different polarizations [11]. In such scenarios, unwanted coupling from one TL to another can degrade the systems' performance by deteriorating the desired radiation patterns. Similarly multiple coupled CRLH-TLs have been realized in super-resolution imaging applications [12]. Therefore analysis of crosstalk voltages to mitigate mutual coupling is an important design parameter to obtain the desired performance metrics. In [7], analysis of noise voltage coupling between right-handed (RH) and CRLH-TLs has been formulated.

The research work in the paper differs from previous work as follows: In [4]-[6] coupling between CRLH-TLs has been investigated from intentional coupling point of view, that is to couple more power to the receptor TL (ideally 0 dB). In the proposed work, coupling from EMC point of view has been analyzed, that is the objective is to mitigate the coupled voltages from generator CRLH-TL to the receptor CRLH-TL. The work in [7] assumes weak coupling between RH-TL and CRLH-TL, that is the effects of coupling only from generator RH-TL to victim CRLH-TL has been considered and not the effects of coupling back from CRLH-TL to RH-TL has been included. In [1-2 and 7], derivations of NEXT and FEXT is done with the assumptions of weak coupling between coupled transmission lines, and therefore the models cannot predict the crosstalk voltages for strong coupling between the PCB lands, where the transmission lines are printed in close proximity on the printed boards. In contrast to [7], the proposed work here considers the two-way effects of mutual coupling (coupling from generator CRLH-TL to receptor CRLH-TL and back to the generator circuit by the receptor circuit) to compute crosstalk voltages. Therefore, the proposed crosstalk model predicts the near- and far-end coupled voltages for any arbitrary spacing between the coupled transmission lines. Different commercially available simulators are

Submitted On: August 3, 2019
Accepted On: December 28, 2019

available to analyze the crosstalk between transmission lines of different structures. However, these techniques are based on method of moments (MoM), finite difference time domain (FDTD) numerical techniques [19] which are computationally expensive, time consuming and needs large amount of memory to analyze the crosstalk, particularly for complex transmission structures. In addition, they do not give insight behavior and relationship of crosstalk noise voltages with different parameters of the coupled transmission lines. The frequency domain analytical model proposed in this work to derive expressions for near- and far-end crosstalk voltages is generic and can be applied to other complex coupled transmission lines on printed circuit boards for any arbitrary spacing in between them. The analytical expressions developed can be used as an aiding tools for theoretical support, validation, comparison and design guidelines for reducing the unintentional coupling from generator to receptor circuit or vice-versa.

Rest of the paper is organized as follows: In Section II, analytical expressions to compute NEXT and FEXT voltages for a unit-cell coupled CRLH-TLs have been derived. Section III describes the simulation methodology to validate the derived analytical expressions. Section III also discusses the parametric study of left-handed parameters C_L and L_L on NEXT and FEXT voltages. Section IV describes the measurement procedure to compute the crosstalk voltages and Section V finally concludes the paper.

II. DERIVATION OF ANALYTICAL EXPRESSIONS TO COMPUTE NEXT AND FEXT VOLTAGES

To introduce the problem statement, consider the coupled unit-cell CRLH-CRLH TL shown in Fig. 1 (a), and its equivalent circuit model [15] shown in Fig. 1 (b). The microstrip Interdigital capacitor comprising of ten long conductors (or fingers), each having length L_f and width W_f is represented by left-handed (LH) series capacitance (C_L) in series with a right-handed (RH) parasitic inductance (L_R). The shunted stub (shorted with a metallic via) having length L_s and width W_s is represented by LH shunt inductance (L_L) in parallel with a RH parasitic capacitance (C_R).L_{GR} and C_{GR} represents mutual inductance and mutual capacitance between generator and receptor circuits respectively. To introduce the two-way effects of mutual coupling, dependent voltage sources in the generator and receptor circuits have been incorporated as shown in Fig. 1 (b). The dependent voltage source $sL_{GR}I_G$ in the receptor circuit represents the effects of generator current and the dependent voltage source $sL_{GR}I_R$ in the generator circuit represents the back-way effect of receptor current, where by definition $= j\omega$. Port 1 is driven by the voltage source V_s, ports 2, 3 and 4 are terminated by load resistance R_L, near-end resistance R_{NE} and far-end resistance R_{FE} respectively.

Next, the goal is to derive analytical expressions to determine near-end crosstalk (NEXT) voltage V_{NE} and far-end crosstalk (FEXT) voltageV_{FE}. In [7], analytical expressions for NEXT and FEXT voltages have been derived using weak coupling assumptions, while the proposed coupling model here in Fig. 1 (b) will be considered in entirety without weak coupling assumptions. Then design guidelines will be provided by parametric study of the left-handed parameters L_L and C_L in the receptor circuit for mitigation of NEXT and FEXT voltages.

To determine NEXT voltage V_{NE} and FEXT voltage V_{FE} in Fig. 1 (b), the generator and receptor currents are given by:

$$I_G = \frac{V_4 - V_1}{sL_R + \frac{1}{sC_L}} = \frac{sC_L(V_4 - V_1)}{1 + s^2 L_R C_L} = A(V_4 - V_1), \tag{1}$$

$$I_R = \frac{V_2 - V_3}{sL_R + \frac{1}{sC_L}} = \frac{sC_L(V_2 - V_3)}{1 + s^2 L_R C_L} = A(V_2 - V_3), \tag{2}$$

$$\text{where } A = \frac{sC_L}{1 + s^2 L_R C_L}. \tag{3}$$

and V_1, V_2, V_3, V_4 are node voltages in Fig. 1 (b).

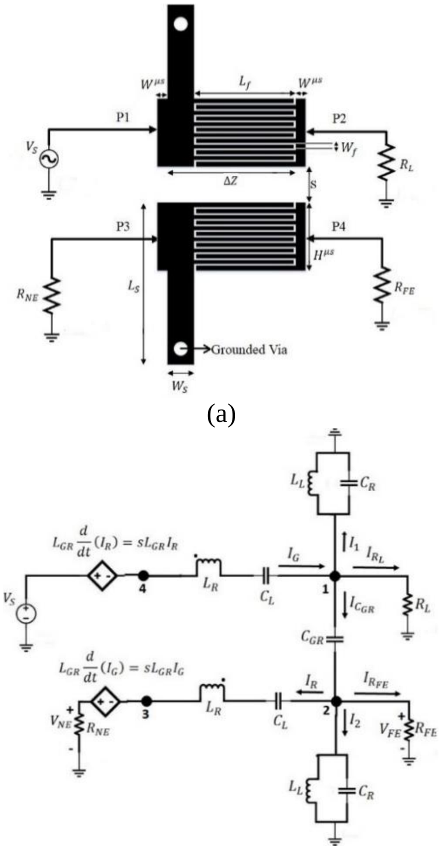

(a)

(b)

Fig. 1. (a) Microstrip layout of a unit-cell CRLH-CRLH coupler, (b) Proposed equivalent circuit model of the unit-cell CRLH-CRLH coupler.

Applying KCL at node 1: $I_G = I_{C_{GR}} + I_1 + I_{R_L}$, (4)

or

$$A(V_4 - V_1) = (V_1 - V_2)sC_{GR} + \frac{V_1}{\frac{1}{sC_R + \frac{1}{sL_L}}} + \frac{V_1}{R_L}. \quad (5)$$

Let,

$$B = \frac{1}{sC_R + \frac{1}{sL_L}}, \quad (6)$$

and then re-arranging (5), we get:

$$\left(-A - B - sC_{GR} - \frac{1}{R_L}\right)V_1 + sC_{GR}V_2 + AV_4 = 0. \quad (7)$$

Applying KVL around V_s and node 4 in Fig. 1 (c), we can write:

$$V_s - sL_{GR}I_R - V_4 = 0. \quad (8)$$

Using (2) and (8) in (7), and re-arranging, we obtain:

$$\left(-A - sC_{GR} - B - \frac{1}{R_L}\right)V_1 + (sC_{GR} - sL_{GR}A^2)V_2 + sL_{GR}A^2V_3 + AV_s = 0. \quad (9)$$

Similarly, applying KCL and KVL at nodes 2 and 3 respectively in the receptor circuit, we obtain:

$$sC_{GR}V_1 + \left(-A - B - sC_{GR} - \frac{1}{R_{FE}}\right)V_2 + AV_3 = 0, \quad (10)$$

$$-sL_{GR}AV_1 + \left(AR_{NE} - s^2{L_{GR}}^2A^2\right)V_2 + \left(-AR_{NE} - 1 + s^2{L_{GR}}^2A^2\right)V_3 + sL_{GR}AV_s = 0. \quad (11)$$

Suppose,

$$K_1 = -A - sC_{GR} - B - \frac{1}{R_L}, K_2 = sC_{GR} - sL_{GR}A^2, K_3 = sL_{GR}A^2, K_4 = -sC_{GR} - \frac{1}{R_{FE}} - A - B, K_5 = AR_{NE} - s^2{L_{GR}}^2A^2, K_6 = -AR_{NE} - 1 + s^2{L_{GR}}^2A^2. \quad (12)$$

Then (9), (10) and (12) becomes:

$$K_1V_1 + K_2V_2 + K_3V_3 + AV_s = 0, \quad (13)$$

$$sC_{GR}V_1 + K_4V_2 + AV_3 = 0, \quad (14)$$

$$-sL_{GR}AV_1 + K_5V_2 + K_6V_3 + sL_{GR}AV_s = 0. \quad (15)$$

Solving (13), (14) and (15) simultaneously, we can compute V_2, and V_3 to find out NEXT and FEXT voltages as follows:

$$V_2 = \frac{-AV_S}{M_1} - \frac{M_2(M_3 - sL_mM_1)AV_S}{M_1(M_1M_4 - M_2M_3)}, \quad (16)$$

$$V_3 = \frac{(M_3 - sL_mM_1)AV_S}{M_1M_4 - M_2M_3)}, \quad (17)$$

where

$$M_1 = \frac{(K_1 - sC_{GR})(sC_{GR} - K_2)}{sC_{GR}} + (sC_{GR} - sL_{GR}A^2), M_2 = sL_{GR}A^2 - \frac{A(K_1 - sC_{GR})}{sC_{GR}}, M_3 = -sL_{GR}A + \frac{AK_2L_{GR}}{C_{GR}} + AR_{NE} - s^2{L_{GR}}^2A^2, M_4 = \frac{L_{GR}}{C_{GR}}A^2 - AR_{NE} - 1 + s^2{L_{GR}}^2A^2. \quad (18)$$

The NEXT voltage is given by:

$$V_{NE} = I_RR_{NE} = A(V_2 - V_3)R_{NE}, \quad (19)$$

where A can be computed from (3) and V_2, V_3 can be determined using (16) and (17). The FEXT voltage is given by:

$$V_{FE} = I_{R_{FE}}R_{FE} = V_2. \quad (20)$$

Notice that the expressions in (19) and (20) are complex and depends on circuit parameters in Fig. 1 as well on frequency, indicating the generality of the expressions.

III. SIMULATION METHODOLOGY

A. NEXT and FEXT voltages for unit-cell CRLH-CRLH coupling

In this section, a unit-cell CRLH-CRLH coupler of Fig. 1 is used to validate the previously derived NEXT and FEXT voltages in (19) and (20) in both Momentum (Fig. 1 (a)) and circuit simulator (Fig. 1 (b)) of ADS. The unit-cell coupler was simulated with port 1 driven by voltage source $V_s = 1$ V and ports 2, 3, and 4 were terminated with $R_L = 50\Omega$, $R_{NE} = 50\Omega$, and $R_{FE} = 50\Omega$ terminations respectively. The circuit parameter values chosen were $L_R = 1.76\,nH$, $C_R = 0.53\,pF$, $L_L = 0.47\,nH$, $C_L = 0.55\,pF$. These circuit values were extracted for the unit-cell microstrip CRLH-TL shown in Fig. 1 (a) using the design procedure in [13] with the following parameters: $L_f = 5$ mm, $W_f = 0.3$ mm, $L_s = 10$ mm, $W_s = 2$ mm and all spacing between fingers of 0.2 mm. Two extra small microstrip transmission lines with dimensions $H^{\mu s} = 4.8$ mm, $W^{\mu s} = 1$ mm were added at both ends of the structure for matching and feeding purpose and their effects must be excluded by de-embedding (extending the ports P1 and P2 to the structure in the simulator). The methodology of parameters extraction is based on ABCD parameters approach explained in [13] and outlined here briefly:

1) Simulate Interdigital capacitor (IDC) separately to extract its S-parameters at three frequencies, namely design frequency f_0 and two edge frequencies f_1 and f_2 around f_0. In this paper, the chosen values were f_0 = 3 GHz, f_1 = 2.9 GHz and f_2 = 3.1 GHz.

2) Repeat step 1 for shunted stub inductor.

3) Convert S-parameters into Z and Y parameters.

4) Use following expressions to compute circuit values [4],

$$L_R = L_S^{IDC}, C_R = 2C_p^{IDC} + C_p^{stub}, L_L = L_p^{stub}, C_L = C_S^{IDC}, \quad (21)$$

where

$$C_p^{IDC} = \frac{Y_{11}^{IDC} + Y_{21}^{IDC}}{j\omega}, L_S^{IDC} = \frac{1}{2j\omega}\left[\omega\frac{\partial\left(\frac{1}{Y_{21}^{IDC}}\right)}{\partial\omega} + \frac{1}{Y_{21}^{IDC}}\right], C_S^{IDC} = \frac{2}{j\omega}\left[\omega\frac{\partial\left(\frac{1}{Y_{21}^{IDC}}\right)}{\partial\omega} - \frac{1}{Y_{21}^{IDC}}\right]^{-1}, L_S^{stub} = \frac{Z_{11}^{stub} - Z_{21}^{stub}}{j\omega}, C_p^{stub} = \frac{1}{2j\omega}\left[\omega\frac{\partial(Y_{21}^{stub})}{\partial\omega} + Y_{21}^{stub}\right], L_p^{stub} = \frac{2}{j\omega}\left[\omega\frac{\partial(Y_{21}^{stub})}{\partial\omega} - Y_{21}^{stub}\right]^{-1}. \quad (22)$$

All the values to be computed at ω_0 and $\frac{\partial(Y)}{\partial\omega} \cong \frac{Y_{at\,\omega_2} - Y_{at\,\omega_1}}{\omega_2 - \omega_1}$.

The values of mutual coupling parameters L_{GR} and C_{GR} were computed by first simulating the unit-cell

CRLH-CRLH coupler in ADS Momentum and then tuning the parameters L_{GR} and C_{GR} in ADS schematic to match the results with the Momentum results. The extracted parameters corresponding to 3 mm edge to edge separation between the unit-cell CRLH-CRLH coupler are $L_{GR} = 1.04$ nH and $C_{GR} = 0.8$ pF. The separation of 3 mm was chosen to investigate the strong coupling case between CRLH-CRLH coupler. A weak coupling case with separation of 10 mm has also been investigated in Section IV. The ADS circuit (using Fig. 1 (b)), ADS Momentum (using Fig. 1 (a)) and MATLAB analytical results using (19) and (20) with these extracted parameters are shown in Fig. 2. The analytical and circuit simulation results completely overlap each other, which validates the accuracy of (19) and (20) for computation of NEXT and FEXT voltages. It can be seen that the behavior of NEXT and FEXT voltages is similar except for the frequency range of 2-3 GHz, which is a left-hand propagation band of CRLH-TL. It is shown in [13] that the near-end coupling is increased in the left-hand propagation band due to opposite direction of Poynting vector (power flow) and propagation vector. Therefore in next sections, only results for NEXT voltage would be discussed.

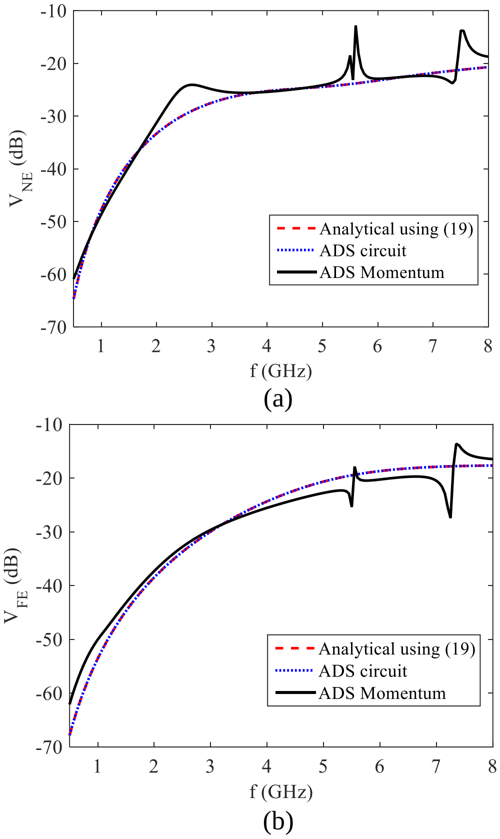

(a)

(b)

Fig. 2. Comparison of the analytical (MATLAB), ADS circuit simulation and ADS Momentum for: (a) NEXT and (b) FEXT voltages of unit-cell (UC) CRLH-CRLH coupler.

B. Parametric study of left-handed parameters

Next, to consider a more practical realization of EMC coupling, seven unit-cells of microstrip CRLH-CRLH coupler in Fig. 1 (a) were cascaded in ADS Momentum (3D planar EM simulator). The ADS Momentum results for NEXT voltages using 3 mm edge-to-edge separation between two seven unit-cells CRLH- TLs for various parameters are shown in Figs. 3 and 4. The parametric study is mainly focussed on the left-hand (LH) band of CRLH-TL, which is a band extending from high pass left-hand cutoff frequency (f_{CL}) to transition frequenct (f_0). The f_{CL} represents the lowest frequency above which the CRLH-TL will support left-handed propagation, and f_0 represents the frequency at which the CRLH-TL transitions from supporting left-handed propagation to right-handed (RH) propagation. These frequencies are computed using the following expressions [13]:

$$f_{CL} = f_0\sqrt{\frac{P_1 - P_2}{2}}, \qquad (23)$$

where

$$P_1 = \left[K + \left({}^{2}/_{\omega_L}\right)^2\right]\omega_0{}^2,\ P_2 = f_0\sqrt{P_1{}^2 - 4}, \qquad (23a)$$

$$f_0 = \frac{1}{2\pi\sqrt[4]{L_R C_R L_L C_L}},\ f_L = \frac{1}{2\pi\sqrt{L_L C_L}}, \qquad (23b)$$

$$\text{and } K = L_R C_L + L_L C_R. \qquad (23c)$$

These cut-off and transition frequencies along with extracted circuit parameters are shown in Tables 1 and 2.

1) Effects of finger length (L_f) on NEXT voltage

To investigate the effects of finger length (L_f) in Fig. 1 (a) on NEXT voltage in left-hand (LH) band, two seven unit-cells CRLH-CRLH TL coupler with edge to edge separation of 3 mm (strong coupling case) was simulated in ADS Momentum. The extracted circuit parameters and LH band for various finger lengths are shown in Table 1. These values were computed using the simulation methodology in Section III and using equations (23). The NEXT voltage for various values of L_f is shown in Fig. 3. Other parameters of Fig. 1 (a) were $W_f = 0.3$ mm, $L_s = 10$ mm, $W_s = 2$ mm and all spacing in the fingers of 0.2 mm. As can be seen in Table 1, by increasing the finger length, the cut-off frequency f_{CL} is decreased resulting in shifting the LH band towards the lower frequency and can also be observed in Fig. 3. The NEXT voltage stays maximum up to around -10 dB for frequencies above 3 GHz and it is below -20 dB for frequencies below 3 GHz for all values of L_f in both LH and RH bands.

2) Effects of stub width (W_s) on NEXT voltage

Similarly the NEXT voltage was investigated for different values of stub width (W_s) and the results are shown in Table 2 and Fig. 4. Other parameters of Fig. 1 (a) were $L_f = 5$ mm, $W_f = 0.3$ mm, $L_s = 10$ mm and all spacing in the fingers of 0.2 mm. As can be seen in Table 2, the bandwidth of LH band decreases from

3.74 GHz (for $W_s = 2$ mm) to 2.77 GHz (for $W_s = 6$ mm). The value of NEXT voltage increases for increasing value of W_s and is approximately 10 dB higher for $W_s = 6$ mm than for $W_s = 2$ mm in both LH and RH bands. This is an important investigation for reducing NEXT voltages in LH and RH bands of coupled CRLH TLs, which should be kept in mind while deigning CRLH-TLs for EMC coupling reduction.

Table 1: Extracted parameters for various finger lengths using (21)

L_f (mm)	C_L (pF)	L_R (nH)	L_L (nH)	C_R (pF)	LH band ($f_{CL} - f_0$)
5	0.55	1.76	0.47	0.53	3.44 – 7.18
7	0.85	2.24	0.47	0.53	2.64 – 6.06
9	1.13	2.75	0.47	0.53	2.17 – 5.36

Table 2: Extracted parameters for various stub widths using (21)

W_s (mm)	C_L (pF)	L_R (nH)	L_L (nH)	C_R (pF)	LH band ($f_{CL} - f_0$)
2	0.55	1.76	0.47	0.53	3.44 – 7.18
4	0.55	1.76	0.96	0.69	2.66 – 5.62
6	0.55	1.76	1.27	0.75	2.36 – 5.13

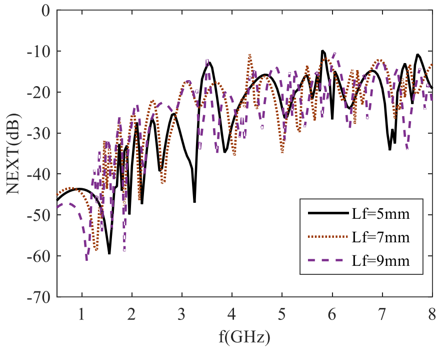

Fig. 3. Effects of length of finger (L_f) on NEXT voltage between two seven unit-cells CRLH-CRLH coupler in ADS Momentum.

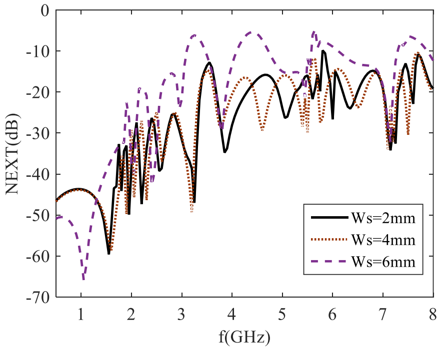

Fig. 4. Effects of width of stub (W_s) on NEXT voltage between two seven unit-cells CRLH-CRLH coupler in ADS Momentum.

IV. MEASUREMENT PROCEDURE AND RESULTS

Next, to measure the NEXT voltage between two 7 unit-cells CRLH-CRLH coupler TLs, two test cases were considered: case 1: edge to edge separation between TLs of 3 mm (strong coupling case) and case 2: edge to edge separation between TLs of 10 mm (weak coupling case). The two cases were printed on a 1.575 mm thick Rogers RT/duroid 5880 ($\mathcal{E}_r = 2.2, tan\delta = 0.0009$) substrate and are shown in Fig. 5 for cases 1 and 2 respectively. The specified dimensions denoted with notations in Fig. 1 (a) are $H^{\mu s} = 4.8$ mm, $W^{\mu s} = 1$ mm, $L_f = 5$ mm, $W_f = 0.3$ mm, $L_s = 10$ mm, $W_s = 2$ mm and all spacing in the fingers of 0.2 mm. These are the same values as were discussed in Section III. The measurement procedure is as follows and also mentioned in [1]: P1 (driven port) of the manufactured boards in Fig. 5 was connected with port 1 of the network analyzer, P3 (near-end port) was connected with port 3 of the network analyzer and P2 (load), P4 (far-end port) were terminated with 50Ω terminations. Then near-end crosstalk was measured from P1 to P3. Next, again P1 was connected with port 1 of the network analyzer, P4 with port 4 of the network analyzer and P2 and P3 were terminated with 50Ω terminations. Then far-end crosstalk was measured from P1 to P4. In-house fully calibrated Agilent four port network analyzer (300 kHz-20 GHz, model E5071C) was used for measurements purpose. The measured, circuit and ADS Momentum simulated results for the two cases are shown in Figs. 6 and 7 and are in good agreement. Cross-correlation metric has always been used for determining the similarity between two data series. Its value when normalized between -1 and 1 is called the correlation coefficient ρ which is a more meaningful measure of similarity between two date series. The results in the Table 3 give ρ values obtained between the proposed circuit method to that of the momentum method and the measured values for two data sets. Very high ρ values ranging from 0.97 to 0.974 indicate a very high degree of correlation between the results. The analytical expressions obtained in (19) and (20) can also be used directly to compute the crosstalk voltages (NEXT and FEXT) as was demonstrated in Section III.A.

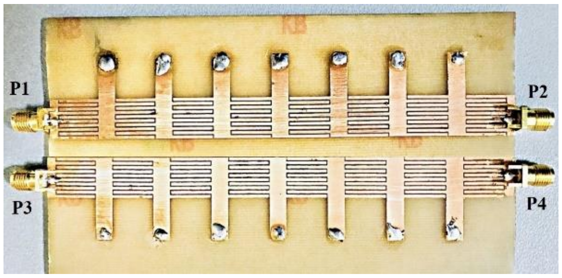

(a)

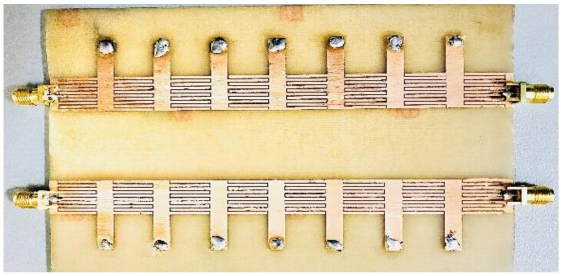

(b)

Fig. 5. Photographs of the printed microstrip seven unit-cells CRLH-CRLH coupler (top layer) for: (a) case 1 and (b) case 2.

Table 3: Cross-correlation metric for similarity determination

	Data 1 for Case 1		Data 2 for Case 2	
	Measured Data	Momentum Method	Measured Data	Momentum Method
Correlation Coefficient ρ	0.972	0.974	0.97	0.974

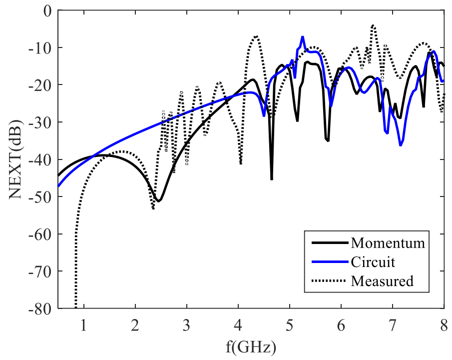

Fig. 6. Measurement and simulation results for case 1 (strong coupling).

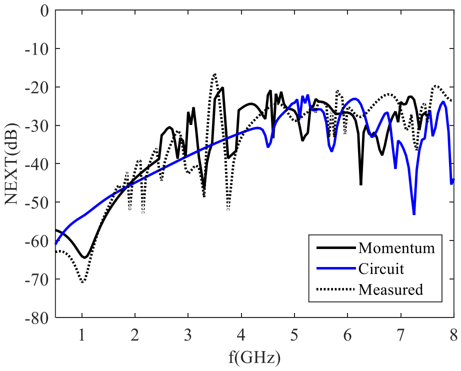

Fig. 7. Measurement and simulation results for case 2 (weak coupling).

V. CONCLUSION

EMC coupling between CRLH transmission lines has been investigated. Analytical expressions have been derived to compute near- and far-end crosstalk voltages and were validated with the simulation and measurement results for two 7 unit-cells CRLH-CRLH transmission lines. It was shown that using left-handed parameters of CRLH structure, the near and far-end crosstalk voltages can be reduced in left-handed band of the structure. The effects of left-handed capacitance and inductance on left-handed band and crosstalk voltages were discussed.

REFERENCES

[1] C. Paul, *Introduction to Electromagnetic Compatibility*. John Wiley and Sons, Inc, Hoboken NJ, 2006.

[2] H. W. Ott, *Electromagnetic Compatibility Engineering*. John Wiley and Sons, Inc, Hoboken NJ, 2009.

[3] T. Tobana, T. Sasamori, and Y. Isota, "Analysis of electromagnetic coupling between microstrip line and ground slot on a printed circuit board," *Proc. of the International Symposium on Electromagnetic Compatibility - EMC Europe 2016*, Wroclaw, Poland, Sep. 5-9, 2016.

[4] C. Caloz, A. Sanda, and T. Itoh, "A novel composite right-/left-handed coupled-line directional coupler with arbitrary coupling level and broad bandwidth," *IEEE Transactions on Microwave Theory and Techniques*., vol. 52, no. 3, pp. 980-992, Mar. 2004.

[5] I. A. Mocanu, G. I. Sajin, and F. Craciunoiu, "Electromagnetic study of strong coupled CRLH transmission lines for use in antenna construction," *IEEE Asia-Pacific Conference on Antennas and Propagation*, Singapore, Aug. 27-29, 2012.

[6] A. A. Ibrahim, M. A. Abdalla, and D. Budimir, "Coupled CRLH transmission lines for compact and high selective bandpass filters," *Microwave and Optical Technology Letters*, vol. 59, no. 6, pp. 1248-1251, Mar. 2017.

[7] Irfanullah, S. Nariyal, S. Roy, M. M. Masud, B. Ijaz, and B. D. Braaten, "Analysis of the noise voltage coupling (crosstalk) between right-handed and composite right/left-handed (CRLH) transmission lines on printed circuit boards," *IEEE Trans. Electromn. Compat.*, vol. 55, no. 4, pp. 788-797, Aug. 2013.

[8] B. Ijaz, S. Roy, M. M. Masud, A. Iftikhar, S. Nariyal, Irfan Ullah, K. Asirvatham, B. Booth, and B. D. Braaten, "A series-fed microstrip patch array with interconnecting CRLH transmission lines for WLAN applications," *7th European Conference on Antennas and Propagation (EuCAP)*, Gothenburg, pp. 2088-2091, Apr. 8-12, 2013.

[9] M. S. Khan, A.-D. Capobianco, A. Iftikhar, S. Asif, B. Ijaz, and B. D. Braaten, "A frequency-reconfigurable series-fed microstrip patch array

with interconnecting CRLH transmission lines," *IEEE Antennas and Wireless Propagation Letters*, vol. 15, pp. 242-245, June 2016.

[10] A. Lai, K. M. K. H. Leong, and T. Itoh, "Novel series divider for antenna arrays with arbitrary element spacing based on a composite right/left-handed transmission line," *European Microwave Conference*, Paris, Oct. 4-6, 2005.

[11] J. M. Kovitz, Y. R. Samii, and J. Choi, "Dispersion engineered right/left-handed transmission lines enabling near-octave bandwidths for wideband CP patch arrays," *IEEE International Symposium on Antennas and Propagation & USNC/URSI National Radio Science Meeting*, Vancouver, BC, July 19-24, 2015.

[12] T. Tsukagoshi, K. Fujimori, M. Sanagi, and S. Nogi, "A metamaterial mirror with multiple CRLH transmission lines and its imaging quality," *Proceedings of the 39th European Microwave Conference*, Rome, Sep. 29-Oct. 1, 2009.

[13] C. Caloz and T. Itoh, *Electromagnetic Metamaterials: Transmission Line Theory and Applications*. John Wiley and Sons, Inc, Hoboken NJ, pp. 124-128, 2006.

[14] B. D. Braaten, S. Roy, I. Ullah, S. Nariyal, B. Ijaz, M. M. Masud, S. A. Naqvi, and A. Iftikhar, "A cascaded reconfigurable RH/CRLH zero-phase microstrip transmisison line unit cell," Proceedings of the *IEEE Intern. Conf. on Wireless Infor. Tech. and Systems*, Maui, Hawaii, Nov. 11-16, 2012.

[15] N. Kou, Y. Shi, and L. Li, "New equivalent circuit analysis and synthesis for broadband composite right/left-handed transmission line metamaterials," *ACES Journal*, vol. 31, no. 8, Aug. 2016.

[16] N. Soleimani, Mohammad G. H. Alijani, and Mohammad H. Nishati, "Crosstalk analysis of uniform and nonuniform lossy microstrip-coupled transmission lines*," International Journal of RF and Microwave Computer-Aided Engineering*, vol. 29, no. 11, July 2019.

[17] Y. Sun, J. Wang, W. Song, and R. Xue, "Frequency domain analysis of lossy and non-uniform twisted wire pair," *IEEE Access*, vol. 7, Apr. 2019.

[18] X. Liu, Y. Li, and L. Zhao, "Investigation and analysis on crosstalk of the parallel meander transmission lines," *ACES Conf.*, Beijing, July 29-Aug. 1, 2018.

[19] Y. X. Sun, Q. Li, W. H. Yu, Q. H. Jiang, and Q. K. Zhuo, "Study on crosstalk between space transient interference microstrip lines using finite difference time domain method," *ACES Journal*, vol. 30, no. 8, Aug. 2015.

700 MHz (4G) Indoor Propagation - Measurement and Correlation with Different Numerical Methods

Marcelo B. Perotoni [1], Roberio D. Araujo [1], Kenedy M. G. Santos [2], and Danilo B. Almeida [2]

[1] CECS/UFABC
Federal University of ABC, Santo Andre, SP, 09210-580, Brazil
marcelo.perotoni@ufabc.edu.br, roberiodonizeth@yahoo.com.br

[2] Department of Electrical Engineering
Federal Institute of Bahia, Vitória da Conquista, BA, 45030-220, Brazil
kenedymarconi@gmail.com, engedanilo@gmail.com

Abstract ─ This article details the comparison of three different approaches of indoor propagation modeling – Ray Tracing, Dominant Path Model and the empirical Multi-Wall, the latter based on the COST-231. These methods are implemented inside the Altair Winprop suite, and are correlated with measurements taken at the frequency of 700 MHz. The choice of this frequency is due to its future use as LTE (4G) for applications in public security services.

Index Terms ─ Indoor Wave Propagation, Propagation Measurements, Ray Tracing, Wave Propagation Modeling.

I. INTRODUCTION

The importance of indoor propagation has become relevant not only due to the widespread use of wireless communication systems but also due to the wide deployment of IoT (Internet of Things) devices [1, 2]. The efficient use of the crowded electromagnetic spectrum depends on careful planning, due to its use by different services. Numerical prediction can then help plan the use of the spectrum, obtaining the maximum output from a given channel. Since propagation measurements might not always be possible for each and every case, confidence in numerical prediction tools is advantageous to use the existing hardware with full capacity. Nevertheless, empirical formulations based on a comprehensive set of measurements are still useful and adequate for first-order addressing of propagation in indoor/office spaces [2].

This paper compares three different numerical approaches - Ray Tracing (RT), Dominant Path Model (DPM) and Multi-wall (MW), in descending order of complexity. They are presented applied to an indoor measurement site, at the frequency of 700 MHz, chosen because of its possible assignment use by 4G (Long Term Evolution), particularly by the Police, enabling data and video transmission. A short description of the numerical methods is presented, followed by the measurements and finally, conclusions are shown regarding the performance of the three approaches.

II. NUMERICAL METHODS

Three different numerical methods were tested against measurements. In order to keep a neutral approach, each one of the methods did not have its settings changed, they were left as default.

The RT method is a deterministic model, which follows the wave propagation in a similar way to a light ray. It is a time-consuming method since it computes for each point the complex sum of all the arriving rays, under certain energy thresholds (for instance after a certain number of diffractions or reflections the ray might be discarded due to its low amplitude). A ray can reach its destination by four different physical mechanisms – line of sight (LOS), refraction, diffraction and scattering [3]. Fig. 1 shows a basic scheme of an RT propagation – four different rays, indexes 1 to 4 are launched from the antenna. They propagate in straight lines, and upon facing a reflection (rays 1 and 4) they are computed accordingly (generating rays 1a and 4a). The ray 3 undergoes a knife-edge type diffraction and generates the 3a ray, whereas ray 2 goes through a window – its amplitude will be reduced as it goes out (2a). All these propagation mechanisms follow analytical formulations, whose respective parameters might be further adjusted by the user. Unlike the basic scheme of Fig. 1, the real simulation sweeps the whole 3D space with different rays emerging from the transmitter site [4]. RT offers the possibility of computing further propagation parameters, such as impulse response and angle of arrival, unlike empirical methods. It is a method sometimes too demanding for outdoor prediction, but adequate for indoor environments [3, 5]

Submitted On: November 2, 2018
Accepted On: December 2, 2019

and has been applied even to address the reception of medical implants inside human bodies [6].

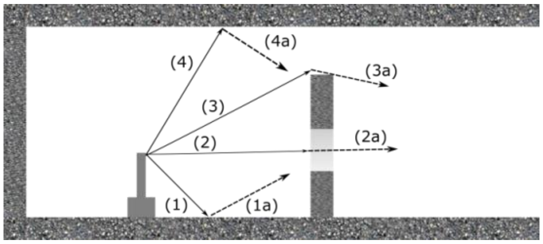

Fig. 1 Ray tracing idea, lateral view.

The DPM chooses before effectively launching the simulation only the ray paths which reach the receiving points with the strongest amplitudes [7,8,9]. As Fig. 2 shows, the rays which undergo multiple diffractions or reflections and which present large losses are discarded. Therefore by choosing only the dominant path a substantial shorter processing time can be obtained, in contrast to the RT. Besides that, geometrical description of the model and their material description errors impact less on the final result, because DPM minimizes this error by focusing on the rays with the most energy only.

On Fig. 2 a top view of an indoor environment is shown, where three rays reach the receiver from the transmitter. Only the red trace will be considered for this case, since it undergoes fewer reflections and refractions, thereby reaching the RX point with higher energy. This reasoning is applied to every receiver site on the simulation domain, and it allows gains in terms of computational time and resources. Winprop particularly uses only one ray for the DPM approach, the one with reaches the receiving point with the most energy [10].

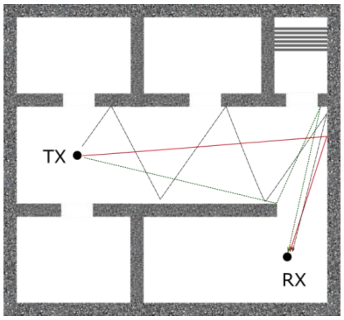

Fig. 2. DPM Dominant Path Model, top view of the propagation rays.

The third method hereby analyzed is the so-called Multi-Wall, based on an adaptation of the COST-231 regulation (idealized for small cells [11]) and originally based on [12,13]. It analyzes only the direct connection between the transmitter and receiver. This ray has its loss computed as the sum of the Free space propagation loss (by Friis formula) and an additional loss term relative to the number of walls and floors that the ray goes through until it reaches the receiving point [14,15]. The factors acting on the wall/floor propagation loss are taken from empirical measurement sets. Fig. 3 depicts a simple application – only the direct ray is taken into account, though there is not a line of sight between the two points the loss is computed from analytical formulations. Though apparently simple the method has the advantage of its fast simulation time and the small dependency on the geometrical and material model accuracies, in contrast to the RT and DPM alternatives. It does not take into account diffraction (therefore becomes more pessimistic as the receiving point moves further away from the transmitter) [10].

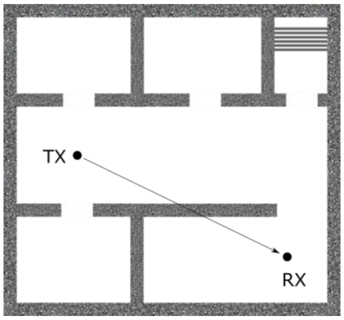

Fig. 3 Multi-Wall Method basic schematic.

Fig. 4. Spectrum analyzer used as receiver, with telescopic antenna, measuring the environment noise floor.

III. MEASUREMENTS

Measurements took place on the seventh floor of a concrete building in the UFABC Campus, with walls made out of concrete and plaster, mainly occupied by research laboratories and data centers. A spectrum analyzer connected to a telescopic antenna sampled the electric field on the receiving sites. The transmitter was set to 700 MHz and with its maximum amplitude (20 dBm), also using a telescopic antenna. Figure 4 shows the spectrum analyzer set as a receiver, displaying the ambient noise floor, without the generator powered on - visually there is no RF power on the vicinity of 700 MHz, only a carrier at 788 MHz. The antennas were kept with vertical polarization all along. A set of 12 points were taken, seven of them inside the lab and the other outside, spread on the common hall connecting the different laboratories.

Fig. 5. Blueprint of the measurement site with the transmitter and receiver points. The gray area on the top is shown in detail on the inferior part.

Figure 5 shows the indoor environment with the respective receiver (in red) and transmitter (blue) points. According to Fig. 5, there is a maximum (straight) distance between the transmitter and the furthest point (number 5) of about 35 meters. Points 1 up to 5 are outside the laboratory; the other ones are inside (i.e. the signal does not have to go through walls or door, only subjected to diffractions on the furniture). The maximum distance taken for the measurement was set by the spectrum analyzer sensitivity - points further away do not result in accurate received power measurements since they are on the same level as the ambient noise floor. The measurements were taken with both spectrum analyzer and signal generator kept at floor level; condition consistent to the simulation.

Figure 6 shows both the transmitter site and its position just across the door, with the generator shown in detail with the actual operational settings. It can be seen that it is positioned just across the wood door, kept closed throughout the test, and close to a metallic power distribution box (not considered in the simulation).

IV. NUMERICAL PREDICTION

The virtual model is constructed from the scratch based on an uploaded blueprint, which contains the information necessary to draw the walls and apertures (windows and doors) and contains the reference for distances. Materials are assigned in a proper way (concrete, wood, and glass). Furniture was not included, for the sake of simplification, and it is, therefore, an error source - affecting all numerical methods to different degrees according to the observed in Section II. The antennas were considered to be omnidirectional, for the sake of simplicity – they were positioned against varied walls, doors, metallic frames, etc as they were moved along the measurement points, thereby distorting their patterns. Figure 7 shows the three predicted power plots, along with the CAD model that describes the scenario. It can be seen that in general the DPM prediction pattern is smoother, without the acute lower amplitude areas from RT and MW, located on the lower half of the area. MW also, in particular, predicts a more pessimist coverage (i.e. with lower amplitudes) in the areas further from the transmitter (right half of the respective plot figure). In terms of computing time and resources, DPM took 2 seconds and approximately 0.8 Mbytes; Multi-Wall 1 second and 0.1 Mbyte and RT 15 seconds with 87 Mbytes.

Fig. 6. Transmitter site and the generator shown in detail.

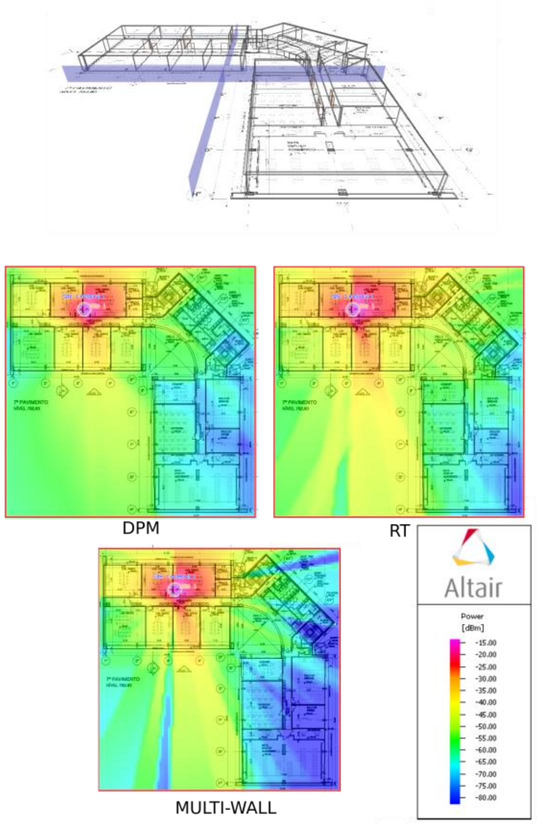

Fig. 7. Predicted results from the three different numerical methods; on top the CAD model used by the simulation.

Taking into account the measurements, Fig. 8 shows their correlation with the predicted sets, for the three numerical methods. The points are presented following the convention in Fig. 5 - i.e. they are not organized in ascending order of distance.

The largest discrepancy with the measurement took place with point number 2; 17 dB for the worst (DPM) case. It can be inferred that this specific spot, on the wall in front of the lab where the transmitter is located, is subjected to a strong spatial field amplitude variation (visualized in Fig. 7), so that it is more sensitive to the receiver position. All three methods generated, for this specific point, poor correlation, so an error on the actual measured position might be possible.

Another correlation parameter is the Mean Square Error, hereby called E, for each one of the numerical methods, as (1) shows:

$$E_{method} = \frac{\sum_{i=1}^{N} (p_{i,predicted} - p_{i,measured})^2}{N}, \qquad (1)$$

where E_{method} is the error associated with the specific method; N the total number of sampled points and $p_{predicted}$ and $p_{measured}$ the respective computed and measured individual power values. Table 1 summarizes the parameter for the three different methods. The subscripts indicate which method the error parameter refers to.

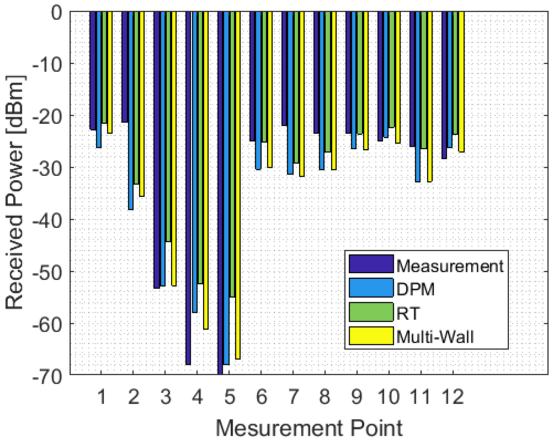

Fig. 8. Comparison between the three different numerical methods and measurements.

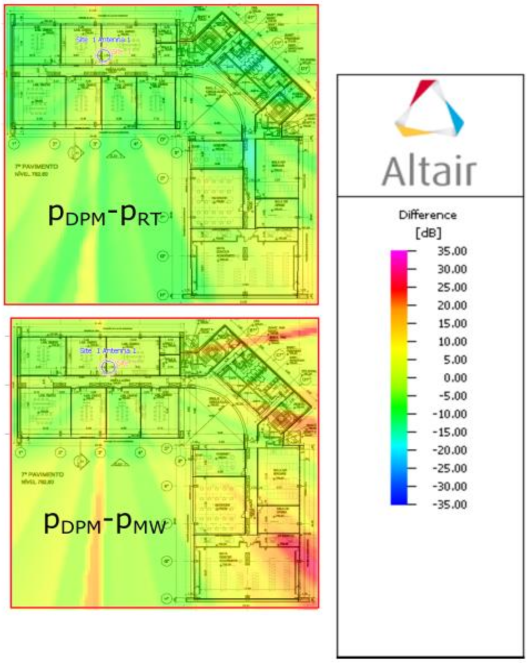

Fig. 9. Plots of the difference between predicted received powers from sets of two different methods.

Table 1: Error parameter

E_{DPM}	52.41
E_{RT}	65.36
E_{MW}	40.78

It can be seen that for the points in question the Multi-Wall method provided the smaller overall error, with Ray Tracing showing the worse performance. It needs to be stressed that if the points were distributed further away from the transmitter it is likely that the Multi-Wall results would be farther from the measurements, since it generates more pessimistic values for these cases as Fig. 7 showed. The concentration of measured points near the transmitter, due to the spectrum analyzer sensitivity, helped MW in relation to DPM and RT methods.

The subtraction of the predicted received power values across the simulation plane is shown in Fig. 9. Both differences are shown with the same scale, so that it is apparent that the DPM has a larger similarity with the RT method than the Multi-Wall, notably as the distances from the transmitter increase.

Similar study, used for address the Lora protocol at the frequency of 865 MHz in an office building concluded that the Multi-Wall method, though less precise, offers advantages mainly due to the fact of being less demanding in terms of a precise virtual model of the building [14], in comparison to the Ray Tracing method.

V. CONCLUSION

This paper presented the comparison between measurements and simulations, using three different numerical methods, on an indoor scenario at 700 MHz. It was shown good correlation with the measurement set, and characteristics of each method were pointed out. It was seen that the empirical method Multi-Wall based on the COST-231 regulation generated closer results to the measurements, due to the fact the sampled points were distributed at distances not far from the transmitter site.

REFERENCES

[1] L. Gregora, L. Vojtech, and M. Neruda, "Indoor signal propagation of LoRa technology", *17th International Conference on Mechatronics – Mechatronika (ME)*, Prague Czeck Republic, pp. 13-16, Dec. 2016.

[2] Y. Wang, W. J. Lu, and H. B. Zhu, "An empirical path-loss model for wireless channels in indoor short-range office environment," *International Journal of Antennas and Propagation*, vol. 2012, pp. 1-7, 2012.

[3] S. Salous, *Radio Propagation Measurement and Channel Modelling*, Wiley, West Sussex, 2013.

[4] R. Hoppe, G. Wolfle, and U. Jakobus, "Wave propagation and radio network planning software WinProp added to the electromagnetic solver package FEKO," *ACES 2017 International Applied Computational Electromagnetics Society Symposium*, Florence, Italy, pp. 3-4, Mar. 2017.

[5] M. Xue, S. Q. Jian, Y. F. Rong, and L. Y. Jian, "A novel ray tracing method for predicting indoor channel characteristics map," *APCAP 2014 3rd Asia-Pacific Conference on Antennas and Propagation*, Harbin, China, pp. 661-662, July 2014.

[6] S. Chamaani, S. A. Mirtaheri, Y. Nechayev, and P. S. Hall, "MICS band indoor channel modeling using ray tracing method," *IST 2010 5th International Symposium on Telecommunications*, Tehran, Iran, pp. 126-131, Dec. 2010.

[7] G. Wölfle, R. Wahl, P. Wertz, P. Wildbolz, and F. Landstorfer, "Dominant path prediction model for indoor scenarios," Gemic *2005 German Microwave Conference*, Ulm, Germany, pp. 176-179, Apr. 2005.

[8] R. Wahl and G. Wolfle, "Combined urban and indoor network planning," *2006 First European Conference on Antennas and Propagation*, Nice, France, pp. 1-6, Oct. 2006.

[9] T. K. Geok, F. Hossain, and A. T. W. Chiat, "A novel 3D ray launching technique for radio propagation prediction in indoor environments," *PLoS One*, vol. 13, no. 8, pp. e0201905, 2018.

[10] Altair WinProp, v. 2018, Troy MI., 2018.

[11] H. Sizun, *Radio Wave Propagation for Telecommunication Applications*, Springer, Berlin, 2005.

[12] J. Walfisch and H. L. Bertoni, "A theoretical model of UHF propagation in urban environments," *IEEE Trans. Antennas Propag.*, vol. 36, no. 12, pp. 1788-1796, 1988.

[13] F. Ikegami, S. Yoshida, T. Takeuchi, and M. Umehira, "Propagation factors controlling mean field strength on urban streets," *IEEE Trans. Antennas Propag.*, vol. 32, no. 8, pp. 822-829, 1984.

[14] S. Hosseinzadeh, H. Larijani, K. Curtis, A. Wixted, and A. Amini, "Empirical propagation performance evaluation of LoRa for indoor environment," *IEEE 15th International Conference on Industrial Informatics (INDIN)*, Emden, Germany, pp. 26-31, July 2017.

[15] M. Lott and I. Forkel, "A multi-wall-and-floor model for indoor radio propagation," *53rd IEEE Veh. Technol. Conf.*, Rhodes, Greece, pp. 464-468, May 2001.

Marcelo B. Perotoni Electrical Engineer (UFRGS, Porto Alegre, Brazil), Ms.C. and Ph.D. in Electrical Engineering from USP (Sao Paulo, Brazil). He has been involved with electromagnetic simulation since 2002 and is interested in RF and EMC. He is currently a Professor at UFABC.

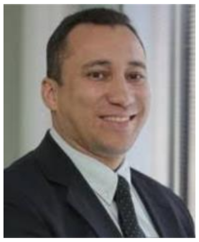

Roberio D. Araujo Electrical Engineer (Faculdade Engenharia Barretos), currently pursuing a Ms.C. in Electrical Engineering at UFABC. He has experience on Propagation measurements, having worked for Harris and Motorola.

Kenedy Marconi G. Santos is B.Sc. in Electrical Engineering (2006) - Pontifícia Universidade Católica of Minas Gerais, M.Sc. in Electrical Engineering (2011) – Federal University of Mina Gerais - UFMG, Ph.D. in Electrical Engineering (2018) – Federal University of Bahia. Currently is Professor at the Federal Institute of Bahia. He has experience in Electrical Engineering with emphasis on Electromagnetic Compatibility, Microwave and Antennas.

Danilo B. Almeida Elec. Eng. (2005) - UNIP - SP, specialist in occupational safety and energy efficiency. Currently is Professor at the IFBA and FAINOR.

Micro-motion Forms Classification of Space Cone-shaped Target Based on Convolution Neural Network

Gaogui Xu [1,2], Hongcheng Yin [1,2], and Chunzhu Dong [2]

[1] School of Information Engineering
Communication University of China, Beijing 100024, China
edward2016@cuc.edu.cn

[2] Science and Technology on Electromagnetic Scattering Laboratory
Beijing 100854, China

Abstract ─ In this paper, the echo models with different micro-motion forms (spin, tumbling, precession, and nutation) of space cone-shaped target are built. Different from the ideal point scatterers model, the radar echo contains the contribution from the complex radar cross section (RCS) of point scatterer *vs* aspect angle. And a convolution neural network (CNN) model for micro-motion forms classification based on the micro-Doppler characteristics in spectrograms is presented. The simulation results show that our method can discriminate different micro-motion forms effectively and the overall accuracy is 97.24%. Different levels of additive white Gaussian noise are added to simulate noise-contaminated radar echo. It has been found that the presented method has a stronger anti-noise ability than support vector machine (SVM). When the Signal-to-Noise Ratio (SNR) of Gaussian white noise is 10 dB, the overall accuracy of our algorithm is 29.79% higher than that of SVM.

Index Terms ─ Convolution neural network, micro-Doppler, micro-motion forms classification, space cone-shaped target.

I. INTRODUCTION

The micro-Doppler effect refers to Doppler modulations on the radar echo due to micro-motion dynamics (such as mechanical vibrations or rotations) of the target or any structure on the target, in addition to the constant Doppler frequency shift induced by the bulk motion of a radar target [1, 2]. Micro-Doppler is a unique signature of the target with movements and provides additional target features that are complementary to existing methods [2]. The micro-Doppler effect can be used to classify and identify the target, for example, human detection and activity classification [3] and the warhead and decoys of ballistic target [4].

Due to the interference by releasing decoys and the wobble under the action of the Earth's atmosphere, besides the translation along the line of sight (LOS) of the radar, the warhead will have spin, precession, and nutation. Many researches indicated that the micro-Doppler signatures can be used to recognize and discriminate the warhead and the decoys [4-6]. The micro-motion parameters of the ballistic target reflect the important characteristics such as its structure, size, and micro-motion period. For radar imaging, to obtain a clear body image, the micro-Doppler component must be separated [7-9]. The premise of the success of these methods is to extract stable and effective micro-motion signatures.

Conventionally, the micro-motion parameters estimation methods are based on the micro-motion form [10, 11]. However, it's hard to know the micro-motion form of the target, since radar usually observes non-cooperative targets. And the traditional classification methods of micro-motion forms can be regarded as a kind of feature engineering, which means that they need to extract discriminative features from the raw echo data for classification algorithms.

In general, the domain knowledge of micro-Doppler signals is required either in the design of time-varying signatures or from the extraction of features. These limitations result in poor adaptability of the algorithm and low anti-noise capability. In this paper, we propose a deep convolution neural network (CNN) model, which is based on the classical CNN devised by LeCun *et al* [12]. It can effectively discriminate the micro-motion forms from the radar echo, which makes the application of the parameter estimation methods more successful. CNN is an end-to-end learning that automatically learns features and discriminates patterns from data. Compared with the traditional method, CNN takes feature design, feature selection, feature extraction, and pattern recognition as a whole by optimizing a certain loss function. Through automatic learning features, it has achieved state-of-the-art results in many fields, such as

Submitted On: July 24, 2019
Accepted On: December 28, 2019

image classification [13, 14] and speech recognition [15, 16]. Thus, the influence of the preorder algorithm module on the subsequent algorithm module is reduced.

This paper is organized as follows: in Section II, we develop the echo models of space cone-shaped target with four different micro-motion forms, and the details of the classification algorithm based on CNN are described. Next, in Section III, the simulation results are given, followed by the conclusion in Section IV.

II. MICRO-MOTION FORMS CLASSIFICATION

A. Mathematical model

With the development of modern penetration technology, cone-shaped decoys have appeared. Since the attitude control of the decoy is weak, the angle of precession and nutation will be larger, and even the decoy will tumble. Therefore, the echo models of four different forms of micro-motion (spin, tumbling, precession, and nutation) are given.

Figure 1 gives the geometry of radar and cone-shaped target with spin, tumbling, precession, and nutation. Three coordinate systems are introduced. The radar is stationary and located at the origin of the radar coordinate system (U, V, W). The cone-shaped target is located at the local coordinate system (x, y, z) and spinning around its symmetric axis $\overrightarrow{O'z}$. The origin of the local coordinate system is at the center of mass of the target. The reference coordinate system (u, v, w) is parallel to the radar coordinate system and shares the origin with the local coordinate system. The origin O' is assumed to be at a distance R_0 from the radar.

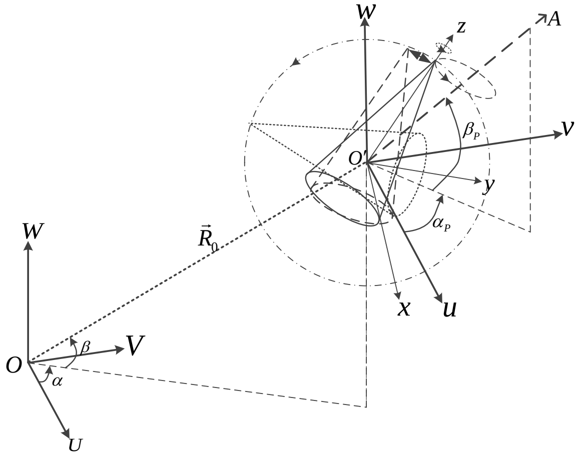

Fig. 1. Geometry of radar and cone-shaped target with spin, tumbling, precession, and nutation.

For simplicity, a target can be represented as a set of point scatterers. In the interest of brevity, the scatterer in the following text refers to the point scatterer. Under high-frequency electromagnetic waves, the scatterers of a cone-shaped target are mainly composed of cone top P_0 and two cone bottoms P_1 and P_2. If the radar transmits a sinusoidal waveform with a carrier frequency f_0, then the baseband of the returned signal from the cone-shaped target is:

$$\begin{aligned} s(t) &= \sum_{i=0}^{2} \sqrt{\sigma_i} \exp\{j\varphi_i\} \exp\left\{ j2\pi f_0 \frac{2R_i}{c} \right\} \\ &= \sum_{i=0}^{2} RCS_i \exp\left\{ j2\pi f_0 \frac{2R_i}{c} \right\}, \end{aligned} \tag{1}$$

where c is the speed of the electromagnetic wave propagation, R_i is the range from the radar to the scatterer P_i, and $RCS_i = \sqrt{\sigma_i}\, exp\{j\varphi_i\}$ is the complex radar cross section (RCS) of the scatterer P_i, which will vary in different attitudes, as shown in the Appendix.

It is worth noting that the location of the scatterer $P_i (i = 0, 1, 2)$ is not fixed, and it will slide on the surface of the target. For example, scatterer P_0 is a moving scatterer that slides on the surface of the spherical crown with the change of incident direction. The location of P_0 is the point at which the incident ray passes through the center of the sphere and intersects with the sphere.

Suppose a scatterer P is located at $\overrightarrow{r_0} = (x_0, y_0, z_0)^T$ represented in the target local coordinate system (x, y, z) at instant of time $t = 0$, where the superscript T means transposition. Generally, the local coordinate system and the reference coordinate system do not coincide at the initial time. For the reference coordinate system, the position of point P at time $t = 0$ can be calumniated as $R_{init} \cdot \overrightarrow{r_0}$, where R_{init} is an initial rotation matrix determined by Euler angles. After rotation, the point P in the radar coordinate system at time $t = 0$ is located at $\overrightarrow{R_0} + R_{init} \cdot \overrightarrow{r_0}$.

Since the space cone-shaped target is rotationally symmetrical, its spin does not affect radar echo. Thus, the echo is obtained as:

$$s_1(t) = \sum_P RCS_P \exp\left(j\frac{4\pi}{\lambda_0} \left\| \left(\overrightarrow{R_0} + R_{init} \cdot \overrightarrow{r_0} \right) \right\| \right), \tag{2}$$

where λ_0 is the wavelength and $\|\cdot\|$ represents the Euclidean norm.

In the process of unfolding, the force of decoy is more complex, which will cause its tumbling motion to be irregular. For simplicity, suppose that the target will tumble around the center of mass about its axes x, y, z with an angular velocity $\vec{\omega} = (\omega_x, \omega_y, \omega_z)^T$. Therefore, the unit vector of $\vec{\omega}$ is $\vec{\omega}' = (\omega_x', \omega_y', \omega_z')^T = \vec{\omega}/\|\vec{\omega}\|$. According to Rodrigues formula [17], at time t the rotation matrix becomes:

$$R_t = I + \hat{\omega}' \sin\Omega t + \hat{\omega}'^2 (1 - \cos\Omega t), \tag{3}$$

where $\Omega = \|\vec{\omega}\|$, $\hat{\omega}'$ is a skew symmetric matrix constructed by $\vec{\omega}'$.

After tumbling, the echo can be expressed as:

$$s_2(t)=\sum_P RCS_P \exp\left(j\frac{4\pi}{\lambda_0}\left\|\left(\overrightarrow{R_0}+R_t\cdot R_{init}\cdot\overrightarrow{r_0}\right)\right\|\right). \quad (4)$$

Precession refers to the coning motion of a target along the axis $\overrightarrow{O'A}$, in addition to spinning around its symmetry axis $\overrightarrow{O'z}$, as shown in Fig. 1. The angle between axis $\overrightarrow{O'A}$ and axis $\overrightarrow{O'z}$ is called the precession angle. Spinning and coning are both rotating motions, except that the axis of rotation is different. Therefore, Precession can be regarded as the spin of the target in the local coordinate system and then the coning motion in the reference coordinate system. At time t, the location of the scatterer P in the reference coordinate system is $R_c\cdot R_{init}\cdot R_s\cdot\overrightarrow{r_0}$, where R_c is the rotation matrix of coning motion and R_s is the rotation matrix of spinning motion, both of which are determined by equation (3). Thus, the echo of micro-Doppler modulations induced by precession is:

$$s_3(t)=\sum_P RCS_P \exp\left(j\frac{4\pi}{\lambda_0}\left\|\left(\overrightarrow{R_0}+R_c\cdot R_{init}\cdot R_s\cdot\overrightarrow{r_0}\right)\right\|\right). \quad (5)$$

If the precession angle does not remain at a constant, the target will oscillate up and down between two limits. This motion is called nutation. After precession, the transient position vector of symmetry axis $\overrightarrow{O'z}$ is $\overrightarrow{z_t}=R_c\cdot R_{init}\cdot[0,0,1]^T$. The target will then oscillates in the plane composed of vector $\overrightarrow{z_t}$ and unit vector $\hat{x}=\overrightarrow{O'A}$. It is equivalent to rotating about the axis $\hat{z}=\overrightarrow{O'A}\times\overrightarrow{z_t}$, where × represents cross multiplication.

Therefore, $x'=\hat{x}$, $y'=\hat{z}\times\hat{x}/\|\hat{z}\times\hat{x}\|$, and $z'=\hat{z}/\|\hat{z}\|$ form a new coordinate system. The transition matrix from the reference coordinate system (X,Y,Z) to the new coordinate system is $A=(x',y',z')$. The rotation matrix of the target rotating around the z' axis is B, which is determined by oscillating frequency f_o and oscillating amplitude θ_o. Then, the echo is obtained as [2]:

$$s_4(t)=\sum_P RCS_P \exp\left(j\frac{4\pi}{\lambda_0}\left\|\left(\overrightarrow{R_0}+R_v\cdot R_c\cdot R_{init}\cdot R_s\cdot\overrightarrow{r_0}\right)\right\|\right), \quad (6)$$

where $R_v=A\cdot B\cdot A^T$.

B. Micro-motion forms classification based on convolution neural network

As shown in equations (2), (4), (5), and (6), the echoes of the target with different micro-motion forms are very different. In frequency domain, the common method for analyzing echo signal is Fourier transform. Due to lack of localized time information, it is not suitable for analyzing a signal whose frequency changes over time. Compared with Fourier transform, a joint time-frequency analysis can provide localized time-dependent frequency information, which is used to extract time-varying signatures for micro-motion forms classification. In this paper, the Wigner-Ville distribution (WVD) [18] is used to analyze the micro-Doppler.

Different micro-motion forms present their unique micro-Doppler signatures. The micro-Doppler modulation caused by different micro-motion forms can be seen in the high-resolution spectrogram. By using spectrograms, we convert the micro-motion forms classification problem to an image recognition problem. Figure 2 shows the hierarchical structure of the CNN, which stacks multiple layers of simple neural network architecture, thus extracting the representation of data layer by layer. It takes color spectrograms as the input and learns the mapping between the spectrogram and its corresponding micro-motion form. CNN is mainly composed of four components. The first component is the convolution layer which consists of a set of learnable filters. Each filter has small receptive fields of input data and can be seen as a specific feature extractor. However, in convolution operation, if there is no nonlinear transformation in the network, the network will only learn the linear characteristics of the input, resulting in the network can't deal with nonlinear problems, and the application scene is limited. The second component is the nonlinear activation function that carries on the nonlinear transformation to the result of the linear transformation. The commonly used activation functions are the Sigmoid function, the Restricted Linear Units (ReLU) function, and their variants. In this paper, we choose ReLU as the activation function, the formula of which is $f(x)=max(0,x)$. The third component is the pooling layer, which subsamples the data according to certain rules while retaining the main information. By performing 2×2 pooling operation with max pooling, the data size will be halved. Thus, The pooling layer greatly reduces the network parameters and prevents overfitting.

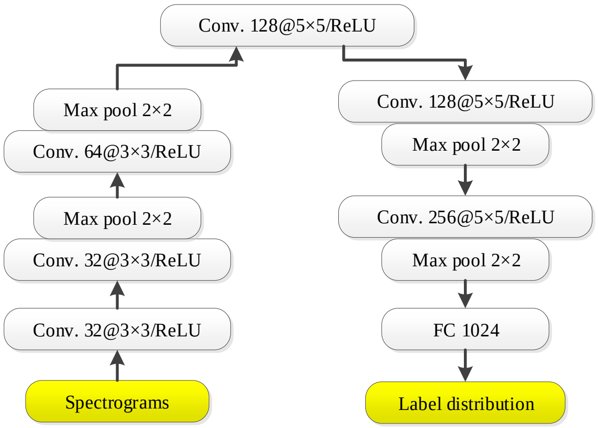

Fig. 2. The hierarchical structure of the CNN.

The last component is the full connection layer

(FCN), where all the input nodes are connected to all the output nodes. In the classification problem, Softmax function is typically used as an activation function for the output layer to obtain the probability of the category and can be expressed as:

$$a_i = e^{z_i} / \sum_{j=1}^{L} e^{z_j} , \tag{7}$$

where L represents the total number of target categories.

The category of the target is determined by the neuron with the highest probability, which is $argmax(a)$.

Suppose the difference between the network output and the real value is $loss(x)$, which is called the error function. The training of CNN can be divided into two processes: forward propagation and backward propagation. In the forward propagation, the output of the network is calculated according to the input image. And in the backward propagation, the network parameters are automatically updated by the error function. This parameter update method is called gradient descent (GD). It is an optimization method to find a local (preferably global) minimum of a function. For the network parameter w_{ij}, it is updated using:

$$w_{ij}^{\tau+1} = w_{ij}^{\tau} + \Delta w_{ij}^{\tau} , \tag{8}$$

where τ is the gradient descent iteration and Δw_{ij}^{τ} is the weight update.

Δw_{ij}^{τ} is determined by:

$$\Delta w_{ij} = -\eta \frac{\partial loss(x)}{\partial w_{ij}} , \tag{9}$$

where η is the learning rate and x is the input spectrogram.

According to the number of input samples used for each update of the weights, two variants of GD are generally used, namely on-line learning and batch learning. In on-line learning, the weights are updated for every input. In batch learning, the error function is calculated for a batch of input samples. If the selection of the input samples is random, the GD optimization method is called stochastic gradient descent (SGD). In this paper, the SGD is used and the batch size is 256.

III. SIMULATION RESULT

The echoes of four micro-motion forms are simulated and WVD is used to obtain the spectrograms. Assume that the operating frequency of radar is 10 GHz and the center of mass of the target is located at $(U = 1000m, V = 5000m, W = 5000m)$. The azimuth angle α_P and elevation angle β_P of the coning axis $\overrightarrow{O'A}$ range from $10°$ to $80°$ with an interval of $5°$. Thus, there are 225 combinations of (α_P, β_P) pairs. The initial Euler angles are $(30°, 30°, 45°)$. For spin, the spinning frequency is from 1 Hz to 20 Hz with an interval of 0.5 Hz. Assume that the range of each component of the angular velocity of rotation $\vec{\omega}$ is from $\pi/2$ rad/s to 8π rad/s with an interval of $\pi/4$. Compared with spin, precession has rotation around the coning axis, and the frequency of rotation is from 2 Hz to 5 Hz with an interval of 0.5 Hz. Nutation is a periodic transformation of the precession angle based on precession. Assume that the wobble frequency is from 5 Hz to 7 Hz with an interval of 0.5 Hz and that the oscillating amplitude ranges from $1°$ to $5°$ with an interval of $1°$.

Suppose that the radar pulse repetition frequency (PRF) is 2000. The spectrograms are obtained by WVD analysis of 2s echo data. Since the RCS is related to polarization, the horizontal to horizontal (HH) and vertical to vertical (VV) polarization are considered. If the simulation is carried out according to the above conditions, the samples of each micro-motion form are uneven. Combined with the limited information contained in the spin, for precession, we randomly select 21 frequencies from the spin frequencies, resulting in 66,150 data. For nutation, we randomly select one frequency from the spin frequencies, resulting in 78,750 data. The size of the spectrogram is normalized to 256×256.

In order to further approach the actual case, we consider not only the contribution from the complex RCS of point scatterer *vs* aspect angle, but also the change of the scatterer's location with target motion. They will have an impact on micro-Doppler modulation, making it difficult for the feature-based classification algorithms to discriminate different micro-motion forms. Figure 3 shows an example of spectrograms of a cone-shaped target with precession for HH and VV polarization. There are two visible scatterers in the time of 2 seconds, as shown in Fig. 3 (a). The curves of scatterer P_0 and scatterer P_1 are sinusoidal curve. The RCS of scatterer P_1 is smaller for VV polarization than for HH polarization, resulting in discontinuity of its curve, as shown in Fig. 3 (b). Different polarization only affects the continuity of the curve and does not change the micro-Doppler characteristics of the target. Among the 176,400 data, 80% of spectrograms of each micro-motion form are used as the training set and the rest as the test set. The convolution neural network shown in Fig. 2 is constructed.

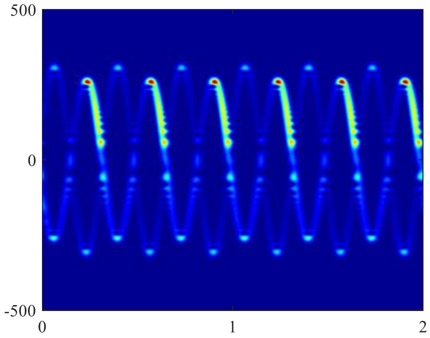

(a)

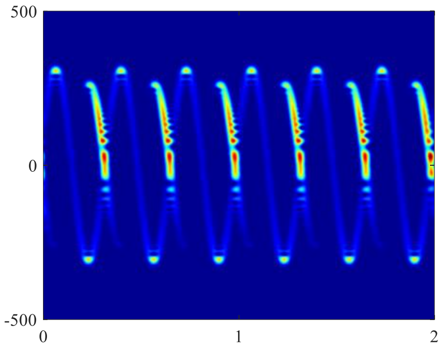

(b)

Fig. 3. Micro-Doppler modulations of cone-shaped target induced by precession for (a) HH and (b) VV polarization.

Different micro-motion parameters, such as the rotation frequency, will have effect on the amplitude and the period of the curve in spectrograms. The distinctions of different micro-motion forms are the curve characteristics of scatterers. The rotationally symmetrical target with spin does not effect micro-Doppler modulation. The micro-Doppler frequency shift is approximately 0. Thus, there is not much information contained in spectrogram, which is often a widened straight line. As far as tumbling is concerned, the amplitudes of different scatterers are the same. The difference between precession and tumbling is the amplitude of the curves. Although they are both sinusoidal curves, for precession, the amplitudes of curves are different. For nutation, there will be no more sinusoidal curves. The micro-Doppler of scatterers is modulated by the mixing of spinning, coning, and oscillating. At the same time, different polarizations will affect the continuity of the curve. Therefore, the method based on feature engineering is difficult to extract effective curve features from spectrograms, especially under noise. Different from other feature based classification algorithms, CNN learns from a large number of spectrograms to extract the common features in the same class and ignore the differences. It automatically extracts the features related to the classification tasks, so as to achieve higher accuracy than the traditional algorithm.

With the increase of training epochs, the error on the training set becomes smaller and smaller, while the error on the test set decreases first and then increases. At this time, the network is overfitted. After 200 epochs, the parameters of the network are approximately optimal, and the overall accuracy is 97.24%. The confusion matrix for the micro-motion forms classification based on CNN is listed in Table 1. Each column in the table is the predicted label, each row is the true label, and the diagonal element is the number correctly classified. The last column is the classification accuracy of each category. In order to measure the overall performance of the algorithm in multiple classification problems, the overall accuracy is introduced, which can be expressed as:

$$OA = \frac{1}{N}\sum_{i=1}^{n} C_{ii}, \tag{10}$$

where N is the number of total samples, n is the number of categories, and C_{ii} is the number correctly classified for class i.

For spinning and tumbling, due to their simple micro-motion, their classification accuracy is higher. When the oscillating amplitude of the target is small or the wobble frequency is slow, the difference between nutation and precession will become smaller, and it is easy to misjudge the nutation as precession. However, the classification accuracy of nutation is still above 95%. In contrast, the support vector machine (SVM) which is a feature-based classification algorithm is also used for micro-motion forms classification. Since the size of spectrograms is 256×256, the number of features is too large for SVM. Therefore, we use the principal component analysis (PCA) as a pre-processing. The overall accuracy of SVM is 72.69%. It is 24.55% lower than that of CNN, which is identical to the theoretical analysis.

Table 1: Confusion matrix for the micro-motion forms classification based on CNN

	Spin	**Tumbling**	**Precession**	**Nutation**	**Accuracy (%)**
Spin	3510	0	0	0	100
Tumbling	0	2715	63	12	97.31
Precession	0	59	12704	467	96.02
Nutation	0	139	548	15063	95.64

Additive Gaussian white noise of various Signal-to-Noise Ratio (SNR) levels (5, 10, 15, and 20 dB) are added to simulate noise-contaminated radar echoes. Figure 4 demonstrates the anti-noise capability of the two algorithms. With decreasing SNR, the performance of these algorithms decreases. The key point used to distinguish precession from nutation is that the micro-Doppler modulation of scatterer P_0 is a sinusoidal curve. The sinusoidal curve will be destroyed in a low SNR, thus the classification error will be increased. But it is clearly seen that the performance of our algorithm is very good. When the SNR is 10 dB, the overall accuracy of our algorithm is still 91.03%, which is 29.79% higher than that of SVM. Therefore, our method has strong anti-noise capability.

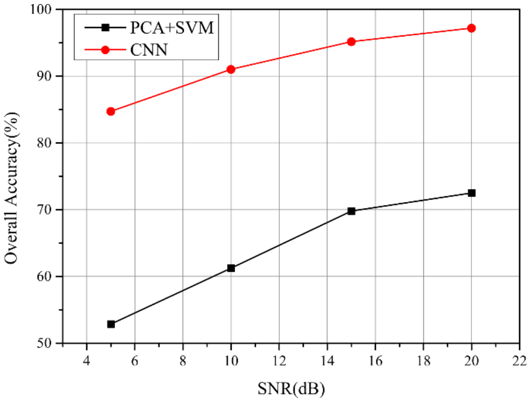

Fig. 4. The anti-noise capability with Gaussian noise.

IV. CONCLUSION

In this paper, we describe the complex RCS variation in the target's different attitudes; develop the echo models of space cone-shaped target with different micro-motion forms (spin, tumbling, precession, and nutation); propose a CNN model for micro-motion forms classification based on spectrograms. Compared with SVM, the method avoids artificial feature selection and feature extraction. Simulated results illustrate that CNN can exploit micro-Doppler features of space cone-shaped target and effectively discriminate different micro-motion forms. Since precession is a special kind of nutation with the oscillating amplitude $\theta_n = 0$, the overall accuracy of them has decreased somewhat. However, compared with SVM, ours has a higher overall accuracy. As a result, we found that our algorithm effectively suppresses noise. When the SNR is higher than 10 dB, the overall accuracy of our algorithm is higher than 90%.

APPENDIX

The sharp cone is a special case of the blunt cone, at which the radius of the spherical crown of the blunt cone is 0. Suppose the bottom radius of the blunt cone is a, the half cone angle is α, and the spherical crown radius is b, as shown in Fig. 5.

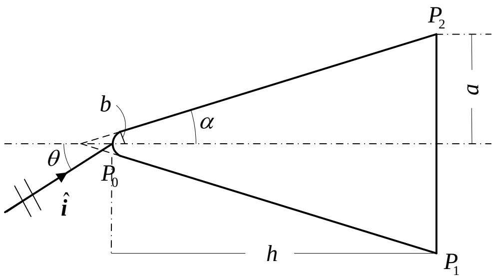

Fig. 5. Geometry of blunt-cone target.

The three scatterers are spherical crown P_0 and two scatterers P_1, P_2 on the bottom edge (the intersections of the incident surface and the bottom edge). Since the blunt cone is axisymmetric, its attitudes can be characterized by the included angle θ between the incident ray and the symmetry axis of cone. Here, θ ranges from 0 to π. For scatterer P_0, it is only visible in $0 \leq \theta < \pi/2 - \alpha$. Thus, the complex RCS of P_0 is [19]:

$$\sqrt{\sigma_0} = \begin{cases} \pi^{\frac{1}{2}} b \left(1 - \dfrac{\sin(2k_0 b(1-\sin\alpha))}{k_0 b \cos^2\alpha}\right)^{\frac{1}{2}}, & \theta = 0 \\ \pi^{\frac{1}{2}} b, & 0 < \theta < \dfrac{\pi}{2} - \alpha \\ 0 & \theta \geq \dfrac{\pi}{2} - \alpha \end{cases} \tag{11}$$

$$\varphi_0 = 0,$$

where $k_0 = 2\pi/\lambda_0$.

For scatterer P_1, its RCS is not only related to θ, but also affected by polarization, which can be described as:

$$\sqrt{\sigma_1} = \frac{\sin\frac{\pi}{n}}{n}\sqrt{\frac{a}{k_0 \sin\theta}}\left(\left(\cos\frac{\pi}{n} - 1\right)^{-1} \mp \left(\cos\frac{\pi}{n} - \cos\frac{3\pi - 2\theta}{n}\right)^{-1}\right) \tag{12}$$

$$\varphi_1 = \frac{\pi}{4}.$$

Here $n = 3/2 + \alpha/\pi$. The upper sign applies when the polarization is VV polarization while the lower sign applies if it is HH polarization.

When the electromagnetic wave is incident perpendicular to the conical surface, the divisor of equation (12) is 0. The RCS of scatterer P_1 is mainly caused by the specular reflection of the conical surface. $\sqrt{\sigma_1}$ should be calculated by the physical optical method [20, 21] and the maximum value is reached. At this point, θ is equal to $\pi/2 - \alpha$, and the equation (12) can be modified to:

$$\sqrt{\sigma_1} = \left\{\frac{4}{9} k_0 \frac{\cos^3\alpha}{\sin^2\alpha}\left[a^{\frac{3}{2}} - (b\cos\alpha)^{\frac{3}{2}}\right]^2\right\}^{\frac{1}{2}}. \tag{13}$$

Near $\pi/2 - \alpha$, if $\sqrt{\sigma_1}$ calculated by equation (12) is greater than the maximum, it should be smoothed.

Unlike scatterer P_1, scatterer P_2 is visible only when $0 < \theta \leq \alpha$ or $\theta \geq \pi/2$. Its RCS is:

$$\sqrt{\sigma_2}\begin{cases} = \dfrac{\sin(\pi/n)}{n}\sqrt{\dfrac{a}{k_0\sin\theta}}\Bigg(\left(\cos\dfrac{\pi}{n}-1\right)^{-1}\mp\left(\cos\dfrac{\pi}{n}-\cos\dfrac{3\pi+2\theta}{n}\right)^{-1}\Bigg)\Bigg), & 0<\theta\le\alpha \\ = 0, & \alpha<\theta<\dfrac{\pi}{2}\,. \\ = \dfrac{\sin(\pi/n)}{n}\sqrt{\dfrac{a}{k_0\sin\theta}}\left(\left(\cos\dfrac{\pi}{n}-1\right)^{-1}\mp\left(\cos\dfrac{\pi}{n}-\cos\dfrac{\pi-2\theta}{n}\right)^{-1}\right) & \theta\ge\dfrac{\pi}{2} \end{cases} \tag{14}$$

$$\varphi_2 = -\frac{\pi}{4}$$

The equations (12) and (14) give the variation of the RCS of the bottom scatterers P_1 and P_2 with different attitudes. When θ is approximately 0 or π, $sin\,\theta$ will approach zero, at which point the equations (12) and (14) will become meaningless and need to be modified. When $0\le\theta\le\alpha$, the contribution from scatterers P_1 and P_2 can be expressed as :

$$\begin{aligned}\sqrt{\sigma_1}e^{j\Psi_1}+\sqrt{\sigma_2}e^{j\Psi_2} = \frac{2\sqrt{\pi}a\sin\dfrac{\pi}{n}}{n}\Bigg(&\left(\cos\frac{\pi}{n}-\cos\frac{3\pi}{n}\right)^{-1}J_0\left(2k_0a\sin\theta\right)\\ &-\frac{j\dfrac{2\tan\theta}{n}\sin\dfrac{3\pi}{n}}{\left(\cos\dfrac{\pi}{n}-\cos\dfrac{3\pi}{n}\right)^2}J_1\left(2k_0a\sin\theta\right)\mp\left(\cos\frac{\pi}{n}-1\right)^{-1}J_2\left(2k_0a\sin\theta\right)\Bigg),\end{aligned} \tag{15}$$

where $J_i\,(i=0,1,2)$ represents the Bessel function of first kind of order i.

When $\theta>\pi-\theta_{ca}$ and $2k_0a\,sin\,\theta_{ca}=2.44$, the contribution from scatterers P_1 and P_2 can be expressed as [22]:

$$\sqrt{\sigma_1}e^{j\Psi_1}+\sqrt{\sigma_2}e^{j\Psi_2}=\sqrt{\pi}a\frac{J_1\left(2k_0a\sin\theta\right)}{\sin\theta}e^{-j\frac{\pi}{2}}. \tag{16}$$

ACKNOWLEDGMENT

This work was supported by The Major Research Plan of National Natural Science Foundation of China under Grant no. 61490690, 61490695.

REFERENCES

[1] V. C. Chen, F. Y. Li, S. S. Ho, and H. Wechsler, "Analysis of micro-doppler signatures," *IEEE IET Proc.-Radar Sonar Navig.*, vol. 150, no. 4, pp. 271-276, 2003.

[2] V. C. Chen, F. Y. Li, S. S. Ho, and H. Wechsler, "Micro-Doppler effect in radar: Phenomenon, model, and simulation study," *Trans. Electron Syst.*, vol. 42, no. 1, pp. 2-21, 2006.

[3] Y. Kim and T. Moon, "Human detection and activity classification based on micro-doppler signatures using deep convolutional neural networks," *IEEE Geoscience and Remote Sensing Letters*, vol. 13, no. 1, pp. 1-5, 2015.

[4] H. W. Gao, L. G. Xie, S. L. Wen, and Y. Kuang, "Micro-doppler signature extraction from ballistic target with micro-motions," *IEEE Transactions on Aerospace and Electronic Systems*, vol. 46, no.4, pp. 1969-1982, 2010.

[5] J. Lei, "Target classification based on micro-doppler signatures," *Proceedings of the IEEE International Radar Conference*, pp. 179-183, 2005.

[6] Y. Yang and J. Lei, "Target classification and pattern recognition using micro-doppler radar signatures," *Proceedings of the Seventh ACIS International Conference on Software Engineering, Artificial Intelligence, Networking, and Parallel/ Distributed Computing*, pp. 213-217, 2006.

[7] J. Li and H. Ling, "Application of adaptive chirplet representation for ISAR feature extraction from targets with rotating parts," *IEE Proceedings of Radar Sonar and Navigation*, vol. 150, no. 4, pp. 284-291, 2003.

[8] S. Ljubisa, D. Igor, and T. Thayananthan, "Separation of target rigid body and micro-doppler effects in ISAR imaging," *IEEE Transactions on Aerospace and Electronic Systems*, vol. 42, pp. 1496-1506, 2006.

[9] A. Bultan, "A four-parameter atomic decomposition of chirplets," *IEEE Transactions on Signal Processing*, vol. 47, pp. 731-745, 1999.

[10] K. Li, Y. Liu, and K. Huo, "Estimation of micro-motion parameters based on cyclostationary analysis," *IET Signal Processing*, vol. 4, no. 3, pp. 218-223, 2010.

[11] Y. Liu, K. Li, and Z. Zhuang, "Estimation of micro-motion parameters based on micro-doppler," *IET Signal Processing*, vol. 4, no.3, pp. 213-217, 2010.

[12] Y. LeCun, B. Boser, J. S. Denker, D. Henderson, R. E. Howard, W. Hubbard, and L. D. Jackel, "Handwritten digit recognition with a back-propagation network," *Advances in Neural Information Processing Systems*, vol. 2, no. 2, pp. 396-404, 1990.

[13] A. Krizhevsky, I. Sutskever, and G. Hinton, "ImageNet classification with deep convolutional neural networks," *Adv. Neural Inf. Process. Syst.*, vol. 25, pp. 1090-1098, 2012.

[14] C. Szegedy, W. Liu, Y. Jia, et al., "Going deeper with convolutions," *2015 IEEE Conference on Computer Vision and Pattern Recognition (CVPR) IEEE*, 2015.

[15] G. Hinton, et al., "Deep neural networks for acoustic modeling in speech recognition," *IEEE Signal Process. Mag.*, vol. 29, no. 29, pp. 82-97, 2012.

[16] T. Mikolov, A. Deoras, D. Povey, L. Burget, and J. Cernocky, "Strategies for training large scale neural network language models," *Automatic Speech Recognition & Understanding*, pp. 196-201, 2011.

[17] R. M. Murray, Z. Li, and S. S. Sastry, *A Mathematical Introduction to Robotic Manipulation*. CRC Press, Boca Ration, 1994.

[18] J. M. O'Toole and B. Boashash, "Fast and memory-efficient algorithms for computing quadratic time–frequency distributions," *Applied and Computational Harmonic Analysis*, vol. 35, no. 2, pp. 350-358, 2013.

[19] L. C. Potter, D. M. Chiang, R. Carriere, and M. J. Gerry, "A gtd-based parametric model for radar scattering," *IEEE Transactions on Antennas and Propagation*, vol. 43, no. 10, pp. 1058-1067, 2002.

[20] A. B. Gorji, B. Zakeri, and R. C. Janalizadeh, "Physical optics analysis for RCS computation of a relatively small complex structure," *The Applied Computational Electromagnetics Society Journal*, vol. 29, no. 7, pp. 530-540, 2014.

[21] J. Perez and M. F. Catedra, "Application of physical optics to the RCS computation of bodies modeled with NURBS surfaces," *IEEE Transactions on Antennas and Propagation*, vol. 42, no. 10, pp. 1404-1411, 1994.

[22] R. A. Ross, *Investigation of Scattering Principles. Vol III. Analytical Investigation General Dynamics*, Forth-worth, Texas, 1969.

Gaogui Xu received the B.S. degree and the M.S. degree in Computer Application Technology from China Three Gorges University, Hubei Province, China, in 2014 and 2017 respectively.

He is currently pursuing the Ph.D. degree of Electromagnetic Field and Microwave Technology at Communication University of China, Beijing, China. His research interests include micro-Doppler, micro-motion, target recognition, and deep learning.

HongCheng Yin was born in Yujiang, Jiangxi Province, China, in 1967. He received the B.S. degree in 1986 from Northwest Telecommunication Engineering Institute, Xi'an, China; the M.S. degree in 1989 from the Science and Technology on Electromagnetic Scattering Laboratory, and the Ph.D. degree in 1993 from Southeast University, Nanjing, China, all in electromagnetic field and microwave technique.

He is now a Research Scientist of Science and Technology on Electromagnetic Scattering Laboratory, Beijing, China. He has coauthored four books and published more than 130 papers in technical journals and conferences. His research interests include electromagnetic scattering, radar target signature, and radar target identification.

He is a fellow of Chinese Institute of Electronics.

Chunzhu Dong was born in 1981. He received the B.S. degree in Zhengzhou University, Henan Province, China, in 2004; the M.S. degree and the Ph.D. degree in Electromagnetic Field and Microwave Technology from the Communication University of China, Beijing, China, in 2007 and 2015 respectively.

Currently he is a Senior Engineer of Science and Technology on Electromagnetic Scattering Laboratory, Beijing, China. His research interests include radar target signature, electromagnetic scattering, and microwave technique.

Shallow Water Three-Dimensional Transient Electromagnetic Modelling by Using Fictitious Wave Field Methods

Yanju Ji [1,2], Xiangdong Meng [1], and Guiying Ren [1]

[1] College of Instrumentation and Electrical Engineering
Jilin University, Changchun, China
{jiyj@jlu.edu.cn,1581900057}@qq.com

[2] Key Laboratory of Geophysical Exploration Equipment
Ministry of Education, Jilin University, Changchun, China
261479384@qq.com

Abstract **─** The marine transient electromagnetic method is a valuable means for locating mineral resources because of its higher detection resolution as well as other advantages. However, this method is easily affected by the air layer and complex terrain, which significantly increase its calculation times. We addressed this problem by developing a three-dimensional finite-difference method based on the principle of correspondence between the diffusive and fictitious wave fields. Using a fast-iteration formula appropriate for a large time step, solving the Maxwell equations in a fictitious wave field, and the effects of air and seawater parameters on the electromagnetic response in shallow water are discussed. Choosing the first derivative of a Gaussian as a source, the 3D numerical simulation of transient electromagnetics in a shallow water area is realized. Comparing to the existing methods, the effectiveness of the proposed method is verified. The results show that this method enables fast and high-precision numerical calculations for 3D models and provides theoretical guidance for detecting seabed mineral resources in complex geological environments in shallow water.

Index Terms **─** Air layer, complex terrain, fictitious wave field, shallow water, three-dimensional modeling.

I. INTRODUCTION

There are transitional zones between land and the sea. Such areas, also known as the coastal ocean, have a complex geological structure. Because the coastal marine shelf contains abundant hydrocarbon reservoirs and mineral resources, marine electromagnetic detection in shallow waters has become a research hotspot. The transient electromagnetic method has a higher resolution in shallow-sea high-resistance reservoirs compared to that of the frequency-domain electromagnetic method [1] because the latter is seriously affected by air wave interference in shallow water, whereas the former can effectively separate the air waves and the response from the submarine formation [2]. Therefore, considerable attention has been paid to the use of the transient electromagnetic method in shallow waters [3]. However, the complex structure of the shallow continental shelf makes 3D numerical simulation extremely time-consuming, particularly if calculation of the air layer is included. This consideration is problematic because, when ocean exploration is carried out in areas with complex seabed topography, ignoring its effects may lead to misinterpretation of the seabed geological structure. Therefore, it is necessary to discover a means to carry out effective and rapid simulation that incorporates the air layer and complex terrain.

Analysis of a one-dimensional numerical simulation of a transient electromagnetic field in shallow water revealed that, when calculating a deep high-resistance model, the influence of the air layer can be neglected; however, when calculating a medium- or shallow-depth high-resistance body, the accuracy of the electromagnetic calculation will be impacted if the air layer is neglected in the calculations [4]. Applying both the time-domain finite-difference method and frequency-domain method to one-dimensional numerical simulation of shallow waters, it was found that the time-domain method can be effectively used to isolate the air layer, and it resolves seabed gas hydrate resources better than the frequency-domain method [5]. Mao et al. proposed a new absorbing boundary condition (ABC). When ABC is used in FDTD, it can effectively improve the computational efficiency [6]. Inoue and Asai proposed a new finite-difference time-domain (FDTD) based on hybrid implicit-explicit and multi-GPU techniques that can effectively improve the calculation efficiency [7]. Further, Ji et al. achieved good results when using the fictitious wave domain finite-difference method to simulate the three-dimensional

Submitted On: September 18, 2019
Accepted On: December 15, 2019

transient electromagnetism of land using a magnetic source [8].

The time-domain marine electromagnetic method is an effective means of shallow water resource detection. The distribution of seabed resources is uneven and spatially varies. One-dimensional and two-dimensional models cannot accurately simulate the real electromagnetic response from the subsurface. Moreover, achieving rapid iteration and efficient calculation for models incorporating the air layer and a complex seabed topography has become an urgent 3D computing problem. This study effectively resolves the inefficiency of three-dimensional electromagnetic numerical simulation for these cases and achieves numerical simulation of transient electromagnetism from a finite-length wire source in a shallow water region.

II. TRANSFORMATION BETWEEN DIFFUSIVE AND FICTITIOUS WAVE FIELDS

When the time-domain finite-difference method is used to simulate the 3D electromagnetic field in shallow water, it is necessary to include the air layer for differential iteration. Because of the high resistivity of the air layer, the iterative calculation requires a large time step making it difficult for ordinary computers to complete the numerical calculations. We refer readers to read [8-9] for the details of its theory. This study expanded upon the basis of the research of [8]. The difference in [8] is that in document 8, the uniform grid is used to cut the three-dimensional model. It is assumed that the grid size in all calculation areas is equal. However, this will greatly reduce the computational efficiency. To improve the computational efficiency, in this study, the air layer is divided into a non-uniform grid, loading the CFS-PML boundary conditions in a fictitious wave field. In addition, the loop source is used in [8]. In this paper, a long wire source is selected, and the iterative relationship in the real diffusion field is transformed into the fictitious wave field for calculation. After the calculation is completed, the electromagnetic response in the fictitious wave field is transformed back to the real diffusion field. This process effectively solves the problem of an excessively long iteration time. The process of transformation proceeds as follows.

The first step is to transform the real diffusion field to a fictitious wave field. The frequency domain quasi-static Maxwell equation of the true diffusion field is as follows:

$$-\nabla \times H + \sigma E = -J\,, \tag{1}$$

$$\nabla \times E - i\omega\mu H = -K\,, \tag{2}$$

where ω is the angular frequency in the real diffusion field; ε is the permittivity in the real diffusion field; μ is the scalar-magnetic constant $\mu = 4\pi \times 10^{-7}$; σ is the electric conductivity; J and K are the current density and magnetic current density, respectively; and E and H are the electric and magnetic fields, respectively.

The angular frequencies in the real diffusion field and the fictitious wave field satisfy the following relationship:

$$-i\omega' = \sqrt{-2i\omega\omega_0}\,, \tag{3}$$

where $\omega_0 = 2\pi \times f_0$ is the scaling parameter, $f_0 = 1Hz$, and ω' is the conversion parameter between the fictitious wave field and real diffusion field.

To realize the transformation between the real and fictitious fields, we define a fictitious dielectric permittivity tensor from a conductivity tensor as follows:

$$\sigma = 2\omega_0 \varepsilon'\,. \tag{4}$$

Formula (3) can be used to convert the electric and magnetic fields in the real domain into the fictitious wave domain. The frequency domain form is expressed as follows:

$$-\nabla \times H + 2\omega_0 \varepsilon' E = -J\,, \tag{5}$$

$$\nabla \times E - i\omega\mu H = -K\,. \tag{6}$$

The Fourier transform is then applied to equations (5) and (6) to obtain the expression of the time-domain fictitious wave domain as follows:

$$-\nabla \times H' + \varepsilon' \partial_{t'} E' = -J'\,, \tag{7}$$

$$-\nabla \times E' + \mu' \partial_{t'} H' = -K'\,, \tag{8}$$

where J' and K' are the current density and magnetic current density in the fictitious wave domain, respectively, and E and H are the electric and magnetic fields in the fictitious wave domain.

The second step is the transformation from the fictitious wave field to the real diffusion field.

The purpose of transforming the real diffusion field into the fictitious wave field is to facilitate the calculation and improve the calculation efficiency. We can regard the real diffusion field as the real domain, the fictitious wave field as the fictitious domain, and the electromagnetic wave in the fictitious wave field as the fictitious wave. However, the fictitious wave field and fictitious wave itself have no physical significance; they have a hypothetical existence. Further, the calculated electromagnetic response in the fictitious wave field has no practical physical significance. Therefore, to obtain the real electromagnetic response, it is necessary to transform the calculation result of the fictitious wave field into the real diffusion field. The transformation relationship is as follows:

$$J(\omega) = \int_0^T J'(t') e^{-\sqrt{\omega\omega_0 t'}} e^{i\sqrt{\omega\omega_0 t'}} dt'\,, \tag{9}$$

$$E(\omega) = \sqrt{\frac{-i\omega}{2\omega_0}} \int_0^T E'(t') e^{-\sqrt{\omega\omega_0 t'}} e^{i\sqrt{\omega\omega_0 t'}} dt'\,, \tag{10}$$

$$H(\omega) = \int_0^T H'(t') e^{-\sqrt{\omega\omega_0 t'}} e^{i\sqrt{\omega\omega_0 t'}} dt'\,, \tag{11}$$

$$K(\omega) = \sqrt{\frac{-i\omega}{2\omega_0}} \int_0^T K'(t') e^{-\sqrt{\omega\omega_0 t'}} e^{i\sqrt{\omega\omega_0 t'}} dt'\,, \tag{12}$$

where T is the total calculation time in the fictitious wave field and t' is the sampling time.

III. SHALLOW WATER FICTITIOUS TIME-DOMAIN FINITE-DIFFERENCE METHOD

A. Difference equation in the fictitious wave field

When the finite-difference method is applied to solve the governing equation of the time domain in the fictitious wave field, a non-uniform mesh is used. Smaller meshing is used at the centre of the calculation, and a larger grid calculation is used at more distant locations. The finite-difference forms of the magnetic field and electric field are as follows:

$$E^{n+1}_{x_{i+1/2,j,k}} = E^{n}_{x_{i+1/2,j,k}} + \Delta t \frac{2\omega_0}{\sigma} (\partial^-_y H^{n+1/2}_{z_{1+1/2,j+1/2,k}} - \partial^-_z H^{n+1/2}_{y_{i+1/2,j,k+1/2}}) - \Delta t \frac{2\omega_0}{\sigma} J_x, \quad (13)$$

$$E^{n+1}_{y_{i,j+1/2,k}} = E^{n}_{y_{i,j+1/2,k}} + \Delta t \frac{2\omega_0}{\sigma} (\partial^-_z H^{n+1/2}_{x_{i,j+1/2,k+1/2}} - \partial^-_x H^{n+1/2}_{z_{i+1/2,j+1/2,k}}) - \Delta t \frac{2\omega_0}{\sigma} J_y, \quad (14)$$

$$E^{n+1}_{z_{i,j,k+1/2}} = E^{n}_{z_{i,j,k+1/2}} + \Delta t \frac{2\omega_0}{\sigma} (\partial^-_x H^{n+1/2}_{y_{i+1/2,j,k+1/2}} - \partial^-_y H^{n+1/2}_{x_{i,j+1/2,k+1/2}}), \quad (15)$$

$$H^{n+1/2}_{x_{i,j+1/2,k+1/2}} = H^{n-1/2}_{x_{i,j+1/2,k+1/2}} - \frac{\Delta t}{\mu} (\partial^+_y E^{n}_{z_{i,j,k+1/2}} - \partial^+_z E^{n}_{y_{i,j+1/2,k}}), \quad (16)$$

$$H^{n+1/2}_{y_{i+1/2,j,k+1/2}} = H^{n-1/2}_{y_{i+1/2,j,k+1/2}} - \frac{\Delta t}{\mu} (\partial^+_z E^{n}_{x_{i+1/2,j,k}} - \partial^+_x E^{n}_{z_{i,j,k+1/2}}), \quad (17)$$

$$H^{n+1/2}_{z_{i+1/2,j+1/2,k}} = H^{n-1/2}_{z_{i+1/2,j+1/2,k}} - \frac{\Delta t}{\mu} (\partial^+_x E^{n}_{y_{i,j+1/2,k}} - \partial^+_y E^{n}_{x_{i+1/2,j,k}}), \quad (18)$$

where $\mathrm{e_x}(\mathrm{i,j,k})'$, $\mathrm{e_y}(\mathrm{i,j,k})'$, and $\mathrm{e_z}(\mathrm{i,j,k})'$ are the electric fields in the three directions, x, y, and z, in the fictitious wave field, respectively; $\mathrm{h_x}(\mathrm{i,j,k})'$, $\mathrm{h_y}(\mathrm{i,j,k})'$, and $\mathrm{h_z}(\mathrm{i,j,k})'$ are the magnetic fields in the x, y, and z directions in the fictitious wave field; and Δt' is the time step in the fictitious wave field. $\partial^+_{x,y,z}$ is the forward derivative operator, $\partial^-_{x,y,z}$ is the backward derivative operator.

During the process of solving the equations, we need to pay attention to σ, which is the average conductivity of adjacent grids. In this paper, the current source is used to simulate the emission source of the time-domain electromagnetic method; therefore, the magnetic current source can be set to zero.

B. Fast iterative time step method

When using variable time steps for the 3D electromagnetic numerical calculation for shallow water, as time increases, the step size increases, resulting in a long calculation time that is not conducive to efficiency. Therefore, in the fictitious wave field, the variable time step expression is re-determined incorporating the electromagnetic response speed in seawater as follows:

$$\Delta t' = \frac{\Delta x}{\sqrt{3} C_{\max}}. \quad (19)$$

We assume the resistivity isotropic is equal to $\rho(\mathrm{x})$, where $C(x)_{max} = \sqrt{\frac{2\omega_0 \rho(x)_{max}}{\mu}}$ is the maximum propagation velocity of the signal in seawater and Δx is the minimum spacing length in the mesh. The maximum time required for the signal to reach the Rmax (offset distance) in the fictitious wave field is as follows:

$$T_{\max} = \frac{R_{\max}}{C_{\min}}, \quad (20)$$

where $R_{\max}$ and $C_{\min}$ are the maximum distance between the transmission and reception and the minimum electromagnetic wave propagation speed, respectively.

The number of iteration steps in the fictitious wave field is expressed as follows:

$$N_t = \frac{T^{\max}}{\Delta t} = \frac{\sqrt{3} R_{\max}}{\Delta \mathrm{x}} \times \sqrt{\frac{\rho_{\max}}{\rho_{\min}}}, \quad (21)$$

where $\rho_{\max}$ and $\rho_{\min}$ are the maximum resistivity and minimum resistivity, respectively; Δx is the minimum spacing length in the grid; and Rmax is the maximum distance between transmission and reception.

The computational efficiency of the time step in the diffusive and fictitious wave fields can be compared by using the time step calculation formula in the diffusive field as follows:

$$\Delta t = \alpha \sqrt{\frac{\mu \sigma^{\min} t}{6}} \Delta x, \quad (22)$$

where α is 0.1–0.2, $\sigma^{\min}$ is the minimum conductivity, and t is the length of time determined according to the selected initial moment. We use an evenly spaced half-space model for testing. The grid size is set to 100 m; the conductivity is 10, 50, and 100 S/m; and the transceiver distance is 10,000 m. The computer used for this test is configured with an i7-7700 CPU and 32.0 GB of RAM. The iteration time step and number of iterations are listed in Table 1.

Table 1: Comparison of computational efficiency between the fictitious wave domain FDTD (finite difference time domain) and traditional FDTD

	FDTD		**FWD-FDTD**	
Half Space Resistivity	Iteration Steps	Calculation Time	Iteration Steps	Calculation Time
$\sigma = 10 S/\mathrm{m}$	2933	1552 s	302	160 s
$\sigma = 50 S/\mathrm{m}$	6556	3269 s	675	346 s
$\sigma = 100 S/\mathrm{m}$	9266	4246 s	954	447 s

Comparison of the computational efficiency of the fictitious wave domain finite-difference time domain (FWD-FDTD) and the traditional FDTD indicates that the FDTD iteration step is positively correlated with conductivity: as conductivity increases, the number of iteration steps gradually increases. However, in the fictitious wave field, the increase in the number of iteration steps is smaller than that in the diffusive field. The number of iterations is reduced by more than 9 times in the fictitious wave field because the ratio of the maximum and minimum conductivity determines the speed of the iterative calculation in the fictitious domain; in the diffusive domain, the number of iteration steps depends only on the minimum conductivity, and the calculation time depends on the change in conductivity. As the conductivity increases, the calculation time also increases; however, in the fictitious domain, the time is increased by more than 9 times, and a fast calculation is realized.

IV. PARAMETRIC ANALYSIS FOR SEAWATER AND AIR LAYERS IN SHALLOW WATER

A. Influence of the seawater layer thickness

In this section, we use a three-layer model comprising air, seawater, and seabed to analyse the influence of seawater depth on the electric field. The air conductivity is 10-10 S/m, the seawater conductivity is 3.3 S/m, and the submarine conductivity is 0.1 S/m. Values of 0, 200, 400, and 1200 m are used for the seawater thickness. The electric field response curve is shown in Fig. 1.

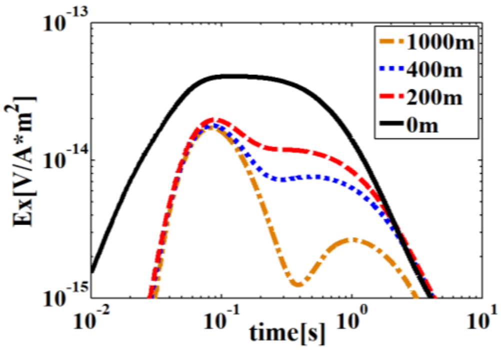

Fig. 1. Influence of seawater thickness.

The black, red, blue, and yellow response curves in Fig. 1 represent seawater thicknesses of 0, 200, 400, and 1200 m, respectively. The figure shows that as the thickness of the seawater decreases, the air wave interference becomes more pronounced, and the response attributable to the direct wave decreases. When the thickness of the seawater approaches zero, only the air wave exists during the early stages. Thus, in shallow water areas, the peak of the direct wave is not obvious due to interference from air waves. It can be concluded that the response of the air and the seawater cannot be considered negligible in shallow water areas. During the actual detection process, the presence of air waves is real and inevitable. When the FWD-FDTD method is used to simulate the air wave, its influence is mainly concentrated during the early stages, while the influence of the high-resistance and low-resistance anomalies is mainly concentrated during the late stages. Therefore, the influence of the air can be eliminated by choosing an appropriate time point.

B. Optimization of the air layer model

In the diffusion field, the number of iteration steps is proportional to the minimum conductivity; air has a low conductivity. If the air is directly divided, it will lead to a large increase in the number of iteration steps. The calculation of the air layer is typically avoided by means of upward continuation, but the accuracy of the early calculations is significantly reduced. In the fictitious wave field, the number of iteration steps depends on the ratio of the maximum and minimum conductivity and does not depend on a fixed number. Thus, the high-resistance air layer can be directly divided and calculated. In this study, the air layer is divided into a non-uniform grid with the Cartesian coordinate system, as shown in Fig. 2. During the modelling process, we need to pay attention to the selection of the air layer conductivity. The real air layer conductivity tends to be infinitesimal. If the conductivity is too large, it will not represent the actual situation. If the conductivity is too small, it will increase the calculation efficiency. Considering the calculation efficiency of the fictitious wave field, the air layer conductivity in this paper is 10^{-10} S/m.

The z axis is positive, assuming that the conductivity and permeability are constant within each prism. The Courant-Friedrichs-Lewy (CFL) limitation is employed as the stability condition in the fictitious wave domain as follows: $\Delta t \le \dfrac{1}{c_{\max}\sqrt{\dfrac{1}{\Delta x^2}+\dfrac{1}{\Delta y^2}+\dfrac{1}{\Delta z^2}}}$.

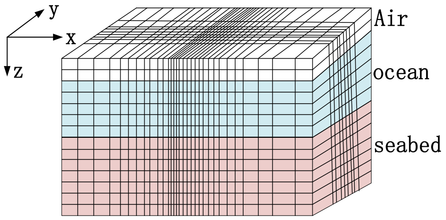

Fig. 2. Air layer grid diagram.

V. LIMITED LENGTH WIRE SOURCE LOADING IN SHALLOW WATER TRANSIENT ELECTROMAGNETIC MEASUREMENT

A. Pulse emission excitation source loading

In shallow water, the source is near the sea–air interface and will be disturbed by air; thus, the initial time will be difficult to determine. Thus, loading the initial field is no longer applicable. Furthermore, in reality, the excitation source of a marine electromagnetic measurement system is a pulse or trapezoidal wave, not a step wave. To solve the problem of complex excitation source loading, we directly load the source in the fictitious wave field. This loading process can be decomposed into two steps.

First, it is necessary to select the basic emission current signal of the excitation source according to the point source Green function expression, $G_E(\omega) = \frac{E_r(\omega)}{J_s(\omega)}$. An important principle to be followed is that the zero-frequency component of the emission current signal is not zero. The second step is to convert the fictitious into the actual emission current signal. The fictitious emission source is different from the actual; it does not have any real meaning. There is a proportional integral relationship between the two that can be used to convert between the fictitious and actual emission sources.

When using the transient electromagnetic method for shallow water, a pulse source provides a higher resolution than that of a step source [10]. The first derivative of a Gaussian source is thus selected as follows:

$$T_{\max} = \frac{R_{\max}}{C_{\min}}, \tag{23}$$

where $f^2_{\max}$ is the maximum frequency of the electromagnetic field transmission in the fictitious wave field and $\beta = \pi f^2_{\max} t_0 = \pi / f_{\max}$.

We choose the first derivative of a Gaussian as a fictitious source. It is dimensionless and not real, as follows:

$$J_{\mathrm{n}}(\omega) = 2\omega_0 e^{\frac{-i\omega\omega_0}{2\beta_0}} e^{-\sqrt{\omega\omega_0} t_0} e^{\sqrt{\omega\omega_0} t_0}. \tag{24}$$

If $\omega = 0$, formula (24) provides the current density as $\mathrm{J}_{\mathrm{n}}(\omega) = 2\omega_0$; thus, the principle that the zero-frequency component is not zero is satisfied. The loading mode and emission signal waveform in the fictitious wave field are shown in Figs. 3 and 4. When loading the emission current signal, it is necessary to ensure that the fictitious emission current has an independent direction. The fictitious emission source current is consistent with the direction and density distribution of the real current. In this paper, the electric source excitation ensures that the z-direction electric field component of the fictitious source is zero.

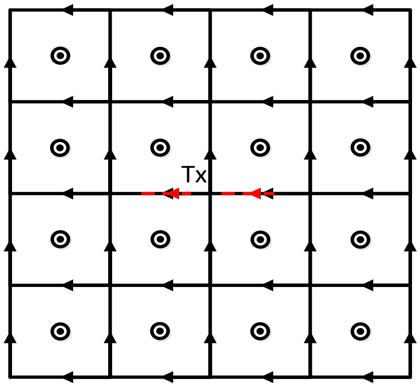

Fig. 3. Long wire source loading method.

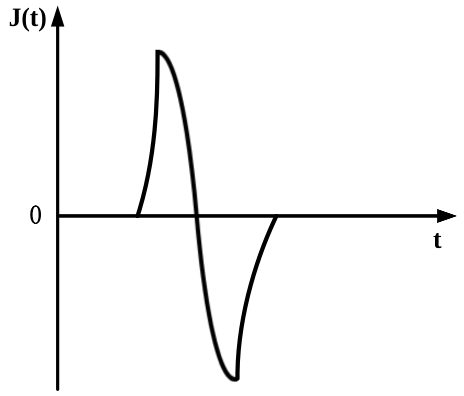

Fig. 4. Source waveform.

B. Analysis of the influence of the launch source wire length

In marine numerical simulations, the source is often approximated to an electric dipole [11], ignoring the source length. Because of geographical terrain and other constraints, the observation point and the emission source in actual ocean exploration often do not meet the appropriate conditions to assume this. Therefore, the electromagnetic response of a finite-length source needs to be calculated. This study examines the influence of the field source length by calculating the electric field response under different wire length excitations. The three-dimensional model is shown in Fig. 5. The air layer has a conductivity of 10^{-10} S/m, and the seawater layer has a conductivity of 3.3. S/m and a thickness of 200 m. The conductivity of the sea bottom layer is 0.1 S/m. A high-resistance body with a conductivity of 0.01 S/m is placed at a distance of 100 m from the seabed. The electromagnetic response is then calculated for a 200-, 400-, and 1000-m-long wire source. The resulting electric field response curves are shown in Fig. 6.

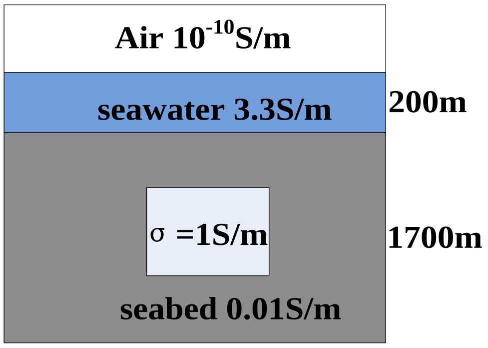

Fig. 5. Three-dimensional high-resistance model.

With an increase in the wire source length, the amplitude of the response also increases. There is a significant change in the response of the anomaly during the late stages. When the distance between the transmission and reception is 2000 m, a wire source 200 and 400 m in length can be approximated as a point source; however, during the actual detection process, the basic characteristics of a point source cannot be satisfied in many cases. Thus, the length of the source needs to be fully considered in the three-dimensional numerical simulation.

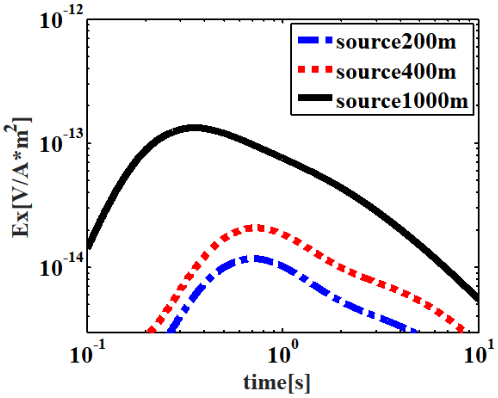

Fig. 6. Electric field response curves for different wire lengths.

C. Loading the CFS-PML boundary conditions in the fictitious wave field

The perfectly matched layer (PML) has been able to absorb the electromagnetic wave in the FDTD [12]. Roden proposes a convolutional PML (CFS-PML) based on PML and recursive convolution [13].

CFS-PML is widely used because of its good absorption effect and savings in computational memory. Hu applied CFS-PML to the solution of a wave equation in a fictitious wave domain, which improved the absorbing effect of the boundary on evanescent and low frequency waves [14]. To improve the calculation efficiency, this paper uses CFS-PML as a boundary condition to absorb the electromagnetic wave.

Taking the X direction as an example, in this coordinate space, we use Maxwell's curl equations as follows:

$$\nabla_s \times \mathrm{H}'(\omega') + \mathrm{i}\omega'\varepsilon'\mathrm{E}'(\omega') = 0\,, \tag{25}$$

$$\nabla_s = \frac{1}{\hat{\mathrm{s}}_x}\frac{\partial}{\partial \mathrm{x}}\mathrm{i} + \frac{1}{\hat{\mathrm{s}}_y}\frac{\partial}{\partial \mathrm{y}}\mathrm{j} + \frac{1}{\hat{\mathrm{s}}_z}\frac{\partial}{\partial \mathrm{z}}\mathrm{k}\,, \tag{26}$$

where $\hat{\mathrm{s}}_x$, $\hat{\mathrm{s}}_y$, $\hat{\mathrm{s}}_z$ is the nondimensional stretching variable, $\hat{\mathrm{s}}_i = \mathrm{k}_i + \dfrac{\sigma_i}{\alpha_i + \mathrm{i}\omega\varepsilon'}(i = x, y, z)$; $\sigma_i(i = x, y, z)$ is the conductivity of the CFS-PML layers; and k_i and α_i are the positive real numbers $\alpha_i > 0$, $\sigma_i > 0$, and $\mathrm{k}_i \geq 1$. When the $k_i = 1$ and $\alpha_i = 0$, it will degenerate into the original PML boundary condition.

Taking the E'_x direction as an example, from equations (25) and (26), we can obtain the following:

$$\mathrm{i}\omega'\varepsilon'\mathrm{E}'_x(\omega') = -\left(\frac{1}{\hat{\mathrm{s}}_y}\frac{\partial \mathrm{H}'_z(\omega')}{\partial \mathrm{y}} - \frac{1}{\hat{\mathrm{s}}_z}\frac{\partial \mathrm{H}'_y(\omega')}{\partial \mathrm{z}}\right). \tag{27}$$

Using Laplace transform, from formula (29), the iterative expression of E'_x can be obtained as follows:

$$\begin{aligned} E'^{\,n+1}_{x_{i+1/2,j,k}} &= E'^{\,n}_{x_{i+1/2,j,k}} + \Delta t' \frac{2\omega_0}{\sigma}[\partial_y^{-1} H'^{\,n+1/2}_{z_{i+1/2,j+1/2,k}} - \partial_z^{-1} H'^{\,n+1/2}_{y_{i+1/2,j,k+1/2}}] + \\ &\Delta t' \frac{2\omega_0}{\sigma}(\Psi^{n+1/2}_{e_{xy_{i+1/2,j,k}}} - \Psi^{n+1/2}_{e_{xz_{i+1/2,j,k}}}), \end{aligned} \tag{28}$$

$$\Psi^{n+1/2}_{e_{xy_{i+1/2,j,k}}} = b_y \Psi^{n-1/2}_{e_{xy_{i+1/2,j,k}}} + a_y (H'^{\,n+1/2}_{z_{i+1/2,j+1/2,k}} - H'^{\,n+1/2}_{z_{i+1/2,j-1/2,k}}) / \Delta_y\,, \tag{29}$$

$$\Psi^{n+1/2}_{e_{xz_{i+1/2,j,k}}} = b_z \Psi^{n-1/2}_{e_{xz_{i+1/2,j,k}}} + a_z (H'^{\,n+1/2}_{y_{i+1/2,j+1/2,k}} - H'^{\,n+1/2}_{y_{i+1/2,j-1/2,k}}) / \Delta_z\,. \tag{30}$$

VI. NUMERICAL CALCULATION OF THE ELECTROMAGNETIC RESPONSE OF A COMPLEX MODEL IN SHALLOW WATER

A. Algorithm verification

We verify the algorithm by considering a classic layered model with a seawater depth of 300 m and resistivity ρ=0.3 Ω·m, as shown in Fig. 7. Two values are used for the distance between the receiver and transmitter: 1000 and 1100 m. The calculated results are compared to those of [7] as shown in Fig. 8. The calculation results plotted in Fig. 8 indicate that the electromagnetic response curve is consistent at the different offsets.

To further validate the algorithm, we evaluate its validity for complex three-dimensional geological conditions by using the three-dimensional complex geological models presented by [6] for comparative analysis. The model settings are shown in Fig. 9. The air conductivity is 10^{-10} S/m, and the background conductivity is 0.02 S/m. There is a mountain and valley to the left and right of the transmitting source, Tx is the transmitting source position, and Rx is the receiving source position. The electric field response is shown in Fig. 9, and the relative error is shown in Fig. 10.

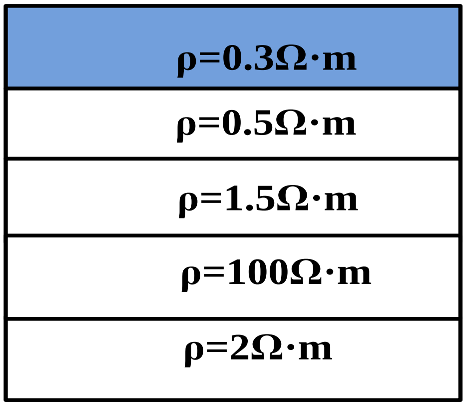

Fig. 7. Shallow water high-resistivity layered model.

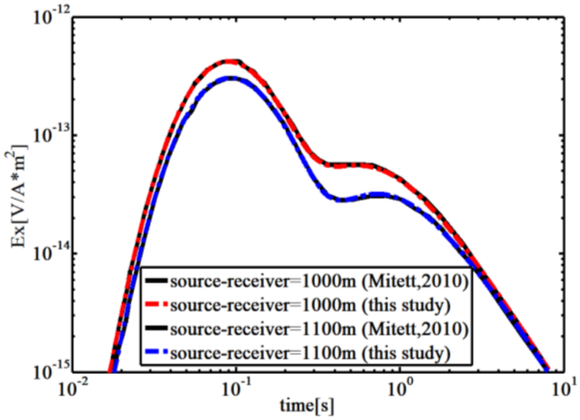

Fig. 8. Response curve of the layered model.

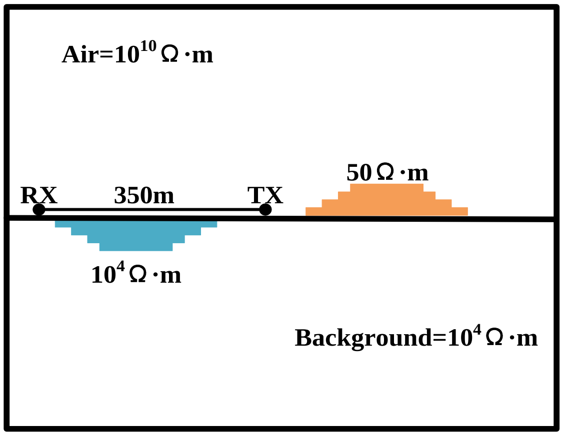

Fig. 9. 3D complex geological model.

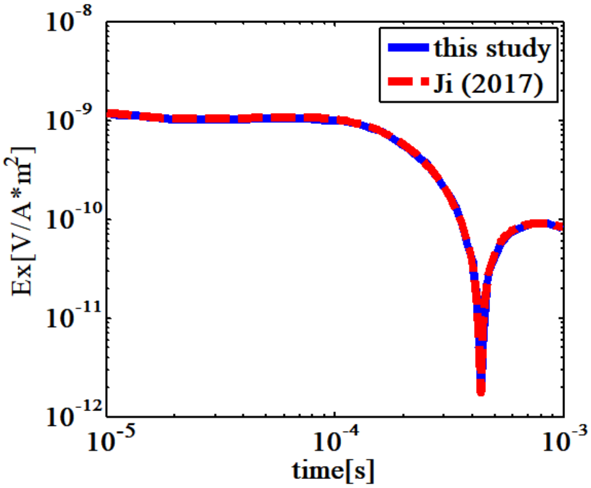

Fig. 10. Comparison of the electric field response at the R_{X1} receiving position.

Figure 10 shows that the response curve and results of [6] are basically consistent for undulating terrain, which supports the validity of the present method for such terrain.

B. Multi-object model in shallow water

The 3D transient electromagnetic response of shallow anomalies was analysed by designing a layered earth model with 3D anomalous bodies as shown in Fig. 11. The grid dimensions are 100×100×70, the air layer thickness is 2000 m, the air conductivity is 10^{-10} S/m, the seawater layer thickness is 100 m, the low-resistance layer beneath the sea is 300 m thick, the conductivity of the low-resistance layer is 1 S/m, and the conductivity of the seabed layer is 0.1 S/m. There are three abnormal bodies that have an electrical conductivity of 30 S/m. The electric field response is shown in Fig. 12. Figures 13 (a) and (b) show profile views of the induced current in the fictitious wave field.

Figure 13 clearly shows the positions of the high-resistance layer and anomalous bodies. Under the influence of the high-resistance layer, the propagation direction of the electromagnetic wave no longer symmetrically propagates. The overall trend of the curve is similar to that of the layered model. For the responses of the air and sea layers, the response of the anomalous body occurs during a late stage.

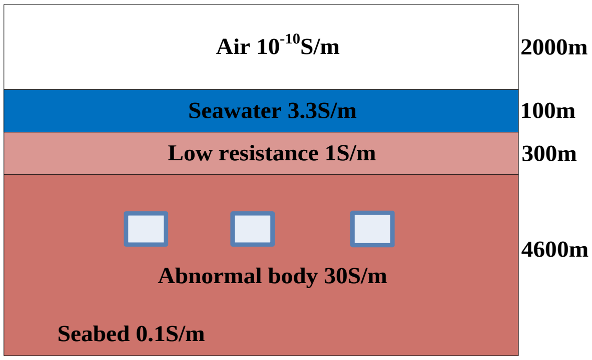

Fig. 11. 3D low-resistance complex model.

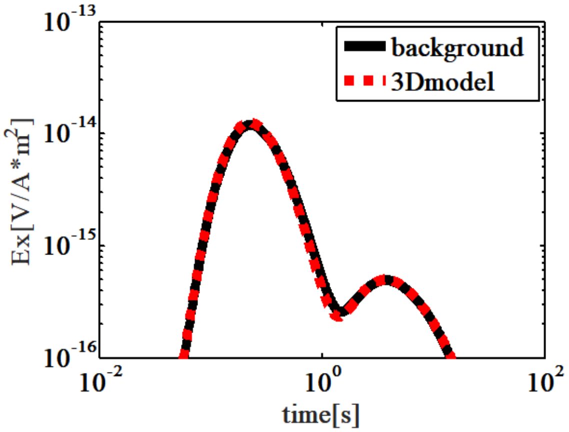

Fig. 12. Response curve of the three-dimensional model.

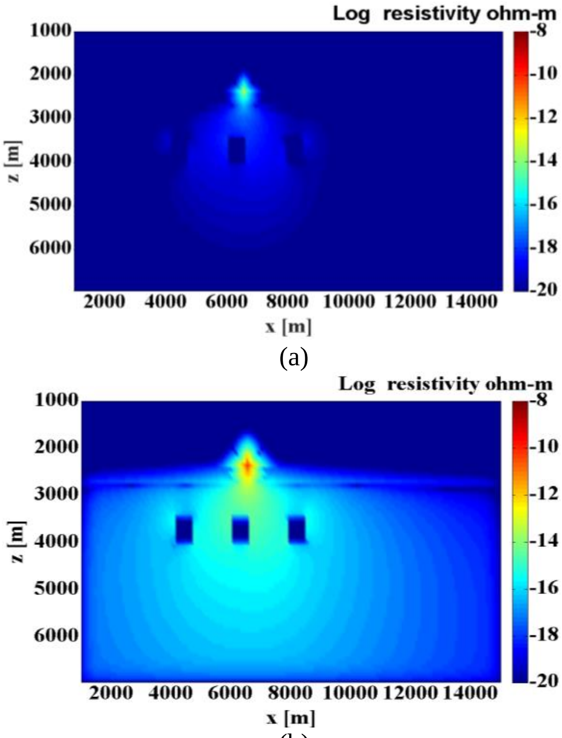

(a)

(b)

Fig. 13. Snapshots of the induced current system in the fictitious wave field (y direction 2000 m).

C. High-resistance model of complex terrain in shallow water

Complex terrain environments were simulated by designing a 3D model, as shown in Fig. 14. Tx represents the source location, which is 200 m in length. Rx represents the receiving point. The transmission and reception distance is 600 m, the seawater layer resistivity is 0.3 Ω·m, and the sea bottom resistivity is 0.5 Ω·m. There is convex and concave topography on the left and right sides of the emission source, the seawater layer is 200 m in thickness, and the thickness of the rock layer beneath the sea is 800 m.

The results for the calculated response are shown in Fig. 15. The response of a high-resistance anomaly under the undulating terrain is blue, whereas that of pure undulating terrain is red. To better analyse the influence of the undulating terrain, Figs. 16 (a) and (b) show snapshots of the induced current system in the fictitious wave field at different times.

The seabed topography can be clearly seen in Fig. 16. The peaks and valleys are, respectively, located on the left and right sides of the transmission source, and there is a high-resistance anomaly on the seabed. Because of the influence of the topography, the response curve has significantly changed, and the electric field response can be seen during the early and late stages, confirming the necessity of simulating the terrain. In the fictitious wave field, the change in the transmission source is clearer than that in the diffusion field. Therefore, the generated induced current will more violently fluctuate. The means by which the electromagnetic field is transmitted is changed by undulating the submarine terrain such that it no longer symmetrically spreads. The influence of undulating terrain on the response curve is mainly concentrated during the early stages, whereas the response of the three-dimensional anomaly on the seabed is mainly concentrated during the late stages. Therefore, undulating terrain cannot be ignored in a shallow-sea ocean transient electromagnetic simulation.

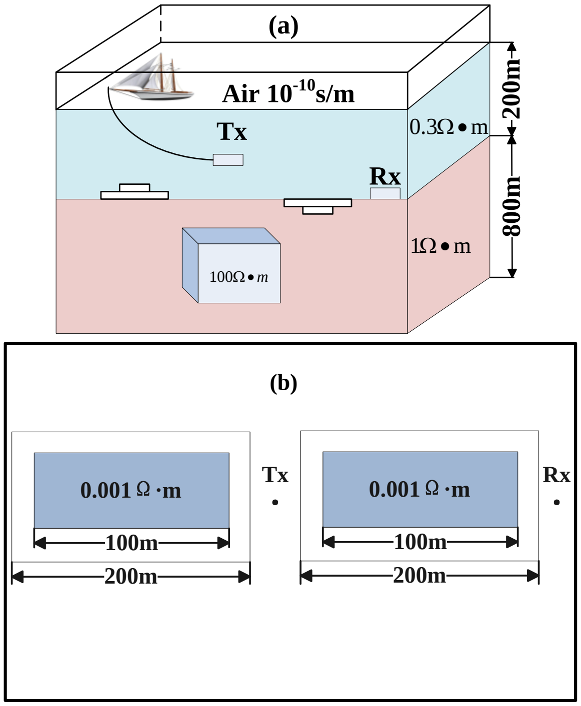

Fig. 14. Schematic diagram of undulating terrain: (a) front view and (b) top view.

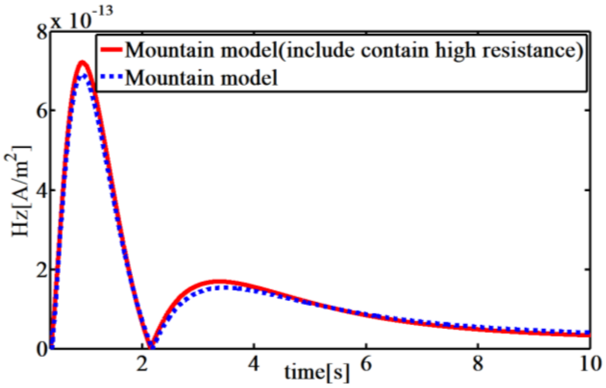

Fig. 15. Electromagnetic response for complex seabed geomorphology, including a high-resistance anomaly.

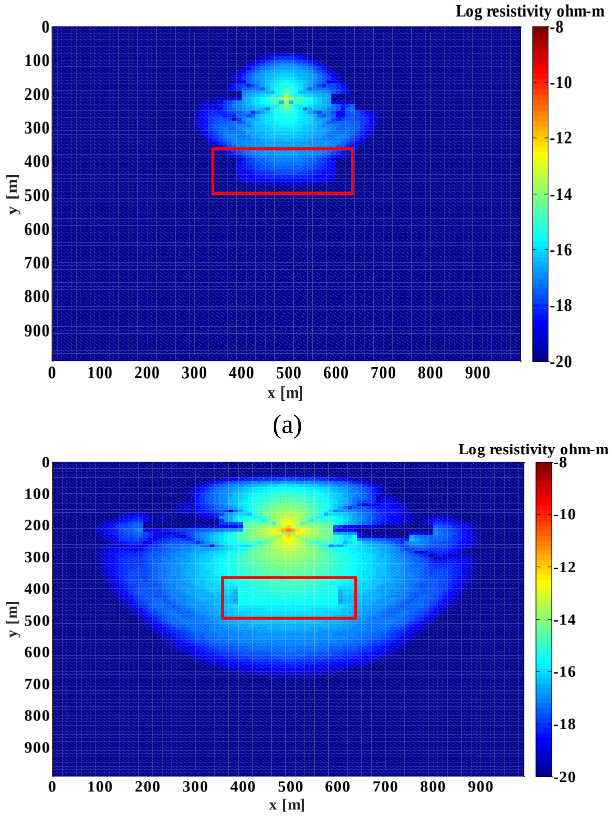

(a)

(b)

Fig. 16 Snapshots of the induced current system of undulating terrain in the fictitious wave field (y direction 2000 m).

V. CONCLUSION

We propose a new, fast method for shallow water three-dimensional electromagnetic forward modelling. The method is based on the correspondence between the diffusive and fictitious wave fields and can be applied to the forward calculation of undulating terrain in shallow water. The efficiency of electromagnetic numerical calculation is improved by defining the iteration time step size formula in the fictitious wave field. When the depth of the seawater layer or the anomalous body is shallow, there is a non-negligible response from the air and seawater layers. Using a pulse source signal in the governing equation allows direct calculations incorporating the source to be realized, in turn enabling three-dimensional electromagnetic numerical simulation of complex terrain. The complexity of the seabed topography affects the normal propagation of the electromagnetic wave, which greatly influences the resolution of shallow abnormal bodies. Forward simulation is the basis of data interpretation and imaging. In this paper, a shallow water 3D numerical simulation is realized, including the air layer and undulating terrain, which makes the simulation results more closely match the real geological conditions. It can not only provide a basis for the exploration of underwater resources but also theoretical guidance for detection instrument design.

Given the scarcity of terrestrial resources, countries around the world have increased their demand for offshore seabed and deep seabed energy. The marine transient electromagnetic method can play an important role in marine resource detection. Although this paper realizes three-dimensional forward modelling of shallow waters, the distribution of geological structures and resources in the seabed is extremely complicated; their detection is made more challenging because of the polarization of seawater in ocean electromagnetic detection. Therefore, further research is necessary to study the electromagnetic and polarization responses in complex geological models.

ACKNOWLEDGMENT

We thank editor and an anonymous reviewer for constructive suggestions. This work was supported by the National Natural Science Foundation of China (Grant Number 3A416AQ50537).

REFERENCES

[1] K. M. Strack, T. Hanstein, C. H. Stoyer, et al., “Time domain controlled source electromagnetics for hydrocarbon applications,” 2011.

[2] C. J. Weiss, “The fallacy of the “shallow-water problem” in marine CSEM exploration,” [J]. *Geophysics*, vol. 72, no. 6, pp. A93-A97, 2007.

[3] P. O. Barsukov and E. B. Fainberg, “Transient marine electromagnetics in shallow water: A sensitivity and resolution study of the vertical electric field at short ranges,” *Geophysics*, vol. 79, no. 1, pp. E39-E49, 2014.

[4] Y. G. Li and S. Constable, “Transient electro-magnetic in shallow water: Insights from 1D modeling,” *Chinese Journal of Geophysics*, vol. 53, no. 3, pp. 737-742, 2010.

[5] D. Connell and K. Key, “A numerical comparison of time and frequency-domain marine electro-magnetic methods for hydrocarbon exploration in shallow water,” *Geophysical Prospecting*, vol. 61, no. 1, pp. 187-199, 2013.

[6] Y. Mao, A. Z. Elsherbeni, S. Li, and T. Jiang, “Non-uniform surface impedance absorbing boundary condition for FDTD method,” *Applied Computational Electromagnetics Society Journal*, vol. 33, no. 2, pp. 232-235, 2018.

[7] Y. Inoue and H. Asai, “Efficient electromagnetic simulation including thin structures by using multi-GPU HIE-FDTD method,” *Applied Computational Electromagnetics Society Journal*, vol. 33, no. 2, pp. 212-215, 2018.

[8] Y. Ji, Y. Hu, and N. Imamura, “Three-dimensional transient electromagnetic modeling based on

fictitious wave domain methods," *Pure & Applied Geophysics*, vol. 174, no. 5, pp. 2077-2088, 2017.

[9] R. Mittet, "High-order finite-difference simulations of marine CSEM surveys using a correspondence principle for wave and diffusion fields," *Geophysics*, vol. 75, no. 1, pp. F33-F50, 2010.

[10] A. Avdeeva, M. Commer, and G. A. Newman, "Hydrocarbon reservoir detectability study for marine CSEM methods: Time-domain versus frequency-domain," *Seg. Technical Program Expanded Abstracts*, vol. 26, no. 1, p. 3124, 2007.

[11] S. Constable, "Review paper: Instrumentation for marine magnetotelluric and controlled source electromagnetic sounding," [J]. *Geophysical Prospecting*, vol. 61, pp. 505-532, 2013.

[12] J. P. Berenger, "A perfectly matched layer for the absorption of electromagnetic waves," [M]. *Academic Press Professional, Inc*., 1994.

[13] J. A. Roden and S. D. Gedney. "Convolution PML (CPML): An efficient FDTD implementation of the CFS–PML for arbitrary media," *Microwave and Optical Technology Letters*, vol. 27, no. 5, 2000.

[14] Y. Hu, G. Egbert, Y. Ji, et al., "A novel CFS-PML boundary condition for transient electromagnetic simulation using a fictitious wave domain method," *Radio Science*, vol. 52, no. 1, pp. 118-131, 2017.

Yanju Ji in 1997, graduated from Changchun University and received a master's degree. Graduated from Jilin University in 2004, majoring in Earth Exploration and Information Technology and received a doctorate degree. The main research direction is time domain electromagnetic theory and detection technology.

Xiangdong Meng graduated from Jilin University of Architecture in 2015, majoring in Industrial Design Engineering and received a Master's degree. In 2016, studying in Jilin University for a Ph.D. The main research area is three-dimensional numerical simulation of transient electromagnetic in time domain.

Guiying Ren graduated from Jilin University in 2017 and received a bachelor's degree. In 2017, studying in Jilin University for a master's degree. The main research area is three-dimensional numerical simulation of transient electromagnetic in time domain.

Near-Field Analysis and Design of Inductively-Coupled Wireless Power Transfer System in FEKO

Dowon Kim, Adrian T. Sutinjo, and Ahmed Abu-Siada

Department of Electrical and Computer Engineering
Curtin University, Bentley, Perth Western Australia 6102, Australia
dowon.kim@postgrad.curtin.edu.au, adrian.sutinjo@curtin.edu.au, and a.abusiada@curtin.edu.au

Abstract ─ Inductively-coupled wireless power transfer (WPT) system is broadly adopted for charging batteries of mobile devices and electric vehicles. The performance of the WPT system is sensitively dependent on the strength of electromagnetic coupling between the coils, compensating topologies, loads and airgap variation. This paper aims to present a comprehensive characteristic analysis for the design of the WPT system with a numerical simulation tool. The electromagnetic field solver FEKO is mainly used for studying high-frequency devices. However, the computational tool is also applicable for not only the analysis of the electromagnetic characteristic but also the identification of the electrical parameters in the WPT system operating in the near-field. In this paper, the self and mutual inductance of the wireless transfer windings over the various airgaps were inferred from the simulated *S*-parameter. Then, the formation of the magnetic coupling and the distribution of the magnetic fields between the coils in the series-parallel model were examined through the near-field analysis for recognizing the efficient performance of the WPT system. Lastly, it was clarified that the FEKO simulation results showed good agreement with the practical measurements. When the input voltage of 10 V was supplied into the transmitting unit of the prototype, the power of 5.31 W is delivered with the transferring efficiency of 97.79% in FEKO. The actual measurements indicated 95.68% transferring efficiency. The electrical parameters; V_{in}, V_{out}, Z_{in}, θ, I_{in}, and I_{out}, had a fair agreement with the FEKO results, and they are under 8.4% of error.

Index Terms ─ Compensation topology, FEKO, inductive power transfer, near-field analysis, magnetic coupling, wireless power transfer design.

I. INTRODUCTION

The principle of wireless power transfer (WPT) was introduced a century ago by N. Tesla [1]. He suggested that electric energy can be delivered through free space efficiently when the resonance frequency is well-tuned between the transmitting (*Tx*) and receiving (*Rx*) coil by the compensating capacitors, and modern inductively-coupled WPT systems are based on his practical model [2]. As the demands of mobile devices and electric vehicles (EVs) increase, the WPT system is broadly adopted for charging their batteries simply and safely [3-6]. WPT methods are classified into a non-radiative (also known as near-field) and radiative (also known as far-field or microwave) application. In general, the non-radiative WPT system employs the resonant coupling phenomenon between the transmitter and receiver, and it also categorized into an inductively and capacitively-coupled method [3, 7]. The capacitively-coupled WPT is used for the biomedical device and EV charging apparatus [8, 9]. However, the inductively-coupled method is widely used for the high power and the power transfer applications in the range from millimeters to a few meters [10, 11]. In this paper, WPT is used to refer to inductively-coupled WPT.

For the optimized design of the WPT device, it is essential to analyze both electromagnetic phenomena (i.e., magnetic field and coupling between the coils) and electrical components (i.e., inductance and transferred power) prior to the practical implementation. FEKO is the electromagnetic field solver [12], and it is mainly employed for analyzing radio frequency components, antennas and radiations [13-15]. The previous research presented that FEKO is employed to examine the power transfer efficiency of the near-field WPT system in different material between the antennas [16]. The application of FEKO was introduced for analyzing scattering parameter (*S*-parameter), input impedance and wire structure in the range of frequency of 10-11.5 MHz [17], however, the magnetic coupling study was not presented. In addition, the numerical value of the magnetic field between *Tx* and *Rx* of the WPT system were examined over the variation of transfer distance [18, 19]. However, it did not cover the application for the design or analysis of WPT performance, and the simulation tool was utilized for the partial inspection of WPT performance. This paper aims to introduce the comprehensive implementation process of the 20 kHz WPT system using FEKO. The various frequency ranges

Submitted On: January 30, 2019
Accepted On: December 28, 2019

such as 140 kHz, 85kHz, and 20 kHz have been adopted in different regions based on the frequency allocation [20-23]. For reducing the high-frequency loss and the emission of the electromagnetic field, this study conducted in the frequency of 20 kHz.

A WPT system is mainly composed of the high-frequency (HF) source, *Tx* and *Rx* coils, and load unit, as shown in Fig. 1. In the practical WPT device, the HF source is generated by a switching device such as a half or full-bridge inverter, and the load unit has a rectifying device to obtain DC power from the transferred HF source. For accurate analysis of the switching process in the DC/AC or AC/DC circuit, specialized simulation tools are required. However, the HF source and load unit in FEKO can be described on the wire ports, and the inductive coupling behavior in the transferring part can be simulated in the numerical simulation software. Furthermore, the self and mutual inductance of the WPT coils can be extracted from the results of the *S*-parameter, and the transferred power in different load and air-gap are predictable. Accordingly, FEKO provides precise analysis for the formation and distribution of magnetic coupling between the coils. Also, it provides the electrical parameters of the simplified WPT circuit in the wire ports, as shown in Fig. 1.

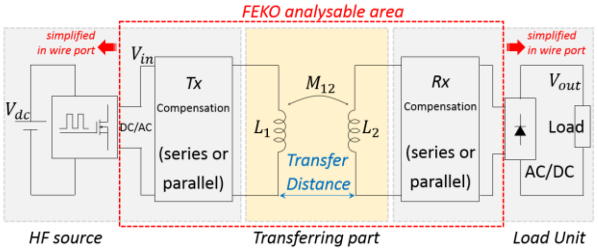

Fig. 1. Inductively-coupled WPT system.

In Section II, it is presented how the self and mutual inductance of the *Tx* and *Rx* coil are identified. Sections III and IV explain the compensating topologies for tuning the resonance frequency, then, the strength of the magnetic coupling over the various airgaps is explored at the resonance frequency of 20 kHz. Consequently, the practical measurements to examine the transferred power, output voltage and other electrical parameters of the WPT prototype are conducted, and the results are compared with the FEKO results in Section V.

II. SELF AND MUTUAL INDUCTANCE OF COILS

The traditional transformer can be described as a two-port network, as indicated in Fig. 2, and the impedance parameter (*Z*-parameter) in the network is convertible to the *S*-parameter [24]. Therefore, the self-inductance (L_1 and L_2) and mutual-inductance, M_{12}, constructed in the simulation tool can be inferred from the *S*-parameters. When the voltage source V_{in} with the resistance R_o excites the two-port networks in the *Tx*, the impedance matrix is expressed in (1), and the self and mutual impedance of coils are determined through (2) and (3):

$$\begin{bmatrix} V_{in} \\ 0 \end{bmatrix} = \begin{bmatrix} R_o + j\,\omega L_1 & j\,\omega M_{12} \\ j\,\omega M_{12} & R_L + j\,\omega L_2 \end{bmatrix} \begin{bmatrix} I_1 \\ I_2 \end{bmatrix} = \begin{bmatrix} R_o + Z_{11} & Z_{12} \\ Z_{21} & R_L + Z_{22} \end{bmatrix} \begin{bmatrix} I_1 \\ I_2 \end{bmatrix}, \tag{1}$$

$$Z_{11} = Z_{22} = \frac{(R_o + S_{11}R_o)(1-S_{22}) + S_{12}S_{21}R_o}{(1-S_{11})(1-S_{22}) - S_{12}S_{21}}, \tag{2}$$

$$Z_{12} = Z_{21} = \frac{2S_{21}(R_oR_L)^{1/2}}{(1-S_{11})(1-S_{22}) - S_{12}S_{21}}. \tag{3}$$

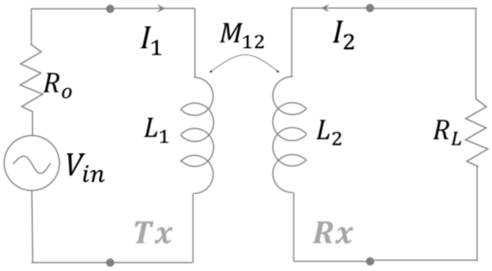

Fig. 2. Traditional transformer model.

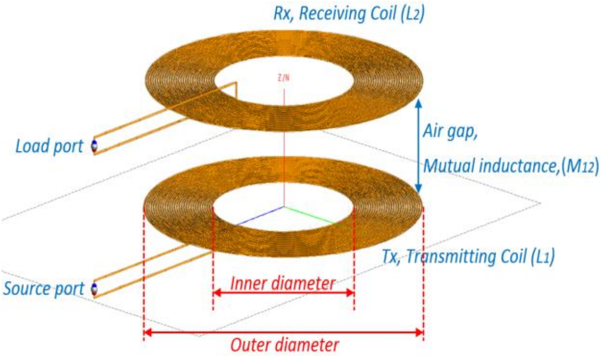

Fig. 3. WPT system model for calculating the self and mutual inductance of coils.

Table 1: Property of the practical coils

Property	Value
Inner Diameter of *Tx* and *Rx*	210 mm
Outer Diameter of *Tx* and *Rx*	400 mm
Number of Turns	30
Type of Wire	Litz-wire 1,650 filaments (0.05 mm diameter)
Radius of Wire	1.5 mm
Parasitic Resistance of Wire	5.962 Ω/km up to 850 kHz
Medium of Space	Air

The planar spiral coil was built to economize the space, as shown in Fig. 3, and the properties of the practical coil are presented in Table 1. The loss caused by the skin effect at 20 kHz was ignored in this study. However, the actual coil was built with 1,650 stranded filaments Litz-wire to secure the versatility for the higher frequency systems. Besides, the WPT system at low frequency can be free from the skin effect. However, the system needs more turns of coils to produce enough magnetic field, and the transferring distance can be decreased at the low frequency because of the low value of the quality factor. For example, the WPT system at the utility frequency of 60 Hz was introduced and The application implemented with the coil of 450 turns [25].

The simulations to obtain the *S*-parameters were conducted in the different transfer distance (10, 55, 100, 150, and 200 mm) over the frequency range from 15 kHz to 25 kHz as shown in Fig. 4. The source R_o and load resistance R_L are set 50 Ω, respectively, during the simulations. The value of self-inductance L_1 and L_2 is constant regardless of the air-gap, and the mutual-inductance M_{12} and the coupling coefficient k_{12} are correctly calculated based on (4) and (5). The coils in the simulation were constructed by the copper wire. It was also found that the inductance values present repetitively in the various frequency range,

$$L_1 = \frac{|Z_{11}|}{\omega}, L_2 = \frac{|Z_{22}|}{\omega}, \tag{4}$$

$$M_{12} = \frac{|Z_{12}|}{\omega}, k_{12} = \frac{M_{12}}{\sqrt{L_1 L_2}}. \tag{5}$$

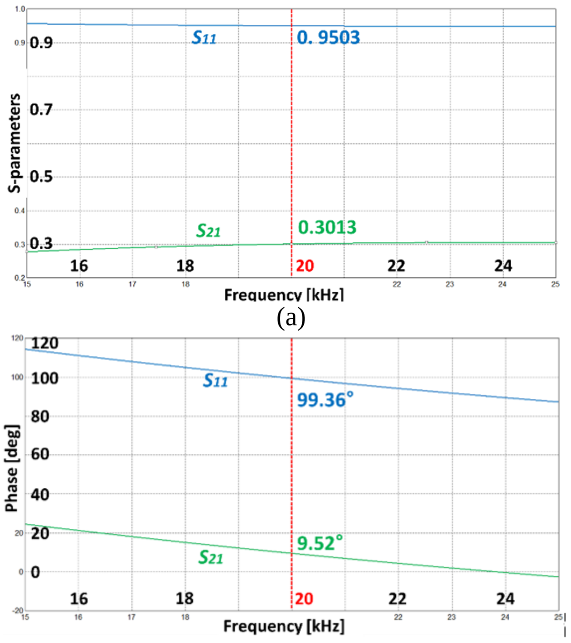

(a)

(b)

Fig. 4. Example of *S*-parameter result at 100 mm air gap: (a) absolute and (b) phase angle.

Table 2: *S*-parameter at 20 kHz

Air-Gap [mm]	S_{11} at 20 kHz		S_{21} at 20 kHz	
	Magnitude	**Phase Angle**	**Magnitude**	**Phase Angle**
10	0.6038	114.71°	0.7929	24.94°
55	0.8719	103.08°	0.4831	13.25°
100	0.9503	99.36°	0.3013	9.52°
150	0.9793	97.94°	0.1870	8.09°
200	0.9896	97.42°	0.1214	7.58°

This work considered the implantation of the WPT system for the charging device at the frequency of 20 kHz. Hence, the magnitude and phase angle of *S*-parameter at the frequency of 20 kHz are shown in Table 2. To verify the accuracy of the FEKO results, the actual inductance value of the built coil was measured by frequency response analyzer (FRA, DOBLE M5300). For reference, the passive electrical parameters; resistance (*R*), inductance (*L*) and capacitance (*C*), in the network can be precisely measured at the various range of frequency up to 2 MHz [26].

The results from the computational calculation in Table 3 are comparable to the experimental value, and the percentage difference of the self-inductance ($\%\Delta L_1$ and $\%\Delta L_2$) and the coupling coefficient ($\%\Delta M_{12}$ or $\%\Delta k_{12}$) is under 0.17% and 3.59%, respectively. Besides, the FEKO result indicated the resistance value of the copper coil by 0.143 Ω whereas the actual value of the parasitic resistance of L_1 and L_2 are 0.49 Ω and 0.48 Ω at 20 kHz, respectively.

III. COMPENSATION FOR RESONANCE

For tuning the resonance frequency in the *Tx* and *Rx* coil, the compensating capacitor can be implemented in mainly four topologies: series-series (*SS*), series-parallel (*SP*), parallel-series (*PS*), and parallel-parallel (*PP*) as shown in Fig. 5. As the *SS* topology as illustrated in Fig. 5 (a) is simple, and the value of the compensating capacitor C_1 at the *Tx* coil is not a function of the air gap and the load impedance, many devices use this WPT system for wireless charging applications [27-29].

However, the transfer efficiency of the *SS* topology decreases significantly when the transfer distance varies [18], and the voltage-source-type *SS* system can damage the power supply when the *Tx* does not have a coupling with the *Rx* unit [30]. Also, the transfer efficiency can be reduced significantly when the two coils are coupled at the nearer distance than the critical distance. It is defined as a frequency bifurcation [31]. To avoid this phenomenon, it might be necessary to adjust the switching frequency, value of compensating capacitance or load resistance [32]. *SP*, *PS*, and *PP* topologies are illustrated in Figs. (b), (c), and (d). They require the precise technique for tuning the resonance frequency [33].

Table 3: Comparison of inductance value between FEKO results and practical measurements

Air Gap [mm]	**Parameters Extracted by FEKO**			**Practical Measurement and Accuracy**						
	L_1, L_2 **[μH]**	M_{12} **[μH]**	k_{12}	L_1 **[μH]**	$\%\Delta L_1$	L_2 **[μH]**	$\%\Delta L_2$	M_{12} **[μH]**	k_{12}	$\%\ \Delta M_{12}$ *or* $\%\Delta k_{12}$
10	351.7	308.5	0.877	352.2	-0.14%	351.1	0.17%	311.4	0.885	-0.91%
55	351.7	175.0	0.498	352.2	-0.14%	351.1	0.17%	175.7	0.500	-0.40%
100	351.7	107.7	0.306	352.2	-0.14%	351.1	0.17%	111.6	0.317	-3.59%
150	351.7	66.6	0.189	352.2	-0.14%	351.1	0.17%	64.9	0.184	2.65%
200	351.7	43.2	0.123	352.2	-0.14%	351.1	0.17%	41.9	0.119	3.25%

The performance degradation due to the frequency bifurcation in these topologies should also be considered. For supplying a sinusoidal HF voltage into the WPT resonant circuit, additional series inductor is required for the *Tx* side in *PS* and *PP* system to filter the harmonics from the square waveform generated by the switching device [34], and the *SS* and *SP* topologies are more suitable for the high power WPT applications [35].

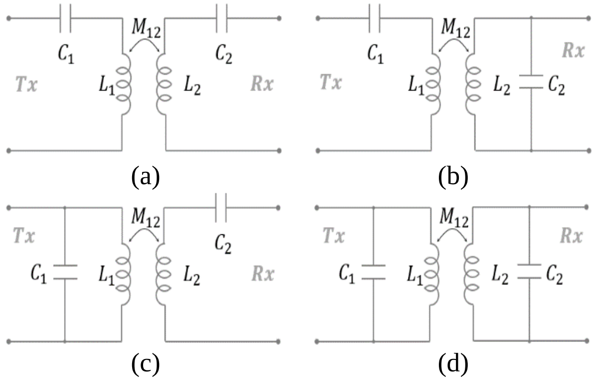

(a) (b)

(c) (d)

Fig. 5. Compensating topologies based on C_1 location: (a) series-series (*SS*), (b) series-parallel (*SP*), (c) parallel-series (*PS*), and (d) parallel-parallel (*PP*).

The input voltage V_{in} across the *Tx* terminals of the *SS* and *SP* topology, as shown in Figs. 5 (a) and (b) is described as in the following equations:

$$V_{in,ss} = Z_{in,ss} I_1 = \left(jX_1 + \frac{\omega^2 M_{12}^2}{R_L + r_1 + jX_2}\right) I_1 \ , \qquad (6)$$

$$V_{in,sp} = Z_{in,sp} I_1 = \left(jX_1 + \frac{\omega^2 M_{12}^2}{j\,\omega L_2 + r_2 + \frac{R_L}{1 + j\,\omega C_2 R_L}} \right) I_1 \ . \qquad (7)$$

Where $X_1 = \omega L_1 - (1/\omega C_1)$, $X_2 = \omega L_2 - (1/\omega C_2)$, and R_L is the load resistance. r_1 and r_2 are the parasitic resistance at *Tx* and *Rx*, respectively. As this prototype aims to achieve maximum power efficiency, it is assumed that the source impedance is zero [36, 37].

In (6) and (7), the equivalent input impedances are $\omega^2 M_{12}^2/R_L$ and $M_{12}^2 R_L/L_2^2$, respectively, when the reactive components are eliminated by C_1 and C_2, and the parasitic resistance is ignored. If the resonance frequency is determined as follows:

$$f_o = \frac{1}{2\pi\sqrt{L_2 C_2}} \ . \qquad (8)$$

The compensating capacitor C_1 in the *SS* and *SP* system, respectively, is as follows:

$$C_{2,sp} = \frac{1}{(2\pi f_o)^2 L_2} \ , \qquad (9)$$

$$C_{1,sp} = \frac{1}{(2\pi f_o)^2 (L_1 - M_{12}^2/L_2)} \ . \qquad (10)$$

It is clarified that the elimination of the imaginary part of the input impedance in the *SS* topology is not affected by the variation of mutual inductance M_{12} or load resistance R_L. On the other hand, the value of the compensating capacitor $C_{1,sp}$ at the *Tx* side must be correctly selected due to the variation of M_{12} which represents the amount of the air gap between the coils.

Also, the compensating topology should be selected with the consideration of the load resistance value. If the load resistance R_L is smaller than the characteristic impedance at *Rx*, *SS* compensating system is beneficial because the input impedance $(\omega^2 M_{12}^2/R_L)$ at the resonance frequency is inversely proportional to load resistance. It means that the WPT system can deliver much power to the input impedance, including the load resistance. The characteristic impedance Z_o is determined in (11), and Z_o of the prototype is about 44 Ω at the frequency of 20 kHz,

$$Z_o = \sqrt{L_2/C_2} \ . \qquad (11)$$

Besides, if the load resistance R_L is higher than the characteristic impedance Z_o, *SP* topology is superior to the *SS* system. Hence, *SS* and *SP* system should not be compared with the identical value of the load resistance. In this study, the near-field analysis in *SP* compensating topology is conducted in this work.

IV. MAGNETIC COUPLING AND FIELD DISTRIBUTION IN NEAR-FIELD

In the previous Sections II and III, the required electrical parameters: L_1, L_2 and M_{12}, were obtained precisely, then the value of the compensating capacitor C_1 and C_2 at the *Tx* and *Rx* side can be calculated based on (9) and (10).

When the *Tx* and *Rx* coil are loosely coupled in the magnetic field at the resonance frequency, the electric energy transfers efficiently through free space [7]. For tuning the resonance frequency of 20 kHz in the simulation models, the compensating capacitor C_2 at the *Rx* side was selected as 180 nF at the self-inductance value of 351 μH on L_2 at the frequency of 20 kHz.

The compensating capacitor C_1 for the *SP* topology should be employed from (10) with respect to the air gap as the mutual inductance M_{12} varies over the transfer distance. The value of the compensating capacitor is independent of the load resistance in the *SP* system. However, the low load resistance and near airgap can cause a frequency bifurcation and efficiency reduction [31]. The compensating capacitors at both *Tx* and *Rx* side were implemented on the wire port and the AC voltage of 10 V_{peak} at 20 kHz was supplied into the *Tx* unit during the simulation. As mentioned earlier, the process of the high-frequency switching is not assessable in FEKO, however, the peak magnitude of the voltage input V_{in} to the *Tx* unit can be extracted by the Fourier series analysis in (12):

$$V_{in} = V_{dc}\, \frac{4}{\pi} \sum_{k=1}^{\infty} \frac{\sin\{(2n-1)\omega t\}}{(2n-1)}\ [\mathrm{V}]\ . \qquad (12)$$

The input voltage V_{in} is generated in the shape of a square waveform by the DC to AC inverter across the terminal of the *Tx* coil. Hence, the sinusoidal waveform of the input voltage; also, it represents the first harmonic of the square waveform, where V_{dc} is the magnitude of the square waveform, and n is the number of harmonics. In the experiments, the square wave voltage of 7.9 V is to be injected into the *Tx* unit, the AC voltage of 10 V is applied for the FEKO simulation based on (12).

Furthermore, the equivalent load resistance R_{eq} can be determined through (13) when the full-bridge rectifier is utilized between the *Rx* unit and the road resistance R_L [38],

$$R_{eq} = \frac{8}{\pi^2} R_L\ [\Omega]. \qquad (13)$$

In the FEKO analysis, the equivalent resistance R_{eq} was set as 97 Ω at the AC output terminals of *Rx* unit. It states that the actual load resistance across the DC output terminal is about 120 Ω. The induced magnetic field in the *Rx* coil by *Tx* coil, strength and distribution of the magnetic field are illustrated in Fig. 7. The simulation results confirm that the efficiency of the WPT system declines when the air gap is over the limit of magnetic coupling range discovered by the simulation result. For reference, this electromagnetic analysis of FEKO was conducted by the student edition.

The level of the magnetic field at both *Tx* and *Rx* coil indicates about 40 A/m and 100 A/m at the 10 mm and 55 mm air gap, respectively as shown in Figs. 7 (a) and (b). At the distance of 100 mm, the amplitude of magnetic field in the *Tx* coil is higher than in the *Rx* coil, but *Rx* coil has the similar amount of the magnetic field in *Tx* coil as shown in Fig. 7 (c). The highest level of the 500 A/m magnetic field is recorded at the 150 mm airgap though the *Rx* coil has the induced magnetic field of 250 A/m as shown in Fig. 7 (d).

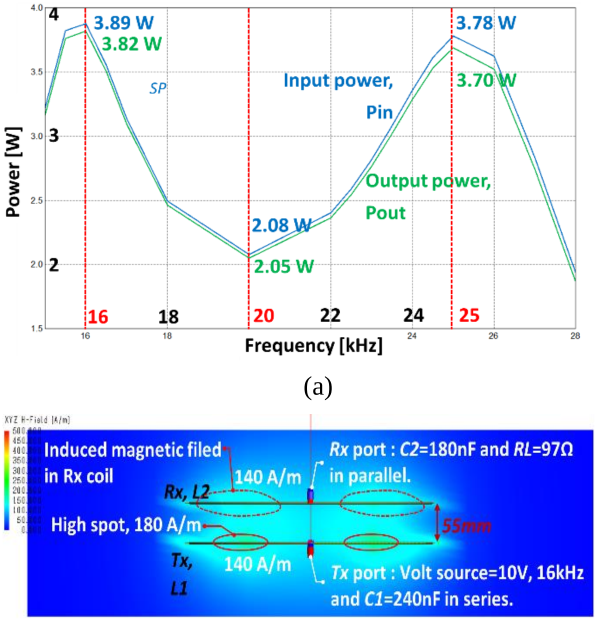

(a)

(b)

Fig. 6. Transferring power and magnetic field distribution in *SP* topology at 55 mm: (a) Supplied power and transferred power across the load, and (b) magnetic coupling at the frequency of 16 kHz.

It is verified that the low magnetic field is formed between the *Tx* and *Rx* coil at the near gap at the frequency of 20 kHz; hence, low power is delivered from the *Tx* unit to the *Rx* unit. It is caused by the phenomena of frequency bifurcation, which occurs when two coils are coupled in the over-coupled region. The FEKO simulation can also clarify the frequency bifurcation. For instance, at the distance of 55 mm, the transferring power is only 2.05 W at 20 kHz, however, at the frequency of 16 kHz and 25 kHz, the power of 3.82 W and 3.70 W is delivered to the Rx unit, respectively as illustrated in Fig 6 (a). Also, the higher magnetic field of 140 A/m at the frequency of 16 kHz than at 20 kHz frequency is formed as shown in Fig. 6 (b) and Fig. 7 (b). To achieve the improved performance of the WPT system at the near distance, it is required to shift the switching frequency or utilize the different value of the compensating capacitor for avoiding the frequency bifurcation.

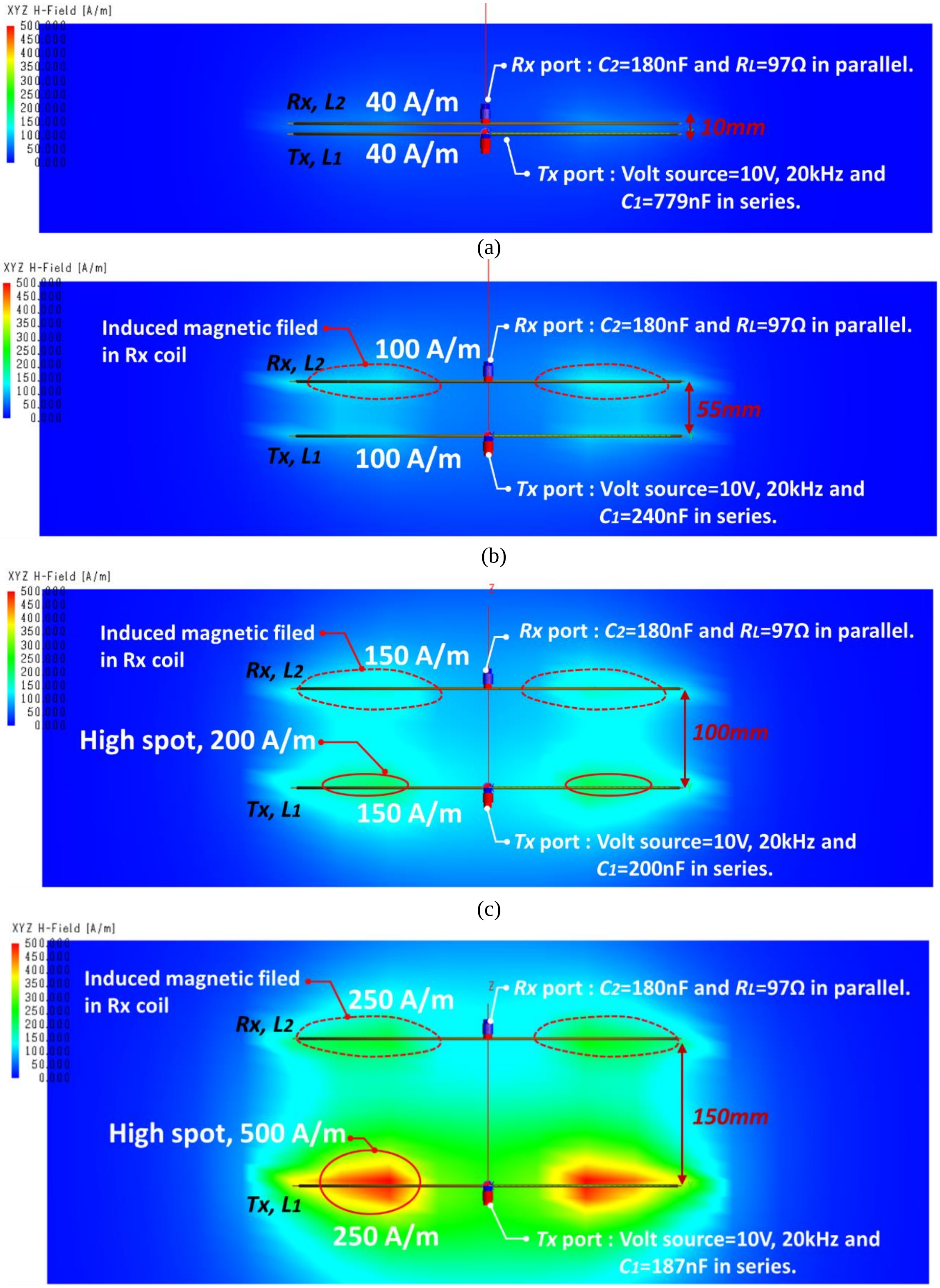

(a)

(b)

(c)

(d)

Fig. 7. Magnetic coupling and field distribution in *SP* topology over the different airgap (C_2 =180 nF) at 20 kHz: (a) 10 mm, C_1 =779 nF, (b) 55mm, C_1 =240 nF, (c) 100 mm, C_1 =200 nF, and (d) 150 mm, C_1 =187 nF.

V. POWER TRANSFERRED AND PRACTICAL VERIFICATION

For the verification of the simulation results, the transferred power and the related parameters were measured in the *SP* model at the air gap of 100 mm, as shown in Fig. 8 (a). The WPT model at the distance of 100 mm was selected as the magnetic coupling between the coils is well maintained, and the frequency bifurcation is not found at the distance. The full-bridge with gate driver (PWD 13F60, STMicroelectronics) was implemented, and the gate signals with the duty cycle of 50% at the 20 kHz frequency were given to the switching device from the micro-controller (Analog discovery 2, Digilent), as shown in Fig. 8 (b).

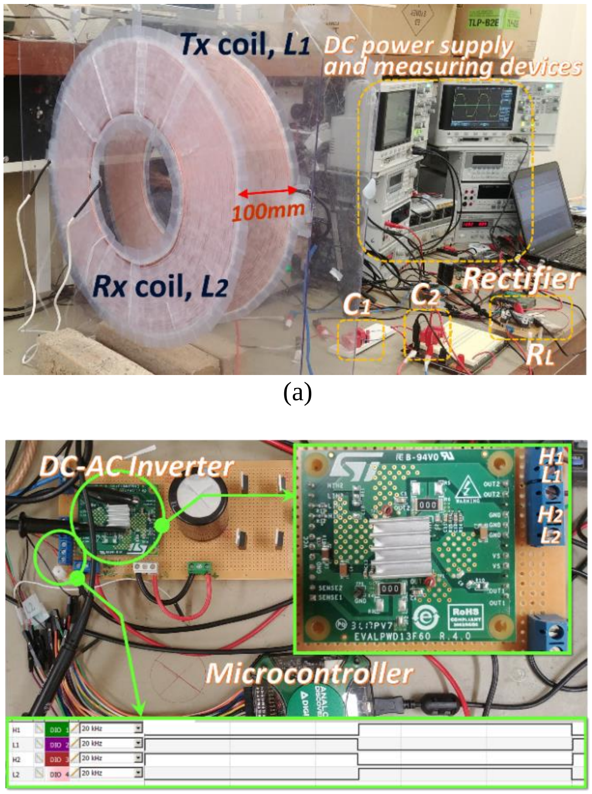

(a)

(b)

Fig. 8. Experimental measurement set-up: (a) *Tx* and *Rx* coils with compensating capacitors, and (b) full-bridge switching device and pulse (gate) signals.

In the practical experiment, the low voltage of 10 V_{peak} was supplied into the circuit due to the considerations of high voltage resonance oscillation and electromagnetic interference. As a DC power supply and HF switching devices could not be configured in the simulation tool, the overall efficiency η_o between the DC power supply and the load resistance was not evaluated. However, the transferring efficiency η_T from the *Tx* unit to the load resistance was correctly identified.

The distribution of the electric and magnetic field between two coils with the wire ports in the *SP* system at 100 mm air gap is illustrated, and it represents that the electric and magnetic fields at the middle of the coil are about 400 V/m and 200 A/m, respectively. At the vicinity of the coils, the values are under 200 V/m and 70 A/m, respectively, as shown in Figs. 9 (a) and (b). Therefore, the level of the electromagnetic field can be estimated for the safety clarification in the near-field area based on the guidelines; IEEE C95.1-2014 or International Commission on Non-Ionizing Radiation Protection [39].

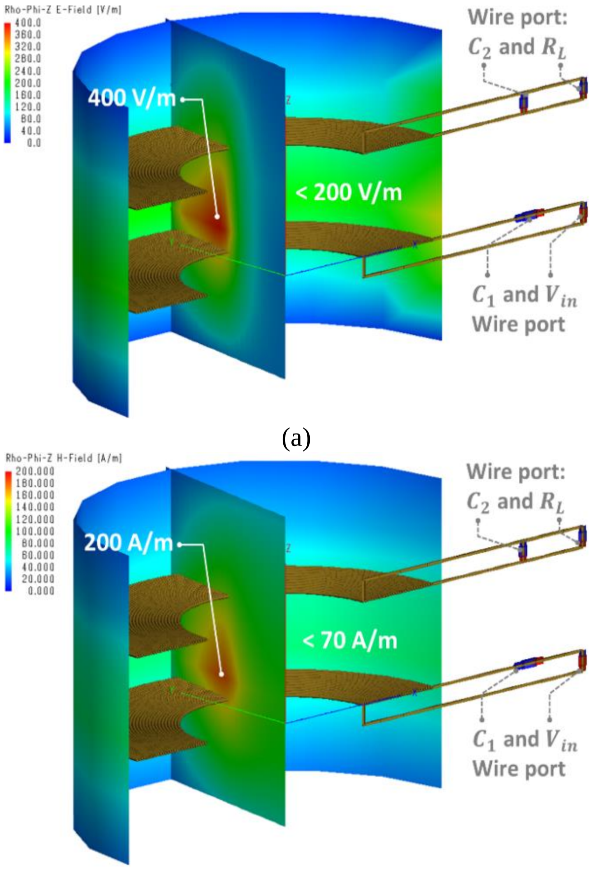

(a)

(b)

Fig. 9. FEKO results of the near-field in the *SP* system at 100 mm air gap at the frequency of 20 kHz: (a) electric field and (b) magnetic field.

The electrical parameters in the WPT model; V_{in}, V_{out}, Z_{in}, θ, I_{in}, I_{out}, P_{in}, and P_{out}, can also be determined in the different frequency range, as shown in Fig. 10. When the peak voltage of 10 V is supplied into the *Tx* unit, the output voltage of 32.1 V is produced across of the load terminal at the frequency of 20 kHz, and the input and output peak current is recorded as 1.170 A and 0.331 A, respectively, in peak value as shown in Figs. 10 (a) and (b).

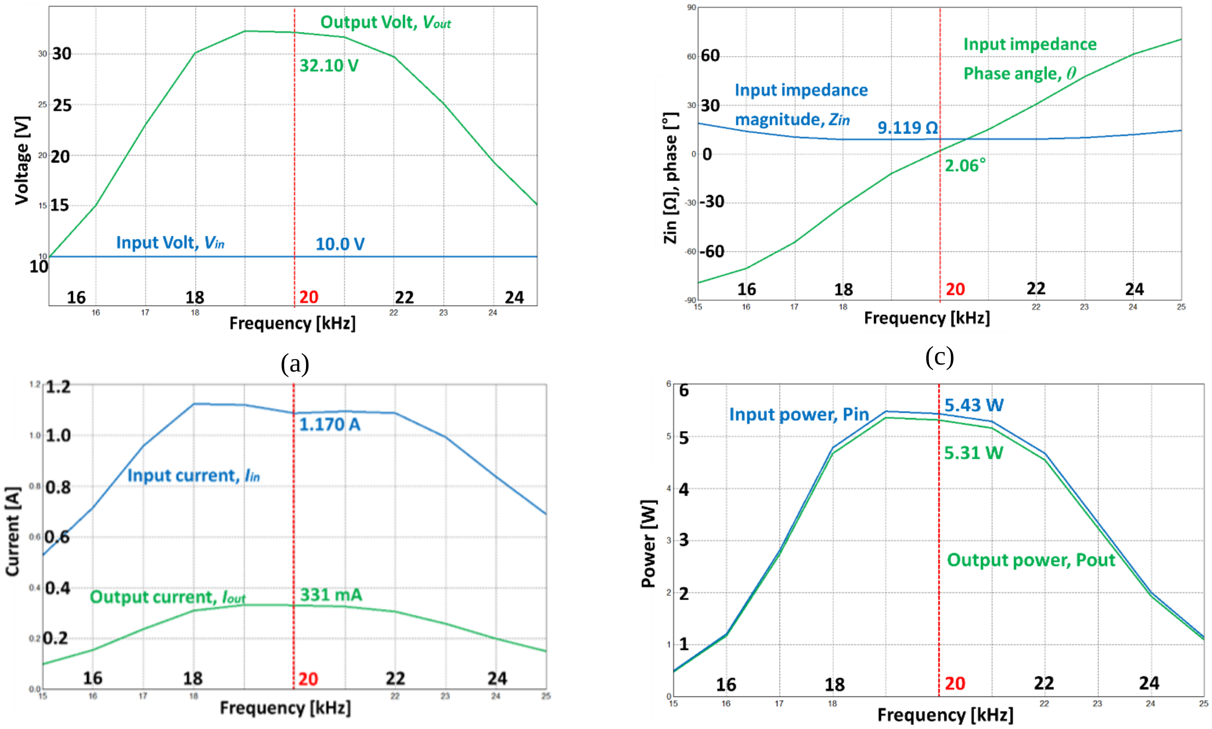

(a) (c)

(b) (d)

Fig. 10. FEKO results of electrical parameters of *SP* WPT system at 100 mm: (a) in/output voltage, (b) in/output current, (c) input impedance, and (d) in/output power.

Table 4: Comparison of the FEKO results and the experiment measurement in the *SP* WPT model at the 100 mm airgap

Parameters	**FEKO**	**Experimental Measurement**	**Δ Difference**	**%Δ**
V_{dc} (DC voltage)	n/a	8.7 V	n/a	n/a
I_{dc} (DC current)	n/a	0.72 A	n/a	n/a
P_{dc_in} (DC power)	n/a	6.264 W	n/a	n/a
P_{in} (Input AC Power)	5.43 W	5.897 W	-0.467 W	-8.600%
V_{in} (Input AC voltage)	n/a 10.00 V_{peak} 7.071 V_{RMS}	7.900 V_{peak} [square wave] 10.06 V_{peak} [1st harmonic] 7.113 V_{RMS}	n/a n/a -0.042 V_{RMS}	n/a n/a -0.594%
I_{in} (AC in *Tx*)	1.170 A_{peak} 0.827 A_{RMS}	n/a 0.829 A_{RMS}	n/a -0.002 A_{RMS}	n/a -0.242%
Z_{in} (Input impedance)	9.119 Ω	8.580 Ω	0.539 Ω	5.911%
Θ (Phase angle of Z_{in})	2.06°	3.54°	-1.480°	n/a
V_{out} (Voltage across load)	32.10 V_{peak} 22.698 V_{RMS}	n/a 22.543 V_{RMS}	n/a 0.155 V_{RMS}	n/a 0.683%
I_{out} (Current through load)	0.331 A_{peak} 0.234 A_{RMS}	n/a 0.250 A_{RMS} [Calculated]	n/a -0.016 A_{RMS}	-6.834%
P_{out} (Output power on *Rx*)	5.31 W	5.642 W	-0.332 W	-6.252%
η_T (Transfer efficiency)	97.790%	95.676%	2.114%	2.162%
P_{dc_out} (Output power on DC Load)	n/a	4.752 W	n/a	n/a
η_o (DC to DC, Overall efficiency)	n/a	75.862%	n/a	n/a

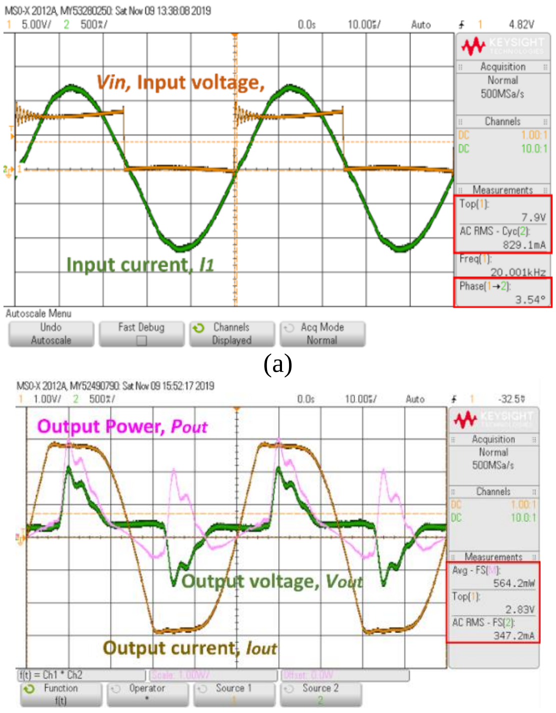

(a)

(b)

Fig. 11. Practical measurement of *SP* system at 55 mm air gap: (a) Input power and (b) output power.

The source resistance Ro was set as 0 Ω, and the load resistance of 97 Ω was implemented in the wire ports in FEKO analysis. As the compensating capacitors C_1 and C_2 were correctly utilized, the phase angle of the input impedance $Z_{in,sp}$ in (7) was 2.06°; it presents almost zero degrees, as indicated in Fig. 10 (c).

Furthermore, the transferred power between the coils was calculated and, the maximum value of the 5.31 W power was delivered at the 20 kHz frequency, as presented in Fig. 10 (d). The actual values of the parameters: V_{in}, I_{in}, V_{out}, I_{out}, and the phase angle in the prototype were measured by the oscilloscope (Agilent Technologies: MSO-X 2012A) and the current probe: Tektronix A622) as shown in Fig. 11. The results of the comparison between the simulation result and practical measurements of the WPT model are presented in Table 4. Besides, the input impedance Z_{in} of the experimental measurement in Table 4 was calculated based on the voltage and current reading on the oscilloscope.

It was observed that the percentage error of the input parameters (input voltage V_{in}, current I_{in} and impedance Z_{in}) is under 6%. The deviation value in the phase angle θ of the input impedance Z_{in}, is only 1.48°. The input and output power (P_{in} and P_{out}) in the practical measurement indicates the percentage error of -8.60% and -6.252%, respectively. The value of transfer efficiency η_T is recorded as 95.676%, and it is comparable to the FEKO result of 97.790%.

This practical measurement was conducted with the implementation of DC to HF AC inverter on the *Tx* unit and HF AC to DC rectifier. Therefore, the square waveform was indicated at the *Tx* unit, and the distorted waveforms of output voltage and current were recorded at the across of the load resistance due to the full-bridge rectifier. It is clarified that the zero-phase switching in the HF inverter was achieved as the phase difference between the voltage and current at both ends is almost zero, as shown in Figs. 11 (a) and (b).

For reference, the overall efficiency or DC to DC efficiency η_T of 75.862% is presented in the prototype due to the heat loss on the switching devices, the full-bridge rectifier, the ohmic loss in the cooper winding, etc. Consequently, the computational electromagnetic field analysis provides acceptable results for the design of the WPT systems. The formation and distribution of electromagnetic coupling between the coils, self and mutual inductance, output voltage, the rate of transferred power can be identified prior to the practical WPT implementations.

VI. CONCLUSION

The performance of the inductively-coupled WPT system is sensitive to the structure of the *Tx* and *Rx* coil, and the variation of the air gap. In this work, the characteristic of the electromagnetic field and the electrical parameters of the WPT system were correctly identified through the computational analysis and practical experiment. To demonstrate the WPT system, the *Tx* and *Rx* coil in the radius of 200 mm were implemented, and the *S*-parameter results accurately extracted the self and mutual inductance of the coils. Then, the characteristic of magnetic coupling between the two coils in the *SP* compensating WPT system at the resonance frequency of 20 kHz was observed by the near-field analysis. Also, it was found that the prototype of the *SP* system efficiently delivers electric energy when the air gap is under 100 mm. The electrical parameters (i.e., V_{in}, I_{in}, P_{in}, Z_{in}, V_{out}, I_{out}, and P_{out}) of the WPT system examined by the simulation tool are comparable to the experimental measurements of the prototype. Therefore, this study clarified that the use of FEKO facilitates the comprehensive and accurate analysis of the electromagnetic and electrical behavior of near-field WPT system.

ACKNOWLEDGMENT

This work was supported in part by the Australian Government Research Training Program and in part by the Curtin Postgraduate.

REFERENCES

[1] A. S. Marincic, "Nikola Tesla and the wireless transmission of energy," *IEEE Transactions on Power Apparatus and Systems*, vol. PAS-101, no.

10, pp. 4064-4068, doi:10.1109/TPAS.1982.317084, 1982.

[2] S. Y. R. Hui, “Past, present and future trends of non-radiative wireless power transfer,” *CPSS Transactions on Power Electronics and Applications*, vol. 1, no. 1, pp. 83-91, doi: 10.24295/CPSSTPEA.2016.00008, 2016.

[3] G. A. Covic and J. T. Boys, “Modern trends in inductive power transfer for transportation applications,” *IEEE Journal of Emerging and Selected Topics in Power Electronics*, vol. 1, no. 1, pp. 28-41, doi: 10.1109/ JESTPE. 2013. 2264473, 2013.

[4] A. Bindra, “Wireless power transfer is fueling the electric vehicles market [from the editor],” *IEEE Power Electronics Magazine*, vol. 4, no. 2, pp. 4-8, doi: 10.1109/MPEL.2017.2692382, 2017.

[5] Wireless EV Charging Market Worth 7,094.8 Million USD by 2025, *India Automobile News*, Available: http:// www . marketsandmarkets .com/ Market - Reports / wireless-ev-charging-market-170963517. html, Sept. 2017.

[6] X. Lu, D. Niyato, P. Wang, and D. I. Kim, “Wireless charger networking for mobile devices: fundamentals, standards, and applications,” *IEEE Wireless Communications*, vol. 22, no. 2, pp. 126-135, doi: 10.1109/MWC.2015.7096295, 2015.

[7] S. Y. R. Hui, “Magnetic resonance for wireless power transfer [A look back],” *IEEE Power Electronics Magazine*, vol. 3, no. 1, pp. 14-31, doi: 10.1109/MPEL.2015.2510441, 2016.

[8] J. Dai and D. C. Ludois, “Capacitive power transfer through a conformal bumper for electric vehicle charging,” *IEEE Journal of Emerging and Selected Topics in Power Electronics*, vol. 4, no. 3, pp. 1015-1025, doi:10.1109/JESTPE.2015.2505622, 2016.

[9] K. V. T. Piipponen, R. Sepponen, and P. Eskelinen, “A biosignal instrumentation system using capacitive coupling for power and signal isolation,” *IEEE Transactions on Biomedical Engineering*, vol. 54, no. 10, pp. 1822-1828, doi:10.1109/TBME. 2007.894830, 2007.

[10] J. C. Lin, “Wireless power transfer for mobile applications, and health effects [Telecommunications health and safety],” *IEEE Antennas and Propagation Magazine*, vol. 55, no. 2, pp. 250-253, doi: 10.1109/MAP.2013.6529362, 2013.

[11] C. Park, S. Lee, G. H. Cho, and C. T. Rim, “Innovative 5-m-off-distance inductive power transfer systems with optimally shaped dipole coils,” *IEEE Transactions on Power Electronics*, vol. 30, no. 2, pp. 817-827, doi:10.1109/TPEL.2014. 2310232, 2015.

[12] *FEKO Computational Electromagnetics Software*, [Online], Available: http://www.altairhyperworks.com/product/FEKO, 2019.

[13] U. Jakobus, M. Bingle, M. Schoeman, J. J. V. Tonder, and F. Illenseer, “Tailoring FEKO for microwave problems,” *IEEE Microwave Magazine*, vol. 9, no. 6, pp. 76-85, doi:10.1109/MMM.2008. 929557, 2008.

[14] S. Clarke and U. Jakobus, “Dielectric material modeling in the MoM-based code FEKO,” *IEEE Antennas and Propagation Magazine*, vol. 47, no. 5, pp. 140-147, doi:10.1109/MAP.2005.1599186, 2005.

[15] S. Chai, L. Guo, K. Li, and L. Li, “Combining CS with FEKO for fast target characteristic acquisition,” *IEEE Transactions on Antennas and Propagation*, vol. 66, no. 5, pp. 2494-2504, doi: 10.1109/TAP.2018.2816599, 2018.

[16] I. Yoon and H. Ling, “Investigation of near-field wireless power transfer in the presence of lossy dielectric materials,” *IEEE Transactions on Antennas and Propagation*, vol. 61, no. 1, pp. 482-488, doi:10.1109/TAP.2012.2215296, 2013.

[17] J. Moshfegh, M. Shahabadi, and J. Rashed-Mohassel, “Conditions of maximum efficiency for wireless power transfer between two helical wires,” *IET Microwaves, Antennas & Propagation*, vol. 5, no. 5, pp. 545-550, doi:10.1049/iet-map. 2010.0134, 2011.

[18] D. Kim, A. Abu-Siada, and A. Sutinjo, “State-of-the-art literature review of WPT: Current limitations and solutions on IPT,” *Electric Power Systems Research*, vol. 154, pp. 493-502, doi: https://doi.org/10.1016/j.epsr.2017.09.018, 2018.

[19] D. Kim, A. Abu-Siada, and A. Sutinjo, “A novel application of frequency response analysis for wireless power transfer system,” in *2017 Australasian Universities Power Engineering Conference (AUPEC)*, pp. 1-6, doi:10.1109/AUPEC. 2017.8282474, Nov. 19-22, 2017.

[20] S. Park, “Evaluation of electromagnetic exposure during 85 kHz wireless power transfer for electric vehicles,” *IEEE Transactions on Magnetics*, vol. PP, no. 99, pp. 1-1, doi:10.1109/TMAG.2017. 2748498, 2017.

[21] C. Zheng, *et al.*, “High-efficiency contactless power transfer system for electric vehicle battery charging application,” *IEEE Journal of Emerging and Selected Topics in Power Electronics*, vol. 3, no. 1, pp. 65-74, doi:10.1109/JESTPE.2014. 2339279, 2015.

[22] P. Machura and Q. Li, “A critical review on wireless charging for electric vehicles,” *Renewable and Sustainable Energy Reviews*, vol. 104, pp. 209-234, doi:https://doi.org/10.1016/j.rser.2019.01.027, Apr. 2019.

[23] *IEC 61980-1:2015 Electric Vehicle Wireless Power Transfer (WPT) Systems*, 2015.

[24] D. A. Frickey, "Conversions between S, Z, Y, H, ABCD, and T parameters which are valid for complex source and load impedances," *IEEE Transactions on Microwave Theory and Techniques*, vol. 42, no. 2, pp. 205-211, doi:10.1109/22.275248, 1994.

[25] H. Ishida and H. Furukawa, "Wireless power transmission through concrete using circuits resonating at utility frequency of 60 Hz," *IEEE Transactions on Power Electronics*, vol. 30, no. 3, pp. 1220-1229, doi:10.1109/TPEL.2014.2322876, 2015.

[26] D. Kim, A. Abu-Siada, and A. T. Sutinjo, "Application of FRA to improve the design and maintenance of wireless power transfer systems," *IEEE Transactions on Instrumentation and Measurement*, pp. 1-13, doi:10.1109/TIM.2018.2889360, 2019.

[27] G. Guidi, J. A. Suul, F. Jenset, and I. Sorfonn, "Wireless charging for ships: High-power inductive charging for battery electric and plug-in hybrid vessels," *IEEE Electrification Magazine*, vol. 5, no. 3, pp. 22-32, doi:10.1109/MELE.2017.2718829, 2017.

[28] Z. Li, C. Zhu, J. Jiang, K. Song, and G. Wei, "A 3-kW wireless power transfer system for sightseeing car supercapacitor charge," *IEEE Transactions on Power Electronics*, vol. 32, no. 5, pp. 3301-3316, doi:10.1109/TPEL.2016.2584701, 2017.

[29] J. H. Kim, *et al.*, "Development of 1-MW inductive power transfer system for a high-speed train," *IEEE Transactions on Industrial Electronics*, vol. 62, no. 10, pp. 6242-6250, doi:10.1109/TIE.2015.2417122, 2015.

[30] Y. H. Sohn, B. H. Choi, E. S. Lee, G. C. Lim, G. H. Cho, and C. T. Rim, "General unified analyses of two-capacitor inductive power transfer systems: Equivalence of current-source SS and SP compensations," *IEEE Transactions on Power Electronics*, vol. 30, no. 11, pp. 6030-6045, doi:10.1109/TPEL.2015.2409734, 2015.

[31] W. Chwei-Sen, G. A. Covic, and O. H. Stielau, "Power transfer capability and bifurcation phenomena of loosely coupled inductive power transfer systems," *IEEE Transactions on Industrial Electronics*, vol. 51, no. 1, pp. 148-157, doi:10.1109/TIE.2003.822038, 2004.

[32] M. Kim, J. W. Lee, and B. Lee, "Practical bifurcation criteria considering inductive power pad losses in wireless power transfer systems," *J. Electr. Eng. Technol.*, vol. 12, no. 1, pp. 173-181, doi:10.5370/JEET.2017.12.1.173, 2017.

[33] C. Jiang, K. Chau, C. Liu, and C. Lee, "An overview of resonant circuits for wireless power transfer," *Energies*, vol. 10, no. 7, p. 894, doi:10.3390/en10070894, 2017.

[34] A. J. Moradewicz and M. P. Kazmierkowski, "Contactless energy transfer system with FPGA-controlled resonant converter," *IEEE Transactions on Industrial Electronics*, vol. 57, no. 9, pp. 3181-3190, doi:10.1109/TIE.2010.2051395, 2010.

[35] Z. Bi, T. Kan, C. C. Mi, Y. Zhang, Z. Zhao, and G. A. Keoleian, "A review of wireless power transfer for electric vehicles: Prospects to enhance sustainable mobility," *Applied Energy*, vol. 179, pp. 413-425, doi:https://doi.org/10.1016/j.apenergy.2016.07.003, 2016.

[36] C. S. Kong, "A general maximum power transfer theorem," *IEEE Transactions on Education*, vol. 38, no. 3, pp. 296-298, doi:10.1109/13.406510, 1995.

[37] W. X. Zhong, C. Zhang, X. Liu, and S. Y. R. Hui, "A methodology for making a three-coil wireless power transfer system more energy efficient than a two-coil counterpart for extended transfer distance," *IEEE Transactions on Power Electronics*, vol. 30, no. 2, pp. 933-942, doi:10.1109/TPEL.2014.2312020, 2015.

[38] Z. Huang, S. C. Wong, and C. K. Tse, "Design of a single-stage inductive-power-transfer converter for efficient EV battery charging," *IEEE Transactions on Vehicular Technology*, vol. 66, no. 7, pp. 5808-5821, 2017, doi:10.1109/TVT.2016.2631596.

[39] V. Marché, "Contactless energy transfer systems finite elements modeling with flux," https://insider.altairhyperworks.com/flux-finiteelements-modeling-opitmize-contactless-energy-transfer-systems-efficiency/ (accessed), Dec. 2017.

Dowon Kim received the B.Sc. and M.Sc. degrees in Electrical Engineering from the Seoul National University of Science and Technology, Seoul, South Korea, in 2003 and 2009, respectively. He is currently pursuing the Ph.D. degree with Curtin University, Bentley, WA, Australia. From 1998 to 2011, he was a Transmission and Substation Engineer and an Engineering Lecturer with Korea Electric Power Corporation. He is a Senior Testing and Commissioning Engineer with Global Testing Services, WA, Australia since 2012. His current research interests include wireless power transfer, electromagnetics, frequency response, and power system protection.

Adrian T. Sutinjo received the B.S.E.E. degree from Iowa State University, Ames, IA, USA, in 1995, the M.S.E.E. degree from the Missouri University of Science and Technology, Rolla, MO, USA, in 1997, and the Ph.D. degree in Electrical Engineering from the University of Calgary, Calgary, AB, Canada, in 2009. From 1997 to 2004, he was an RF Engineer with Motorola, Chicago, IL, USA, and with Murandi Communications Ltd., Calgary, AB, Canada. He is currently a Senior Lecturer with the School of Electrical Engineering, Computing and Mathematics, Curtin University, Perth, WA, Australia, where he has been with the International Centre for Radio Astronomy Research since 2012. His current research interests include antennas, RF and microwave engineering, electromagnetics, and radio astronomy engineering.

Ahmed Abu-Siada received the B.Sc. and M.Sc. degrees in Electrical Engineering from Ain Shams University, Cairo, Egypt, in 1998, and the Ph.D. degree in Electrical Engineering from Curtin University, Bentley, WA, Australia, in 2004. He is currently a Discipline Lead of the Electrical and Computer Engineering, Curtin University. His current research interests include power system stability, condition monitoring, power electronics, and power quality. Abu-Siada is an Editor-in-Chief of the International Journal Electrical and Electronic Engineering, a regular reviewer for various IEEE Transactions, and a Vice-Chair of the IEEE Computation Intelligence Society, WA Chapter.

High Order On Surface Radiation Boundary Conditions For Radar Cross-Section Application

Adel Al Weshah [1] and S. I. Hariharan [2]

[1]School of Electrical and Computer Engineering
University of Georgia, Athens, GA 30602 USA
adel.alweshah@uga.edu

[2]Department of Electrical and Computer Engineering
The University of Akron, Akron, OH 44325 USA

Abstract – Solving problems governed by two and three-dimensional wave equations in exterior domains are a complex task. There are techniques to reduce the computational complexities, one such technique is On-Surface Radiation Boundary Conditions (OSRBC). There have been recent interests in revisiting this technique for two and three-dimensional problems [1]. In this paper, we explore the implementation of a new high order OSRBC based on the high order local boundary conditions introduced by [2] for two and three dimensions to solve the wave equation in unbounded domains. In most cases, it is difficult to construct exact solutions. For comparisons of numerical solutions, we use solutions obtained from large domains as approximate exact solutions. The implementation involves a two step novel approach to handle time derivatives. First, the governing equations and boundary conditions are converted to Laplace transform domain. Then, based on bilinear transformation the procedure was converted to z domain which simplified the implementation process. In particular, this process leads to higher accuracy compared to the different types of finite difference schemes used to approximate the first and second order partial derivative in the new high order OSRBC and the auxiliary functions that define the high order boundary conditions. A series of numerical tests demonstrate the accuracy and efficiency of the new high order OSRBC for two and three-dimensional problems. Both the long domain solutions as well as the new OSRBC solutions are compared for accuracies and useful results for radar cross-section calculations are presented.

Index Terms – On surface radiation boundary conditions, scattering problems, time-domain analysis, numerical analysis, bilinear transformation, radar-cross section, two and three-dimensional.

I. INTRODUCTION

Computational electromagnetics is a vast area of research and has gained a considerable amount of attention during the last four decades. This fact is due to new technological requirements and scientific applications such as electromagnetic waves scattered around an antenna and radar cross section calculations [3, 4]. This field yields yet challenging questions that require the development of efficient and accurate computational techniques for the simulation of electromagnetic scattering problems. Several computational difficulties limit the application of classical numerical approaches. The first obstacle is related to the open domain where many wave propagation problems are described in the unbounded domain. This makes it difficult to extend the computational domain to the far field due to the dissipative and dispersive nature of the direct numerical method. The other important obstacle is that the relevant calculations depend on the accuracy of the radiation boundary conditions (RBCS) and are linked to the fact that the wavelength of the incident field is smaller than the characteristic size of the scatterer [5].

The past two decades have seen many attempts to create accurate radiation boundary condition formulations to simulate scattering from two and three-dimensional obstacles. Examples are the Perfectly Matched Layer (PML) [6–8], integral equation formulations [9, 10] and the infinite element method [6, 11]. However, the computational effort needed for these methods limits their application range even if it provides some valuable results. Besides, these procedures are limited to frequency domain problems. Furthermore, PML and infinite element method cannot be used as the on surface boundary conditions because they have to be placed far away from the surface of the scatterer, and we need to derive an expression for a normal derivative on the surface of the scatterer.

An alternative approach is the On-Surface Radiation Boundary Condition (OSRBC) which is considered as the frontier between classical methods and asymptotic techniques [5]. It was introduced in the middle of the

Submitted On: May 23, 2019
Accepted On: December 15, 2019

eighties by [12, 13]. It is an approximate technique that applies local artificial boundary conditions [14–16] directly on the surface of the scatterer to determine the normal derivative. In these papers, the authors also introduce the basic method to compute the electromagnetic scattered filed from a two dimensional infinite cylinder. This method leads to the numerical solution of a set of partial differential equations set over the surface of the scatterer Γ (or on contour for a 2-D object). Specifically, this principle involves the calculation of normal derivatives on Γ. Unfortunately, the closer one brings the radiation boundary to the scatterer, the more precise the radiation condition should be. In [12, 13] the authors used either the first or second order radiation conditions. Again their work was limited to frequency domain problems namely, those of high frequencies. In this work, we present an arbitrary order OSRBC in the time domain in both two and three dimensions. The work presented here can be reduced to frequency domain analysis for time-harmonic incident fields.

In a sequence of works developed by [2] and [17], the authors consider arbitrary order boundary conditions for wave equations that use only a local operator on the boundary. In these works, they removed the use of higher order spatial normal derivatives found in the work of Bayliss and Turkel's boundary conditions [14]. In particular, the work found in [2] replaces the difficulties using only higher order time derivatives which are easier to implement. The work presented in this paper uses these results to formulate a new high order on-surface radiation boundary conditions. This forms the basis for the implementation of OSRBC in both two and three dimensions. In essence, we start with the introduction of two and three-dimensional Dirichlet problems governed by wave equations in the exterior domain. Then, we describe the long domain problems in both two and three dimensions. This yields the required normal derivative expressions ($\frac{\partial u}{\partial n}$) in both dimensions. To avoid differences in time, we consider the high order OSRBC in the $s-$domain using the Laplace transform. Then, we apply a new approach to discretize the high order OSRBC using the bilinear transformation method to implement a mapping from the $s-$domain to the $z-$domain. This eliminates choosing different types of finite difference implementations in time. We show the effectiveness of this approach vs time differencing in the numerical implementation section. Next, we apply the inverse $z-$transform and solve the high order OSRBC numerically in the form of a recursively defined sequence of equations. Finally, we verify our proposed results using numerical solutions.

II. PROBLEM DESCRIPTION

To describe the wave propagation problem, we assume that there is a TM wave incident on the bounded

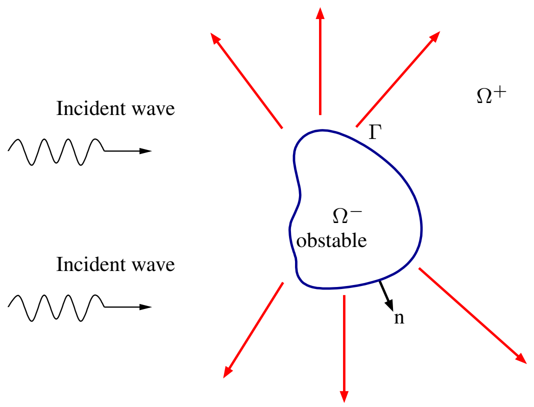

Fig. 1. Scattering Problem Configuration.

domain of $R^N(N = 2, 3)$ which represents a perfectly conducting scatterer bounded by a boundary Γ as shown in Fig. 1. We assume this domain is sufficiently smooth and **n** is the unit normal vector to Ω^-. We consider an incident TM wave field (E) illuminating the obstacle. This only has one scalar component that we denote $u(\underline{x}, t)$:

$$E_{inc} = u_{inc}(\underline{x}, t), \quad E_s = u_s(\underline{x}, t),$$

Where $\underline{x} = (x_1, ..., x_N)$ a point of R^N, $u_{inc}(\underline{x}, t)$ denotes the incident field and $u_s(\underline{x}, t)$ denotes the scattered field. This source generates a scattered field (u_s) to the obstacle (Ω^-) which satisfies the so called wave equation:

$$\bigtriangledown^2 u_s - \frac{1}{c^2}\frac{\partial^2 u_s}{\partial t^2} = 0 \qquad \text{in } \Omega^+, \tag{1}$$

For the well-posedness of the problem, the field $u_s(\underline{x}, t)$ must also satisfy a boundary condition at the surface (Γ) of the body as well as the Sommerfeld radiation condition at infinity:

$$\lim_{|\underline{x}|\to\infty} |\underline{x}|^{\frac{(N-1)}{2}} \left(\bigtriangledown u_s \cdot \frac{\underline{x}}{|\underline{x}|} + \frac{\partial u_s}{\partial t} \right) = 0,$$

Because the equation (1) is of order two, we need two boundary conditions - one on the boundary of the scatterer, and the Sommerfeld radiation condition. The first boundary condition is the Dirichlet (perfect conductor) boundary condition. Here, the scatterer is assumed to be perfectly conducting on the surface Γ (or on contour for a $2-D$ object), so the field satisfies:

$$u_s(\underline{x}, t) = -u_{inc}(\underline{x}, t) \qquad \text{on } \Gamma,$$

A second condition is an implementable approximation of the Sommerfeld radiation condition. The authors of [2] derived higher order local version of Sommerfeld boundary conditions that are both asymptotically exact and easy to implement. The derivation of this boundary condition procedure originates from the [14] whose applications are typically restricted to the first order and second order formulations due to the fact that the higher order normal derivatives are difficult to implement numerically. In contrast, the work found in [2] overcomes this difficulty by a new formulation that involves only a single order normal derivative and which is coupled with a sequence of first differential equations in time via the use of auxiliary variables. The higher order local boundary conditions are expressed in the polar coordinates form for the two-dimensional problems and spherical coordinates for the three-dimensional problems as follows:

The high order local boundary conditions for two-dimensional case are:

$$\frac{1}{c}\frac{\partial u_s}{\partial t}+\frac{\partial u_s}{\partial r}+\frac{1}{2r}u_s=w_1, \tag{2}$$

$$\frac{1}{c}\frac{\partial \omega_j}{\partial t}+\frac{j}{r}\omega_j=\frac{(j-\frac{1}{2})^2}{4r^2}\omega_{j-1}+\frac{1}{4r^2}\frac{\partial^2\omega_{j-1}}{\partial\theta^2}+\omega_{j+1}, \quad j=1,2,... \tag{3}$$

The high order local boundary conditions for three-dimensional case are:

$$\frac{1}{c}\frac{\partial u_s}{\partial t}+\frac{\partial u_s}{\partial r}+\frac{1}{r}u_s=w_1, \tag{4}$$

$$\frac{1}{c}\frac{\partial \omega_j}{\partial t}+\frac{j}{r}\omega_j=\frac{1}{4r^2}(\bigtriangledown_s^2+j(j-1))\omega_{j-1}+\omega_{j+1}, \quad j=2,3,... \tag{5}$$

Where the spherical Laplacian given by:

$$\bigtriangledown_s^2\omega_{j-1}=\frac{1}{\sin\theta}\frac{\partial}{\partial\theta}(\sin\theta\frac{\partial\omega_{j-1}}{\partial\theta})+\frac{1}{\sin^2\theta}\frac{\partial^2\omega_{j-1}}{\partial\phi^2},$$

and ω_j's are auxiliary functions defined recursively and known as remainders, we have set:

$$\omega_0=2u_s.$$

An interesting observation here is that when we set $\omega_1=0$ the condition reduces to the well known Bayliss and Turkel condition. By a direct computation, it has been proven in [2] that:

$$\omega_j=O(r^{-2j+\frac{1}{2}}) \quad \text{for } 2-D,$$
$$\omega_j=O(r^{-2j-1}) \quad \text{for } 3-D,$$

The equations (3) and (5) can be solved to find ω_1 in terms of u_s. Using reminders of order (p) and set the order ($p+1$) to be as follows:

$$\forall j>p,\ \omega_j=0.$$

Equations (2), (3) (two-dimensional case) and (4), (5) (three-dimensional case) are designed to be implemented at a far field boundary that encloses the scatterer. They can be solved to find the radial derivative $\frac{\partial u}{\partial r}$, which represents the normal derivative $\frac{\partial u}{\partial n}$ at the surface of the far field boundary. The principle of the OSRBC is that one brings the far field boundary to coincide with the boundary of the scatterer itself. The remainder of the paper analyses the impact of this process bringing the far field conditions directly on the scatterer.

III. NUMERICAL IMPLEMENTATION

In this paper, we solve the higher order local boundary conditions in two and three dimensions to find the normal derivatives on the surface of the scatterers. A new novel numerical approach to handle the time derivative is introduced. Typically, the time derivatives approximated with finite differences. Thus, for the stability and accuracy, one must be careful how these differences are handled. They can yield implicit or explicit schemes based on the differencing used to discretize the equations (2), (3) (two-dimensional case) and (4), (5) (three-dimensional case). Now, this leads to our new approach. First, these sets of boundary conditions are transformed into Laplace transform domain because of the linearity. The Laplace transform domain problem is converted to $z-$ transform based on the bilinear transformation [18]. The bilinear transformation preserves the stability and causality when mapping a continuous time equation to discrete time. This avoids the uncertainty involving choices of time derivative difference approximations. We start by implementing the Laplace transform for the higher order local boundary conditions. Assuming the boundary Γ is a perfect conductor, $c=1$ and cylindrical mode:

$$\frac{\partial^2\omega_{j-1}}{\partial\theta^2}=-m^2 \qquad \text{for } 2-D,$$

Likewise, for spherical modes we obtain:

$$\bigtriangledown_s^2\omega_{j-1}=-m(m+1) \qquad \text{for } 3-D,$$

So, the Laplace transform for (2) and (3) are given below:

$$\frac{\partial\hat{u}}{\partial r}+(s+\frac{1}{2r})\hat{u}=\hat{w}_1, \tag{6}$$

$$(s+\frac{j}{r})\hat{\omega}_j=\frac{(j-\frac{1}{2})^2-m^2}{4r^2}\hat{\omega}_{j-1}+\hat{\omega}_{j+1}, \quad j=1,2,.... \tag{7}$$

and the Laplace transform for (4) and (5) are given below:

$$\frac{\partial\hat{u}}{\partial r}+(s+\frac{1}{r})\hat{u}=\hat{w_1}, \tag{8}$$

$$(s+\frac{j}{r})\hat{\omega}_j=\frac{j(j-1)-(m^2+m)}{4r^2}\hat{\omega}_{j-1}+\hat{\omega}_{j+1}, \quad j=1,2,3,.... \tag{9}$$

Then, we implement the mapping from the $s-$domain to the $z-$domain via bilinear transform $s=\frac{2}{T}\frac{1-z^{-1}}{1+z^{-1}}$, in the equations (6) and (7) as given below, for convenience T is taken as 1:

$$\frac{\partial\hat{u}}{\partial r}+(2\frac{1-z^{-1}}{1+z^{-1}}+\frac{1}{2r})\hat{u}=\hat{w}_1, \tag{10}$$

$$(2\frac{1-z^{-1}}{1+z^{-1}}+\frac{j}{r})\hat{\omega}_j=\frac{(j-\frac{1}{2})^2-m^2}{4r^2}\hat{\omega}_{j-1}+\hat{\omega}_{j+1}, \quad j=1,2,... \tag{11}$$

and for (8) and (9) are given below:

$$\frac{\partial \hat{u}}{\partial r} + (2\frac{1-z^{-1}}{1+z^{-1}} + \frac{1}{r})\hat{u} = \hat{w}_1, \tag{12}$$

$$(2\frac{1-z^{-1}}{1+z^{-1}} + \frac{j}{r})\hat{\omega}_j = \frac{j(j-1)-(m^2+m)}{4r^2}\hat{\omega}_{j-1} + \hat{\omega}_{j+1}, \quad j = 1, 2, 3, ... \tag{13}$$

Finally, in order to solve for the normal derivative in time domain we apply the inverse $z-$transform to the equations (10) and (11) as given below:

$$\frac{\partial \bar{u}(n,r)}{\partial r} + \frac{\partial \bar{u}(n-1,r)}{\partial r} + 2[\bar{u}(n,r) - \bar{u}(n-1,r)] + \frac{[\bar{u}(n,r) + \bar{u}(n-1,r)]}{2r} = \bar{\omega}_1(n,r)+\bar{\omega}_1(n-1,r)', \tag{14}$$

$$2(\bar{\omega}_j(n,r) - \bar{\omega}_j(n-1,r)) + \frac{j}{r}(\bar{\omega}_j(n,r)+ \bar{\omega}_j(n-1,r)) = \frac{(j-\frac{1}{2})^2 - m^2}{4r^2}(\bar{\omega}_{j-1}(n,r)+ \bar{\omega}_{j-1}(n-1,r)) + (\bar{\omega}_{j+1}(n,r) + \bar{\omega}_{j+1}(n-1,r)), \quad j = 1, 2, ... \tag{15}$$

and for (12) and (13) are given below:

$$\frac{\partial \bar{u}(n,r)}{\partial r} + \frac{\partial \bar{u}(n-1,r)}{\partial r} + 2[\bar{u}(n,r) - \bar{u}(n-1,r)] + \frac{[\bar{u}(n,r) + \bar{u}(n-1,r)]}{r}) = \bar{\omega}_1(n,r)+\bar{\omega}_1(n-1,r), \tag{16}$$

$$2(\bar{\omega}_j(n,r) - \bar{\omega}_j(n-1,r)) + \frac{j}{r}(\bar{\omega}_j(n,r)+ \bar{\omega}_j(n-1,r)) = \frac{j(j-1)-(m^2+m)}{4r^2}(\bar{\omega}_{j-1}(n,r)+ \bar{\omega}_{j-1}(n-1,r)) + (\bar{\omega}_{j+1}(n,r) + \bar{\omega}_{j+1}(n-1,r)), \quad j = 1, 2, 3, ... \tag{17}$$

Solving (15) numerically to find ω_j's remainders, one needs to write these equations in the matrix form as below [19], [20]:

$$A_j\bar{\omega}^{j-1} = T_j\bar{\omega}^j - B\bar{\omega}^{j+1}, \tag{18}$$

Where A_j, T_j and B are $N \times N$ matrices given by:

$$A_j = \begin{pmatrix} a_j & 0 & 0 \dots 0 \\ a_j & a_j & 0 \ddots \vdots \\ 0 & a_j & \ddots \ddots 0 \\ \vdots & \ddots & \ddots \ddots 0 \\ 0 \dots & 0 & a_j \; a_j \end{pmatrix}$$

$$T_j = \begin{pmatrix} c_j & 0 & \dots\dots 0 \\ b_j & c_j & \ddots \quad \vdots \\ \vdots & \ddots & \ddots \ddots \vdots \\ \vdots & & \ddots \ddots 0 \\ 0 & \dots\dots & b_j \; c_j \end{pmatrix}$$

$$B = \begin{pmatrix} 1 & 0 & \dots\dots 0 \\ 1 & 1 & \ddots \quad \vdots \\ \vdots & \ddots & \ddots \ddots \vdots \\ \vdots & & \ddots \ddots 0 \\ 0 & \dots\dots & 1 \; 1 \end{pmatrix}$$

With:

$$a_j = \frac{(j-\frac{1}{2})^2 - m^2}{4r^2},$$

$$b_j = \frac{j}{r} - 2,$$

$$c_j = 2 + \frac{j}{r},$$

We use p auxiliary function such that $\bar{\omega}^j = 0 \; \forall j > p$, so $\bar{\omega}^{p+1} = 0$. From (18) we find that:

$$\begin{cases} \bar{\omega}^{j-1} = A_j^{-1}T_j\bar{\omega}^j - A_j^{-1}B\bar{\omega}^{j+1} \\ \bar{\omega}^{p-1} = A_p^{-1}T_p\bar{\omega}^p \end{cases},$$

we can write:

$$\begin{cases} \bar{\omega}^{p-1} = P_{p-1}\bar{\omega}^p \\ \bar{\omega}^p \quad = P_p\bar{\omega}^p \end{cases}, \tag{19}$$

where:

$$P_p = I_N and P_{p-1} = A_p^{-1}T_p,$$

To prove that $\bar{\omega}^m = P_m\bar{\omega}^p$ for every $m \leqslant p$. Using (18) we can write:

$$\begin{aligned} \bar{\omega}^{m-1} &= A_m^{-1}T_m\bar{\omega}^m - A_m^{-1}B\bar{\omega}^{m+1} \\ &= A_m^{-1}T_mP_m\bar{\omega}^p - A_m^{-1}BP_{m+1}\bar{\omega}^p \\ &= \underbrace{(A_m^{-1}T_mP_m - A_m^{-1}BP_{m+1})}_{P_{m-1}}\bar{\omega}^p, \end{aligned} \tag{20}$$

where $m \in \{1, 2, \dots, p-1\}$: From(19) and (20), we can calculate the matrices P_m's numerically using the recursive definition as given below:

$$\begin{cases} P_{m-1} = A_m^{-1}(T_mP_m - BP_{m+1}) \; \forall m \in \{1; \dots; p-1\} \\ P_{p-1} = A_p^{-1}T_p \\ P_p \quad = I_N \end{cases}, \tag{21}$$

From (21) and using the fact that $\bar{\omega}^0 = 2\bar{U}$ we can show that:

$$\bar{\omega}^0 = 2\bar{U} = P_0\bar{\omega}^p \quad \Rightarrow \quad \bar{\omega}^p = 2P_0^{-1}\bar{U},$$

and

$$\bar{\omega}^1 = P_1 \bar{\omega}^p = 2P_1 P_0^{-1} \bar{U}, \tag{22}$$

Solving (14) numerically to find $\frac{\partial \bar{u}(n,r)}{\partial r}\Big|_{r\in\Gamma}$, , we write it in matrix form as below:

$$\bar{V} = \bar{\omega}^1 + B^{-1} C \bar{U}, \tag{23}$$

where,

$$\bar{U} = [\bar{u}(1,R), \bar{u}(2,R), \ldots, \bar{u}(N,R)]^T$$
$$\bar{V} = [\bar{v}(1,R), \bar{v}(2,R), \ldots, \bar{v}(N,R)]^T$$

and

$$\bar{v}(n,R) = \frac{\partial \bar{u}(n,r)}{\partial r}(ndt, r \in \Gamma),$$

Also,

$$C = \begin{pmatrix} a & 0 & \ldots\ldots & 0 \\ b & a & 0 & \vdots \\ \vdots & \ddots & \ddots & \ddots \vdots \\ \vdots & & \ddots & \ddots 0 \\ 0 & \ldots\ldots & b & a \end{pmatrix} \quad \text{is an (N)} \times \text{(N) matrix},$$

with:

$$a = -(2 + \tfrac{1}{2r}),$$

$$b = 2 - \tfrac{1}{2r},$$

Then using (22) in (23) :

$$\bar{V} = (2P_1 P_0^{-1} + B^{-1} C)\bar{U}, \tag{24}$$

So, for the two-dimensional case calculation of P_0 and P_1 can be done using the recursive definition given in (21). Once calculated, they allow the calculation of $\bar{V}$ which represents the normal derivative in time domain $\frac{\partial \bar{u}(n,r)}{\partial r}(ndt, r \in \Gamma)$.

For the three-dimensional case we follow the same procedure as in the two dimensional. We do this by solving (16) and (17) numerically and finding the normal derivative in the time domain $\frac{\partial \bar{u}(n,r)}{\partial r}(ndt, r \in \Gamma)$ for the three dimensional case. The only difference between the three and two dimensions solution procedure is the elements of matrix A_j and C. For matrix A_j:

$$a_j = \tfrac{j(j-1)-(m^2+m)}{4r^2},$$

and for matrix C:

$$a = -(2 + \tfrac{1}{r}),$$

$$b = 2 - \tfrac{1}{r},$$

To evaluate the long domain solutions for the boundary conditions in the two and three-dimensional cases and obtain the normal derivative at the boundary Γ, we assume a perfect conductor, $c = 1$, cylindrical modes for two dimensions and spherical modes for three dimensions. We start by deriving the finite difference scheme for the wave equations in two and three dimensions:

The cylindrical mode the two-dimensional equation reduces to:

$$\frac{\partial^2 u}{\partial t^2} = \frac{\partial^2 u}{\partial r^2} + \frac{1}{r}\frac{\partial u}{\partial r} - \frac{n^2}{r^2}u, \tag{25}$$

For the three-dimensional case, spherical mode equation reduces to:

$$\frac{\partial^2 u}{\partial t^2} = \frac{\partial^2 u}{\partial r^2} + \frac{2}{r}\frac{\partial u}{\partial r} - \frac{n(n+1)}{r^2}u, \tag{26}$$

By letting $u_k^p = u(r_k, t_p)$, thus equations (25) and (26) can be approximated by:

For two-dimensional:

$$\frac{\partial^2 u_k^p}{\partial t^2} = \frac{\partial^2 u_k^p}{\partial r^2} + \frac{1}{r_k}\frac{\partial u_k^p}{\partial r} - \frac{n^2}{r_k^2}u_k^p, \tag{27}$$

For three-dimensional:

$$\frac{\partial^2 u_k^p}{\partial t^2} = \frac{\partial^2 u_k^p}{\partial r^2} + \frac{2}{r_k}\frac{\partial u_k^p}{\partial r} - \frac{n(n+1)}{r_k^2}u_k^p, \tag{28}$$

The second order partial derivative can be approximated by second order central differences and the first order partial derivative can be approximated by an average central difference. Where the second order central differences and the first order partial derivatives are defined in section VI.

For two-dimensional:

$$\frac{u_k^{p+1} - 2u_k^p + u_k^{p-1}}{(dt)^2} = \frac{u_{k+1}^p - 2u_k^p + u_{k-1}^p}{(dr)^2} + \frac{1}{2r_k}\frac{u_{k+1}^p - u_{k-1}^p}{dr} - \frac{n^2}{r_k^2}u_k^p, \tag{29}$$

For three-dimensional:

$$\frac{u_k^{p+1} - 2u_k^p + u_k^{p-1}}{(dt)^2} = \frac{u_{k+1}^p - 2u_k^p + u_{k-1}^p}{(dr)^2} + \frac{1}{r_k}\frac{u_{k+1}^p - u_{k-1}^p}{dr} - \frac{n(n+1)}{r_k^2}u_k^p, \tag{30}$$

To discretize the high order local boundary conditions, an explicit finite difference approximation is derived as follows:

By letting $w_j^p = w_j(t_p)$, the two-dimensional equations (2) and (3) can be approximated by:

$$\frac{\partial u_k^p}{\partial t} + \frac{\partial u_k^p}{\partial r} + \frac{1}{2r_k}u_k^p = w_1^p, \tag{31}$$

$$\frac{\partial w_j^p}{\partial t} + \frac{j}{r_k}w_j^p = \frac{(j-\frac{1}{2})^2 - n^2}{4r_k^2}w_{j-1}^p + w_{j+1}^p, \quad j = 1, 2, \ldots \tag{32}$$

For the case of three-dimensional equations (4) and (5) can be approximated by:

$$\frac{\partial u_k^p}{\partial t} + \frac{\partial u_k^p}{\partial r} + \frac{1}{r_k}u_k^p = w_1^p, \tag{33}$$

$$\frac{\partial w_j^p}{\partial t} + \frac{j}{r_k}w_j^p = \frac{j(j-1) - (n^2+n)}{4r_k^2}w_{j-1}^p + w_{j+1}^p, \quad j = 1, 2, 3, \ldots \tag{34}$$

The radial derivative is approximated using a backward difference and average the terms with respect to time in (31) and (33) see section VI. A forward average for time and a backward average for the radius are used to approximate the third term in (31) and (33). Lastly, use a weighted average in time to approximate w_1^p:

$$w_1^p = \frac{3}{2}w_1^p - \frac{1}{2}w_1^{p-1},$$

Similarly, the time derivative in the auxiliary functions that define the higher order boundary condition (32) and (34) can be approximated using a first order forward difference, and a forward average in time to approximate w_j^p and w_{j-1}^p. The last term w_{j+1}^p approximate using a weighted average in time.

For two-dimensional problem:

$$\frac{1}{2dt}((u_k^{p+1}+u_{k-1}^{p+1})-(u_k^p+u_{k-1}^p))+\frac{1}{2dr}((u_k^{p+1}+u_k^p) - (u_{k-1}^{p+1}+u_{k-1}^p))+\frac{1}{8R}(u_k^{p+1}+u_{k-1}^{p+1}+u_k^p+u_{k-1}^p) = \frac{3}{2}w_1^p - \frac{1}{2}w_1^{p-1}, \quad (35)$$

$$\frac{1}{dt}(w_j^{p+1}-w_j^p)+\frac{j}{2R}(w_j^{p+1}+w_j^p) = \frac{(j-\frac{1}{2})^2-n^2}{8R^2}(w_{j-1}^{p+1}+w_{j-1}^p)+\frac{3}{2}w_{j+1}^p-\frac{1}{2}w_{j+1}^{p-1}, \quad (36)$$

For the three-dimensional problem:

$$\frac{1}{2dt}((u_k^{p+1}+u_{k-1}^{p+1})-(u_k^p+u_{k-1}^p))+\frac{1}{2dr}((u_k^{p+1}+u_k^p) - (u_{k-1}^{p+1}+u_{k-1}^p))+\frac{1}{4R}(u_k^{p+1}+u_{k-1}^{p+1}+u_k^p+u_{k-1}^p) = \frac{3}{2}w_1^p - \frac{1}{2}w_1^{p-1}, \quad (37)$$

$$\frac{1}{dt}(w_j^{p+1}-w_j^p)+\frac{j}{R}(w_j^{p+1}+w_j^p) = \frac{j(j-1)-(n^2+n)}{8R^2}(w_{j-1}^{p+1}+w_{j-1}^p)+\frac{3}{2}w_{j+1}^p-\frac{1}{2}w_{j+1}^{p-1}, \quad (38)$$

and in both cases the normal derivative ($\frac{\partial u}{\partial r}$) can be approximated using a backward difference and average the terms with respect to time as follows:

$$\frac{\partial u}{\partial r} = \frac{(u_k^{p+1}+u_k^p)-(u_{k-1}^{p+1}+u_{k-1}^p)}{2dr}, \quad (39)$$

We solve these equations sequentially. In [2] the authors prove that:

$$\omega_j = O(r^{-2j+\frac{1}{2}}) \text{ for } 2-D,$$
$$\omega_j = O(r^{-2j-1}) \text{ for } 3-D,$$

We can infer that the remainder becomes zero after fixed arbitrarily j depending on the desired accuracy. Let us call the last non-zero remainder ω_N, that is all remainder ω_j with $j > N$ is neglected and assumed to be zero. Therefore, (w_{j+1}) is smaller than (w_j) and (w_1) is smaller than (w_0). The boundary conditions are applied halfway between the last two meshes.

This procedure allows the calculation of the long domain normal derivative of the scattered field ($\frac{\partial u_s}{\partial r}$) at the surface of the scatterer. The radar cross section (RCS) of a scatterer can be solved using the on surface radiation boundary conditions. The scattered field ($U_s(\underline{x})$) at some distance from the scatterer boundary Γ is given by [12]:

$$U_s(\underline{x}) = \int_\Gamma \left[G(\underline{x},\underline{y})\frac{\partial U_s(\underline{y}))}{\partial n} - U_s(\underline{y})\frac{\partial G(\underline{x},\underline{y})}{\partial n}\right] ds, \quad (40)$$

Where $G(\underline{x},\underline{y})$ is the free space Green's function given by:

$$G(\underline{x},\underline{y}) = -(i/4)H_0^1(kd) \quad \text{for } 2-D,$$
$$G(\underline{x},\underline{y}) = \frac{e^{ikd}}{4\pi d} \quad \text{for } 3-D,$$

and, $d = \left|\underline{x}-\underline{y}\right|$, $\frac{\partial}{\partial n}$ is the outward normal derivative on Γ, $\underline{y}$ is on Γ, $\underline{x}$ is some distance from Γ, U_s is the Fourier transform of u_s, and k is the wave number. It is known that the far field expansion of (40) for two and three dimensional can be written as:

$$U_s(\underline{x}) = A_0\frac{e^{ikr}}{\sqrt{r}} \quad \text{for } 2-D, \quad (41)$$

$$U_s(\underline{x}) = \bar{A}_0\frac{e^{ikr}}{r} \quad \text{for } 3-D, \quad (42)$$

Where the term A_0 in (41) is given by (see section VII):

$$A_0 = \frac{e^{j\pi 4}}{\sqrt{8k\pi}}\int_\Gamma \left[\frac{\partial U_s(\underline{y})}{\partial n} - jk\cos\delta U_{inc}(\underline{y})\right] e^{-jk\psi} ds, \quad (43)$$

and $\bar{A}_0$ in (42) is given by (see section VII):

$$\bar{A}_0 = \frac{1}{4\pi}\int_\Gamma \left[\frac{\partial U_s(\underline{y})}{\partial n} - jk\cos\delta U_{inc}(\underline{y})\right] e^{-jk\psi} ds, \quad (44)$$

Where $\cos\delta = \underline{\hat{x}}.\hat{n}$ and $\psi = \underline{\hat{x}}.\underline{y}$. The RCS can be calculated using A_0 by the following expression:

$$RCS = 10\log_{10}(2\pi R\left|A_0\right|^2) \quad \text{for } 2-D, \quad (45)$$

$$RCS = 10\log_{10}(4\pi R^2\left|\bar{A}_0\right|^2) \quad \text{for } 3-D, \quad (46)$$

IV. RESULTS

To demonstrate the results obtained for a circular and spherical scatterer, we developed a series of numerical tests. The first example is for the incident field on the perfectly conducting sphere of radius one for the three dimensional case (a disk of radius one for the two dimensional case).

For two dimensional:

$$u_{inc}(\underline{x},t) = \frac{1-\cos 2\pi t}{1+t^2}\cos n\theta, \quad (47)$$

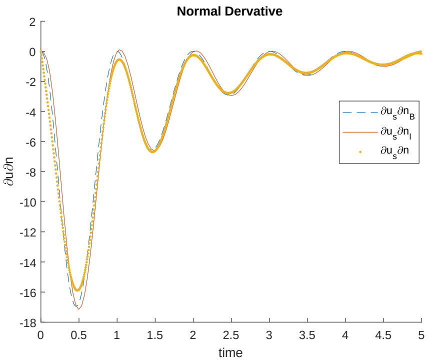

Fig. 2. Comparison of long domain ($\partial u_s \partial n_l$), the finite difference scheme for OSRBC ($\partial u_s \partial n$) and the bilinear method for OSRBC ($\partial u_s \partial n_B$) solutions for normal derivative at $t = 5$ for the two-dimensional case.

For three dimensional:

$$u_{inc}(\underline{x},t)=\frac{1-\cos 2\pi t}{1+t^2}(\cos m\phi+\sin m\phi)P_n^m(\cos n\theta), \tag{48}$$

The normal derivative for the long domain solution ($\frac{\partial u_{long}}{\partial n}$) is calculated for the artificial boundary condition at the location $R = 10$. The long domain solution ($\frac{\partial u_{long}}{\partial n}$) compared with the normal derivative ($\frac{\partial u}{\partial n}$) calculated using the high order OSRBC at the surface of the scatterer. Two numerical approaches are used to discretize the high order OSRBC at the surface of the scatterer in a time domain. The first approach is the finite difference scheme. The second approach is the bilinear method. Both approaches are described in section 3. Figure 2 compares the normal derivatives (2-dimensional case) at $dr = 0.8dt$, $t = 5$, $c = 1$, the order of auxiliary functions $N = 5$, the high order boundary conditions at the surface of the scatterer with $R = 1$ and $n = 10$. Figure 3 compares the results for the same conditions but for $t = 10$ and the order of auxiliary functions $N = 8$. The figures show that discretize the high order OSRBC in the time domain using the bilinear method leads to higher accuracy compared to a finite difference scheme under the same variable values. Also, Fig. 3 clearly shows that the error decreases when t and the number of auxiliary functions N are increased. Figure 4 and Fig. 5 compare the results for the three-dimensional case. The results are almost identical to the two-dimensional case where the bilinear method gives the smallest error compare to the finite difference scheme. Clearly, the normal derivative ($\frac{\partial u}{\partial n}$) calculated using the high order OSRBC at the surface of the scatterer in the time domain gives better results for the three- dimensional case compared to the two-dimensional case. To compare the long domain solution for the normal derivative ($\partial u_{sl} \partial n$) with the high order on surface radiation boundary conditions solution

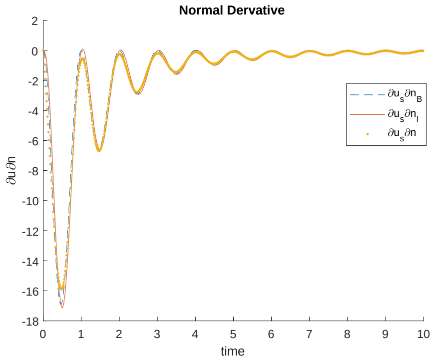

Fig. 3. Comparison of long domain ($\partial u_s \partial n_l$), the finite difference scheme for OSRBC ($\partial u_s \partial n$) and the bilinear method for OSRBC ($\partial u_s \partial n_B$) solutions for normal derivative at $t = 10$ for the two-dimensional case.

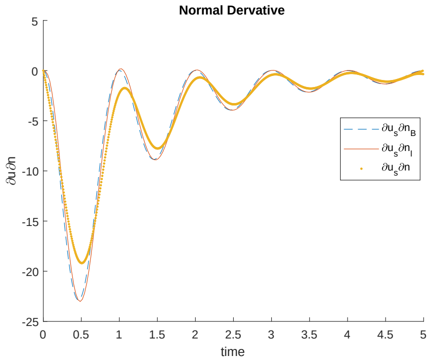

Fig. 4. Comparison of long domain ($\partial u_{sl} \partial n$), the finite difference scheme for OSRBC ($\partial u_s \partial n$) and the bilinear method for OSRBC ($\partial u_s \partial n_B$) solutions for normal derivative at $t = 5$ for the three-dimensional case.

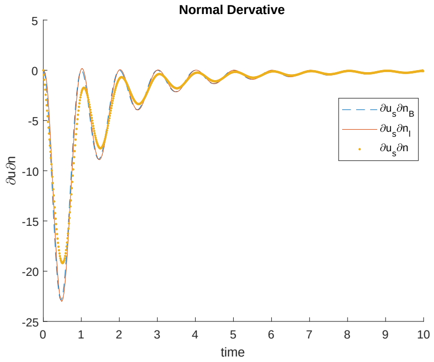

Fig. 5. Comparison of long domain ($\partial u_{sl} \partial n$), the finite difference scheme for OSRBC ($\partial u_s \partial n$) and the bilinear method for OSRBC ($\partial u_s \partial n_B$) solutions for normal derivative at $t = 10$ for the three-dimensional case.

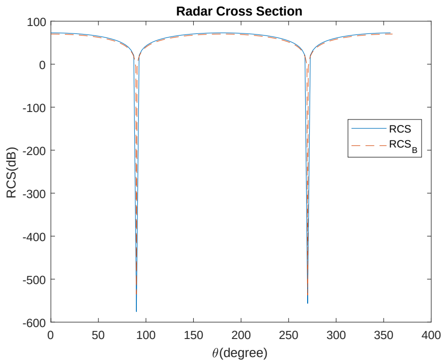

Fig. 6. Comparison of RCS calculation using the long solution and the OSRBC solution based on bilinear method for the two-dimensional case.

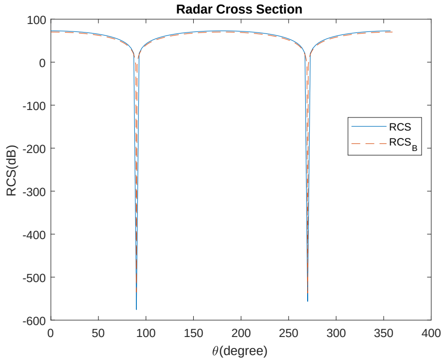

Fig. 7. Comparison of RCS calculation using the long solution and the OSRBC solution based on bilinear method for the three-dimensional case.

($\partial u_s \partial n_B$), we did numerical computations to calculate the Radar Cross Section (RCS) as defined by equations (45) and (46) and shown in Fig. 6 and Fig. 7. We observe that the results are almost identical for both solutions and calculating the RCS using the bilinear method solution for the normal derivative ($\partial u_s \partial n_B$) needed less computational time compared to the long domain solution for the normal derivative ($\partial u_{sl} \partial n$).

V. CONCLUSION

This paper presents a new high order time domain OSRBCs based on high order boundary condition introduced by [2] in two and three dimensions. The thrust of the OSRBC is to calculate the normal derivative on the scatterer. Once the normal derivative is calculated, an application to calculate radar cross sections is presented. As shown in the analysis and the numerical implementations, two different procedures have been used to calculate the normal derivative ($\partial u \partial n$). The first procedure based on the new high order OSRBC which calculates accurately and efficiently the normal derivatives ($\partial u \partial n$) on the surface of the scatterer. The second procedure is the exact solution based on long domain solutions ($\partial u_{sl} \partial n$). These two procedures are used to calculate errors. The new high order OSRBC results in a smaller error when the order of the auxiliary functions is increased. Numerical examples are provided for calculating the normal derivatives and radar cross section. Bilinear transform techniques used to discretize the new high order OSRBC and the auxiliary functions. This technique is contrasted with the traditional differencing to approximate time derivatives. The use of the bilinear transformation leads to higher accuracy and substantial simplifications in implementations when compared to the different types of standard finite difference schemes used to discretize the higher order OSRBCs and the auxiliary functions. This procedure can be extended to full Maxwell's equations and is currently under investigation.

VI. PARTIAL DERIVATIVES APPROXIMATION

It can be shown in [21] that the partial derivatives can be approximated by second order central differences as:

$$\frac{\partial^2 u_k^p}{\partial t^2} = \frac{u_k^{p+1} - 2u_k^p + u_k^{p-1}}{(dt)^2}, \tag{49}$$

$$\frac{\partial^2 u_k^p}{\partial r^2} = \frac{u_{k+1}^p - 2u_k^p + u_{k-1}^p}{(dr)^2}, \tag{50}$$

The average central differences approximation for first order partial derivative define as:

$$\frac{\partial u_k^p}{\partial r} = \frac{u_{k+1}^p - u_{k-1}^p}{2dr}, \tag{51}$$

The backward difference and average the term with respect to time is used to approximate the first order partial derivative is define as:

$$\frac{\partial u_k^p}{\partial r} = \frac{1}{2dr}((u_k^{p+1} + u_k^p) - (u_{k-1}^{p+1} + u_{k-1}^p)), \tag{52}$$

The forward average for time and a backward average for the radius is define as:

$$\frac{u_k^p}{r_k} = \frac{u_k^{p+1} + u_{k-1}^{p+1} + u_k^p + u_{k-1}^p}{4r}, \tag{53}$$

VII. RADAR CROSS SECTION CALCULATION

A. Radar cross section calculation for two-dimensional case

For the scatterer with boundary Γ, the Green's second identity is used to calculate the scattered field ($U_s(\underline{x})$) at some distance from the scatterer boundary Γ is given by [12]:

$$U_s(\underline{x}) = \int_\Gamma \left[G(\underline{x}, \underline{y}) \frac{\partial U_s(\underline{y})}{\partial n} - U_s(\underline{y}) \frac{\partial G(\underline{x}, \underline{y})}{\partial n} \right] ds_{\underline{y}}, \tag{54}$$

Where $G(\underline{x},\underline{y})$ is the free space Green's function given by:

$$G(\underline{x},\underline{y}) = -(i/4)H_0^1(kd) \quad \text{for } 2-D, \tag{55}$$

$$G(\underline{x},\underline{y}) = \frac{e^{ikd}}{4\pi d} \quad \text{for } 3-D, \tag{56}$$

and, $d = \left|\underline{x}-\underline{y}\right|$, $\frac{\partial}{\partial n}$ is the outward normal derivative on Γ, $\underline{y}$ is on Γ, $\underline{x}$ at some distance from Γ, $U_s(\underline{x})$ is the Fourier transform of $u_s(\underline{x})$, and k is the wave number. To evaluate the integral in (54), we need to find the $\frac{\partial G(\underline{x},\underline{y})}{\partial n}$ for two dimensions:

$$\frac{\partial G(\underline{x},\underline{y})}{\partial n} = \frac{ik}{4}H_1^1(k\left|\underline{x}-\underline{y}\right|)\frac{\partial}{\partial n}\left|\underline{x}-\underline{y}\right|, \tag{57}$$

$$\begin{aligned}\tfrac{\partial}{\partial n}\left|\underline{x}-\underline{y}\right| &= \tfrac{\partial}{\partial n}\sqrt{(x_1-y_1)^2+(x_2-y_2)^2}\\ &= \bigtriangledown(\sqrt{(x_1-y_1)^2+(x_2-y_2)^2})\cdot\hat{n_{\underline{y}}},\\ &= \tfrac{(y_1-x_1)i+(y_2-x_2)j}{\sqrt{(x_1-y_1)^2+(x_2-y_2)^2}}\cdot\hat{n_{\underline{y}}}\end{aligned} \tag{58}$$

When $\underline{x}\to\infty$ the (59) becomes:

$$\begin{aligned}\tfrac{\partial}{\partial n}\left|\underline{x}-\underline{y}\right| &= -\tfrac{(x_1)i+(x_2)j}{\sqrt{(x_1)^2+(x_2)^2}}\cdot\hat{n_{\underline{y}}}\\ &= -\hat{\underline{x}}\cdot\hat{n_{\underline{y}}}\\ &= -\cos\delta,\end{aligned} \tag{59}$$

The asymptotic approximation for the Hankel function [22] H_0^1 and H_1^1 when $d\to\infty$ is given as:

$$\frac{i}{4}H_0^1(d) = \sqrt{\frac{1}{8\pi d}}e^{i(d+\frac{\pi}{4})},$$

$$\frac{i}{4}H_1^1(d) = i\sqrt{\frac{1}{8\pi d}}e^{i(d+\frac{\pi}{4})},$$

Assume $d = k\left|\underline{x}-\underline{y}\right|$ and using the law of cosine:

$$d = k\sqrt{\left|\underline{x}\right|^2+\left|\underline{y}\right|^2-2\left|\underline{x}\right|\left|\underline{x}\right|\cos\gamma},$$

As $\underline{x}\to\infty$,

$$d \simeq k(\left|\underline{x}\right|-\left|\underline{y}\right|\cos\gamma),$$

Now, as $d\to\infty$,

$$d \simeq kr - k\psi, \tag{60}$$

Where r is the distance from the center of the scatterer to the point $\underline{x}$ and $\psi = \left|\underline{y}\right|\cos\gamma = R\cos(\theta-\theta')$. Thus, we can use the (60) in (55). Now the (54):

$$\begin{aligned}U_s(\underline{x}) = &\int_\Gamma \sqrt{\frac{1}{8\pi(kr-k\psi)}}e^{i((kr-k\psi)+\frac{\pi}{4})}\frac{\partial U_s(\underline{y}))}{\partial n}\\ &-U_s(\underline{y})ik\sqrt{\frac{1}{8\pi(kr-k\psi)}}e^{i((kr-k\psi)+\frac{\pi}{4})}\cos\delta ds_{\underline{y}} =\\ &\frac{e^{\frac{-i\pi}{4}}}{\sqrt{8\pi kr}}\int_\Gamma\left[\frac{\partial U_s(\underline{y}))}{\partial n}+ik\cos\delta U_s(\underline{y})e^{ikr}e^{-ik\psi}\right]ds_{\underline{y}},\end{aligned} \tag{61}$$

Where $U_s(\underline{y})\mid_\Gamma = -U_{inc}(\underline{y})$,

$$\begin{aligned}&U_s(\underline{x}) =\\ &\frac{e^{\frac{-i\pi}{4}}}{\sqrt{8\pi kr}}\int_\Gamma\left[\frac{\partial U_s(\underline{y}))}{\partial n}-ik\cos\delta U_{inc}(\underline{y})e^{ikr}e^{-ik\psi}\right]ds_{\underline{y}},\end{aligned} \tag{62}$$

B. Radar cross section calculation for three-dimensional case

For three-dimensional, the Green's function given by:

$$G(\underline{x},\underline{y}) = \frac{e^{ikd}}{4\pi d} \quad \text{for } 3-D, \tag{63}$$

To evaluate the integral in (54), we need to find the $\frac{\partial G(\underline{x},\underline{y})}{\partial n}$ for three dimensions:

$$\frac{\partial G(\underline{x},\underline{y})}{\partial n} = \bigtriangledown G\cdot\hat{n}, \tag{64}$$

Where:

$$\bigtriangledown G = \tfrac{e^{ikd}}{4\pi d}\left[ik-\tfrac{1}{d}\right]\left(\tfrac{(y_1-x_1)i+(y_2-x_2)j+(y_3-x_3)k}{\sqrt{(x_1-y_1)^2+(x_2-y_2)^2+(x_3-y_3)^2}}\right), \tag{65}$$

As $\underline{x}\to\infty$,

$$d \simeq k(\left|\underline{x}\right|-\left|\underline{y}\right|\cos\gamma),$$

and, as $d\to\infty$,

$$d \simeq kr - k\psi, \tag{66}$$

Thus, we can use the (66) in (64).

$$\begin{aligned}\tfrac{\partial G(\underline{x},\underline{y})}{\partial n} &= \tfrac{e^{ik(r-\psi)}}{4\pi(r-\psi)}\left[ik-\tfrac{1}{r-\psi}\right](-\cos\gamma)\\ &\simeq \tfrac{-ike^{ik(r-\psi)}}{4\pi(r-\psi)}\cos\gamma,\end{aligned} \tag{67}$$

Now, using the (67) in (54):

$$\begin{aligned}U_s(\underline{x}) &= \tfrac{e^{ikr}}{4\pi r}\int_\Gamma\left[\tfrac{\partial U_s(\underline{y})}{\partial n}+jk\cos\delta U_s(\underline{y})\right]e^{-jk\psi}ds_{\underline{y}}\\ &= \tfrac{e^{ikr}}{4\pi r}\int_\Gamma\left[\tfrac{\partial U_s(\underline{y})}{\partial n}-jk\cos\delta U_{inc}(\underline{y})\right]e^{-jk\psi}ds_{\underline{y}},\end{aligned} \tag{68}$$

Where $U_s(\underline{y})\mid_\Gamma = -U_{inc}(\underline{y})$.

REFERENCES

[1] H. Alzubaidi, X. Antoine, and C. Chniti, "Formulation and accuracy of on-surface radiation conditions for acoustic multiple scattering problems," *Applied Mathematics and Computation*, vol. 277, pp. 82–100, 2016.

[2] T. Hagstrom and S. I. Hariharan, "A formulation of asymptotic and exact boundary conditions using local operators," *Applied Numerical Mathematics*, vol. 27, no. 4, pp. 403–416, 1998.

[3] X. Antoine, "Advances in the on-surface radiation condition method: Theory, numerics and applications," *Computational Methods for Acoustics Problems*, pp. 169–194, 2008.

[4] Y. Mao, A. Z. Elsherbeni, S. Li, and T. Jiang, "Surface impedance absorbing boundary for terminating fdtd simulations." *Applied Computational Electromagnetics Society Journal*, vol. 29, no. 12, 2014.

[5] X. Antoine, M. Darbas, and Y. Y. Lu, "An improved on-surface radiation condition for acoustic scattering problems in the high-frequency spectrum," *Comptes Rendus Mathematique*, vol. 340, no. 10, pp. 769–774, 2005.

[6] L. L. Thompson, "A review of finite-element methods for time-harmonic acoustics," *The Journal of the Acoustical Society of America*, vol. 119, no. 3, pp. 1315–1330, 2006.

[7] J.-P. Berenger, "A perfectly matched layer for the absorption of electromagnetic waves," *Journal of Computational Physics*, vol. 114, no. 2, pp. 185–200, 1994.

[8] I. Mahariq, M. Kuzuoğlu, and I. Tarman, "On the attenuation of the perfectly matched layer in electromagnetic scattering problems with the spectral element method." *Applied Computational Electromagnetics Society Journal*, vol. 29, no. 9, 2014.

[9] J.-C. Nédélec, *Acoustic and Electromagnetic Equations: Integral Representations for Harmonic Problems*. Springer Science & Business Media, 2001, vol. 144.

[10] D. Colton and R. Kress, *Integral Equation Methods in Scattering Theory*. SIAM, 2013, vol. 72.

[11] F. Ihlenburg, *Finite Element Analysis of Acoustic Scattering*. Springer Science & Business Media, 2006, vol. 132.

[12] G. Kriegsmann, A. Taflove, and K. Umashankar, "A new formulation of electromagnetic wave scattering using an on-surface radiation boundary condition approach," *IEEE Transactions on Antennas and Propagation*, vol. 35, no. 2, pp. 153–161, 1987.

[13] G. A. Kriegsmann and T. Moore, "An application of the on-surface radiation condition to the scattering of acoustic waves by a reactively loaded sphere," *Wave Motion*, vol. 10, no. 3, pp. 277–284, 1988.

[14] A. Bayliss and E. Turkel, "Radiation boundary conditions for wave-like equations," *Communications on Pure and applied Mathematics*, vol. 33, no. 6, pp. 707–725, 1980.

[15] A. Bayliss, M. Gunzburger, and E. Turkel, "Boundary conditions for the numerical solution of elliptic equations in exterior regions," *SIAM Journal on Applied Mathematics*, vol. 42, no. 2, pp. 430–451, 1982.

[16] B. Engquist and A. Majda, "Absorbing boundary conditions for numerical simulation of waves," *Proceedings of the National Academy of Sciences*, vol. 74, no. 5, pp. 1765–1766, 1977.

[17] S. I. Hariharan and S. Sawyer, "Transform potential-theoretic method for acoustic radiation from structures," *Journal of Aerospace Engineering*, vol. 18, no. 1, pp. 60–67, 2005.

[18] J. G. Proakis and D. K. Manolakis, *Digital Signal Processing (4th Edition)*. Prentice-Hall, Inc., 2006.

[19] N. Berrabah, "On high order on-surface radiation boundary conditions," 2014.

[20] A. Al Weshah and S. Hariharan, "A fourier spectral method to solve high order on-surface radiation boundary conditions in electromagnetics," in *Electrical and Electronics Engineering Conference (JIEEEC), 2017 10th Jordanian International*. IEEE, 2017, pp. 1–6.

[21] D. Colton, *Partial Differential Equations: An Introduction*. Dover Publications, 2012.

[22] M. Abramowitz and I. A. Stegun, *Handbook of Mathematical Functions: With Formulas, Graphs, and Mathematical Tables*. Courier Corporation, 2012.

Shielding Effectiveness of HSD Connector – Simulation and Measurement

Nikola Jurgec [1], Ivan Vukosav [2], Darko Marinac [2], and Bojan Trkulja [3]

[1] Koncar D&ST, Zagreb, 10000, Croatia
nikola.jurgec@koncar-dst.hr

[2] Yazaki Europe Ltd., Zagreb 10000, Croatia
ivan.vukosav@yazaki-europe.com, darko.marinac@yazaki-europe.com

[3] Faculty of Electrical Engineering and Computing
University of Zagreb, Zagreb, 10000, Croatia
bojan.trkulja@fer.hr

Abstract **─** The goal of designing a shielded High-Speed Data (HSD) connectors is to find the ideal balance between economy and performance. The connectors are a part of many systems and they influence their performance. The connectors should be designed to avoid possible negative effects on system properties. Thus, it is necessary to analyze the shielding effectiveness of connectors to ensure the electromagnetic compatibility (EMC) of the whole system. The transfer impedance is an effective shield parameter used to evaluate the shielding effectiveness of cables and connectors. Based on the analysis of the limitation of available test methods, a 3D model is developed to numerically calculate the transfer impedance of the HSD connector. Even though numerical methods were used, the theoretical foundations necessary to interpret the obtained results are revisited. The theory associated with cable shielding is revisited through solving known equations for the transfer impedance of a coaxial cable with a braided shield and foil.

Index Terms **─** electromagnetic compatibility, shielding effectiveness, transfer impedance.

I. INTRODUCTION

The concept of transfer impedance introduced by Schelkunoff [1] is used to measure the shielding effectiveness of cable shields [2, 3]. Transfer impedance is the property of the shield that relates the voltage induced in the shielded circuit to the current in the shield. To consider the employment of transfer impedance for practical purposes, it should be easily evaluated and measured. There are many developed measurement techniques, standardized tests, guides and descriptions in the literature that give good analytical and empirical approaches for determining transfer impedance of common geometries such as the tubular and braided shield. According to the evaluations in the literature, the transfer impedance at low and medium frequency range can be accurately determined. Transfer impedance Z_T is equal to the DC resistance of the shield up to the frequency where the ratio of the thickness of the shield and skin depth is much less than 1, i.e., $\varDelta\backslash\delta \ll 1$ [4]. The developed analytical expressions for calculation of transfer impedance for higher frequency range, where inductance plays an important role, are lacking accuracy [5].

The known approaches for calculating the transfer impedance for a complex geometry such as the braided shield are primarily based on semi-empirical models where analytical formulations are modified based on the experimental results obtained by measuring many various braids [6]. The Semi-empirical models compare well against the measured values for a limited number of braids where all the construction parameters of the braid are aligned with those proposed by the analytical model.

The objective of this work is to present a model for the computation of the transfer impedance of HSD connector based on the finite element method (FEM). The advantages of this approach, as opposed to the analytical and empirical methods, are the ability to deal with complex materials and geometries. The transfer impedance of the developed FEM model is benchmarked against measurements.

II. COAXIAL CABLE TRANSFER IMPEDANCE CALCULATION AND MEASUREMENT

This section revisits the theoretical foundations necessary for interpreting physical phenomena associated with cable shielding. There are different analytical models available for the evaluation of shielding effectiveness. A summary of a known semi-

Submitted On: June 26, 2019
Accepted On: December 10, 2019

empirical model proposed by Kley [7] is presented for a better understanding of the theory on a known problem. The following parameters define a braided shield:

m	number of carriers,
n	number of wires in each carrier,
d	wire diameter,
D_0	diameter under the braid,
s	lay length,

$D_m = D_0 + 2.5d$	average braid diameter,
$\alpha = \arctan(\pi D_m / s)$	weave angle ,
$G_0 = mnd / (2\pi D_m)$	minimal filling factor,
$G = G_0 / \cos(\alpha)$	filling factor,
$B = G(2-G)$	optical coverage.

The DC resistance of the braid per unit length can be calculated by using the equation:

$$R_{DC} = \frac{4}{\sigma mnd^2 \pi} \frac{1}{\cos(\alpha)} = \frac{1}{\sigma G_0 \cos(\alpha)} \frac{2}{\pi^2 D_m d}. \quad (1)$$

The shield transfer impedance is governed by:

$$Z_T = \frac{1}{I_S} \frac{dV}{dl}, \quad (2)$$

where Z_T is the transfer impedance in ohms per unit length, I_S is the shield current, V is the voltage induced between the internal conductors and the shield, and l is the length of the cable. The smaller the transfer impedance, the more effective the shielding.

Tyni's model [8] gives an equation for the transfer impedance of braided shield as:

$$Z_T = Z_R + i\omega L_T + (q+i)\omega L_S. \quad (3)$$

Z_R is the transfer impedance of a tube with a thickness of d [1].

$$Z_R \approx \frac{1}{\sigma G_0 \cos\alpha} \frac{2}{\pi^2 D_m d} \frac{d_R(1+i)\delta}{sh[d_R(1+i)/\delta]}. \quad (4)$$

Coupling inductance L_T and eddy currents inductance L_S are given as:

$$L_T \approx \frac{\mu_0}{m}[0.875\frac{\pi}{6}(2-\cos\alpha(1-G)^3)e^{-\tau_H}] - \frac{0.11}{n} cos(2k_1\alpha)].$$

$$\omega L_S \approx \frac{1}{\pi\sigma\delta}\frac{1}{D_m}[10\pi G_0^2(\cos\alpha(1-G)e^{-\tau_E} - \frac{3.3}{2\pi G_0}\cos(2k_2\alpha)].$$

$$d_R = 0.67d / \sqrt{\cos\alpha} \qquad \tau_E = 12G\sqrt[3]{B^2 d / D_m}$$

$$k_1 = \frac{\pi}{4}[\frac{2}{3}G_0 + \frac{\pi}{10}]^{-1} \qquad \delta = \sqrt{2/(\omega\mu_0\sigma)} \; (\mu_r = 1) .$$

$$\tau_H = 9.6G\sqrt[3]{B^2 d / D_m} \qquad k_2 = \frac{\pi}{4}[\frac{2}{3}G_0 + \frac{3}{8}]^{-1}$$

Variable τ_H is the magnetic field attenuation factor of the chimney effect. The ωL_S term is used to account for eddy currents in the aperture's walls due to the magnetic field that penetrates the shield. Transfer impedance as the combination of two shields can be calculated by using equation [9]:

$$Z_T = \frac{Z_{T1} Z_{T2}}{Z_{S1} + Z_{S2} + j\omega L_{12}}. \quad (5)$$

Z_{T1}	transfer impedance of outer shield,
Z_{T2}	transfer impedance of inner shield,
Z_{S1}	internal impedance of outer shield,
Z_{S2}	internal impedance of inner shield,
L_{12}	inductance of the shield to shield line.

The comparison of calculated values and measurement on equivalent cable are shown in Fig. 1. The result of measurement follows the analytical model up to a certain frequency, due to several reasons. First, the perfect quality of the shield with no manufacturing related faults is assumed. Also, measurement contains resonances in the line because of the mismatches and the finite length of the measurement sample. These resonances are not taken into account by the analytical model [10].

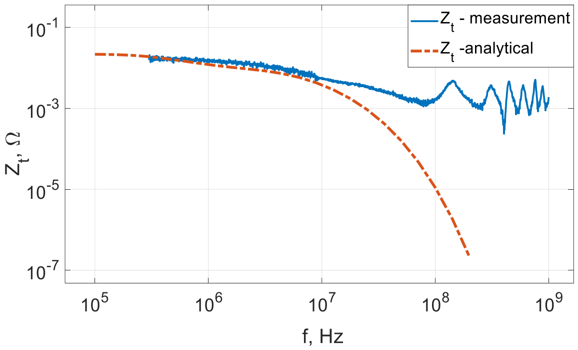

Fig. 1. Comparison of the calculated values of transfer impedance with measurement on a sample with m=16, n=8, $\alpha = 27$, $d = 0.1$ mm, $D_m = 3.3$ mm, $\epsilon_r = 2.1$.

In theoretical evaluations, the curve of transfer impedance is given as a single (deterministic) curve. In reality, that curve is greatly impacted by manufacturing tolerances.

Different shielding effectiveness values can be measured among different manufacturers and sometimes even among sample cables made by the same manufacturer [11]. Production tolerances, deviations in the manufacturing process, test sample preparation techniques or systematic errors can cause that behavior. Production tolerances on shield geometry parameters cause great changes in the values of shielding effectiveness [12]. For example, the optical coverage parameter of the shield is greatly affected by the carrier width. Equation (3) shows that the optical coverage parameter has a major effect on transfer impedance at a higher frequency range.

Even more accurate models and equations do not yield significantly better results and the divergence of measured and calculated values is significant. More accurate analytical models are useful for getting the dependence of optimal solutions on cable design constraints. Also, such models are used to determine the stability and sensitivity of the optimal solutions to the variations of the variables.

A more complex model was introduced by Latham [13], who developed equations that take into account the presence of nearby conductors, shield surface curvature and interaction between neighboring holes. Madle [14] introduced a coupling mechanism named "porpoising", which incorporates a special spirality effect to describe diffusion and aperture penetration.

The data obtained by these models is a great aid because it enables the manufacturing process optimization that leads to enormously improved shield effectiveness. However, even more complex analytical models can rarely evaluate the exact curve of the transfer impedance parameter that does not have a divergence from the measurement data [15].

III. HSD CONNECTOR TRANSFER IMPEDANCE SIMULATION AND MEASUREMENT

To take into account the complex geometry of a connector advanced numerical techniques and computational electromagnetics codes are employed. Transfer impedance was calculated by using numerical methods for the 3D model of the HSD connector shown in Fig. 2 and Fig. 3. There is no analytical solution for such geometry, therefore the use of numerical modeling is required [16]. For this simulation, a High Frequency Structure Simulator (HFSS) is employed. HFSS is 3D electromagnetic simulation software for designing and simulating high-frequency electronic products [17].

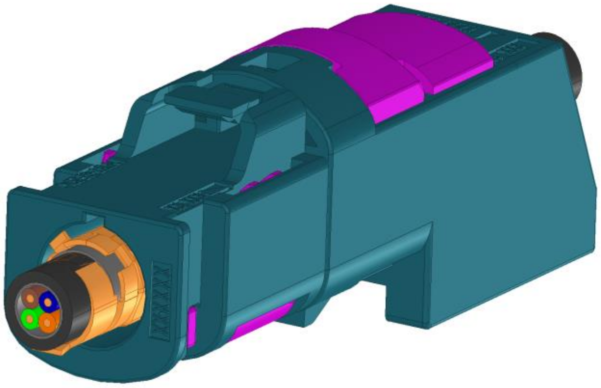

Fig. 2. A 3D model of HSD connector.

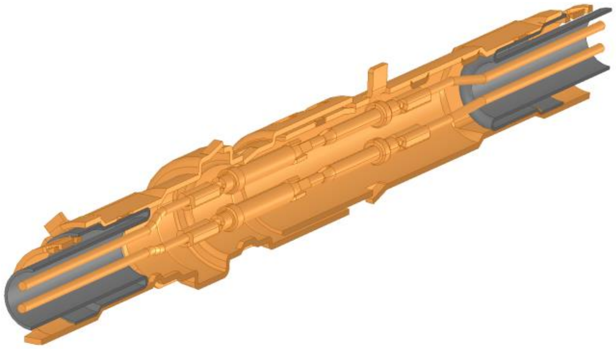

Fig. 3. Cross-section of shield and conductors in HSD connector.

In this case, a solution has to satisfy the given boundary and excitation conditions. Boundary conditions are defined by setting geometry properties in the model. A geometry defined as a perfect electric conductor represents a boundary where the value of tangential electric field is forced to zero. Excitations have to be correctly positioned and oriented to excite the desired model. If a solution that satisfies all of the boundary and excitation conditions is found, then the problem is solved.

The underlying idea of numerical calculation is to expand the unknown solution in terms of known expansion functions with unknown coefficients. The goal is to approximate unknown solution $f(x)$ by a sum of known expansion functions $f_i(x)$

$$f(x) \approx \sum_i a_i f_i(x), \tag{6}$$

where the coefficient a_i of each expansion function have to be such that the sum (6) approaches the function $f(x)$.

A. Setting up the model

By far, one of the most familiar and often used measurement setups for measuring transfer impedance is the triaxial tube in tube method [18]. While propagating through the shield, the EMI energy is attenuated by the shield. If the attenuation of the EMI energy passing through the shield is better, for the same magnitude of induced current I_S there is smaller dV generated by the same field so the shield is better. The parameter Z_t, as a result of voltage by current division, represents impedance per unit length. However, unlike the characteristic impedance, which determines the signal propagation properties along the cable, Z_T characterizes the energy propagation across the cable - through the shield [11].

A full developed assembly, equivalent to measurement setup for the triaxial tube in tube method setup is shown in Fig. 4. With defined excitations, the solver introduces electric field into the model area. Electric field couple to surrounding conductors and dielectrics through induced charges, currents and electromotive forces. From solver's point of view, created 3D model represents a problem of finding coupling mechanisms, parasitic interactions and distributed effects in the model. This problem is solved by finding approximate solutions to Maxwell's equations that satisfy specified conditions. To find such solutions the problem space is subdivided into elements, and then the magnitude of the assumed field at the junction of elements is found. The final solution is the sum of contributions from each element in a domain.

For the modeled problem, the HFSS software attempts to numerically solve the equation:

$$\nabla \times \left(\frac{1}{\mu_r}\nabla \times E(x,y) - k_0^2 \epsilon_r E(x,y)\right) = 0, \qquad (7)$$

where:

$E(x,y)$ is a phasor representing an oscillating electric field,

k_0 is the free space wave number,

μ_r is the complex relative permeability,

ϵ_r is the complex relative permittivity.

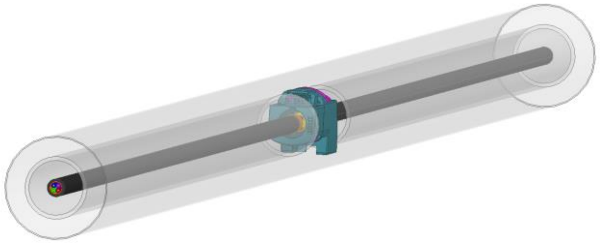

Fig. 4. FEM model of a cable-connector assembly of the triaxial method.

Treating shielding as a transmission line problem with both loss and reflection components as proposed by Ott [12] requires the solver to solve equation (7). For each frequency, a solution is given in the form of phasor $E(x,y)$, which after being multiplied by $e^{-\gamma z}$ becomes a traveling wave.

The internal circuit in a coaxial cable is usually matched to its characteristic impedance to improve the upper frequency limit because it minimizes the reflections in the system. For this measurement, all transmission lines were terminated in their characteristic impedance to avoid standing waves [19]. The common-mode characteristic impedance of the pair of contacts that was used to drive the connector shield was previously measured by using the time domain reflectometry and the results are shown in Fig. 5.

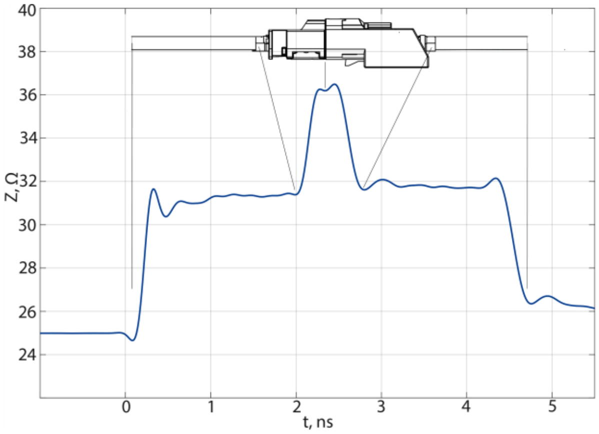

Fig. 5. TDR measurement of a system.

Results of measurement and simulation of the transfer impedance are shown in Fig. 6. At lower frequencies, the transfer impedance in the simulation is equal to the direct current (DC) resistance of the shield. At higher frequencies, the transfer impedance parameter increases with increasing frequency, and the effectiveness of the shield decreases because of the apertures in the shield. Transmission line effects are present up from frequency $f \approx 50$ MHz in measurement results and up from $f \approx 200$ MHz in simulated results. Transmission line effects are present because of the reflections that can never be fully eliminated. Reflections are created by changes in impedance, and the main cause of changes in impedance are transitions in the line's geometry. Primarily at the places where the connector is connected to the cable, and where male and female parts of the connector are connected.

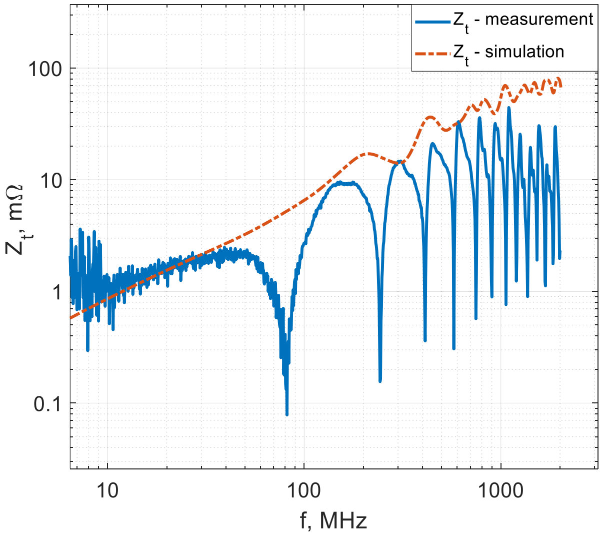

Fig. 6. Measured and simulated transfer impedance parameter of HSD connector.

Manufactured connector has production imperfections that cause discrepancies between simulation and measurement. Discontinuities caused by seams and small gaps, especially those between adjacent surfaces are hard to recreate in 3D model. At those areas, geometry is approximated. In spite of existing differences, the results are useful in design phase of connector.

Simulation data is analyzed with Feature Selective Validation (FSV) method [20-23]. The FSV method allows for objective, quantified comparison of data. It is widely used for validation and assessment of different models in computational electromagnetics. The FSV tool gives GRADE = 3 and SPREAD = 3 for FDM evaluation of the comparison in Fig. 6.

IV. CIRCUIT SIMULATION

The shield exhibits linear electric and magnetic properties, meaning that its performance does not depend on the amplitude of the currents and fields. The transformation data between voltages and currents ensures that wave effects are included in the circuit simulations, but only significant coupling can be transferred.

Extracted circuit model can be imported into a circuit simulator to explore various optimization strategies. For example, combining the connector with other lumped and distributed models for analysis of a larger system with satisfying level of accuracy. In this case, the shield is modelled as a multipole. The ratio of the voltage at one port of such circuit to the current at the other port is Z_{21}. In Fig. 7 the equivalent circuit of the modeled problem is presented, however, instead of S-parameters, Z_t is calculated by using the equation:

$$Z_t = \frac{V_{core}}{I_{shield}}. \tag{8}$$

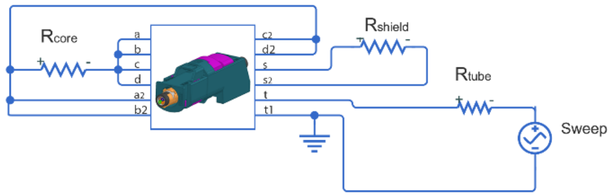

Fig. 7. Circuit model of a triaxial setup.

The computation result of the transfer impedance with circuit theory and its comparison against measurements and calculation with transmission line approach are shown in Fig. 8. The results of both models are in good agreement with the measurements.

A screened symmetrical multi-conductor cable is treated as a quasi-coaxial system as proposed in [24]. The conductors of all pairs are connected together at both ends. All screens, also those of individually screened pairs or quads, are connected together at both ends. The screens are connected over the whole circumference as proposed in [25].

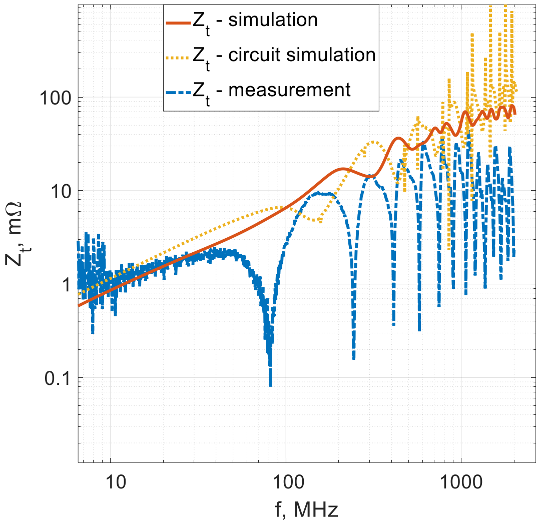

Fig. 8. Measured and simulated transfer impedance parameter of HSD connector.

Many mechanical and manufacturing related constraints affect the final design of the connector and the shield EMI performance. For example, some apertures in the shield of the connector are present because parts of the shield are designed as carriers for the plastic casing of the connector. Other problems are present because the shield is bent into the shape of a cylinder and it is not a seamless tube. Also, the thickness of the shield is primarily defined by mechanical properties, not by electrical properties.

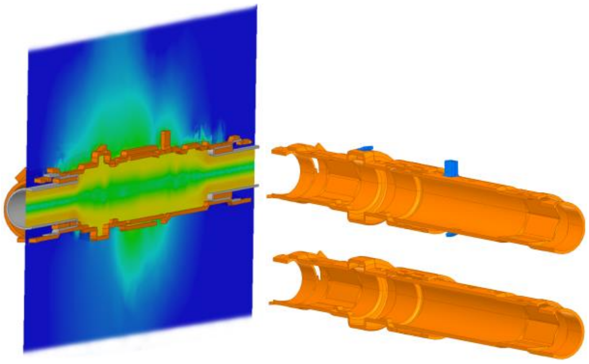

(a) (b)

Fig. 9. Cross-section of the connector shield with plotted magnetic field and identified leakage spots.

Based on the field leakage shown in Fig. 9 (a) the worst parts of the shield were improved to see the possible improvement on the efficiency of the shield at the cost of plastic carriers being designed in another way. The cross section of the connector shields before and after modification is shown in Fig. 9 (b). An improved model, according to Fig. 9 (b) is simulated by using ANSYS HFSS and compared to the original model. Figure 10 shows the result of simulation with the modified model. As expected, the effectiveness of the shield increases due to the improvement in shield geometry.

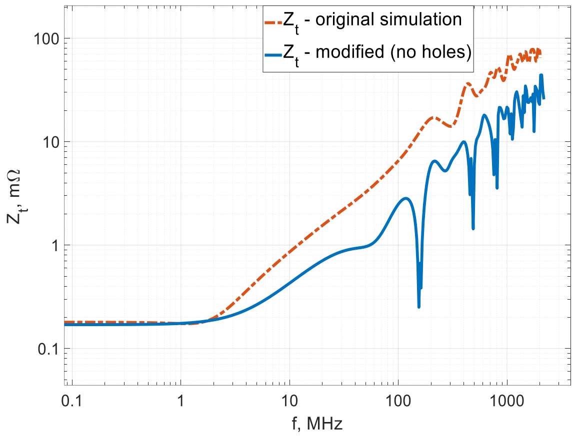

Fig. 10. Effect of shield modifications on transfer impedance.

V. CONCLUSION

A required step before starting the FEM analysis is the generation of CAD geometry to represent the actual device under test. Generating geometry for a braided wire shield, one of the most commonly used type of shields in the cable industry is a time-consuming task. There are numerous researches on creating complex geometries automatically by using different algorithms [26,27]. Also, tools and analytical models for the electromagnetic analysis of braided cable shields with general geometries are in constant development [28].

The complex geometry of the used HSD connector is considered in this paper. Due to complexity, there are no generalized solutions available. The presented work describes methods for the numerical calculation of the transfer impedance of such complex geometry by using FEM. One method is based on the simulation of scattering parameters while the other assumes that the connector is electrically small so that it can be modeled as a lumped element. Numerical solutions are not always suitable for a general analysis of the studied phenomena [29]. That is why the expansion of one numerical solution over a wide class of problems is not always possible. However, numerical solutions can be adapted to a range of connector sizes and different geometry configurations that use complex geometries and materials. Predicting the value of the transfer impedance of the connector shield before its manufacturing saves time and money. It allows the manufacturing process optimization based on the sensitivity of the shield performance to the changes of tolerances in specific parts. It also enables EMI performance optimization because of the possibility of testing a variety of different design possibilities before manufacturing.

REFERENCES

[1] S. A. Schelkunoff, “The electromagnetic theory of coaxial transmission lines and cylindrical shields,” *Bell System Technical Journal*, vol. 13, pp. 532-579, 1934.

[2] E. F. Vance, *Coupling to Shielded Cables*. John Wiley & Sons, p. 183, 1978.

[3] *Morrison R. Grounding and Shielding Techniques in Instrumentation*. John Wiley & Sons, p. 172, 1986.

[4] E. F. Vance, “Shielding effectiveness of braided-wire shields,” in *IEEE Transactions on Electromagnetic Compatibility*, vol. EMC-17, no. 2, pp. 71-77, May 1975.

[5] C. Chrisopoulus, J. F. Dawson, M. D. Ganley, A. C. Marvin, S. J. Porter, M. P. Robinson, T. M. Benson, and D. W. P. Thomas, “Analytical formulation for the shielding effectiveness of enclosures with apertures,” *IEEE Transactions on Electromagnetic Compatibility*, Aug. 1998.

[6] H. Kaden, Wirbelsrrome und Schirmung in der Nachrichtentechnik, pp. 21-24, 1959.

[7] T. Kley, “Optimized single-braided cable shields,” in *IEEE Transactions on Electromagnetic Compatibility*, vol. 35, no. 1, pp. 1-9, Feb. 1993.

[8] M. Tyni, “The transfer impedance of coaxial cables with braided outer conductor,” in *Wroclow EMC Symp.*, pp. 410-419, 1976.

[9] N. Mora, F. Rachidi, P. Pelissou, and A. Junge, “An improved formula for the transfer impedance of two-layer braided cable shields,” in *IEEE Transactions on Electromagnetic Compatibility*, vol. 57, no. 3, pp. 607-610, June 2015.

[10] J. H. G. J. L. Rotgerink, H. Schippers, and J. Verpoorte, “Multi-conductor transmission line modelling of transfer impedance measurement methods,” *2017 International Symposium on Electromagnetic Compatibility - EMC EUROPE*, Angers, pp. 1-7, 2017.

[11] A. Tsaliovich, *Cable Shielding for Electromagnetic Compatibility*, Springer US, 1995.

[12] H. Ott, *Electromagnetic Compatibility Engineering*, Wiley, 2009.

[13] R. W. Latham, “Small Holes in Cable Shields,” Interaction Notes, Note 118, AFWL Kirtland AFB, NM, Sept. 1972.

[14] P. Madle, “Contact resistance and porpoising effects in braid shielded cables,” *Proceedings of the 1980 IEE International Symposium on*

Electromagnetic Compatibility, Baltimore, MD, pp. 206-210, 1980.

[15] S. Cellozzi and M. Feliziani, "FEM Analysis of the plane-wave electromagnetic field coupling to a multiconductor line," *Proceedings of the 9th International Symposium and Technical Exhibition on Electromagnetic Compatibility*, Zurich, Switzerland, pp. 127-132, 1991.

[16] M. Sadiku, *Numerical Techniques in Electromagnetics*, Boca Raton, FL: CRC Press, 1992.

[17] ANSYS HFSS software user's guide, 2017.

[18] S. F. A. Mushtaq, "Transfer impedance simulation and measurement methods to analyze shielding behavior of HV cables used in electric- vehicles and hybrid-electric-vehicles," *Advances in Radio Science*, pp. 139-145, 2016.

[19] L. O. Hoeft, J. L. Knighten, and M. Ahmad, "Measured surface transfer impedance of multi-pin micro-D subminiature and LFH/sup TM/ connector assemblies at frequencies up to 1 GHz," 1999 *IEEE International Symposium on Electromagnetic Compatibility. Symposium Record* (Cat. No. 99CH36261), Seattle, WA, USApp, vol. 2, pp. 577-582, 1999.

[20] IEEE Standard P1597, Standard for Validation of Computational Electromagnetics Computer Modeling and Simulation – Part 1, Feb. 2008.

[21] A. P. Duffy, A. J. M. Martin, A. Orlandi, G. Antonini, T. M. Benson, and M. S. Woolfson, "Feature selective validation (FSV) for validation of computational electromagnetics (CEM). Part I – The FSV method," *IEEE Trans. on Electromagn. Compatibility*, vol. 48, no. 3, pp. 449-459, Aug. 2006.

[22] A. Orlandi, A. P. Duffy, B. Archambeault, G. Antonini, D. Coleby, and S. Connor, "Feature selective balidation (FSV) for validation of computational electromagnetics (CEM). Part II – Assessment of FSV performance," *IEEE Trans. on Electromagn. Compatibility*, vol. 48, no. 3, pp. 460-467, Aug. 2006.

[23] J. Bai, G. Zhang, L. Wang, A. Duffy, C. Liu, and T. Shao, "Comparison of calculation methods of braided shield cable transfer impedance using FSV method," *Applied Computational Electromagnetics Society Journal*, vol. 30, no. 2, pp. 140-47, 2015.

[24] IEC 621 53-4-15, Metallic communication cable test methods. Part 4-3: Electromagnetic compatibility (EMC) surface transfer impedance triaxial method.

[25] IEC 621 53-4-7, Metallic communication cable test methods: Electromagnetic compatibility (EMC) - Test method for measuring of transfer impedance Zt and screening attenuation as or coupling attenuation ac of connectors and assemblies up to and above 3 GHz, triaxial tube in tube method.

[26] J. Jin, *The Finite Element Method in Electromagnetics*, 2nd ed., John Wiley & Sons, 2002.

[27] R. Otin, O. Fruitos, R. Isanta, and R. Mendez, "Gid interface for the parametric generation of simplified braided- wire shields geometries," 2010.

[28] H. Schippers, R. Isanta, R. Otina, and J. Verpoorte, "A finite element tool for the electromagnetic analysis of braided cable shields," *Computer Physics Communications*, 191, pp. 209-220, June 2015.

[29] A. T. Adams, J. Perini, M. Miyabayashi, D. H. Shau, and K. Heidary, "Electromagnetic field-to-wire coupling in the SHF frequency range and beyond," in *IEEE Transactions on Electromagnetic Compatibility*, vol. EMC-29, no. 2, pp. 126-131, May 1987.

Research on Topology of Axial Flux Permanent Magnet Synchronous Generator

Zhu Jun, Cao Di, Li Guanghua, Zhang Zhenyi, Shuaihui Li, and Song Dandan

Department of Electrical Engineering
School of Electrical Engineering and Automation, Henan Polytechnic University,Jiaozuo, 454000, China
zhujunnd@163.com, 18638021265@163.com

Abstract – Through the comparative study of the TORUS-NN and TORUS-NS topologies for the axial flux permanent magnet synchronous generator (AFPMSG), it is shown that the AFG with single stator double rotors topology is suitable for vertical axis wind turbines (VAWT). The basic parameters are designed and their 3D finite element models are established for the two topologies, which are compared and analyzed respectively on the same amount of magnets and windings, the magnetic density, THD value, torque ripple and efficiency. The research shows that the efficiency of TORUS-NN structure is only 0.22% higher than that of TORUS-NS structure with the same amount of magnetic steel, but the torque ripple of TORUS-NN structure is much greater than that of TORUS-NS structure, when the amount of magnet steel and the winding are the same, the efficiency of TORUS-NS structure is 8.5% higher than TORUS-NN structure. Considering their performance and economy, the TORUS-NS structure is superior to TORUS-NN topology structure for VAWT in starting torque and low wind speed. The experimental results and finite element analysis results are within the allowable error range, which verifies the feasibility and superiority of TORUS-NS topology for VAWT.

Index Terms – Efficiency, finite element analysis, TORUS topology, vertical axis wind turbines.

I. INTRODUCTION

Wind power generation is one of the most mature, scalable and commercialized power generation methods in the field of renewable energy besides water energy [1]. Disc permanent magnet motors have been widely used in electric vehicles, wind power generation, ship driving, heart pumps and so on, because of their compact structure, high efficiency and high power density [2,3].

In view of the special working conditions of wind power generation, single stator and double rotors (also known as TORUS structure) have larger moment of inertia, and have better effect on suppressing the EMF fluctuation caused by wind fluctuation [4]. For structures with one or more pairs of axial rotors, their structures can be divided into three categories: TORUS-NS structure, TORUS-NN structure and hybrid structure, among which TORUS-NS structure and TORUS-NN structure are more common. Axial flux generator can be divided into fan-shaped, ring-shaped and fan-ring hybrid windings according to different winding forms [5-7]. The topology structure studied in this paper is applied to small vertical axis wind turbine. It is widely favored because of its simple structure, low starting wind speed, low noise and large moment of inertia [8]. In [9], by comparing the topological structure of single stator and double rotor generator with iron core or coreless, it is showed that the performance of coreless structure is better than the iron core structure though the comprehensive analysis of torque ripple, efficiency and THD value and other parameters. In [10], a permanent magnet synchronous motor (PMSM) with wedge-shaped air gap and no iron core based on Halbach array is proposed. The FEM method is used to model the 16-pole disk permanent magnet synchronous motor. The optimal solution region is obtained by comparing the sizes of different air caps. Then the static magnetic field of uniform air gap and wedge air gap is compared. In [11], three kinds of special axial flux permanent magnet motors are designed and their important dimensions are optimized. At the same time, the electromagnetic performance and stator vibration modes are compared and studied. Reference [12] compares the traditional stator toothed and stator toothless structures of axial permanent magnet motors. Quasi three dimensional finite element method is used to analyze the effect of stator structure change on the copper and iron losses of armature windings. In [13], the efficiency and temperature of coreless permanent magnet generator are taken as optimization objectives, and single variable parametric analysis and multi-dimensional optimization method are adopted. The corresponding parameterized model is established and programmed. The loss of each part of the motor is analyzed by using Matlab. After comprehensive analysis, the optimal values of efficiency and temperature are found in the spatial distribution of multidimensional design. In [14], a kind of Halbach array coreless axial

Submitted On: September 9, 2019
Accepted On: December 15, 2019

permanent magnet motor with combined magnetic poles is proposed. The pole arc coefficients of permanent magnets and soft magnetic materials are determined by using three-dimensional finite element analysis method under the condition that the air gap magnetic density is guaranteed. In [15], a disk permanent magnet generator is designed to be used in the power generation system of weapon platform. According to the basic electromagnetic relationship and the special requirements of the generator, the basic parameters of the generator are obtained and the magnetic field is simulated in Maxwell. Reference [16] presents a multi-objective optimization design method for axial permanent magnet generator based on Taguchi response surface method. The main characteristics such as generator efficiency, power quality and induction induced voltage are optimized. The validity of the optimization method is verified by finite element analysis and prototype test. In [17], the different cogging torque values of the magnet pole-arc are studied for triangle type, oval and fan type magnets. Thereby, a rotor structure with a small cogging torque is obtained. In [18], two torque optimization methods are proposed, and a three-dimensional finite element model is established to verify the analytical results of multi-objective genetic algorithm. Compared with the skew technique to verify the superiority for the two methods.

In summary, the single stator and double rotor structure of disk-type axial permanent magnet generator has a wide range of applications. The TORUS-NS and the TORUS-NN are named according to the distribution of its magnetic circuit and magnetic pole. The magnetization direction of the two relative magnetic poles is opposite for the TORUS-NN structure, and the magnetic circuit formed is shown in Fig. 1 (a). The magnetization direction of the two relative magnetic poles is same for the TORUS-NS structure and the magnetic circuit formed is shown in Fig. 1 (b).

In this paper, the structures of TORUS-NN and TORUS-NS are compared and analyzed, and a suitable topology for low-power wind turbines is selected by comparing the air gap magnetic density, efficiency, torque ripple and power quality. In this paper, TORUS-NN can only use fan-shaped windings with stator core due to the limitation of its topological structure. The magnetic path starts from N pole and passes through air gap, coil and stator core to S pole to form a magnetic path. The magnetic path at left and right ends is symmetrical, so the direction of induced current generated by the coils on both sides is opposite. The TORUS-NS structure adopts a coreless fan-shaped winding. The 3D FEA analysis was performed by Magnet software. In the 3D model, the magnetic field is unsaturated. The magnetic path passes through the winding and the uniform air gap on both sides formed a closed loop, as shown in Fig. 1.

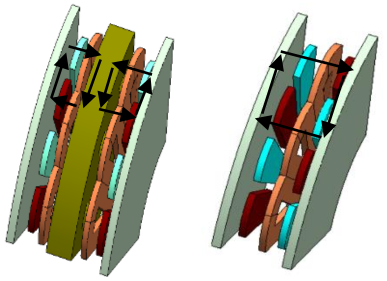
(a) (b)

Fig. 1. Three-dimensional finite element model of generator: (a) structure of TORUS-NN, and (b) structure of TORUS-NS.

II. DESIGN OF AXIAL FLUX GENERATOR

A. Basic electromagnetic relations

For disc generator, if a single conductor is considered, the position of the plane is expressed by radius and polar angle. The air gap flux density is represented by the magnetic flux density at the average radius, which can be written as B_δ. The maximum induced voltage produced by a single conductor can be obtained:

$$e(\theta)=\Omega\int_{Di/2}^{D_o/2}B_\delta(\theta)rdr=\frac{1}{8}\Omega(D_o{}^2-D_i{}^2)B_\delta(\theta). \qquad (1)$$

The average induced voltage produced by a single conductor is:

$$E_{av}=\frac{p}{\pi}\int_0^{\pi/p}e(\theta)d\theta=\frac{1}{8}\Omega(D_o{}^2-D_i{}^2)B_{\delta av}. \qquad (2)$$

Where Ω is the mechanical angular velocity, D_o is generator's magnetic pole outer diameter, D_i is generator's magnetic pole inner diameter, $B_{\delta av}$ is average air gap magnetic density.

Armature induced voltage of generator:

$$E=\frac{NE_{av}}{2a}=C_e\Phi n, \qquad (3)$$

where

$$\begin{cases}C_e=\dfrac{pN}{60a}\\ \Phi=\dfrac{\pi}{8p}B_{\delta v}(D_o{}^2-D_i{}^2),\end{cases} \qquad (4)$$

a is the pairs of parallel branches of winding, N is the number of total conductors, p is number of pole pairs, n is rated speed, C_e is electromotive force constant, Φ is magnetic flux.

The effective conductor of the winding of disc generator radiates radially in space, and the electric load at the inner end of the winding is the largest. If the electric load at the minimum diameter of the generator is taken into account, its electromagnetic power can be obtained from equation (5):

$$p_{em}=EI=\frac{\pi^2}{240}nB_{\delta av}A_{\max}(D_o{}^2-D_i{}^2)D_i, \qquad (5)$$

where A_{max} is maximum electric load.

B. Design of structural parameters

Firstly, the inner and outer diameters of disc generator are determined. According to the output power and operating speed of the axial flux permanent magnet generator selected in this paper, the electric load is 1000A/m. This paper designs a small generator with rated power of 300W and rated speed of 300rpm. Derivative of power ratio between inner and outer diameter is obtained, when $\gamma = \sqrt{3}$, the output power of the generator is the largest, then the outer diameter of the permanent magnet can be obtained from equation (6) [19]:

$$D_o = \sqrt[3]{\frac{\gamma^3 P}{\frac{\pi^2}{120} m n \alpha_i k_w B_\delta A_{av} (\gamma^2 - 1)(\gamma + 1)}} . \tag{6}$$

Where m is armature winding phase number, α_i is the calculation of pole arc coefficient, k_w is the coefficient of armature winding, A_{av} is average electric load, P is generator power.

The length of permanent magnet can be expressed as [20]:

$$L_{\mathrm{PM}} = \frac{\mu_r B_g}{B_{\mathrm{r}} - B_g K_f / K_d} (g + W_{\mathrm{cu}}) . \tag{7}$$

Where K_f is the disc generator air gap flux density in the radial direction of the maximum correction coefficient, K_d is the magnetic leakage coefficient, W_{cu} is armature winding end extension length, $\mathrm{B_g}$ is air gap flux density, g is air gap length, μ_r is relative permeability.

When the speed is constant, the number of pole pairs is 10 can be obtained according to p=60f/n. In this paper, the number of coils can be determined to be 15 when the span electric angle of armature winding is 240 degrees. Polar arc coefficient has an effect on the amplitude of air gap magnetic density. When the pole arc coefficient is too small, the magnitude of magnetic density is low, if the pole arc coefficient is too large, the economy cannot be guaranteed, so pole arc coefficient is 0.78.

Table 1: Structural parameters of two prototype

Parameters	**Value**
Rated power	300 W
Rated speed	300 rpm
Rated line voltage	30 V
Inner diameter of permanent magnet	140 mm
Outer diameter of permanent magnet	240 mm
Back iron inner diameter	110 mm
Back iron outer diameter	270 mm
Pole arc coefficient	0.78
Permanent magnet thickness	4.5 mm
One side air gap length	1 mm

The above design parameters are suitable for two different topologies, but the stator core structure is adopted in the TORUS-NN structure, so the influence of the saturation and thickness of the core on the output power quality should also be considered. Magnet software can get all kinds of data needed in this paper. These analyses are completed with a computer with 2.3GHz Intel Core i5-8300H and 7.86 GB of RAM. The CPU processing time is 37 minutes.

The optimum core thickness is selected by comparing different core thickness, as shown in Fig. 2.

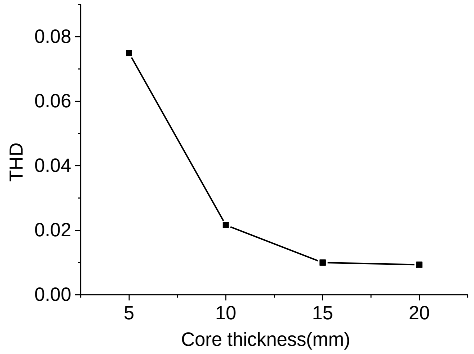

Fig. 2. THD with different core thickness.

As shown in Fig. 2, the THD (total harmonic distortion) value decreases with the increase of core thickness. The output power of the two kinds of topological junctions should be compared quantitatively, and the THD of the TORUS-NS structure is also low. Therefore, the thickness of stator core is 20 mm.

III. COMPARATIVE STUDY OF TWO TOPOLOGICAL STRUCTURES

A. Contrastive study for isomagnetic steel consumption

Because the core of TORUS-NN structure is used as the conducting medium of the magnetic path for the generator, which is stronger than the air conductivity of TORUS-NS structure, it is necessary to adjust the number of coil turns for the TORUS-NN structure so that the output power of the two topological structures is the same. After optimization, the turn number of TORUS-NN coil is 60, and the thickness of one side coil is 4.2 mm. When the amount of permanent magnets used in the two topologies is the same, the efficiency, magnetic density amplitude and total harmonic distortion (THD) of the two topologies are compared under different air gaps.

According to the detailed analysis of Fig. 3 (a), the average magnetic density of TORUS-NN structure is 6.03% higher than that of TORUS-NS structure. From Fig. 3 (b), the efficiency of TORUS-NN structure is 0.22% higher than that of TORUS-NS structure except that the efficiency of TORUS-NN structure is lower when the air gap is 0.7. The maximum THD value of TORUS-NN structure is much lower than that of TORUS-NS structure, as shown in Fig. 3 (c), but both of them meet the requirement of national standard THD not exceeding 5%.

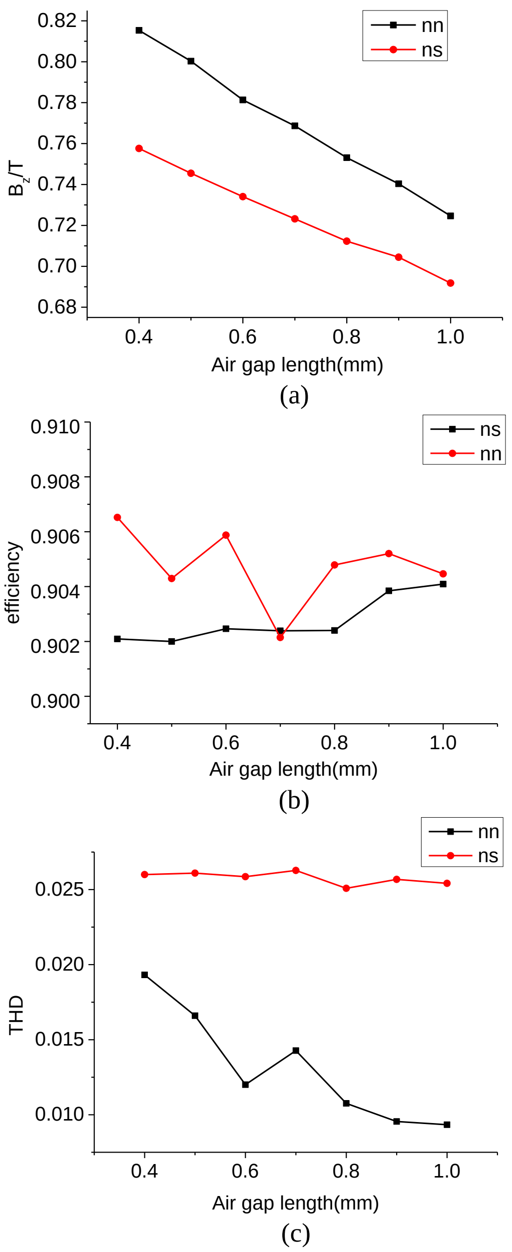

(a)

(b)

(c)

Fig. 3. (a) Comparison of magnetic density, (b) comparison of efficiency, and (c) comparison of THD values.

In the case of 0.4mm air gap and 1mm air gap, the difference between them in the magnitude, efficiency and THD of magnetic density is the smallest and the largest, respectively, and then the fundamental wave and each harmonic wave of the two are compared. According to Fig. 4, the fundamental wave, fifth and seventh harmonics of TORUS-NN structure are higher than those of TORUS-NS structure under two kinds of air gap, but the third harmonic is lower than that of TORUS-NS structure. Because of the factors of topological structure, the cogging torque will be produced in the TORUS-NN structure, then the electromagnetic torque of the generator will fluctuate, so the torque ripple of the TORUS -NS structure will be smaller than that of the TORUS-NN structure. In this paper, two structures with 1 mm air gap are selected to compare the torque ripple, as shown in Fig. 5. The TORUS-NS torque is basically stable at - 11N·m, while the TORUS-NN structure's torque ripple amplification diagram is jagged, and the torque ripple is large.

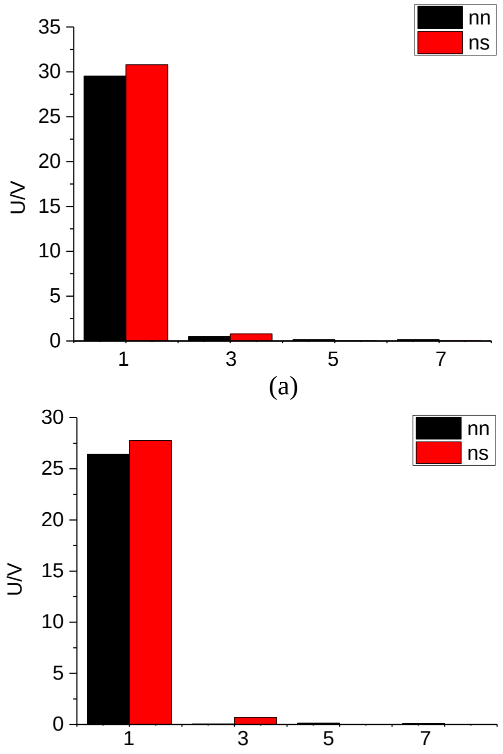

(a)

(b)

Fig. 4. Comparison of harmonic contents of two topological structures in different air gaps: (a) in 0.4mm air gap and (b) in 1 mm air gap.

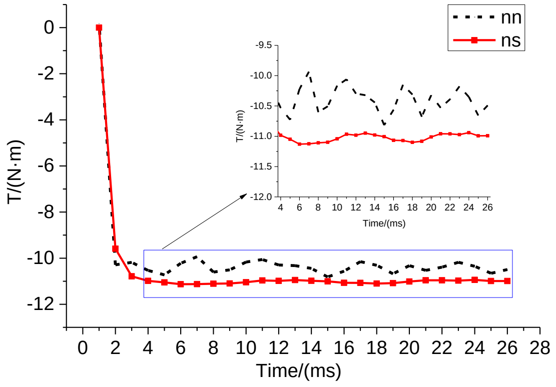

Fig. 5. Comparison of torque ripple of two structures in 1 mm air gap.

B . Contrastive study for equal turns of equal winding thickness with equal magnet steel dosage

The thickness of permanent magnet is set to 4.5mm for the two topological structures. Because the coil of TORUS-NS structure is single layer and the coil thickness is 4.2mm, in order to compare the winding thickness as a fixed value, the thickness of windings on both sides is set to 2.1mm for the TORUS-NN structure. The coil turns of the two structures are set to 155. Change the air gap of the two topologies, and compare the efficiency and THD value of the two topologies under the same air gap, as shown in Fig. 6.

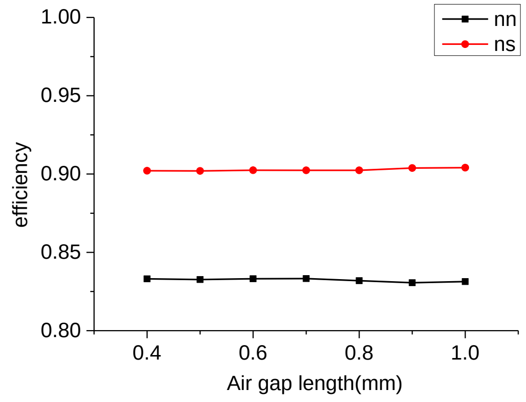

(a)

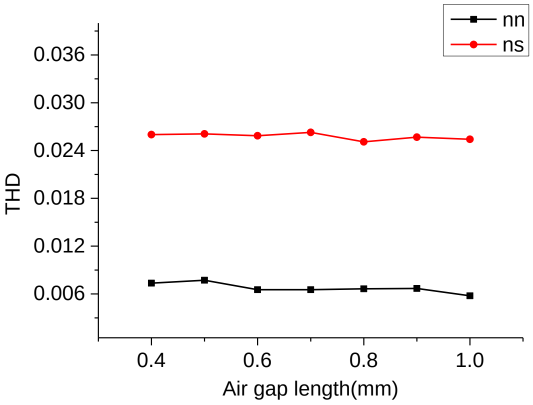

(b)

Fig. 6. (a) Comparison of efficiency, and (b) comparison of THD values.

According to the analysis of Fig. 6 (a), when the thickness of permanent magnet, winding turns and thickness are the same, the efficiency of TORUS-NS structure is 8.5% higher than that of TORUS-NN structure on average. As shown in Fig. 6 (b), the THD value of TORUS-NN structure is lower and its harmonic content is less than that of TORUS-NS structure. Although the total harmonic content of the TORUS-NN structure is low and the sinusoidal waveform is good, the cogging torque of the TORUS-NN structure affects the magnitude and the torque stability. And eddy current loss will occur in the stator core, which reduces the efficiency of the motor. In this case, the performance of TORUS-NS structure is better than that of TORUS-NN structure.

Based on the two kinds of comparative analysis above, the TORUS-NS structure does not need to consider the effect of the iron core on the voltage distortion rate. In terms of efficiency, there is little difference between them, and in the second comparison, the TORUS-NS efficiency is all higher than the TORUS-NN efficiency in different air gaps. The efficiency of TORUS-NS is higher than that of TORUS-NN under different air gaps. In terms of electromagnetic torque, the TORUS-NS structure is superior to the TORUS-NN structure in terms of both the stability and size of the torque. At the same time, in the case of similar performance indicators, there is coreless in TORUS-NS structure, which guarantees the economy of manufacturing generators, and provides the possibility for batch production of motors and the manufacture of this prototype.

IV. EXPERIMENT

In order to verify the correctness of theoretical analysis and finite element simulation results, a generator with TORUS-NS structure is designed and manufactured. The rated speed is 300 rpm. The armature winding adopts concentrated winding to reduce end connection length and copper consumption, and the winding is fixed on the stator disc with epoxy resin. The permanent magnet is glued to the back iron with structural adhesive to prevent the permanent magnet from falling off. After the prototype is completed, the experimental platform is built, as shown in Fig. 7 and Fig. 8. The speed of the induction motor is adjusted by the frequency converter. And the three-phase induction motor drives the permanent magnet generator to rotate through the reducer and coupling. The rated power of the three-phase induction motor is 1500W, and the rated phase voltage is 220V. The input line voltage of the frequency converter is 350-450v, and the output line voltage is 0-380V.The required voltage and current are output by the rectifier inverter device.

Fig. 7. Prototype structure of generator.

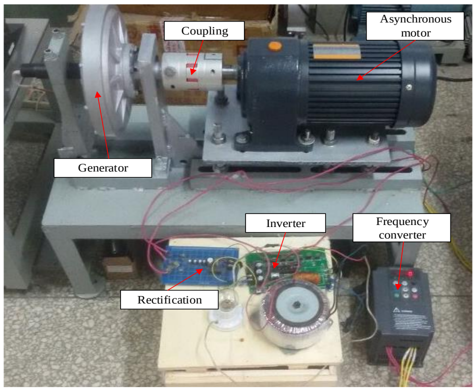

Fig. 8. Experimental platform.

No-load experiments are carried out on the prototype at different rotational speeds. As shown in Fig. 9, the output voltage waveform of the generator at the speed of 150 rpm and 250 rpm contains more harmonics, but the waveform is still sinusoidal. The generator can output relatively smooth sinusoidal waveform when its speed is 300 rpm. The amplitude of the output phase voltage of the prototype is 26.55V, which is similar to 27.2V of the FEM simulation result, as shown in Fig. 10. According to no-load voltage, the experimental THD value is 2.05% and the finite element analysis is 2.5%. In the error range, the experiment and simulation results are similar, which verifies the correctness of the above theoretical analysis.

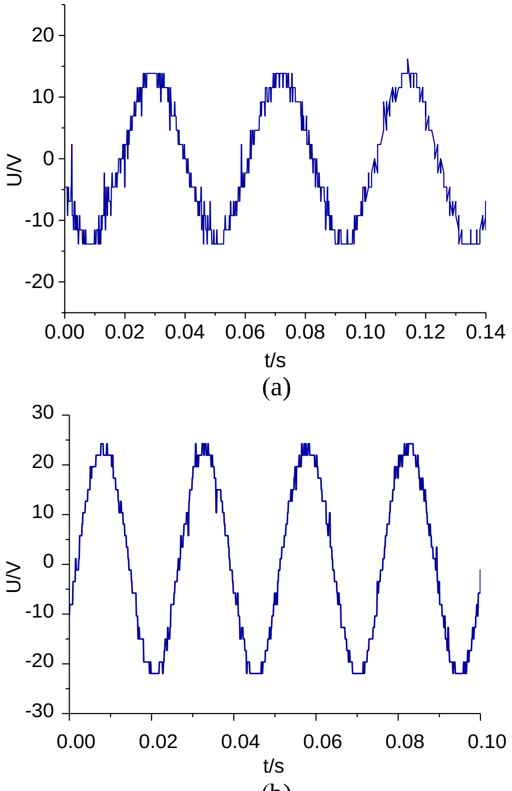

(a)

(b)

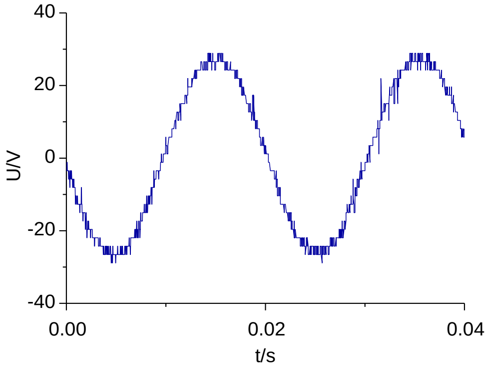

(c)

Fig. 9. Measured output voltage waveform of prototype at different rotational speeds: (a) at 150 rpm speed, (b) at 250 rpm speed, and (c) at 300 rpm speed.

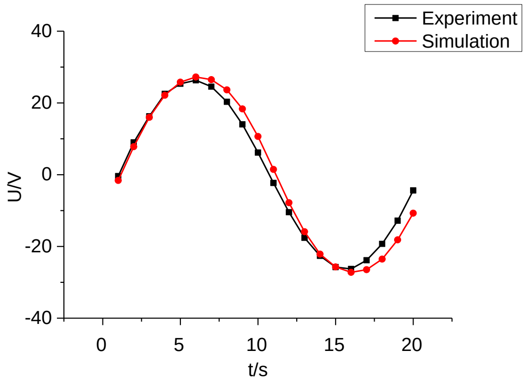

Fig. 10. Comparison of output voltage waveforms.

V. CONCLUSION

This paper divides the structure of TORUS-NN and TORUS-NS into two cases. The efficiency of TORUS-NN structure is only 0.22% higher than that of TORUS-NS structure when the amount of magnet steel is the same, but the efficiency of TORUS-NS structure is 8.5% higher than that of TORUS-NN structure when the amount of magnet steel and winding is the same. Because of the cogging torque, the torque ripple of the TORUS-NN structure is greatly. TORUS-NS structure does not need stator core as magnetic path, which reduces the cost of generators. Comprehensive analysis of TORUS-NS structure as generator structure has great advantages. The prototype data produced are similar to the finite element simulation results, and it is suitable for the generator with vertical axial flux.

ACKNOWLEDGMENT

The study was supported by the key research of development and promotion of Henan Province (182102210052); key development and extension projects in Henan Province and the project supported by special funds for basic research and operation of colleges and universities of Henan Province (NSFRF140115); young backbone teachers program of Henan Polytechnic University (2018XQG-08); mine power electronic device and control innovation type scientific and technological team of Henan Province.

REFERENCES

[1] K.-Y. Shen, "Wind energy resources and wind power generation in China," *Northwest Hydropower*, vol. 29, no. 1, pp. 76-80, 2010.

[2] Y. Huang, T. Zhou, and J. Dong, "An overview on developments and researches of axial flux permanent magnet machines," *Proceedings of the CSEE*, vol. 35, no. 1, pp. 192-204, 2015.

[3] Z. Geng and G. Li, "Overview of axial flux permanent 一 magnet machine," *Small & Special Electrical Machines*, vol. 43, no. 9, pp. 88-99, 2015.

[4] D. He, "The Design Study for Disk-type Permanent-magnet Synchronous Generator in the Wind Power Generation System," *Changsha: Hunan University*, 2006.

[5] X. Wei, "Research of a Multistage Axial Flux Permanent Magnet Machine," *Wuhan: Huazhong University of Science and Technology*, 2015.

[6] F. G. Cappon, G. De Donato, and F. Caricchi, "Recent advances in axial-flux permanent-magnet machine technology," *IEEE Transactions on Industry Applications*, vol. 48, no. 6, pp. 2190-2203, 2012.

[7] T. J. Woolmer and M. D. McCulloch, "Analysis of the yokeless and segmented armature machine," *International Electric Machines & Drives Conference, IEEE*, Antalya, 2007.

[8] T. Sun, "Research on Small Vertical - Axis Wind Turbine for Distributed Power Generation," *Shijiazhuang: Hebei University of Science and Technology*, 2017.

[9] J. Zhu, D.-D. Song, and Q.-L. Han, "Comparative research on performance of iron and ironless axial flux wind generators," *Journal of Astronautic Metrology and Measurement*, vol. 38, no. 4, pp. 79-85, 2018.

[10] X. Wang and R. Tang, "Optimization of disk coreless permanent magnet synchronous motor based on Halbach—the wedgy airgap motor," *Transactions of China Electrotechnical Society*, vol. 22, no. 3, pp. 2-5, 2007.

[11] H. Li and J. Shen, "FEA-based design and comparative study of axial flux permanent magnet machines with various topologies," *Transactions of China, Electrotechnical Society*, vol. 30, no. 14, pp. 32-40, 2015.

[12] A. Arkadan, T. M. Hijazi, and B. Masri, "Design evaluation of conventional and toothless stator wind power axial-flux PM generator," *IEEE Transactions on Magnetics*, vol. 53, no. 6, pp. 1-4, 2017.

[13] C. Chen and Y. Wang, "Optimal design of axial-flux permanent magnet motors based on the efficiency and temperature rise," *Proceedings of the CSEE*, vol. 36, no. 6, pp. 1686-1692, 2016.

[14] Y. Cao, Y. Huang, L. Jin, and M. Hu, "Design and analysis of a stator coreless axial-flux permanent magnet machine with module poles," *Proceedings of the CSEE*, vol. 34, no. 6, pp. 903-907, 2014.

[15] J.-C. Zhao, "Electromagnetic design and simulation of disc type coreless permanent generator," *Small & Special Electrical Machines*, vol. 45, no. 6, pp. 45-53, 2017.

[16] J. Zhu and S. Li, "Multi-objective optimisation design of air cored axial flux PM generator," *IET Electric Power Applications*, vol. 12, no. 9, pp. 1390-1395, 2018.

[17] E. Aycicek, N. Bekiroglu, and I. Senol, "Rotor configuration for cogging torque minimization of the open-slot structured axial flux permanent magnet synchronous motors," *The Applied Computational Electromagnetics Society*, vol. 30, no. 4, pp. 396-408, 2015.

[18] S. Wu and S. Zuo, "Magnet modification to reduce pulsating torque for axial flux permanent magnet synchronous machines," *The Applied Computational Electromagnetics Society*, vol. 31, no. 3, pp. 294-303, 2016.

[19] B. Xia, "Research on Axial Flux Permanent Magnet Machine for Small-scale Vertical-axis Wind Power Application," *Hangzhou: Zhejiang University*, 2011.

[20] D.-R. Luo and Y.-N. Wang, "Design study of disk-type permanent-magnet synchronous generator," *Journal of Hunan University (Natural Sciences)*, vol. 33, no. 3, pp. 46-49.

Zhu Jun is engaged in the research of new energy wind power generation and sensorless control theory. Currently, the author has presided over more than 10 provincial projects; published more than 40 academic papers, including more than 20 SCI/EI; application for more than 10 patents. The current projects are: key scientific and technological breakthrough projects in Henan Province: the research of low-speed direct-drive magnetic levitation axial flux wind turbine is conducted from September 2017 to September 2019 with its project number

Cao Di is a graduate student, engaged in the design of the magnetic levitation new energy wind generator.